

# **Computer Simulation of Ethylene Glycol Oxidation and Methanol – Water Interactions**



**Christopher Andrew Lee**

**Thesis Submitted For The Degree Of PhD**

**May 2013**

**School of Chemistry**

**Cardiff University**

## **Acknowledgements**

I would like to offer my sincerest thanks to everyone who has contributed so much to make this thesis possible.

First of all, my academic supervisor Dr. David Willock and my mentor Professor Stan Golunski for all of their endless help, patience and guidance which has greatly influenced my scientific development.

I would also like to thank all of the members of the Theoretical Chemistry group at Cardiff University: Professor Peter Knowles, Dr. Massimo Mella, Dr. Jamie Platts, Adam Thetford, Niamh Hickey, Shaun Mutter, Soon Wen Hoh, Filippo Marozzelli, James Robinson, Andrew Jenkins, Glib Meleshko, Liam Thomas, Constantinos Zeinalipour-Yazdi, and Carlo Buono, for many hours of thought provoking discussion.

The Glycerol Challenge Group of the Cardiff Catalysis Institute: Professor Graham Hutchings, Professor David Knight, Dr. Stuart Taylor, Dr. Pete Miedziak, Gemma Brett, M. H. Haider, Yulia Ryabenkova and Tatyana Kationova for insights beyond the theoretical.

Thank you to The Materials Chemistry Consortium for use of the HECToR supercomputer, HPCWales for use of the HPCWales supercomputer, ARCCA for use the Merlin and Raven supercomputers, and their support teams with help with technical issues. Without these computational resources none of the calculations performed in this work would have been possible.

I would also like to thank the Cardiff University School of Chemistry, The Glycerol Challenge and DOW Chemical for funding my PhD.

Lastly thank you to my parents, Richard and Sandra without whose endless love, support and encouragement I would never have reached this far.

## **Papers Published**

Oxidative Esterification of Homologous 1,3-Propanediols, *Catal. Lett.*, 2012, **142**, 1114

## **DECLARATION**

This work has not been submitted in substance for any other degree or award at this or any other university or place of learning, nor is being submitted concurrently in candidature for any degree or other award.

Signed ..... (candidate)      Date.....

### **STATEMENT 1**

This thesis is being submitted in partial fulfillment of the requirements for the degree of .....(insert MCh, MD, MPhil, PhD etc, as appropriate)

Signed ..... (candidate)      Date.....

### **STATEMENT 2**

This thesis is the result of my own independent work/investigation, except where otherwise stated.

Other sources are acknowledged by explicit references. The views expressed are my own.

Signed ..... (candidate)      Date.....

### **STATEMENT 3**

I hereby give consent for my thesis, if accepted, to be available for photocopying and for inter-library loan, and for the title and summary to be made available to outside organisations.

Signed ..... (candidate)      Date.....

## Summary

In this project, density functional theory calculations were performed to study the adsorption of ethylene glycol to the MgO (100), MgO (130), Al<sub>2</sub>O<sub>3</sub> (0001), PdO (101) surfaces, as well as Au<sub>38</sub> and Au<sub>38</sub>O<sub>16</sub> nanoparticles. Adsorption of ethylene glycol is favourable to all of these surfaces with Al<sub>2</sub>O<sub>3</sub> (0001) and PdO (101) showing the most favourable adsorption at -168 kJ mol<sup>-1</sup> and -135 kJ mol<sup>-1</sup> respectively. The MgO surfaces showed adsorption energies between -80 kJ mol<sup>-1</sup> and -100 kJ mol<sup>-1</sup>, and the gold nanoparticles showed lower adsorption energies at approximately -35 kJ mol<sup>-1</sup>. Barriers to O-H activation and C-H activation of ethylene glycol were also studied on these surfaces. The barriers to O-H activation were small over each of the surfaces (between 8 and 46 kJ mol<sup>-1</sup>) and large for the gold nanoparticles (108 kJ mol<sup>-1</sup>). The barriers to C-H activation were very large over the MgO surfaces (>300 kJ mol<sup>-1</sup>), and lower over the PdO (101) surface (63 kJ mol<sup>-1</sup>) and the gold nanoparticles (68 kJ mol<sup>-1</sup>). C-H activation was found to not be possible over the Al<sub>2</sub>O<sub>3</sub> (0001) surface.

Classical molecular dynamics studies were performed on various water and methanol mixtures as well as in the presence of a hydroxylated Al<sub>2</sub>O<sub>3</sub> (0001) surface. It was found that in methanol there are on average 1.1 oxygen – oxygen close contacts with other methanol molecules in pure methanol, and water has on average between 2.03 and 2.86 oxygen – oxygen close contacts, with more being present at higher temperatures. The presence of a hydroxylated aluminium oxide surface induces local ordering in the methanol molecules resulting in an increase in methanol – methanol and water – methanol oxygen – oxygen contacts, however there is a decrease in water oxygen – water oxygen contacts.

## Table of Contents

Acknowledgements	I
Papers Published	II
Declaration	III
Summary	IV
<b>1. Introduction</b>	<b>1</b>
Bibliography	5
<b>2. Literature Review</b>	<b>6</b>
<b>2.1. Density Functional Theory Studies of Surfaces and Clusters</b>	<b>6</b>
<b>2.2. Molecular Dynamics Studies of Alcohols and Water</b>	<b>15</b>
<b>2.3. Heterogeneous Catalysis</b>	<b>22</b>
<b>2.4. Summary</b>	<b>26</b>
Bibliography	29
<b>3. Background Theory</b>	<b>32</b>
<b>3.1. Density Functional Theory</b>	<b>32</b>
<b>3.1.1. The PBE Functional</b>	<b>34</b>
<b>3.1.2. DFT+U</b>	<b>35</b>
<b>3.1.3. Hybrid DFT</b>	<b>36</b>
<b>3.2. Pseudopotentials</b>	<b>36</b>
<b>3.3. Periodic Systems</b>	<b>37</b>
<b>3.4. <i>k</i>-Point Sampling</b>	<b>38</b>
<b>3.5. Planewave Basis Sets</b>	<b>39</b>
<b>3.6. Bader Analysis</b>	<b>40</b>
<b>3.7. Density of States</b>	<b>41</b>
<b>3.8. Nudged Elastic Band Calculations</b>	<b>42</b>
<b>3.9. Molecular Dynamics</b>	<b>43</b>
<b>3.9.1. Force Fields</b>	<b>43</b>
<b>3.9.2. Classical Water Models</b>	<b>47</b>
<b>3.9.3. SPC/E</b>	<b>48</b>
<b>3.9.4. TIP4P and TIP4P/2005</b>	<b>48</b>
<b>3.9.5. Classical Molecular Dynamics Simulations</b>	<b>50</b>
<b>3.9.6. The Micro-Canonical Ensemble</b>	<b>52</b>
<b>3.9.7. The Isothermal – Isobaric Ensemble</b>	<b>52</b>
Bibliography	53
<b>4. Density Functional Theory Calculations</b>	<b>55</b>
<b>4.1. Magnesium Oxide</b>	<b>56</b>
<b>4.1.1. Determining the Appropriate Functional</b>	<b>57</b>
<b>4.1.2. Determining the Lattice Parameters</b>	<b>60</b>
<b>4.1.3. The MgO (100) and (130) Surfaces</b>	<b>61</b>
<b>4.1.4. Adsorption of Ethylene Glycol</b>	<b>66</b>

4.1.5.	O-H and C-H Activation Energy Barriers Over Magnesium Oxide	75
4.2.	Aluminium Oxide	81
4.2.1.	The Al <sub>2</sub> O <sub>3</sub> (0001) Surface	83
4.2.2.	Adsorption of Ethylene Glycol	86
4.2.3.	Adsorption of Water	88
4.2.4.	Adsorption of Ethylene Glycol and Water	94
4.2.5.	O-H Activation Barriers Over Aluminium Oxide	97
4.3.	Palladium Oxide	104
4.3.1.	Adsorption of Ethylene Glycol	107
4.3.2.	O-H and C-H Activation Energy Barriers Over Palladium Oxide	111
4.4.	Gold-38 Clusters	115
4.4.1.	Au <sub>38</sub> Cluster	115
4.4.2.	O-H and C-H Activation Energy Barriers With the Au <sub>38</sub> Cluster	119
4.4.3.	Au <sub>38</sub> O <sub>16</sub> Cluster	123
4.4.4.	O-H and C-H Activation Energy Barriers With the Au <sub>38</sub> O <sub>16</sub> Cluster	127
4.5.	Conclusions	131
	Bibliography	137
<b>5.</b>	<b>Classical Molecular Dynamics Calculations</b>	142
5.1.	Water	143
5.1.1.	Creating The Systems	143
5.1.2.	TIP4P/2005 Water	143
5.1.3.	SPC/E	152
5.2.	Methanol	155
5.2.1.	Radial Distribution Functions	157
5.3.	Water – Methanol Mixtures	160
5.3.1.	Combining the Potentials	160
5.3.2.	Simulating the Water – Methanol Mixtures	162
5.4.	The Al <sub>2</sub> O <sub>3</sub> (0001) Surface	175
5.4.1.	TIP4P/2005 Water	176
5.4.2.	PCFF Methanol	178
5.4.3.	TIP4P/2005 Water and PCFF Methanol	179
5.5.	Conclusions	180
	Bibliography	182
<b>6.</b>	<b>Conclusions and Future Directions</b>	184
6.1.	Conclusions	184
6.2.	Future Directions	186
	Bibliography	189
	Appendices	190
	Appendix 1 – DLPOLY FIELD Files	190
	DLPOLY FIELD File For TIP4P/2005 Water	190
	DLPOLY FIELD File For SPC/E Water	190

DLPOLY FIELD File For PCFF Methanol	190
DLPOLY FIELD File For CLAYFF Al <sub>2</sub> O <sub>3</sub> , TIP4P/2005 Water and PCFF Methanol	191
Appendix 2 – Source Codes	194
C Code to Generate a Cubic Box of TIP4P/2005 Water	194

## Chapter 1 – Introduction

In this project, studies have been undertaken looking at the mechanism of the oxidation of ethane-1,2-diol (hereafter referred to as ethylene glycol) using metal oxide catalysts and the interaction of water/alcohol mixtures with metal oxide surfaces using computer simulations.

Computer simulations allow for accurate tracking of the atoms involved in a chemical reaction (and hence the determination of the reaction mechanism) without the difficulty and expense of isotopically labelling the atoms thought to be involved if this were to be done experimentally.

Ethylene glycol is a very commonly used antifreeze, it is also used in the production of polyethylene terephthalate (PET), a very widely used plastic. Ethylene glycol is produced from ethylene oxide, which is itself produced from ethene. Ethene is produced on an industrial scale by the steam cracking of light hydrocarbons which are obtained from fossil fuels. Direct oxidation of ethene using a supported silver catalyst is a commonly used industrial method of producing ethylene oxide. In the presence of an acid catalyst ethylene oxide will react with water to produce ethylene glycol. Given that fossil fuels are a finite resource and their use is not environmentally friendly, alternative sources for ethylene glycol are being sought such as the hydrogenolysis of glycerol.

In 2006 almost one million tonnes of glycerol was produced as a byproduct of biodiesel manufacture, and global production is predicted to steadily increase as governments move to further encourage the production of renewable and more environmentally friendly fuels. Due to this, glycerol is a cheap and easily available molecule. The glycerol molecule itself is created during the transesterification of triglyceride vegetable oils such as sunflower oil, rapeseed oil and others. The methanolysis of a single triglyceride molecule will produce three methyl esters and one glycerol molecule (**Figure 1**) [1].

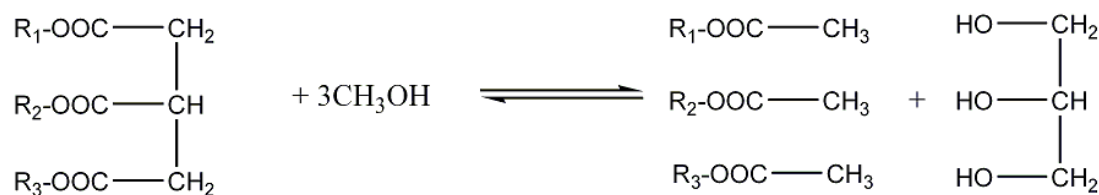


**Figure 1:** The transesterification (methanolysis) of a triglyceride producing three methyl esters and glycerol.

The glycerol molecule has three alcohol groups making it a useful intermediate in the production of more commercially and chemically valuable molecules such as 1,2-propanediol, ethylene glycol, acrolein and methanol among many other molecules (see **Figure 2**).

Many of the reactions using glycerol involve the presence of an acid or base as a catalyst in solution which is then discarded as waste at the end of the reaction. This also presents challenges in purifying and separating the resulting products. This project looks at simulating the action of solid oxide catalysts such as magnesium oxide, aluminium oxide and palladium oxide, as well as transition metal nanoparticles in heterogeneous catalytic reactions.

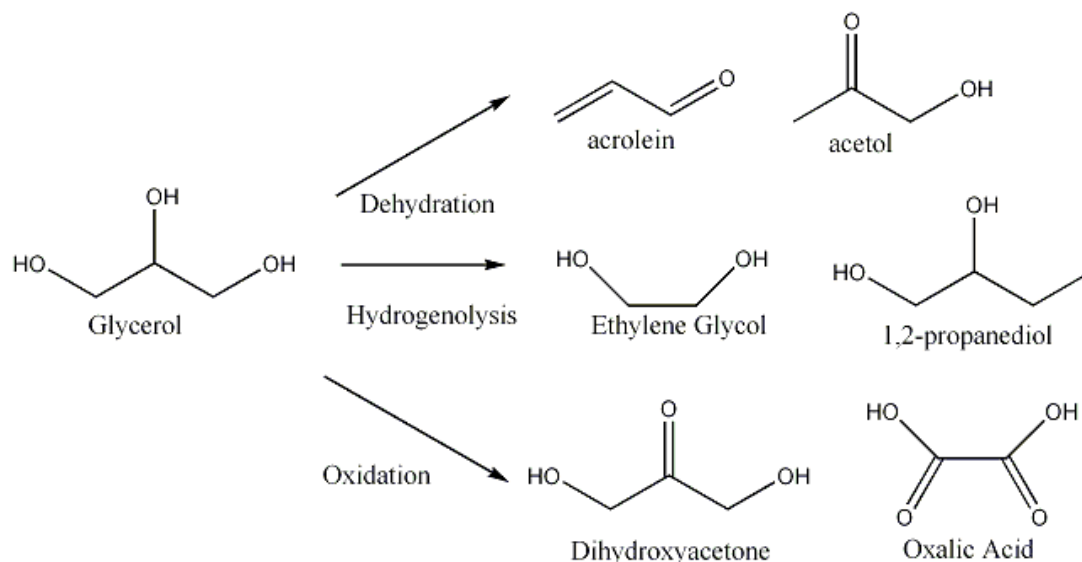


**Figure 2:** Some example molecules that can be made from glycerol.

Ethylene glycol is chemically similar to glycerol, but it is a smaller molecule and hence requires fewer computational resources to model. Methanol is the smallest alcohol molecule and therefore it will be simpler and computationally cheaper to

model large numbers of methanol molecules in classical molecular dynamics simulations.

The surface of a catalyst is an exposed face of a material (often a metal or metal oxide). At this exposed face there are undercoordinated atoms present, which is an energetically unfavourable state. Reactant molecules can then adsorb to these exposed atoms which weakens the bonds in the molecule. This in turn allows for parts of the molecule to dissociate with a lower activation energy than would be possible in the absence of the catalyst.

In heterogeneous catalysis the catalyst and reactants are in different phases (typically solid-liquid or solid-gas). Many catalysts are transition metals or their oxides, such as titanium dioxide or nanoparticles of gold, platinum or palladium. Metal oxides can also act as a support material for a catalyst, common support materials include magnesium oxide, aluminium oxide, titanium dioxide and cerium dioxide. Different support materials can have different effects on the reaction.

Smaller catalyst particles are typically more active than the equivalent mass of larger particles due to greater surface area involved. In addition there will also be more active sites (such as steps or corners) present on the smaller particles. Haruta [2] and co-workers have shown that gold nanoparticles are highly active for low temperature CO oxidation and this has sparked significant interest in the use of late transition metal nanoparticles for oxidation of other organic molecules.

The aim of this project is to simulate the adsorption and subsequent reactions of alcohols, such as methanol and ethylene glycol with metal oxide surfaces and transition metal nanoparticles in an aqueous environment to produce aldehydes.

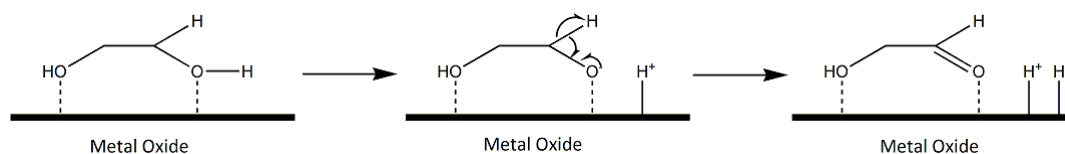


**Figure 3:** A possible mechanism for the oxidation of ethylene glycol to hydroxyethanal using a metal oxide catalyst.

Figure 3 shows a possible mechanism for the oxidation of ethylene glycol to hydroxyethanal using a metal oxide catalyst. In this mechanism ethylene glycol adsorbs to the catalyst via its oxygen atoms, an O-H bond is broken with the

hydrogen atom leaving as a proton which then adsorbs to the surface of the catalyst. Then a C-H bond is broken with the hydrogen atom leaving as a hydride ion which also adsorbs to the catalyst surface resulting in the formation of hydroxyethanal. Different catalyst surfaces may produce different oxidation mechanisms and different products.

The structure of water/alcohol mixtures over metal oxide surfaces is also of interest as water adsorption can inhibit the adsorption of alcohol molecules [3]. In order to simulate these reactions extensive use is made of periodic Density Functional Theory (DFT) and classical molecular dynamics. Density functional theory calculations typically involve from tens to a few hundred atoms, while classical molecular dynamics calculations can involve many thousands of atoms. The complex nature of the calculations involved necessitates the extensive use of supercomputing facilities. The software code VASP (Vienna *Ab Initio* Simulation Program) [4] was used for the periodic DFT calculations and DLPOLY 4 [5] was used for the classical molecular dynamics calculations presented in this thesis. Materials Studio was used to create, manipulate and visualise the molecular geometries of the systems being studied. Where necessary the in-house codes `inter_vasp`, `dlpoly_prep` and `analyse_hist` were used and adapted to prepare input files and analyse the output from VASP and DLPOLY. Various Linux shell scripts were also used for file manipulation and analysis.

## **Bibliography**

- [1] C. Zhou, J. N. Beltramini, Y. Fan and G. Q. Lu, *Chemical Society Reviews*, vol. 37, p. 527, 2007.
- [2] M. Haruta, S. Tsubota, T. Kobayashi, H. Kageyama, M. J. Genet and B. Delmon, *Journal of Catalysis*, vol. 144, p. 175, 1993.
- [3] D. Weber, J. Mitchell, J. McGregor and L. F. Gladden, *J. Phys.Chem. C.*, vol. 113, p. 6610, 2009.
- [4] G. Kresse and J. Hafner, *Phys. Rev. B.*, vol. 47, p. 558, 1993.
- [5] I. Todorov, W. Smith, K. Trachenko and M. T. Dove, *J. Mater. Chem.*, vol. 16, p. 1911, 2006.

## Chapter 2 – Literature Review

This chapter will look into the literature relating to DFT studies of the adsorption of water and alcohol molecules to metal oxide surfaces and clusters, and their subsequent reactions, as well as molecular dynamics studies of alcohol and water mixtures and experimental literature relating to heterogeneous catalysis of alcohols.

### 2.1. Density Functional Theory Studies of Surfaces and Clusters

Thissen *et al.* [1] have shown that water will favourably adsorb to exposed aluminium atoms and dissociate into hydroxyl groups over the  $\alpha$ -Al<sub>2</sub>O<sub>3</sub> (0001) surface. The adsorption energies were found to be approximately -1.5 eV for a single molecule and -1.2 eV per water molecule for a thin film of water molecules. The calculations were performed using VASP [2] with the PW91 [3] functional and a planewave cut off of 360 eV. On metal terminated surfaces it was found that water is adsorbed to exposed aluminium ions which are acting as Lewis acid sites.

Schneider *et al.* [4] have also studied the adsorption of water on the aluminium terminated  $\alpha$ -Al<sub>2</sub>O<sub>3</sub> (0001) surface. The calculations were performed using VASP with the PW91 functional at a planewave cut off of 400 eV and 3×3×1 *k*-point sampling. Lattice constants of  $a = 4.806 \text{ \AA}$  and  $c = 13.119 \text{ \AA}$  were calculated for the bulk cell of aluminium oxide. These values are approximately 1% greater than experimental values, which is typical for GGA functionals. A twelve ion layer 2×2 slab was cleaved from this optimised bulk cell and an 18  $\text{\AA}$  vacuum applied above the surface. The top seven layers were allowed to relax, while the bottom five layers were held fixed. When the surface was relaxed aluminium ions were found to sink slightly into the surface.

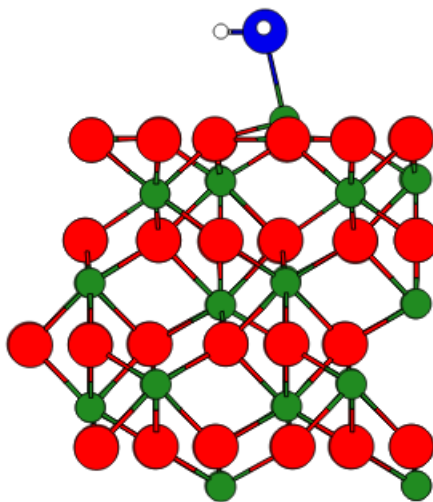


**Figure 1:** A single water molecule adsorbed to the  $\alpha\text{-Al}_2\text{O}_3$  (0001) surface. Oxygen atoms in red (blue for water) aluminium atoms in green. Image from ref. [4].

Successive water molecules were then adsorbed such that their oxygen atoms were bound to the aluminium ions on the surface. Adsorption of water causes the aluminium ions to withdraw slightly from the surface. The water molecules were initially adsorbed with the plane of the molecules perpendicular to the surface (**Figure 1**). A single water molecule adsorbed with an energy of -1.14 eV, and it was found that the adsorption energy per molecule remained almost constant up to the maximum coverage of eight molecules. The aluminium ions are acting as Lewis acid centres by accepting electron density from the lone pairs on the water molecules. Increasing the coverage of water molecules allows for different water molecules to interact with each other via hydrogen bonding, which has the effect of slightly reducing the adsorption energy to the surface. The hydrogen bonds are significantly constrained compared to those of a gas phase water dimer. With four water molecules adsorbed they form a chain, and the addition of subsequent molecules a net is formed, the template of which is determined by the geometry of the surface. With eight adsorbed molecules, the water molecules have adopted a configuration similar to that of hexagonal ice. Adsorption of water molecules causes strain to both the surface and the adsorbed molecules. The difference in adsorption energies between this work and Thissen *et al.* [1] is due to differences in the planewave cut off used in the calculations.

Calatayud [5] has studied the adsorption of ethylene glycol on group 2 metal oxides and has found that on magnesium oxide the ethylene glycol molecule adsorbs above

the magnesium ions via the alcohol groups (**Figure 2**). However for the other oxides ethylene glycol adsorbs by bridging metal ions. Adsorption was also found to be more favourable as the basicity of the oxide increased. The calculations were performed using VASP and the PW91 functional with a 400 eV planewave cut off. The adsorption energy of ethylene glycol on magnesium oxide was found to be 0.77 eV.

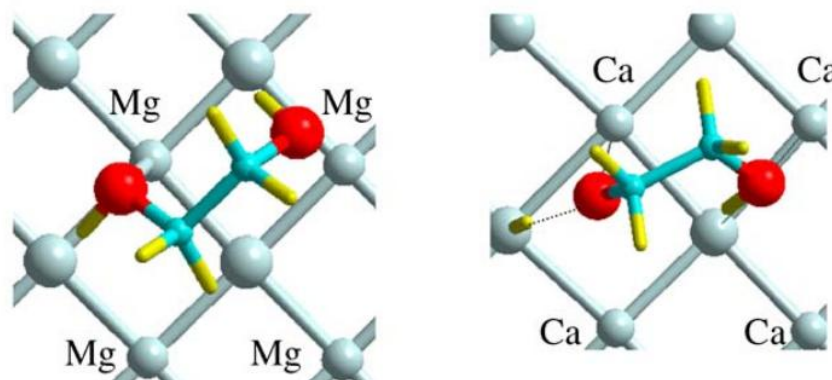


**Figure 2:** Plan views of ethylene glycol adsorbed to the MgO (100) and CaO (100) surfaces. Oxygen atoms are highlighted in red. Image from ref. [5].

Parker *et al.* [6] have studied various  $\alpha$ -Al<sub>2</sub>O<sub>3</sub> surfaces using periodic density functional theory. The (0001), (01 $\bar{1}$ 2), (11 $\bar{2}$ 3), (11 $\bar{2}$ 0), (10 $\bar{1}$ 0), (10 $\bar{1}$ 1) and (22 $\bar{4}$ 3), surfaces were studied. These were generated using the METADISE software package [7], and then imported into VASP for surface energy calculations. All calculations used a thirty atom slab with a planewave cut off of 300 eV and 3 $\times$ 3 $\times$ 1 *k*-point sampling, it is not stated which GGA functional is used, although it is likely to be PW91 or PBE [8]. The (0001) surface was found to be the most stable with a surface energy of 1.98 J m<sup>-2</sup>, with the higher index surfaces having higher surface energies. Non-stoichiometric versions of these surfaces were generated by randomly removing atoms from the stoichiometric slabs and allowing the surface to relax. Phase diagrams for each surface were generated as functions of oxygen and hydrogen chemical potentials and it was found that only stoichiometric and fully hydroxylated surfaces are stable. The (11 $\bar{2}$ 3) surface is the most favourable for hydroxylation. The preference for stoichiometric or hydroxylated surfaces is due to it being energetically unfavourable for aluminium to change its oxidation state (i.e. energy is required to add or remove additional electrons).

Chizallet *et al.* [9] have studied the properties of hydroxyl groups on various  $\gamma$ -Al<sub>2</sub>O<sub>3</sub> (cubic in structure rather than hexagonal like  $\alpha$ -Al<sub>2</sub>O<sub>3</sub>), TiO<sub>2</sub> (anatase) and MgO surfaces. The calculations were performed using the PW91 functional with a planewave cut off of 265 eV (400 eV for vibrational frequency calculations) in VASP. The planewave cut off used for the geometry optimisations is lower than is typically found in similar calculations, this may have been done to reduce the time taken for the calculations to finish. The surfaces studied were  $\gamma$ -Al<sub>2</sub>O<sub>3</sub> (100), (110), (111), TiO<sub>2</sub> (100), (001), (101), (110), and MgO (100) with various defects such as steps and kinks. It was found that water adsorbs favourably as an intact molecule to the five coordinated metal atoms on the flat surfaces of MgO (100), Al<sub>2</sub>O<sub>3</sub> (100) and TiO<sub>2</sub> (101). For surfaces with lower coordinated atoms present water dissociates into two hydroxyl groups where one forms from an OH<sup>-</sup> ion adsorbing to a metal atom and the other form an H<sup>+</sup> ion adsorbing to an oxygen atom in the surface. Although hydrolysis is observed on the TiO<sub>2</sub> (001) surface where an oxygen atom is extracted from the surface after it is protonated (i.e. a Ti-O bond is broken resulting in some deformation of the surface). For defective MgO surfaces with an oxygen vacancy water will dissociate to bridge the magnesium ions and fill the vacancy. Hydration energy of the surfaces was also calculated and it was found that hydration is more energetically favourable for surfaces with lower coordinated metal ions as it brings the coordination of those atoms closer to what would be found in the bulk material. Isolated hydroxyl groups and hydrogen bond acceptors have higher vibrational frequencies than hydrogen bond donors, but the coordination of the oxygen atom does not appear to play a significant role. They conclude by saying that hydrogen bonding is the main parameter governing the stability of hydroxyl groups on the MgO (100) surface as the oxygen – oxygen distance between hydroxyl groups is very similar to that found in water dimers. For more covalent oxides such as Al<sub>2</sub>O<sub>3</sub> and TiO<sub>2</sub> as coordination of the cations decreases it increases the interaction strength of the hydroxyl groups because the lower coordinated cations draw more electron density off the hydroxyl group resulting in a more polar hydroxyl group which interacts more strongly.

Further work by Chizallet *et al.* [10] has studied hydroxyl groups on the surface of MgO with different defects. Both periodic DFT calculations using VASP and cluster calculations using Gaussian 03 [11] were performed. For the periodic calculations

the PW91 functional was used with a planewave cut off of 400 eV, for the cluster calculations the PW91 functional and the B3LYP hybrid functional [12] [13] were used with the 6-311+G(d,p) basis set. These settings offer a good balance between speed and accuracy. In the periodic calculations the slab used is not symmetrical and this induces a dipole between periodic images. A correction is applied to eliminate this effect which did not exceed 0.05% of the total cohesive energy of the system. O-H bond lengths and hydrogen bonding lengths were measured and it was found that for cluster calculations the B3LYP hybrid functional predicts shorter O-H bond lengths and longer hydrogen bond lengths than the PW91 functional. This is due to the inclusion of Hartree-Fock exchange in the hybrid B3LYP functional which allows for a better description of bonding than pure GGA functionals such as PW91. In the periodic calculations the O-H bonds were found to be longer than in the cluster calculations and the hydrogen bond lengths were found to be shorter. The clusters and periodic slabs are representative of the individual defect site being studied with the size of the cluster varying between 29 and 48 atoms depending on the shape of the defect. It is not stated how the clusters and slabs are terminated, but it is likely to be with (100) facets. The MgO clusters and slabs optimised with the PW91 functional were found to exhibit almost the same geometries. For water adsorption on the S1 (monoatomic step site), S2-IN (six coordinated magnesium atom at the bottom of a step site) and C3 (corner) sites (**Figure 3**) increasing the coverage of water causes a decrease in the O-H bond length and an increase in the hydrogen bond length, this however is not observed on the S2-ON system as the hydrogen bonding between the resulting hydroxyl group and proton is very strong. The authors suggest that the S2-ON system is less reactive than the S1 system because of steric hindrance between water molecules leading to a strengthening of hydrogen bonding as the coverage of water molecules increases. Vibrational frequencies were calculated for the O-H bonds in the different environments and it was found that B3LYP gives higher harmonic frequencies than PW91 which is consistent with the short bonds that B3LYP predicts. It is also stated that the frequencies predicted by B3LYP are closer to experimentally measured values. It is also shown that hydroxyl groups bonded to lower coordinated atoms in the MgO clusters have higher vibrational frequencies than those bonded to higher coordinated atoms. Isolated hydroxyl groups are only found at kinks (K) and step di-vacancies (D) on the surface. The isolated and hydrogen bond acceptor hydroxyl groups are

found to have lower vibrational frequencies than hydrogen bond donor hydroxyl groups as they interact more strongly with their environment. Comparing the theoretical results with experimental results it is found that the simulated band positions are similar to those found in experimental spectra, but the absolute values are different. They conclude by saying that the hybrid functional B3LYP provides a closer description of experimental data than the PW91 functional does, and there is little difference between the cluster and periodic calculations when the same functional is used. Given that B3LYP gives results that are closer to experimental data than PW91 it suggest that for calculations similar to these B3LYP would be the more appropriate to use.

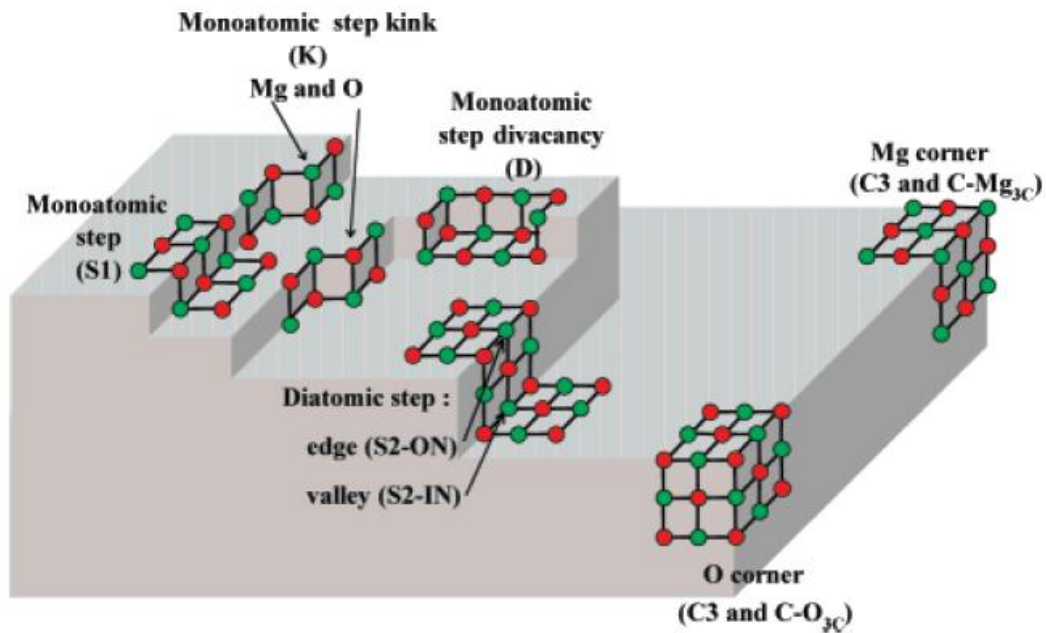


**Figure 3:** Different MgO surface sites from ref. [10]. Oxygen atoms in red, magnesium atoms in green.

Richards *et al.* [14] have studied ten atom gold nanoparticles supported on the MgO (001), (110) and (111) surfaces. DFT studies of these systems were performed using the PBE [8] functional with a planewave basis set cut off of 450 eV and a single  $k$ -point in VASP. The experimental lattice constant of 4.2 Å was used for MgO. The slab thickness was 5, 7 and 7 layers for the (001), (110) and (111) surfaces respectively. During relaxation of the surfaces the bottom two layers were fixed to simulate the behaviour of underlying bulk material. The (111) surface is non-stoichiometric with both faces terminated with either magnesium or oxygen. The Au<sub>10</sub> clusters were three layer pyramids with one, three and six atoms in the top,

middle and bottom layers respectively. Bader analysis [15] was used to characterise the charges of the atoms in the surfaces and clusters. In the bulk and (001) surface the magnesium and oxygen atoms were found to have charges of 1.65 e and -1.65 e respectively. The (110) surface was similar with charges of 1.60 e and -1.60 e. The charges for the (111) surface were significantly different however, with the first magnesium layer having a charge of 1.0 e and the second 1.65 e. The oxygen atoms had a charge of -0.94 e in the first layer and -1.53 e in the second layer. This suggests that during chemisorption to the oxygen terminated (111) surface the oxygen atoms will acquire electron density from the adsorbate in order to attain a charge closer to that of bulk MgO which is a lower energy state. The Au<sub>10</sub> cluster gains a total charge of 0.68 e and 1.08 e on the (001) and (110) surfaces respectively. For the oxygen terminated (111) surface the cluster loses 3.95 e to the surface, and for the magnesium terminated surface it gains 7.15 e. The Au<sub>10</sub> cluster has average Au-Au bond lengths of 2.74 Å, the (001) surface has Mg-O bond lengths of 2.1 Å for both in-plane directions, the (110) has bond lengths of 2.1 Å and 2.97 Å, and the (111) surface has bond lengths of 2.97 Å for both in-plane directions. When the Au<sub>10</sub> cluster is adsorbed to the (001) and (110) surfaces there will be significant deformation of the cluster, however there is much smaller deformation when the cluster is adsorbed to the (111) surface due to the smaller lattice mismatch. Binding energies are also significantly more favourable for the (111) surface than the other surfaces, with the oxygen termination being more favourable than the magnesium termination. This occurs because of greater number of electrons being donated (or withdrawn) from the gold cluster to the (111) surface. Experimental work was also carried out using gold clusters supported on MgO (111) nanosheets. The gold nanoparticles had sizes between 2 nm and 20 nm, with most in the range 2-5 nm. The oxidation of benzyl alcohol was used to test the activity of the catalysts that had been prepared. All runs were carried out in a solvent free environment over a period of six hours at temperatures of 100 °C, 120 °C and 140 °C. At higher temperatures there was greater conversion of the benzyl alcohol, but the selectivity to benzaldehyde decreased due to over oxidation of the benzyl alcohol.

Fernandez and Balbas [16] have simulated the adsorption of carbon monoxide on gold/alumina clusters using the SIESTA code [17] found that a single gold atom will adsorb preferentially on top of an aluminium Lewis acid site. Carbon monoxide will

then adsorb on top of this gold atom. Both the  $\text{Al}_2\text{O}_3$  (0001) surface terminated by aluminium and an  $(\text{Al}_2\text{O}_3)_{20}$  cluster were studied. The cluster was allowed to fully relax and it was found that its structure resembled that of amorphous aluminium oxide. This occurs because there are no constraints on the requiring it to maintain its shape like there would be in a periodic calculation, hence it relaxes to an amorphous geometry which is the lowest energy state. In the periodic calculations the surface consisted of nine layers with the bottom three fixed while the upper six were allowed to relax. The optimal adsorption site for gold adsorption was found by placing the gold atom in various positions on the surface or cluster and calculating the binding energy. The most favourable adsorption site was found to be on top of an aluminium Lewis acid site at 0.78 eV. Adsorption of a gold atom was also found to cause some displacement of the atoms in the surface that are close to the gold atom. When geometrically optimising the position of the gold atom on the  $\text{Al}_2\text{O}_3$  (0001) surface the optimal position for the gold atom was found to be above an aluminium Lewis acid site regardless of its initial position. Due to the amorphous nature of the  $(\text{Al}_2\text{O}_3)_{20}$  cluster there are more possible adsorption sites for a gold atom, but the most favourable is still to an aluminium Lewis acid site at 0.96 eV. Carbon monoxide was then adsorbed in different configurations to the gold atom and the substrates. It was found that in the most favourable configurations carbon monoxide was adsorbed only to the gold atom. On the cluster, adsorption caused some displacement of the gold atom to form an Al-Au-O bridge. A planar  $\text{Au}_8$  cluster was then adsorbed to the  $(\text{Al}_2\text{O}_3)_{20}$  cluster and it was found that in the adsorbed state the Au-Au bonds were longer than in the isolated  $\text{Au}_8$  cluster. This bond stretching also deforms the  $\text{Au}_8$  cluster away from a planar geometry. The  $\text{Au}_8$  cluster was also found to donate some electron density to the alumina cluster. Carbon monoxide was then adsorbed to the  $\text{Au}_8$  cluster supported on the  $(\text{Al}_2\text{O}_3)_{20}$  cluster, and it was found that CO binds most favourably to a gold atom that is bound to an aluminium atom. This adsorption does not significantly change the geometry of the  $\text{Au}_8/(\text{Al}_2\text{O}_3)_{20}$  cluster. However with other less favourable adsorption configurations for CO there is some deformation of the system.

Norskov *et al.* [18] have investigated supported gold nanoparticles. Their computational studies begin with DFT simulations of CO oxidation using a ten atom gold cluster where it was found that CO and  $\text{O}_2$  both adsorb favourably to the cluster

and then react to form CO<sub>2</sub>. The barrier to this reaction is less than 1 eV. Another reaction pathway where the oxygen molecule dissociates before reacting was shown to have a significantly higher barrier. They contrast this with the adsorption of oxygen on the Au (211) surface which is energetically unfavourable which leads to the conclusion that gold nanoparticles are significantly more reactive than extended gold surfaces. The Au<sub>10</sub> cluster is then combined with a rutile (110) surface and CO oxidation is investigated again. Two reaction pathways were studied. In the first only the gold cluster takes part in the reaction. In the second pathway the TiO<sub>2</sub> support was also involved. The second pathway was determined to be slightly more favourable than the first one. The authors move on to show that adsorption of oxygen and CO is more favourable to lower coordinated gold atoms in the cluster. The low coordinated gold atoms have higher d states which interact more strongly with valence states in adsorbate molecules. The authors proceed to study a range of different sizes of gold nanoparticles from 1 nm to 9 nm. In the smaller particles there is a greater fraction of atoms forming a corner or part of an edge, which agrees with experimental data that smaller nanoparticles are more catalytically active than larger ones. They conclude by saying that DFT calculations show that the adsorption of oxygen or CO is not possible on a densely packed gold surface and it only becomes feasible when there are gold atoms with a low coordination number present.

Yang *et al.* [19] have compared the adsorption of molecular oxygen onto various gold clusters using the PW91 and B3LYP functionals with experimental data. It was found that the PW91 functional systematically overestimates the adsorption energy by up to 0.4 eV compared to the B3LYP functional. Electron affinities and ionisation energies were also calculated for both functionals for the gold clusters and oxygen molecules and it was found that in most cases B3LYP was more accurate than PW91.

Boronat *et al.* [20] have studied the oxidation of ethanol with an Au (111), Au (511), Au-rod (two (100) terraces separated by a single atom (111) step) and an Au<sub>38</sub> cluster using VASP with the PW91 functional and a 415 eV planewave basis set cut off. Adsorption of ethanol is most favourable to the Au<sub>38</sub> cluster (-12.1 kcal mol<sup>-1</sup>), followed by the Au-rod structure (-9.6 kcal mol<sup>-1</sup>) and then the Au (511) surface (-4.9 kcal mol<sup>-1</sup>), with the (111) surface being the least favourable (-2.9 kcal mol<sup>-1</sup>). The same trend was followed for O-H activation and the adsorption of the

intermediate. C-H activation is most favourable on Au (111) surface and least favourable on the Au-rod structure, and the adsorption of ethanal is favourable to each surface except the Au<sub>38</sub> cluster. The authors conclude by saying that as the coordination number of atoms in the surface or cluster decreases the activity of the catalyst increases.

Many of the periodic DFT studies cited here use the VASP software code. The PW91 functional is a very commonly used pure DFT functional, and the PBE functional is also commonly used as well. The B3LYP functional is also commonly used and it more accurate than the PW91 functional due to the inclusion of Hartree-Fock exchange, however as it is a hybrid functional using it with a planewave basis set as is common in periodic calculations will incur a significant performance cost over pure DFT functionals which limit its use to smaller systems. The planewave cut off is around 400 eV for most of the studies, as this is typically where the energy converges for most bulk materials.

The papers studied here have shown that both water and alcohols will adsorb favourably to metal oxide surfaces with the adsorbate molecule binding to (or bridging) metal atoms in the surface via the adsorbates oxygen atoms. Water has also been shown to dissociate into hydroxyl groups on MgO and Al<sub>2</sub>O<sub>3</sub> surfaces with dissociation being more favourable at defect sites on the surface where the metal atoms are undercoordinated compared to their bulk arrangement.

## 2.2. Molecular Dynamics Studies of Alcohols and Water

Chialvo *et al.* [21] have compared the TIP4P [22], TIP4P-ice [23] and TIP4P/2005 [24] water potentials to a new parameterisation TIP4P-I. All four potentials are rigid, four body models that share the same molecular geometry: the O-H bond is 0.9752 Å and the H-O-H angle is 104.52°. Bisecting the H-O-H angle is a massless charge centre ‘M’ to which the charge that is normally located on the oxygen atom is moved. The O-M distance varies slightly between the different models, as do the charges on the hydrogen atoms and M, and the Lennard-Jones parameters of the different atoms. Adjusting the O-M distance alters the distribution of charge in the molecule which will alter dipole moment and hence the dielectric constant of the molecule. A more accurate description of the dielectric constant will improve the accuracy of the model. TIP4P-I provides a better prediction of the critical conditions,

melting point and maximum density of water than TIP4P and TIP4P-ice, and a slight improvement over TIP4P/2005. This is due to TIP4P/2005 and TIP4P-I having better parameterisations of their dipole and quadrupole moments. They conclude by saying that due to the simplicity of the TIP4P family of potentials and the fact that they are non-polarisable finding a good match between all properties of interest is impossible.

Vega *et al.* [25] have compared the performance of the TIP3P [22], TIP4P, TIP4P/2005 and TIP5P [26] water potentials. All four models share the same geometry for the arrangement of their hydrogen and oxygen atoms, however the location of the massless charge centres on TIP4P, TIP4P/2005 and TIP5P varies. The Lennard-Jones parameters of each model are similar but vary slightly. Ten properties are compared against their experimental values, they are: vapour-liquid equilibria, surface tension, densities of different ice polymorphs, phase diagram, melting point, maximum density of liquid water, equation of state, self-diffusion coefficient and dielectric constant. Each potential is given a score based on how well it predicts each property compared to the other potentials. For each property except dielectric constant, the TIP4P/2005 potential was rated as the most accurate (TIP5P gave the most accurate prediction for this property). TIP5P and TIP4P were ranked second and third respectively, and TIP3P scored lowest. While not explicitly included in the scoring scheme the SPC and SPC/E [27] models were also considered and the authors suggest that the SPC/E potential would have ranked higher than TIP4P and TIP5P, but not as high as TIP4P/2005. This is due to the SPC/E potential having a better parameterisation of the polarisation of the water model than TIP4P and TIP5P. This parameterisation is included with the construction of the TIP4P/2005 potential. The authors also note that while the TIP4P/2005 potential is better for general use than the other potentials that were studied it still has some deficiencies, but these could be corrected for by including polarisability within the model.

Space *et al.* [28] have simulated various isopropanol/water mixtures. The potentials used were a modification of the OPLS potentials [29] [30] for isopropanol and SPC/E for water. A 16% mixture of 91 *n*-propanol molecules and 477 water molecules was first equilibrated with the NPT ensemble at an initial temperature of 293 K, and then a production run using the NVT ensemble was performed for 2 ns. Systems of pure water and pure *n*-propanol were also simulated for comparison. It was found that in the 16% mixture approximately 51% of the *n*-propanol molecules

did not hydrogen bond to each other, with 35% forming one hydrogen bond and 13% forming two. More than 70% of the *n*-propanol molecules were found to be hydrogen bonded to one or two water molecules with nearly 13% hydrogen bonded to three water molecules and nearly 17% forming no hydrogen bond to water. The majority (approximately 77%) of water molecules formed no hydrogen bonds to *n*-propanol, while 19% formed one hydrogen bond and 3.6% formed two. A smaller number formed three or more hydrogen bonds. The majority of water molecules formed either two or three hydrogen bonds to other water molecules (30% and 36% respectively), 19% formed four hydrogen bonds and almost 12% only formed one hydrogen bond. 1.9% of water molecules were found to form no hydrogen bonds to other water molecules and 1% were found to have formed five hydrogen bonds. For the pure *n*-propanol nearly 82% of the molecules were hydrogen bonded to two others, with 13.5% forming one hydrogen bond, 3.66% forming three, and 1% forming none. For pure water more than 40% of the molecules formed three hydrogen bonds, while 28% formed four, nearly 24% formed two and nearly 6% formed only one. A small fraction (1.78%) formed five hydrogen bonds and on 0.41% formed no hydrogen bonds. Radial distribution functions (RDF) were calculated and it was found that *n*-propanol-*n*-propanol RDF was nearly identical for the 16% mixture and pure *n*-propanol (**Figure 4**), suggesting that the structure of the pure liquid remains when in aqueous solution (there is only a very slight increase in the intermolecular distance for the 16% mixture). The radial distribution functions also provide evidence of the formation of chains of *n*-propanol as well as the aggregation of these chains into micelle structures. There is also significant distortion of the water structure as the water – water radial distribution functions show that there as many as seven water molecules present within hydrogen bonding distance of a central water molecule.

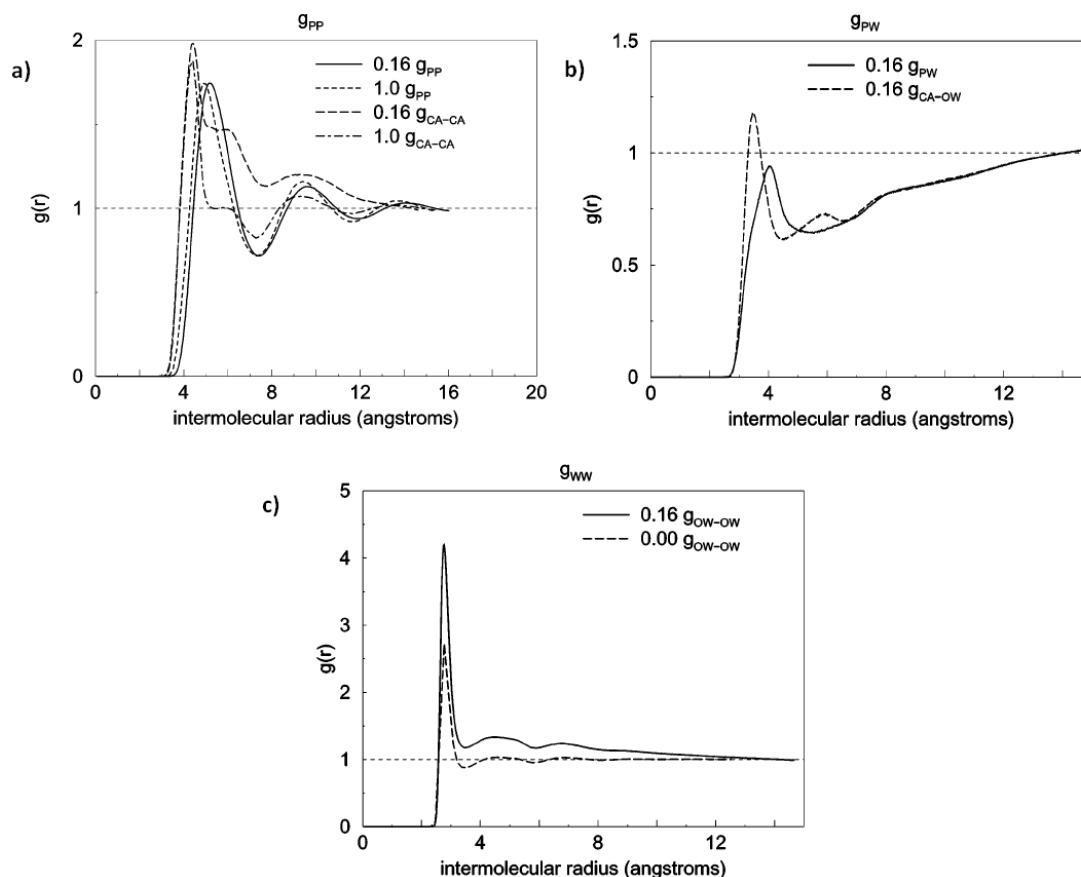


**Figure 4:** Radial distribution functions for a) propanol – propanol interactions, b) water – propanol interactions and c) water – water interactions from ref. [28].  $g_{PP}$ ,  $g_{PW}$ ,  $g_{OW}$  and  $g_{CA}$  are the radial distribution functions for propanol – propanol, propanol – water, water – water and  $\alpha$ -carbon interactions respectively. The y-axis indicates the number of atoms of a certain type at that distance from the central atom.

Youngs *et al.* [31] have performed simulations of various isopropanol/water mixtures and their interactions with  $\gamma$ -alumina surfaces (**Figure 5**). To model the water molecules the SPC/E [27] potential is used, and to model isopropanol a derivative of the OPLS-AA potential was used [32]. The simulations themselves were performed using DLPOLY 2.17 [33]. Randomly ordered configurations of pure water (650 molecules), 124/124 water/isopropanol molecules, 325/76 water/isopropanol molecules, 488/38 water/isopropanol molecules and pure isopropanol (152 molecules) were generated and placed over the alumina surface. Simulations of 6 ns length and 10 fs timestep were conducted using the canonical (NVT) ensemble at a temperature of 300 K. The simulations were contrasted with experimental NMR studies to determine the diffusion of isopropanol and water over the  $\gamma$ -alumina surfaces. In the pure water simulations a layer of water strongly adsorbed to the aluminium ions in the surface via the oxygen atom in the water

molecule, with one O-H bond parallel to the surface to maximise interaction with oxide ions in the surface. In subsequent layers above the surface there was found to be less ordering of the water molecules, with more bulk like behaviour observed. In the pure isopropanol simulations the molecules were found to adsorb with the alcohol group oxygen atom oriented towards the aluminium ions. Steric effects also reduce the number of molecules adsorbed in the same area compared to water. This however leads to greater structuring of the liquid further away from the surface. Due to the strong adsorption of molecules in the first layer above the surface it is likely that those molecules will not move far from the surface during the simulation. In the mixed simulations at 7% and 19% isopropanol it was found that one alcohol molecule could displace three water molecules from the surface, however this was not the case for the 50% mixture as more water molecules than expected were adsorbed at the interface. Integration of the oxygen – oxygen RDF for the pure isopropanol simulations suggests the formation of groups of three alcohol molecules in the liquid for molecules that are not directly interacting with the surface. In the simulations the diffusion coefficients for both water and isopropanol were nearly zero which is not the case for their experimental work. This is probably due to the surface in the simulation not being hydroxylated as it is in the experiment. Since the simulated surface is not hydroxylated it allows for much stronger interactions between the aluminium atoms and the alcohol and water molecules, which will significantly constrain their movement resulting in a much smaller diffusion coefficient.

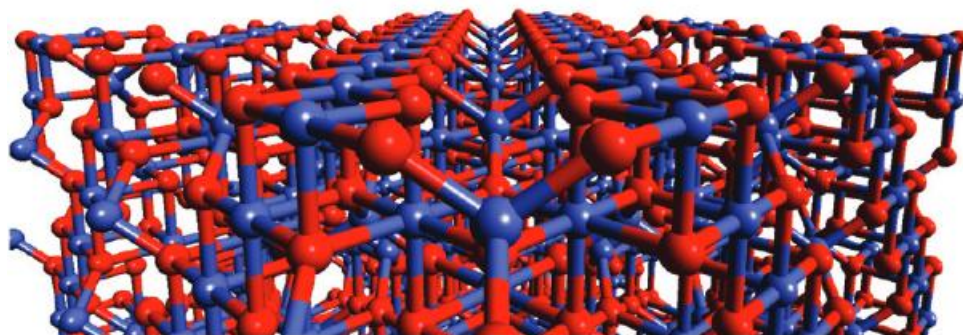


**Figure 5:** The unreaxed  $\gamma\text{-Al}_2\text{O}_3$  (001) surface. Oxygen atoms in red, aluminium atoms in blue. Image from ref. [31].

Pálinkás *et al.* [34] have performed molecular dynamics simulations on two methanol/water mixtures of 10% and 90% concentration. Water-water interactions

were described by the BJH potential [35], and the methanol-methanol interactions were described by a flexible three site model [36]. This model consists of the oxygen atom, the hydrogen atom bonded to it and the methyl group. For the three different possible dimers that can be formed from water and methanol the lowest energy structure was that where a linear hydrogen bond was formed between the molecules. The simulations consisted of two hundred molecules in a cubic cell, of which twenty were randomly replaced by either water or methanol depending on the desired concentration in the equilibrated mixture. To find the dimensions of the cell experimental densities of the mixtures were used, which results in cells of side 18.973 Å and 23.304 Å for the 10% methanol mixture and 90% methanol mixture respectively. The simulations were run for 4.25 ps, but the size of the timestep was not specified. In pure methanol it was found that each molecule has two neighbouring methanol molecules. In the 10% methanol mixture each methanol molecule has almost three neighbouring water molecules and less than 0.1 neighbouring methanol molecules. In pure water each molecule has four nearest neighbours, but this decreases to around three in the 90% methanol mixture. Oxygen – oxygen radial distribution functions show that there is significant ordering in the structure of the methanol molecules in the 10% mixture. The first peak of the water-water RDF for the 90% mixture is very similar to that of pure water suggesting clustering of water molecules. Oxygen – hydrogen radial distribution functions show a large first peak for pure methanol which is much less significant in the 10% mixture. This indicates water – methanol hydrogen bonds are weaker than methanol – methanol hydrogen bonds. In pure water two hydrogen bonds are formed, but in the 90% mixture only one is formed. Looking at the potential energies of the mixtures and pure liquids it is found that the potential energy of methanol in solution is lower than when in pure liquid, and the potential energy of water is lower in the pure liquid than in solution. This indicates a stabilisation of methanol in solution and a destabilisation of water in solution. The authors conclude by saying that structure around a water molecule in the 90% mixture becomes more methanol like, and the opposite for methanol in the 10% mixture.

Meijer and van Erp [37] have used Car-Parrinello [38] molecular dynamics to model the solvation of a single methanol molecule using DFT with the BLYP functional [39] [13]. All calculations were performed using the CPMD package [40]. Three

systems were studied: a small system of one methanol molecule and thirty one water molecules, a large system of one methanol molecule and sixty three water molecules, and a system of thirty two water molecules. All systems were in cubic periodic cells. The small cell was of edge 9.98 Å, the large cell 12.50 Å and the water cell of 9.86 Å. These dimensions correspond to experimental densities of the systems. The temperature of the simulations was fixed at 300 K using a Nosé-Hoover thermostat [41] [42]. The timestep was 0.145 fs. The initial configurations of each system were obtained from classical force field simulations. Each simulation was equilibrated for 1 ps and then the small and water simulations ran for 10 ps, and the large system for 7 ps. Radial distribution functions for each system were plotted and compared (**Figure 6**), and it was found that there was little difference in the water oxygen – water oxygen RDF's between the three systems, indicating that the presence of a single methanol molecule does not have a significant effect on the structure of the local water molecules. The presence of a large peak at 3.7 Å indicates the presence of a shell of water molecules at that distance from the methanol molecule. The difference in position of the second peak of the RDF between the large and small systems is caused by the limited size of the small system and the authors suggest that at least fifty water molecules would be needed to properly model the solvation of a single methanol molecule. Integrating the RDF for the large system to the minimum at 5 Å suggests that the first solvation shell consists of sixteen water molecules. This compares well with experimental data indicating that there are fifteen water molecules in the first solvation shell [43]. The hydrogen bonding of each system was also analysed and it was found that for the pure water system a water molecule donated and accepted on average 1.7 hydrogen bonds. For the large system the methanol molecule donated 0.9 and accepted 1.5 hydrogen bonds. This indicates that the methanol molecule participates significantly in the hydrogen bonding of the system. Given that the average values are not integers it means that some molecules formed one hydrogen bond and others formed two.

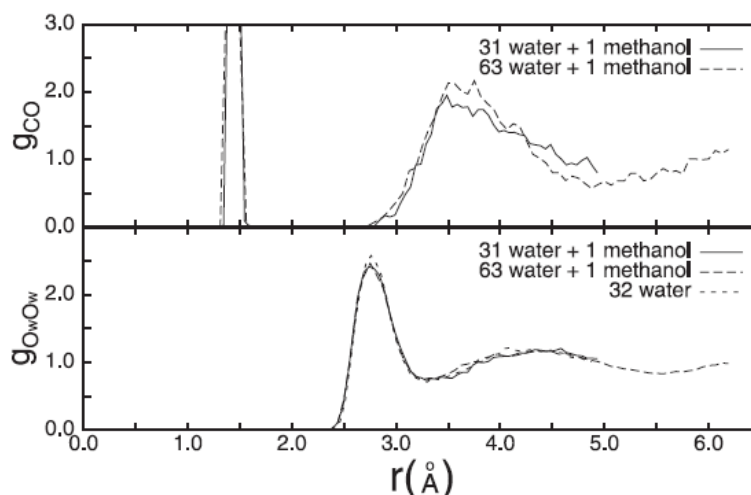


**Figure 6:** Methanol carbon – water oxygen (top) and water oxygen – water oxygen (bottom) radial distribution functions from ref. [37].

### 2.3. Heterogeneous Catalysis

Besson *et al.* [44] have studied the oxidation of glycerol using air and a platinum group catalyst. During the experimental procedure the catalyst was suspended in water under a nitrogen atmosphere and heated to 333 K while being constantly stirred. Glycerol was then added and after ten minutes air was bubbled through the mixture. A 30% sodium hydroxide solution was added to maintain the pH at a constant level. A Pd/C, Pt/C and several PtBi/C catalysts prepared in different ways were tested. For the oxidation of glycerol to glyceric acid using the Pd/C catalyst it was found that reaction rate and selectivity is higher for higher pH levels. For the Pt/C catalyst the reaction rates were significantly higher than those for the Pd/C catalyst, and highest at pH 7. This is due to the palladium surface becoming over oxidised by atmospheric oxygen and losing its ability to adsorb organic molecules. Since platinum is harder to oxidise the Pt/C catalyst is not as easily poisoned as the Pd/C catalyst and therefore retains its activity. The Pt/C catalyst is not however as selective to glyceric acid as the Pd/C catalyst. For the commercially obtained PtBi/C catalyst (5% Pt) at low pH the main product formed was dihydroxyacetone, and after extended contact time this further oxidised to hydroxypyruvic acid. Three different methods of creating the PtBi/C catalysts were tested: platinum loading by ion exchange, platinum loading by impregnation and coimpregnation of platinum and bismuth. It was found that a higher Pt:Bi ratio gives greater selectivity to dihydroxyacetone and a higher rate of reaction except for the catalyst prepared by ion exchange where a higher Pt:Bi ratio gives a lower rate of reaction. None of these

catalysts showed as high a rate of reaction as the Pd/C, Pt/C or commercial PtBi/C catalysts, but they did show a greater selectivity towards dihydroxyacetone. The authors conclude that by altering the nature of the catalyst it is possible tailor the oxidation to primary or secondary alcohol groups, and that this reaction can be used to replace oxidation using mineral acids. In addition by further refining the manufacturing of the catalyst it should be possible to further improve the selectivity towards and yield of the desired products.

Hutchings *et al.* [45] have used a series of bimetallic catalysts containing different ratios of gold and either platinum or palladium supported on magnesium oxide for the selective oxidation of glycerol. The use of a gold-palladium catalyst significantly increases the activity when compared to gold alone, and the use of a gold-platinum catalyst allows the desired reactions to occur in the absence of a base. The catalysts were studied at 1:1 and 1:3 gold:platinum/palladium ratios at 60 °C, 40 °C and 23 °C for periods of four or twenty four hours. Each catalyst showed significant selectivity towards glyceric acid, with some tartronic acid, glycolic acid, formic acid and oxalic acid also being produced. The gold-platinum catalysts showed the highest selectivity to glyceric acid. The gold-platinum catalysts showed greater conversion than the gold-palladium catalysts. Conversion was also greater when there was more platinum or palladium present in the catalyst than gold. Higher temperatures also improved conversion, however at 23 °C a twenty four hour run gave comparable conversion to a four hour run at 60 °C for the 1:3 gold-palladium catalyst. Magnesium oxide on its own was also studied as a catalyst but only a very small conversion of glycerol was observed after four hours indicating that the presence of gold and platinum or palladium is needed for these reactions to occur quickly. The catalyst particles were found to be on average approximately 2 nm in diameter. The gold-palladium particles were determined to be homogeneously mixed rather than having a core-shell structure. The gold-platinum catalyst was also shown to be suitable for the oxidation of diols including ethylene glycol, 1,2-propanediol and 1,4-butanediol.

Lee *et al.* [46] have studied palladium supported on mesoporous aluminium oxide as a catalyst for the oxidation of allylic alcohols. The mesoporous Al<sub>2</sub>O<sub>3</sub> support has a higher surface area than a typical  $\alpha$ -Al<sub>2</sub>O<sub>3</sub> or  $\gamma$ -Al<sub>2</sub>O<sub>3</sub> support, which allows for greater deposition of palladium. Decreasing the size of the palladium clusters favours

the formation of oxide terminated surfaces rather than pure metal clusters. A low concentration of palladium also favours the formation of atomically dispersed Pd<sup>II</sup> which is highly active for the oxidation of allylic alcohols. Using STEM (scanning transmission electron microscopy) imaging it was possible to confirm the presence of individual palladium atoms on the surface of the support (**Figure 7**). No large aggregates were observed, but for higher concentrations of palladium larger particles of palladium were observed. The oxidation of crotyl and cinnamyl alcohols to their respective aldehydes was studied with this catalyst at various palladium concentrations from 0.03 wt% to 4.70 wt%. Very high selectivity (> 88%) was shown for each catalyst, however the yield was low for the low palladium concentrations but increased significantly for higher concentrations. It is stated that the ability of the mesoporous Al<sub>2</sub>O<sub>3</sub> to stabilise the individual palladium atoms confers a tenfold increase in the rate of reaction compared to the amorphous Al<sub>2</sub>O<sub>3</sub> support. Given the greater surface area of the mesoporous support there is higher likelihood of defects being present on the surface which act as nucleation sites for the palladium atoms. Turnover frequencies (4400 h<sup>-1</sup> for the 0.03 wt% at 0.21 atm O<sub>2</sub> and 60 °C) of these oxidation reactions are significantly higher for these catalysts than for Au/CeO<sub>2</sub> (538 h<sup>-1</sup>) and Ru/Al<sub>2</sub>O<sub>3</sub> catalysts (27 h<sup>-1</sup>) at 120 °C. They also compare well with those for AuPd/TiO<sub>2</sub> (12600 h<sup>-1</sup> at 5 atm O<sub>2</sub> and 160 °C).

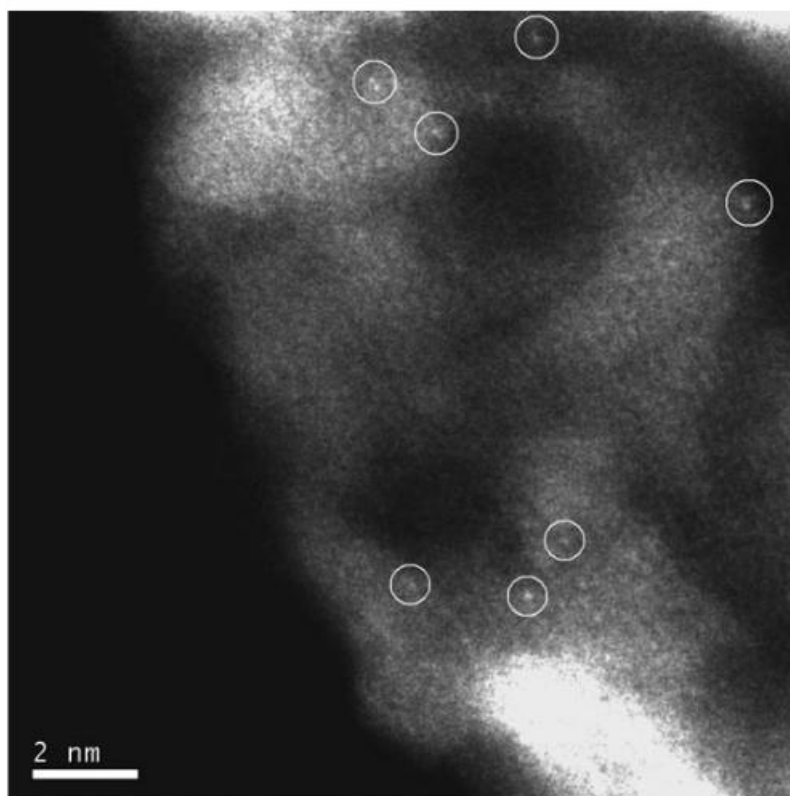


**Figure 7:** STEM image of 0.03 wt% Pd/meso-Al<sub>2</sub>O<sub>3</sub> with the palladium atoms highlighted. Image from ref. [46].

Christensen *et al.* [47] have studied the oxidation of ethanol to acetic acid and ethyl acetate using an Au/TiO<sub>2</sub> (anatase) catalyst. A 5 wt% solution of ethanol was used over a temperature range of 363-473 K for time periods between 15 minutes and 24 hours. As the temperature increases the yield of acetic acid (ethanoic acid) was observed to increase. Gold nanoparticle sizes were measured to be between 3 nm and 6 nm using TEM (tunnelling electron microscopy) (**Figure 8**). Experiments using just the support materials (MgAl<sub>2</sub>O<sub>4</sub> or TiO<sub>2</sub>) gave very low yields of acetic acid (<2%). Over shorter runs the amount of acetaldehyde (ethanal) produced was greater than over longer runs as it does not have sufficient time to fully oxidise to acetic acid. CO<sub>2</sub> produced in these experiments originates from the complete oxidation of a reaction intermediate that is adsorbed to the catalyst. By increasing the concentration of ethanol it is possible to make ethyl acetate by the esterification of acetic acid. For this to occur the concentration of ethanol has to be above 60 wt%, otherwise the major product remains acetic acid. The concentration of water effects the formation of ethyl acetate as water plays a role in the equilibrium for the formation of the ester. These results are similar to earlier work by this group using an Au/MgAlO<sub>4</sub> catalyst,

although that reaction is thought to proceed via an unknown intermediate, and not acetaldehyde [48].

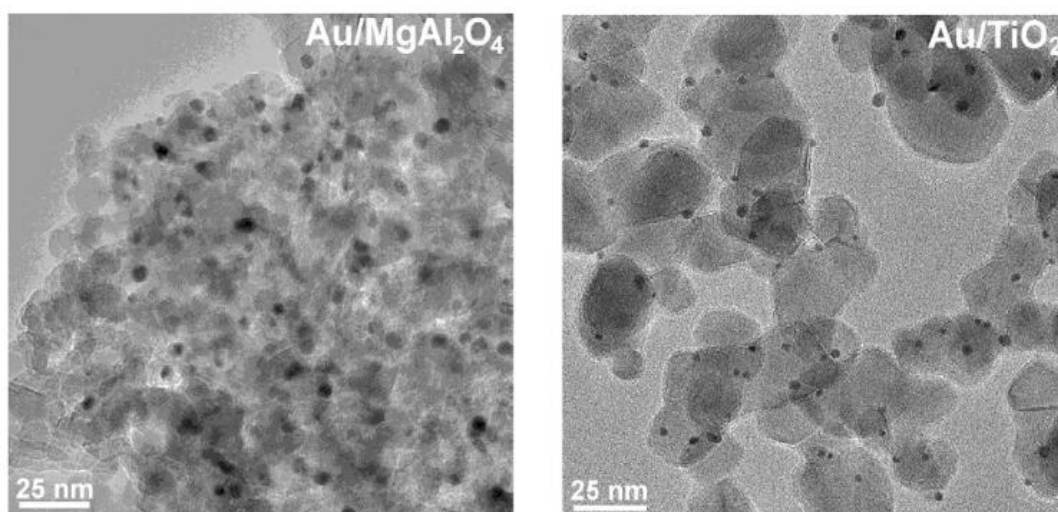


**Figure 8:** TEM images of Au/MgAl<sub>2</sub>O<sub>4</sub> and Au/TiO<sub>2</sub> showing the size of particles on the surface. Image from ref. [47].

Mitchell *et al.* [49] have used the technique of measuring longitudinal ( $T_1$ ) and transverse ( $T_2$ ) NMR relaxation times to measure the interaction strengths of water, 2-propanol and butanone with Ru/SiO<sub>2</sub> and Pd/Al<sub>2</sub>O<sub>3</sub> catalysts and it was found that water has the highest  $T_1/T_2$  ratio as it can hydrogen bond with hydroxyl groups present on the catalyst surface. 2-propanol has a weaker interaction than water as it forms weaker hydrogen bonds, and butanone has weaker interaction still as it cannot hydrogen bond, instead its interactions are dominated by weaker dipole-dipole interactions. For measurements on mixtures of water and the organic molecules it was found that 2-propanol cannot completely displace water from the catalyst surface, but water can fully displace 2-propanol over the timescale of the experiment. This indicates that not only does water interact more strongly with the surface, but that the presence of water adsorbed to the surface will inhibit the adsorption of alcohol molecules to the surface thus reducing the efficiency of the catalyst.

## 2.4. Summary

In order for a heterogeneous catalyst to function, reactant molecules must be able to reach the surface of the catalyst. The most active catalysts are often small nanoparticles suspended in a solution [44] [48]. Smaller particles are more active than an equivalent mass of larger particles as they have a greater surface area and

will have a higher proportion of defect sites which is where most catalytic activity is thought to occur [20] [46]. Most experiments use an alcohol dissolved in water rather than the pure alcohol, and experimentally water is known to interact with catalyst surfaces often by dissociating into hydroxyl groups [49]. Many DFT studies ignore the presence of water and look at the adsorption of the molecule of interest on a clean surface which is unlikely to occur in reality. Explicitly modelled solvent molecules are often ignored because they significantly increase the computational cost of *ab initio* and DFT calculations. Since they are significantly computationally cheaper, classical molecular dynamics calculations allow the study of large numbers of alcohol and water molecules mixed together. This allows for studies to be performed on how these mixtures will interact with a catalyst surface and whether the presence of water will inhibit the adsorption and subsequent reactions of alcohol molecules.

The adsorption of alcohols [5] (and water molecules [1] [49]) is usually quite favourable on metal oxide surfaces provided that the oxygen atom from an alcohol group can approach and physisorb to an exposed metal atom. In many cases water molecules will dissociate into hydroxyl groups on metal oxide surfaces [1] [6] [9] [10]. Often the metal atom will be acting as a Lewis acid centre as the oxygen atom of the adsorbate donates some electron density to it. Since the exposed metal atom is acting as a Lewis acid it removes the need for a mineral acid to be used as an additional catalyst which reduces the cost and environmental impact of the reaction. Basic oxides can also be used as catalysts and this removes the need for an additional liquid phase base [45]. Basic materials act as catalysts by encouraging the deprotonation of the alcohol group, typically forming a water molecule in liquid phase or a hydroxyl group on the surface of a metal oxide. After the deprotonation of the alcohol the intermediate will chemisorb to a metal atom on the surface of the catalyst via its oxygen atom.

Alcohols and water molecules will usually mix well, although larger alcohol molecules such as propanol, tert-butyl alcohol (TBA) and 1-octanol will often form micelle structures [28] [50], chains or a combination of both [51] depending on the concentration of water and alcohol. These structures are usually organised such that the hydrophobic tails are at the centre and the hydrophilic alcohol groups are exposed to water molecules, although reverse micelles can also form where water is

confined at the centre of a micelle structure. Steric hindrance from bulky alkyl chains can also have an effect on the efficiency of a catalyst as adsorption of additional molecules can be inhibited by the presence of molecules already adsorbed to the surface. Typically water will interact strongly with clean catalyst surfaces but it is often possible for alcohols to displace water molecules and adsorb to the surfaces [31] [49].

In order to determine if a material is suitable as a catalyst we must determine if the molecules of interest will adsorb favourably to the surface and if it is possible for the oxidation of the molecule to occur on the surface with a reasonable activation energy barrier. To do this we need to calculate the optimised geometries for the surface and adsorbed molecules, as well as for any intermediates formed in during the reaction and for the final products. Classical molecular dynamics calculations will tell us how an alcohol will interact with large numbers of water molecules and the catalyst surface of interest.

## Bibliography

- [1] P. Thissen, G. Grundmeier, S. Wippermann and W. G. Schmidt, *Phys. Rev. B.*, vol. 80, p. 245403, 2009.
- [2] G. Kresse and J. Hafner, *Phys. Rev. B.*, vol. 47, p. 558, 1993.
- [3] J. P. Perdew and Y. Wang, *Phys. Rev. B.*, vol. 45, p. 13244, 1992.
- [4] V. A. Ranea, W. F. Schneider and I. Carmichael, *Surface Science*, vol. 602, p. 268, 2008.
- [5] M. Calatayud, *Catalysis Today*, vol. 152, p. 88, 2010.
- [6] A. Marmier and S. C. Parker, *Phys. Rev. B.*, vol. 69, p. 115409, 2004.
- [7] G. W. Watson, E. T. Kelsey and N. H. de Leeuw, *J. Chem. Soc. Faraday Trans.*, vol. 92, p. 433, 1996.
- [8] J. P. Perdew, K. Burke and M. Ernzerhof, *Phys. Rev. Lett.*, vol. 77, p. 3865, 1996.
- [9] C. Chizallet, M. Digne, C. Arrouvel, P. Raybaud, F. Delbecq, G. Costentin, M. Che, P. Sautet and H. Toulhoat, *Top. Catal.*, vol. 52, p. 1005, 2009.
- [10] C. Chizallet, G. Costentin, M. Che, F. Delbecq and P. Sautet, *J. Am. Chem. Soc.*, vol. 129, p. 6442, 2007.
- [11] M. J. Frish et al., Gaussian 03, revision C.02, Wallingford, CT: Gaussian Inc., 2004.
- [12] A. D. Becke, *J. Chem. Phys.*, vol. 98, p. 5648, 1993.
- [13] C. Lee, W. Yang and R. G. Parr, *Phys. Rev. B.*, vol. 37, p. 785, 1988.
- [14] Z. Li, C. V. Ciobanu, J. Hu, J. Palomaers-Báez, J. Rodríguez-López and R. Richards, *Phys. Chem. Chem. Phys.*, vol. 13, p. 2582, 2011.
- [15] R. F. W. Bader, *Atoms In Molecules: A Quantum Theory*, New York: Oxford University Press, 1990.
- [16] E. M. Fernandez and L. C. Balbas, *J. Phys. Chem. B.*, vol. 110, p. 10449, 2006.
- [17] J. M. Soler, E. Artacho, J. D. Gale, A. Garcia, J. Junquera, P. Ordejon and D. Sanchez-Portal, *J. Phys. Condens. Matter.*, vol. 14, p. 2745, 2002.

- [18] J. K. Norskov, T. V. W. Janssens, B. S. Clausen, B. Hvolbaek, H. Falsig, C. H. Christensen and T. Bligaard, *Topics In Catalysis*, vol. 44, p. 15, 2007.
- [19] X. Ding, Z. Li, J. Yang, J. G. Hou and Q. Zhu, *J. Chem. Phys.*, vol. 120, p. 9594, 2004.
- [20] M. Boronat, A. Corma, F. Illas, J. Radilla, T. Rodenas and M. J. Sabater, *Journal of Catalysis*, vol. 278, p. 50, 2011.
- [21] A. A. Chialvo, A. Bartók and A. Baranyai, *Journal of Molecular Liquids*, vol. 129, p. 120, 2006.
- [22] W. L. Jorgensen, J. Chandrasekhar, J. D. Madura, R. W. Impey and M. L. Klein, *J. Chem. Phys.*, vol. 79, p. 926, 1983.
- [23] J. L. F. Abascal, E. Sam, R. G. Fernandez and C. Vega, *J. Chem. Phys.*, vol. 122, p. 234511, 2005.
- [24] J. L. F. Abascal and C. Vega, *J. Chem. Phys.*, vol. 123, p. 234505, 2005.
- [25] C. Vega, J. L. F. Abascal, M. M. Conde and J. L. Aragones, *Faraday Discussions*, vol. 141, p. 251, 2009.
- [26] M. W. Mahoney and W. L. Jorgensen, *J. Chem. Phys.*, vol. 112, p. 8910, 2000.
- [27] H. J. C. Berendsen, J. R. Grigera and T. P. Straatsma, *The Journal Of Physical Chemistry*, vol. 91, p. 6269, 1987.
- [28] A. B. Roney, B. Space, E. W. Castner, R. L. Napoleon and P. B. Moore, *J. Phys. Chem. B.*, vol. 108, p. 7389, 2004.
- [29] W. L. Jorgensen, D. S. Maxwell and J. Tirado-Rives, *J. Am. Chem. Soc.*, vol. 118, p. 11225, 1996.
- [30] W. D. Cornell, P. Cieplak, C. I. Bayly, I. R. Gould, K. M. Merz, D. M. Ferguson, D. C. Spellmeyer, T. Fox, J. W. Caldwell and P. A. Kollman, *J. Am. Chem. Soc.*, vol. 117, p. 5179, 1995.
- [31] T. G. A. Youngs, D. Weber, L. F. Gladden and C. Hardacre, *J. Phys. Chem. C*, vol. 113, p. 21342, 2009.
- [32] K. Kahn and T. C. Bruice, *J. Comput. Chem.*, vol. 23, p. 977, 2002.
- [33] W. Smith, T. R. Forester, I. T. Todorov and M. Leslie, *DLPOLY User Manual - version 2.17*, 2006.
- [34] G. Pálinkás, E. Hawlicka and K. Heinzinger, *Chemical Physics*, vol. 158, p. 65, 1991.
- [35] P. Bopp, G. Jancsó and K. Heinzinger, *Chem. Phys. Letters*, vol. 98, p. 129,

- 1983.
- [36] G. Pálinkás, E. Hawalika and K. Heinzinger, *J. Phys. Chem.*, vol. 91, p. 4334, 1987.
- [37] E. J. Meijer and T. S. van Erp, *Chem. Phys. Letts.*, vol. 333, p. 290, 2001.
- [38] R. Car and M. Parrinello, *Phys. Rev. Lett.*, vol. 55, p. 2471, 1985.
- [39] A. D. Becke, *Phys. Rev. A.*, vol. 38, p. 3098, 1988.
- [40] J. Hutter, P. Ballone, M. Bernasconi, P. Focher, E. Fois, S. Goedecker, M. Parrinello and M. Tuckerman, CPMD version 3.0f, MPI für Festkörperforschung and IBM Zurich Research Laboratory, 1990-1997.
- [41] S. Nosé, *J. Chem. Phys.*, vol. 81, p. 511, 1984.
- [42] W. G. Hoover, *Phys. Rev. A.*, vol. 31, p. 1695, 1985.
- [43] A. K. Soper and J. L. Finney, *Phys. Rev. Lett.*, vol. 71, p. 4346, 1993.
- [44] R. Garcia, M. Besson and P. Gallezot, *Applied Catalysis A*, vol. 127, p. 165, 1995.
- [45] G. J. Hutchings, G. L. Brett, Q. He, C. Hammond, P. J. Miedziak, N. Dimitratos, M. Sankar, A. A. Herzing, M. Conte, J. A. Lopez-Snachez, C. J. Kiely, D. W. Knight and S. H. Taylor, *Angew. Chem. Int. Ed.*, vol. 50, p. 10136, 2011.
- [46] S. F. J. Hackett, R. M. Brydson, M. H. Gass, I. Harvey, A. D. Newman, K. Wilson and A. F. Lee, *Angew. Chem.*, vol. 119, p. 8747, 2007.
- [47] B. Jørgensen, S. E. Christiansen, M. L. D. Thomsen and C. H. Christensen, *Journal Of Catalysis*, vol. 251, p. 332, 2007.
- [48] C. H. Christensen, B. Jørgensen, J. Rass-Hansen, K. Egeblad, R. Madsen, S. K. Klitgaard, S. M. Hansen, M. R. Hansen, H. C. Andersen and A. Riisager, *Angew. Chem. Int. Ed.*, vol. 45, p. 4648, 2006.
- [49] D. Weber, J. Mitchell, J. McGregor and L. F. Gladden, *J. Phys. Chem. C*, vol. 113, p. 6610, 2009.
- [50] N. R. Jagannathan, K. Venkateswaran, F. G. Herring, G. N. Patey and D. C. Walker, *J. Phys. Chem.*, vol. 91, p. 4553, 1987.
- [51] J. L. MacCallum and D. P. Tieleman, *J. Am. Chem. Soc.*, vol. 124, p. 15085, 2002.

## Chapter 3 – Background Theory

This chapter will cover the theories behind the work done in this project: Density functional theory, molecular dynamics, periodic systems, Bader analysis, density of states and nudged elastic band calculations.

### 3.1. Density Functional Theory

The aim of any first principles method is to determine the electronic structure of the atoms and molecules within a chemical system using the many body Schrödinger equation. Simplifications such as the Born-Oppenheimer approximation [1] where the motion of the electrons and nuclei are separated are used. This is justified because the mass of an electron is much smaller than that of even the lightest nucleus, and therefore it can be assumed that the nuclei do not move in response to motion of the electrons.

The total energy of a system is given by:

$$H = T + V = E \quad (3.1)$$

Where  $T$  and  $V$  are the kinetic and potential energies respectively,  $E$  is the total energy and  $H$  is the Hamiltonian (an operator corresponding to the total energy of the system).

$$T = \frac{p^2}{2m_e} \quad (3.2)$$

Where  $p$  is the momentum:

$$p = -i\hbar \frac{\partial}{\partial x} \quad (3.3)$$

Thus:

$$H = -\frac{\hbar^2}{2m_e} \frac{\partial^2}{\partial x^2} + V \quad (3.4)$$

In three dimensions **Equation 3.4** generalises to:

$$H = -\frac{\hbar^2}{2m_e} \nabla_{r_i}^2 + V(r) \quad (3.5)$$

Where:

$$\nabla_{r_i}^2 = \frac{\partial^2}{\partial x^2} + \frac{\partial^2}{\partial y^2} + \frac{\partial^2}{\partial z^2} \quad (3.6)$$

And:

$$V = V_{ext}(R_i) + V_{e-e}(r_i) \quad (3.7)$$

Thus the time independent Schrödinger equation is:

$$H\Psi = -\frac{\hbar^2}{2m_e}\nabla_{r_i}^2\Psi + V_{ext}(R_i)\Psi + V_{e-e}(r_i)\Psi \quad (3.8)$$

Therefore:

$$H\Psi = E\Psi \quad (3.9)$$

$\Psi$  is the wave function of the system,  $V_{ext}(R_i)$  is the potential of the nuclei and  $V_{e-e}(r_i)$  is the electron-electron interaction. The physical constants  $\hbar$  and  $m_e$  are Planck's constant over  $2\pi$  and the mass of an electron respectively.

Density functional theory (DFT) is a theory developed by Hohenberg, Kohn and Sham in the 1960's [2] [3]. The theory states that the electronic energy (and therefore any other observable property) of a system is a unique functional of the ground state electron density  $n(r)$  of the system:

$$E[n(r)] = F[n(r)] + \int n(r)V_{ext}(r)d^3r \quad (3.10)$$

Where  $F[n(r)]$  is a universal functional including the kinetic  $T[n(r)]$  and potential  $E_{int}[n(r)]$  energies of the electrons, and  $V_{ext}(r)$  is an external potential (usually of the nuclei). The form of  $F[n(r)]$  is usually unknown.

Therefore:

$$E[n(r)] = T[n(r)] + E_{int}[n(r)] + \int n(r)V_{ext}(r)d^3r \quad (3.11)$$

By expressing the electron density in terms of single particle wavefunctions  $\psi_i$ :

$$n(r) = \sum_i \psi_i(r)^2 \quad (3.12)$$

The kinetic energy can be written as:

$$T[n(r)] = -\frac{\hbar^2}{2m_e}\sum_i \int \psi_i(r_i)\nabla_{r_i}^2\psi_i(r_i)d^3r \quad (3.13)$$

The potential energy of the electrons can be further broken down into coulombic electron-electron interactions and exchange-correlation energy  $E_{XC}[n(r)]$ :

$$E_{int}[n(r)] = \frac{e^2}{2} \iint \frac{n(r)n(r')}{|r-r'|} d^3r d^3r' + E_{XC}[n(r)] \quad (3.14)$$

The Local Density Approximation (LDA) defines the exchange-correlation energy as:

$$E_{XC}^{LDA} = \int \epsilon_{XC} n(r) d^3r \quad (3.15)$$

The exchange – correlation energy is the sum of the exchange and correlation energies i.e.  $E_{XC} = E_X + E_C$

$\epsilon_{XC}$  is the exchange-correlation energy per unit volume of a uniform electron gas. The local density approximation assumes that the electron density of a system is uniform or slowly varying. While it gives good results for a wide variety of systems, it does however tend to slightly underestimate lattice parameters for bulk materials.

Correlation energy ( $E_C$ ) is the instantaneous interaction energy between pairs of electrons, and exchange energy ( $E_X$ ) is a non-classical correction to the coulomb energy due to electrons being fermionic particles.

The Generalised Gradient Approximation (GGA) no longer assumes that the electron density is uniform or slowly varying and includes a term involving the gradient of the electron density to  $E_{XC}$ . In contrast with the LDA, the GGA tends to slightly overestimate lattice parameters.

The exact form of  $E_{XC}$  is unknown for most systems and therefore many functionals are parameterised against experimental or high level *ab initio* data to approximate this for systems of interest.

Density functional theory and many of the commonly used functionals are implemented in a wide variety of computational chemistry software codes.

### 3.1.1. The PBE Functional

The PBE functional [4] (developed by Perdew, Burke and Ernzerhof) is a commonly used Exchange – Correlation functional using the Generalised Gradient Approximation (GGA). It shares a similar construction to the earlier PW91 [5]

functional. It is more accurate for many chemical systems than earlier methods. This functional is designed to only satisfy conditions which are energetically significant. All of the parameters in the PBE functional are fundamental constants except for those in  $\varepsilon_{XC}$ .

The exchange energy is defined by:

$$E_X = \int d^3r n \varepsilon_X(n) F_X(s) \quad (3.16)$$

Where  $\varepsilon_x = \frac{-3e^2 K_F}{4\pi}$ ,  $s = \frac{|\nabla n|}{2K_F n}$ , with  $K_F = (3n\pi^2)^{\frac{1}{3}}$ ,  $F_X(s) = 1 + \kappa - \frac{\kappa}{1 + \frac{\mu s^2}{\kappa}}$ , with  $\kappa = 0.804$  and  $\mu = 0.21951$ .

The correlation energy is defined by:

$$E_C = -\frac{e^2}{a_0} \int d^3r n \gamma \phi^2 \times \ln \left[ 1 + \frac{1}{\frac{\chi s^2}{\phi^2} + \left(\frac{\chi s^2}{\phi^2}\right)^2} \right] \quad (3.17)$$

Where  $a_0 = \frac{\hbar^2}{2me^2}$ ,  $\phi(\zeta) = \frac{1}{2}[(1 + \zeta)^{2/3} + (1 - \zeta)^{2/3}]$  is a spin scaling factor,  $\chi \approx 1.2277$ , and  $\gamma = 0.025$ . It should be noted that  $a_0$  is the Bohr radius.

### 3.1.2. DFT + U

For many systems pure DFT using the local density approximation or generalised gradient approximation will provide a reasonable description of the ground state electronic structure. There are however systems where this fails such as some transition metal oxides and those containing partly filled  $d$  and  $f$  shells. The source of failure in transition metals is an insufficient description of the coulomb repulsion between the  $d$  electrons located on transition metal ions. The DFT+U method is an attempt to correct for this shortcoming.

The DFT+U energy as suggested by Dudarev *et al.* [6] is defined by:

$$E_{DFT+U} = E_{DFT} + \frac{U-J}{2} \sum_{\sigma} (n_{m,\sigma} - n_{m,\sigma}^2) \quad (3.18)$$

Where U is the Hubbard parameter which describes the increase in energy for placing an electron on a specific site. J is a parameter representing screened exchange, and the total number of electrons  $N_{\sigma} = \sum_{\sigma} n_{m,\sigma}$ .  $\sigma$  is the spin of the electrons and m is their orbital angular momentum.

The addition of the  $U$  parameter (with the correct value) to atoms in a system allows for proper localisation of the electrons. It also increases the gap between occupied and unoccupied orbitals which allows for manipulation of the band gap of the system.

### 3.1.3. Hybrid DFT

In hybrid DFT calculations a fraction of the Hartree-Fock exchange energy is added to the pure DFT exchange energy. For many systems this can improve the accuracy of the calculation. For calculations using plane wave basis sets the use of hybrid DFT often makes all but the smallest calculations impractical, due to the increase in computer time compared to pure DFT functional.

For the hybrid functional PBE0 [7] which is based on the pure DFT functional PBE, the exchange correlation energy is given by:

$$E_{XC}^{PBE0} = 0.25E_X^{HF} + 0.75E_X^{PBE} + E_C^{PBE} \quad (3.19)$$

Similar to the PBE0 hybrid functional is the HSE06 hybrid functional [8] which adds a screening parameter which accelerates the spatial decay of the Hartree-Fock exchange interaction. The result of this is a reduction in computational costs for a small reduction in accuracy [8].

## 3.2. Pseudopotentials

Density functional theory scales as  $N^4$  (where  $N$  is the number of electrons in the system), and post Hartree-Fock methods such as Møller-Plesset (MP $n$ ) perturbation theory [9] and Coupled Cluster (CC) [10] have even higher scaling ( $N^5$  for MP2 and  $N^8$  for CCSDT). This can make calculations involving large numbers of heavy atoms impractical on even the most powerful supercomputers. However many phenomena of interest only involve valence electrons, and hence core electrons and effects of the nucleus can be replaced by a fixed potential or pseudopotential. The pseudopotential acts on pseudo wavefunctions rather than true valence wavefunctions [11]. In the core region of atoms the wavefunction oscillates rapidly due to the strong potential of the nucleus. To adequately model this, a great many basis functions would be needed.

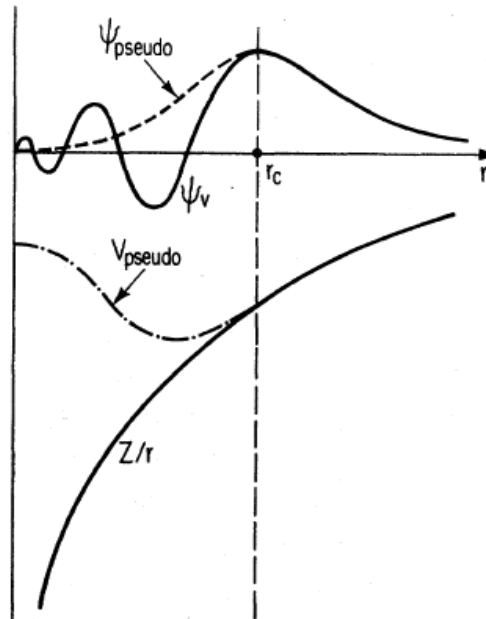


**Figure 1:** Illustration of all electron and pseudo electron potentials and wavefunctions showing how they are identical outside of the core region. Image taken from reference [11].

There are two common types of pseudopotential, projector augmented wave (PAW) [12] and norm-conserving. In PAW pseudopotentials the wavefunction is divided into a partial wave expansion enclosed within a sphere centred on the atom and envelope functions outside the sphere. At the sphere boundary the partial wave expansion and envelope functions are matched smoothly. With norm-conserving pseudopotentials, outside of the core region the pseudo and real valence wavefunctions are identical in their spatial dependences, magnitudes and resulting charge densities. In the core region the rapidly oscillating wavefunction is replaced with a smoother function that is computationally simpler to work with (**Figure 1**).

### 3.3. Periodic Systems

Many problems, particularly those involving extended systems with translational symmetry such as surfaces and bulk materials can be represented as an infinitely repeating periodic system. This however leads to the problem of having an infinite number of electrons, and the wave function extending over the entire system which would require an infinite basis set. Using Bloch's theorem [13] the wave function of the electrons can be expressed as a wave like part and a cell periodic part.

The reciprocal lattice vectors of a periodic cell are defined as:

$$\mathbf{a}^* = \frac{2\pi}{V} \mathbf{b} \times \mathbf{c} \quad \mathbf{b}^* = \frac{2\pi}{V} \mathbf{c} \times \mathbf{a} \quad \mathbf{c}^* = \frac{2\pi}{V} \mathbf{a} \times \mathbf{b} \quad (3.20)$$

Where  $\mathbf{a}$ ,  $\mathbf{b}$  and  $\mathbf{c}$  are the vectors defining the cell in real space, and  $V$  is the volume of the cell.

The vector  $\mathbf{k}$  describing a point in the reciprocal cell is defined as:

$$\mathbf{k} = \frac{l}{N_a} \mathbf{a}^* + \frac{m}{N_b} \mathbf{b}^* + \frac{n}{N_c} \mathbf{c}^* \quad (3.21)$$

$l$ ,  $m$  and  $n$  are integers, and  $N_a$ ,  $N_b$ , and  $N_c$  are the number of cells in the  $a$ ,  $b$  and  $c$  directions respectively.

$$\psi_i(\mathbf{r}) = \exp(i\mathbf{k} \cdot \mathbf{r}) f_i(\mathbf{r}) \quad (3.22)$$

Where the cell periodic part is a Fourier transform of the form:

$$f_i(\mathbf{r}) = \sum_G c_i \exp(i\mathbf{G} \cdot \mathbf{r}) \quad (3.23)$$

$\mathbf{G}$  is reciprocal space vector defined by:

$$\mathbf{G} \cdot \mathbf{T} = 2\pi m \quad (3.24)$$

Where  $\mathbf{T}$  is any lattice vector and  $m$  is an integer.

Combining **Equations 3.22** and **3.23** gives:

$$\psi_i(\mathbf{r}) = \sum_G c_{i,\mathbf{k}+\mathbf{G}} \exp[i(\mathbf{k} + \mathbf{G}) \cdot \mathbf{r}] \quad (3.25)$$

By summing up many of these planewaves is it possible to converge to an accurate representation of the electronic structure of the material in question.

It should be noted that the momentum and energy of a particle described by a planewave of the form  $\exp(i\mathbf{k} \cdot \mathbf{r})$  are  $\hbar k$  and  $\frac{\hbar^2 k^2}{2m}$  respectively.

### 3.4. $k$ -Point Sampling

For an infinite periodic system there are an infinite number of electrons which are accounted for by an infinite number of  $k$ -points. Bloch's theorem allows the calculation of a finite number of electronic wave functions at an infinite number of  $k$ -points. However the electronic wave functions at nearby  $k$ -points are nearly identical [11], which allows representation of the electronic wave functions in a region by a

single  $k$ -point. Therefore only a few  $k$ -points are needed to effectively represent a complete periodic system based on a simple unit cell. Care must be taken however in choosing an appropriate number of  $k$ -points for a calculation as using too few can lead to errors in the total energy of the system [14] and using too many can make a calculation too computationally expensive to be practical as calculations have to be repeated in many different parts of the periodic cell. Symmetry arguments can also be used to reduce the number of  $k$ -points necessary for a calculation.

One common method of  $k$ -point sampling is the Monkhorst-Pack [15] scheme. In this scheme the  $k$ -points are made into an evenly spaced grid in the reciprocal space (Brillouin Zone) of the periodic cell.

### 3.5. Planewave Basis Sets

In calculations involving extended systems it is often more efficient to use plane wave functions (**Equations 3.26 & 3.27**) to approximate the wave functions of the electrons rather than Gaussian (**Equation 3.28**) or Slater functions (**Equation 3.29**) [16].

$$\phi(x) = A \cos kx + B \sin kx \quad (3.26)$$

$$\phi(x) = Ae^{ikx} + Be^{-ikx} \quad (3.27)$$

$$\phi(r) = Ae^{-\zeta r^2} \quad (3.28)$$

$$\phi(r) = Ae^{-\zeta r} \quad (3.29)$$

Due to Bloch's theorem it is possible to express the wave function as a sum of complex exponential or plane wave functions (**Equation 3.25**) [11]. To obtain the exact wave function an infinite number of plane waves would be needed, however the number of plane waves can be truncated as lower energy plane waves are typically more important than higher energy ones (**Figure 2**).

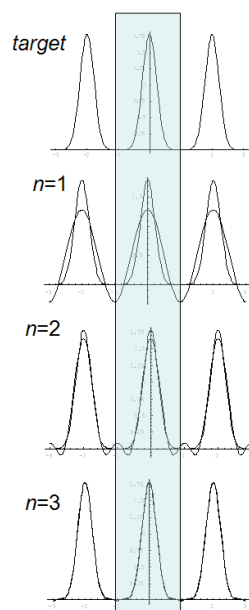


**Figure 2:** A series of plane waves summed together to generate an approximation to a Gaussian function. As more plane waves (increasing  $n$ ) are added the Fourier transform becomes a closer representation of the target periodic Gaussian function.

The energy cut off of a plane wave basis set is defined by:

$$|\mathbf{G}|_{max} = \frac{2\pi}{h} \sqrt{2mE_{cut}} \quad (3.30)$$

Increasing the cut off of a plane wave basis set results in an increase in the magnitude of the  $\mathbf{G}$  vector. When this undergoes a Fourier transform the highest energy (shortest wavelength) waves contribute the least to the transform and hence it is possible to exclude them from the calculation.

Truncating the size of the basis set does however cause errors in the calculated energy, this can be alleviated by increasing the cut off energy of the basis set until the calculated energy has converged.

### 3.6. Bader Analysis

The chemical properties of atoms and molecules are governed by their electric charges. Quantum mechanical calculations produce a continuous distribution of charge of the system, but they do not assign explicit charges to the atoms and molecules within the system. Several different methods of assigning charge to atoms have been proposed such as Mulliken analysis and Bader analysis [17].

In Bader analysis, space is divided into sections (Bader regions) by surfaces which run through minima in the charge density. Typically each Bader region will contain only one atom. By integrating the charge density within each Bader region it is possible to calculate the total charge within that section and hence the charge on that atom.

### 3.7. Density of States

In an isolated system such as an atom or molecule the electronic energy levels are discrete and well defined. In a condensed system like a bulk crystal the electronic energy levels form continuous bands. The density of states (DOS) of a system describes the number of states at each energy level of a system that are possible to be occupied with electrons.

It is defined as:

$$D(E) = \frac{1}{V} \frac{N(E+\Delta E) - N(E)}{\Delta E} = \frac{1}{V} \frac{dN(E)}{dE} \quad (3.31)$$

Where  $N(E)$  is the number of states per unit volume,  $V$  is the volume in reciprocal space and  $E$  is the energy.

A density of states plot shows which energy levels are occupied and which are available for the system in question. A density of states plot shows the number of states available for occupation by an electron at a given energy level. The probability of a state being occupied is determined by Fermi-Dirac statistics:

$$f_{FD}(E) = \frac{1}{\exp\left(\frac{E-\mu}{k_B T}\right) + 1} \quad (3.32)$$

Where  $\mu$  is the chemical potential or Fermi level,  $E$  is the energy level,  $T$  is the temperature and  $k_B$  is Boltzmann's constant.

The Fermi level is at the energy level of zero. At absolute zero all states below the Fermi level will be occupied and all states above the Fermi level will be unoccupied. At higher temperatures electrons can be promoted to higher states provided that there are empty states available.

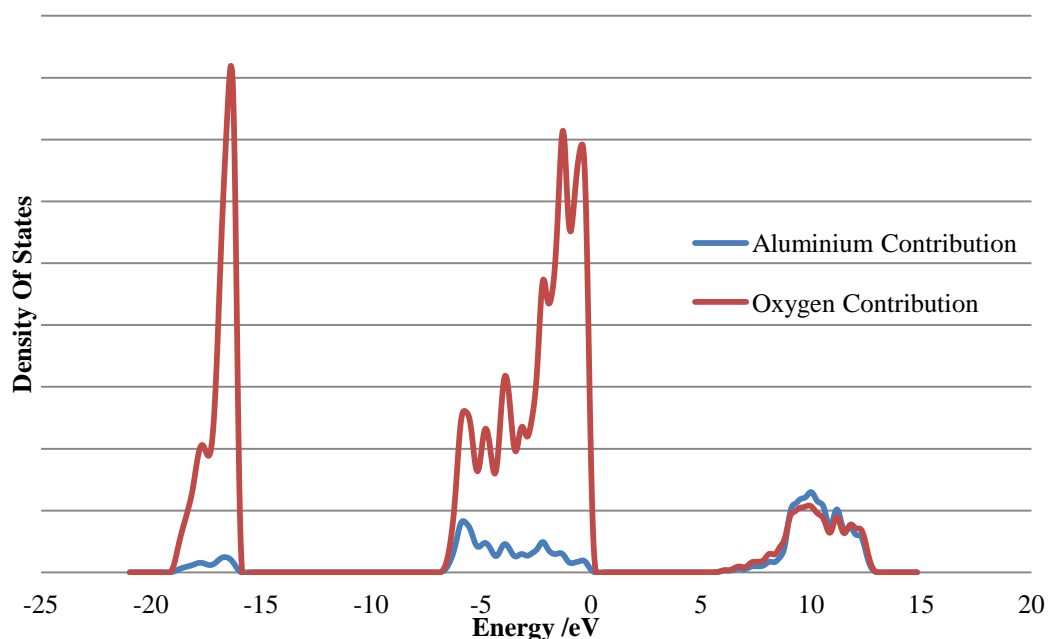


**Figure 3:** Density of states plot for bulk alpha aluminium oxide showing the separate contributions from the aluminium and oxygen atoms. The calculation was carried out using the PBE functional at  $9 \times 9 \times 9$   $k$ -points with a 500 eV planewave cut off. The cell was hexagonal in shape with the **a** and **b** vectors of length 4.8251 Å, the **c** vector of length 13.1713 Å and the angle  $\gamma$  was  $120^\circ$ .

A density of states plot (**Figure 3**) also shows the band gap between the valence and conduction bands in a semi-conductor or insulating material. The large band gap of approximately 5 eV indicates that  $\alpha$ - $\text{Al}_2\text{O}_3$  is an insulator. By comparing the calculated band gap with experimental data it is possible to determine an appropriate  $U$  value for DFT+ $U$  calculations.

### 3.8. Nudged Elastic Band Calculations

An important problem of interest in computational chemistry is that of finding the minimum energy path (MEP) between reactants and products in a chemical reaction. The highest point along the MEP will give the activation energy barrier for the reaction.

In a nudged elastic band (NEB) calculation a set of images between the reactants and products is generated and each image is then optimised. Each image is connected to adjacent images by ‘springs’. The force on each image is projected into parallel and perpendicular components with respect to the reaction coordinate [18]. The projection of the perpendicular component of the force is referred to as nudging.

Given sufficient images a nudged elastic band calculations will converge to the minimum energy path, however this can be very computationally expensive if a large system is being studied.

### 3.9. Molecular Dynamics

There are two different types of molecular dynamics simulation: quantum and classical. In quantum simulations the evolution of the system is determined by solving the time dependant Schrödinger equation. This however is very computationally expensive for large systems due to the number of degrees of freedom, and so is presently only viable for small systems over a short period of time. Classical simulations use pre-defined potentials (or forcefields) for the interactions between particles and their motions are determined by Newtonian mechanics which are much cheaper to model computationally. This therefore allows for the calculation of ensemble average properties over a much longer timescale. The forcefields are determined by parameterisation against the properties of interest from experimental or high level *ab initio* data. Hybrid QM/MM (quantum mechanics/molecular mechanics) methods also exist where part of the system (such as a protein) is modelled using a quantum mechanical method and a large number of solvent molecules are modelled using forcefields. This allows for a more accurate simulation of a larger system than either method would allow for by itself.

#### 3.9.1. Force Fields

A force field describes the interactions between particles in a system. They include bonded interactions such as bond stretching, angle bending and torsion, as well as non-bonded interactions such as electrostatic coulomb interactions and van der Waals interactions. There are many different forms of the potentials used to model the interactions between particles. Graphs of potential energy against distance or angle for some different types of potential are shown in **Figure 4 - Figure 7**.

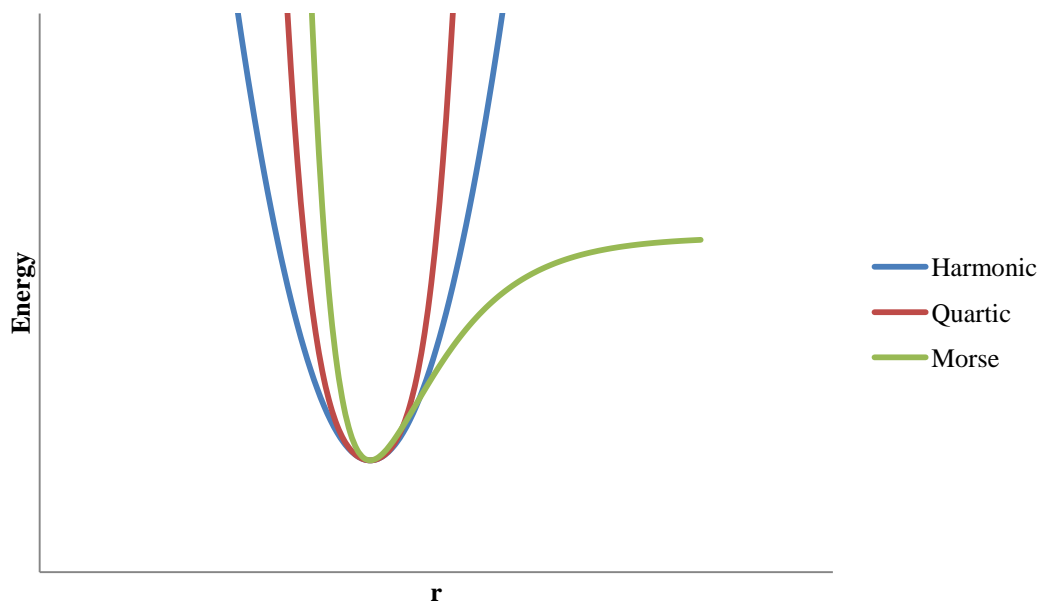


**Figure 4:** Graph showing harmonic, quartic and Morse potentials

Harmonic potentials are of the form  $U = \frac{1}{2}k(r - r_0)^2$ , where  $k$  is the spring constant of the bond and  $r_0$  is the equilibrium bond length. Stretching or compressing a harmonic bond increases the potential energy and a restoring force acts to return the bond to its equilibrium value. This form is commonly used as it approximates a pair of atoms connected by a spring.

Quartic potentials are of the form  $U = \frac{k_1}{2}(r - r_0)^2 + \frac{k_2}{3}(r - r_0)^3 + \frac{k_3}{4}(r - r_0)^4$ . It is similar to the harmonic potential, except it is slightly more accurate as the additional terms in the potential allow for a more accurate description of the potential well.

Morse potentials are of the form  $U = E_0(1 - e^{-k(r-r_0)^2})$ , where  $E_0$  is the depth of the potential well. The Morse potential effectively describes bond breaking at large values of  $r$ , something that the harmonic and quartic potentials do not.

Even though the harmonic potential does not support bond breaking it is commonly used as the inclusion of bond breaking is often not required in a classical molecular dynamics simulation and it is computationally cheap to use.

Bond angle potentials are often modelled with a harmonic or quartic potential.

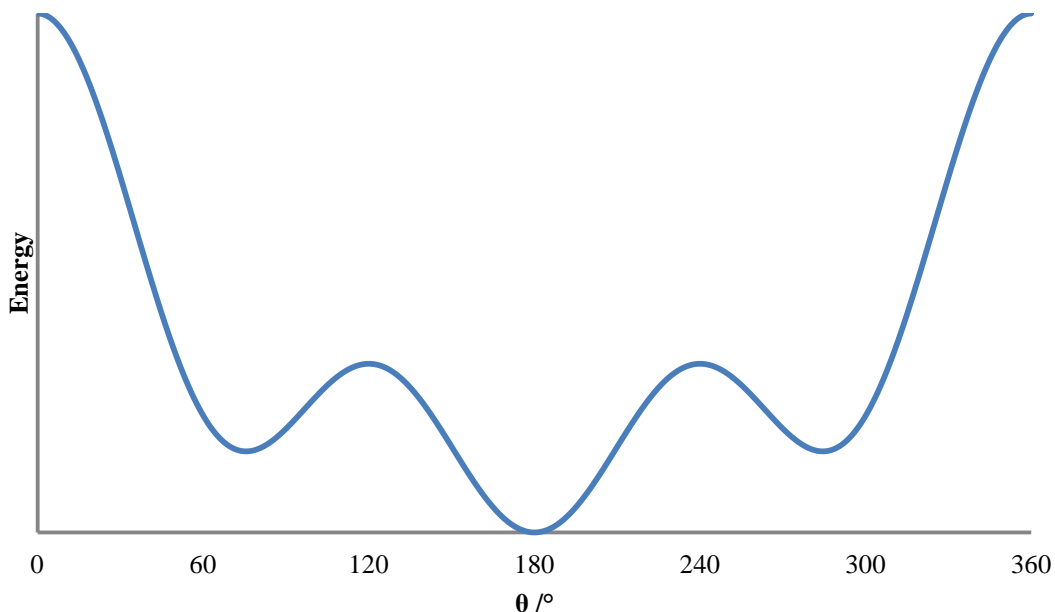


**Figure 5:** An example torsion energy function with  $A_1=0.6$ ,  $A_2=-0.3$  and  $A_3=0.4$ .

The torsion energy potential describes the change in energy as atoms are rotated around a bond. The potential in **Figure 5** is of the form of a triple cosine function:

$$U = \frac{1}{2}[A_1(1 + \cos \theta) + A_2(1 - \cos 2\theta) + A_3(1 + \cos 3\theta)] \quad (3.33)$$

Single cosine and harmonic torsion potentials are also common among many other kinds of torsion potential.

The electrostatic interaction between two charged particles is governed by Coulomb's Law:

$$U = \frac{1}{4\pi\epsilon_0} \frac{q_i q_j}{r} \quad (3.34)$$

Where  $q_i$  and  $q_j$  are the charges on particles  $i$  and  $j$  respectively, and  $\epsilon_0$  is the permittivity of free space. For two positively or negatively charged particles the interaction will always be repulsive (**Figure 6**), and for two oppositely charge particles the interaction will always be attractive. Larger charges will have stronger interactions.

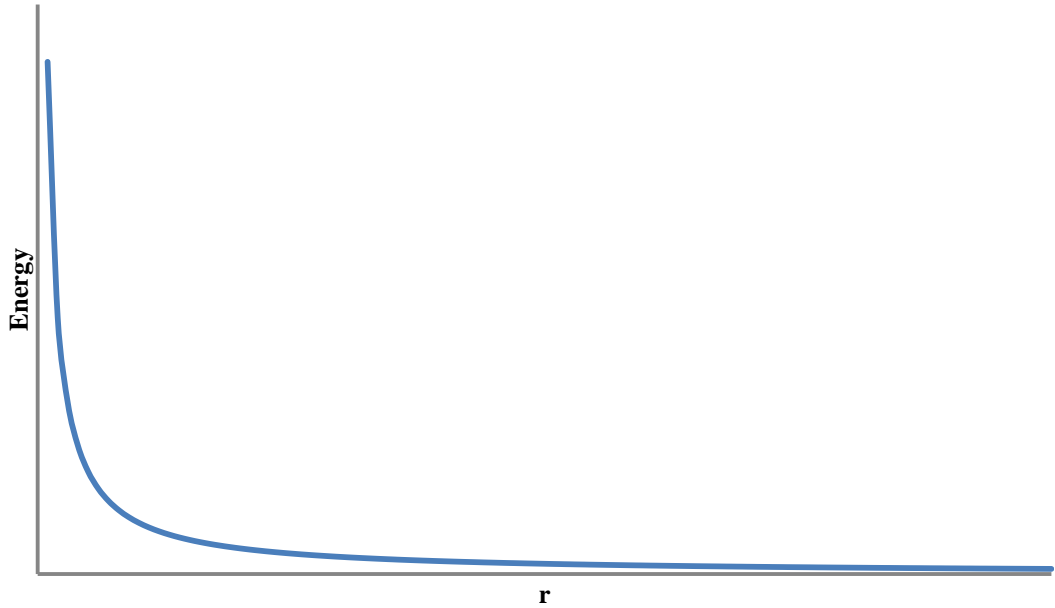


**Figure 6:** Graph showing the electrostatic potential between two identically charged particles.

Van der Waals interactions are often modelled using Lennard – Jones or N-M potentials (**Equations 3.35 & 3.36**) A simple 12-6 potential is also common (**Equation 3.37**). The values for the various coefficients are determined by fitting the potential to experimental or high level *ab initio* data.

$$U = 4\varepsilon \left[ \left( \frac{\sigma}{r} \right)^{12} - \left( \frac{\sigma}{r} \right)^6 \right] \quad (3.35)$$

$$U = \frac{E_0}{n-m} \left[ m \left( \frac{r_0}{r} \right)^n - n \left( \frac{r_0}{r} \right)^m \right] \quad (3.36)$$

$$U = \frac{A}{r^{12}} - \frac{B}{r^6} \quad (3.37)$$

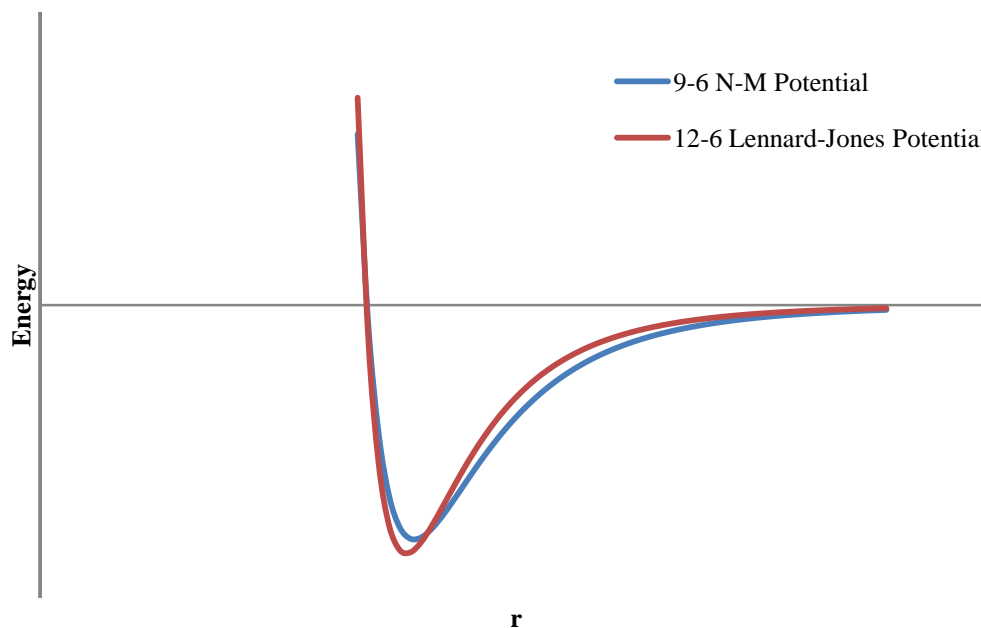


**Figure 7:** Graph showing 9-6 N-M and 12-6 Lennard-Jones van der Waals potentials.

These two different van der Waals interactions in **Figure 7** are quite similar in that they are attractive at distances longer than their equilibrium distance and repulsive at shorter distances, which approximates experimentally observed van der Waals interactions.

These are only some of the many possible forms for bonded and non-bonded interactions that exist, and some may be more suitable than others depending on which properties are most important to be modelled accurately.

### 3.9.2. Classical Water Models

There are a great many different types of water models used within simulation science. They can vary significantly depending on their intended use. In many models the water molecule is modelled as a three centre (representing the two hydrogen atoms and one oxygen atom), flexible model (this allows for bond and angle stretching). There are also four and five centre models in existence (such as TIP4P [19] and TIP5P [20]) as well as rigid body models where no angle bending motions or bond stretching is possible, and constrained models where bond lengths and angles are not allowed to exceed certain parameters. Typically the oxygen atom is modelled as being  $\delta$ -negative and the hydrogen atoms as  $\delta$ -positive to represent

the transfer of electron density from the hydrogen atoms to the oxygen atom, corresponding to the differences in their relative electronegativities.

Classical water models are parameterised against experimental data such as melting and boiling points, and the structures of the different ice polymorphs among many other properties. The hexagonal ice  $I_h$  polymorph is the structure most commonly found in nature. There are fourteen other polymorphs (including liquid water) currently known which can form under a wide variety of different temperature and pressures. They all exhibit different structures such as ice II which is rhombohedral, ice III which is tetragonal and ice VII & VIII which are cubic with differently positioned hydrogen atoms.

### 3.9.3. SPC/E

SPC/E [21] is a three body, constrained model of water. The O-H bond length is 1 Å and the H-O-H angle is 109.47°. The charges on the oxygen and hydrogen atoms are -0.8476 e and +0.4238 e respectively. This model is based on the earlier SPC (simple point charge) model [22]. It improves the earlier model by using a more accurate parameterisation of the polarisation of the water molecule which was determined from the electrostatic interaction of the molecule. The total electrostatic interaction includes the total interaction of induced dipoles instead of only half that value which leads to too large heats of vaporisation. By correcting for the self interaction the predicted heat of vaporisation is reduced and the parameterisation of the model becomes more accurate.

### 3.9.4. TIP4P and TIP4P/2005

TIP4P is a rigid body, four site model (see **Figure 8**). In this model a dummy atom (henceforth referred to as M) is added below the oxygen atom within plane of the molecule such that the O-M bond bisects the H-O-H angle. The  $\delta$ -negative charge that would normally be found on the oxygen atom is transferred entirely to the dummy atom so that oxygen is now electrically neutral. The O-H bond length is fixed at 0.9572 Å, the O-M distance is 0.150 Å and the H-O-H angle is 104.52°. The hydrogen atoms carry a charge of +0.52 e and M carries a charge of -1.04 e. These parameters allow for close reproduction of the experimentally determined properties of water. The parameters were derived by reparameterising the earlier water model TIPS2 [23] which shares identical geometry to the TIP4P model. The charges on the

atoms are slightly higher in TIP4P than TIPS2 and the Lennard-Jones parameters have also been adjusted. This allows higher density and slightly more accurate structural properties than TIPS2.

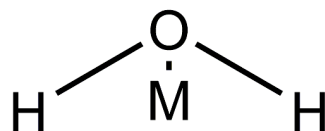


**Figure 8:** A water molecule as described by the TIP4P model.

The TIP4P/2005 [24] revision of the model the O-M distance is extended to 0.1546 Å and the electrical charges increased to +0.5564 e and -1.1128 e on the hydrogen atoms and M respectively. Reparameterisation was done as the availability of greater computational resources allows testing against a wider variety of properties. This model was parameterised against a fit of the maximum density and stability of several ice polymorphs over a temperature range of 123 K to 573 K at pressures of up to 40,000 bar. The parameterisation was made by making a Taylor expansion of the desired properties such as maximum density and melting point, and truncating at first order. A nonlinear fit of these properties is then made such that it minimises the square of the deviation with respect to their experimental values. Shifting the dummy atom M towards the hydrogen atoms prevents overstabilisation of the ice II polymorph [24]. Increasing the charges on the hydrogen atoms and M increases the dipole moment of the water molecule which allows a more accurate determination of the enthalpy of vaporisation.

The TIP4P/2005 model very closely reproduces experimental results and provides significant improvements over the original TIP4P model with regards to density of liquid water, thermal expansion, compressibility and the densities of the different ice polymorphs [24]. Vega *et al.* [25] have compared the TIP3P [19], TIP4P, TIP5P and TIP4P/2005 models to experimental data and it was determined that TIP4P/2005 provides the best description of most experimental properties. Vega *et al.* [26] have also shown that TIP4P/2005 more accurately describes the surface tension of water than other models such as SPC/E and TIP4P. The phase diagram produced by this model is significantly closer to the experimental one than previous models (**Figure 9**). All together TIP4P/2005 is an excellent classical model with which to study systems involving water.

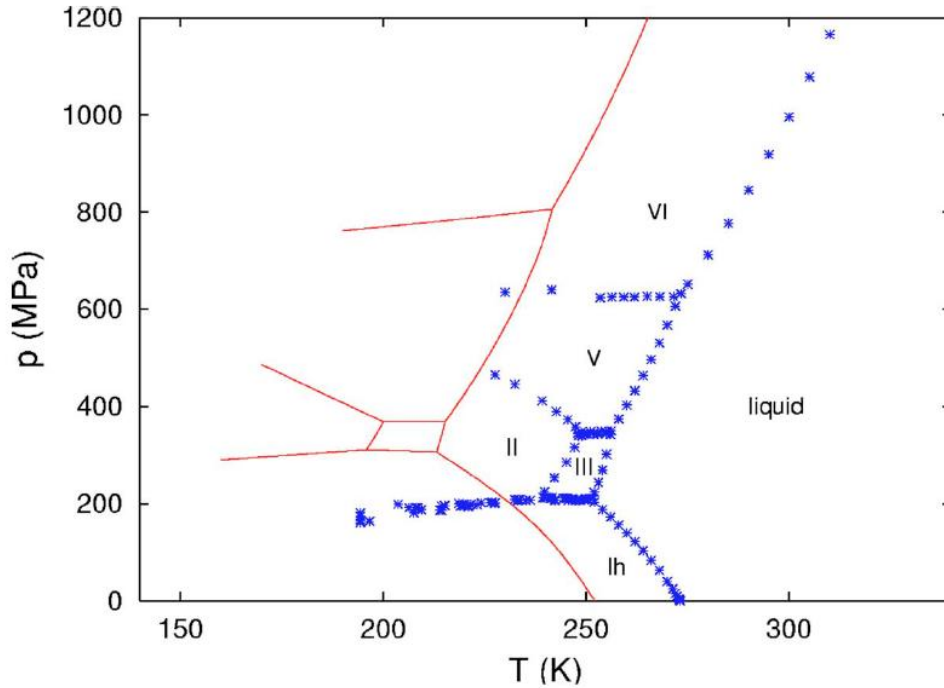


**Figure 9:** Phase diagram of water. The red lines indicate TIP4P/2005 simulation results, and the blues stars indicate experimental results. Image taken from ref. [24].

### 3.9.5. Classical Molecular Dynamics Simulations

Molecular dynamics calculations generate a series of frames (a trajectory) from an initial set of starting coordinates by solving Newton's equations of motion over a series of time steps [27]. Time steps are typically of the order  $10^{-15}$  seconds depending on the phenomena of interest, but the simulations themselves can run for many hundreds of thousands or even millions of steps potentially simulating microseconds of real time. This allows the study of how a system evolves over time and the determination of time dependent properties like diffusion coefficients.

Each particle in a classical molecular dynamics simulation is assigned a potential (or forcefield) which determines how it interacts with other particles in the system. The potential between two particles  $a$  and  $b$  is the sum of electrostatic interactions and Van der Waal's interactions (in this example a simple 12-6 potential):

$$U = \left( \frac{1}{4\pi\epsilon_0} \frac{q_a q_b}{r} \right) + \left( \frac{A}{r^{12}} - \frac{B}{r^6} \right) \quad (3.38)$$

To use these potentials, Newton's second law is written as:

$$-\frac{dU}{dr} = m \frac{d^2 r}{dt^2} \quad (3.39)$$

Where  $\mathbf{r}$  is the vector coordinates of the particles.

After the initial coordinates are set, each particle is given an initial velocity such that the total kinetic energy of the system is consistent with the initial starting temperature. Often the individual velocities of the particles are randomised according to the Maxwell-Boltzmann distribution, provided that the total momentum is zero otherwise there would be a net drift of particles within the system. During the equilibration phase of a molecular dynamics simulation kinetic energy can be added or removed from particles in the system to keep the total energy constant.

From initial coordinates  $\mathbf{r}_i$ , the position after a single timestep can be expanded as a Taylor series:

$$\mathbf{r}_{i+1} = \mathbf{r}_i + \frac{d\mathbf{r}}{dt}\Delta t + \frac{1}{2}\frac{d^2\mathbf{r}}{dt^2}(\Delta t)^2 + \dots \quad (3.40)$$

$$\mathbf{r}_{i+1} = \mathbf{r}_i + \mathbf{v}_i\Delta t + \frac{1}{2}\mathbf{a}_i(\Delta t)^2 + \dots \quad (3.41)$$

For determining the position at earlier timesteps the equation becomes:

$$\mathbf{r}_{i-1} = \mathbf{r}_i - \mathbf{v}_i\Delta t + \frac{1}{2}\mathbf{a}_i(\Delta t)^2 + \dots \quad (3.42)$$

By adding **Equations 3.41** and **3.42** together we obtain:

$$\mathbf{r}_{i+1} = 2\mathbf{r}_i - \mathbf{r}_{i-1} + \mathbf{a}_i(\Delta t)^2 + \dots \quad (3.43)$$

Which is known as the Verlet algorithm [28]. This fits well with the microcanonical or NVE ensemble as the total number of particles, system volume and total energy are all constant. It is however possible to use other ensembles with the Verlet algorithm.

Provided that the timestep used in a simulation is sufficiently small it is possible to discard higher order terms in the Taylor series.

At the start of the simulation the position at the previous timestep is unknown and is estimated by:

$$\mathbf{r}_{-1} = \mathbf{r}_0 - \mathbf{v}_0\Delta t \quad (3.44)$$

**3.9.6. Micro-Canonical Ensemble**

In the micro-canonical (NVE) ensemble the total energy, volume and number of particles in the system remain constant. This ensemble is representative of an isolated system.

**3.9.7. Isothermal-Isobaric Ensemble**

In the isothermal-isobaric (NPT) ensemble the pressure, temperature and number of particles remain constant. The volume of the system is allowed to fluctuate and by averaging the volume over the length of a sufficiently long simulation it is possible to determine the density of the system. In this ensemble thermostats and barostats are needed to maintain temperature and pressure respectively. In the Nosé-Hoover [29] [30] thermostat the system is coupled to a fictional heat bath with which to exchange energy so as to maintain temperature. Pressure is maintained by altering the volume of the system by adjusting the periodic boundary conditions of the simulation cell appropriately. There are defined thermostat and barostat periods which determine how often energy is exchanged with the heat bath and how rapidly the cell vectors change respectively.

## Bibliography

- [1] M. Born and R. Oppenheimer, *Ann. Physik*, vol. 84, p. 457, 1927.
- [2] P. Hohenberg and W. Kohn, *Phys. Rev.*, vol. 136, p. B864, 1964.
- [3] W. Kohn and L. J. Sham, *Phys. Rev.*, vol. 140, p. A1133, 1965.
- [4] J. P. Perdew, K. Burke and M. Ernzerhof, *Physical Review Letters*, vol. 77, p. 3865, 1996.
- [5] J. P. Perdew and Y. Wang, *Phys. Rev. B.*, vol. 45, p. 13244, 1992.
- [6] S. L. Dudarev, G. A. Botton, S. Y. Savrasov, C. J. Humphreys and A. P. Sutton, *Phys. Rev. B.*, vol. 57, p. 1505, 1998.
- [7] C. Adamo and V. Barone, *Journal Of Chemical Physics*, vol. 110, p. 6158, 1999.
- [8] A. V. Krukau, O. A. Vydrov, A. F. Izmaylov and G. E. Scuseria, *The Journal Of Chemical Physics*, vol. 125, p. 224106, 2006.
- [9] C. Møller and M. S. Plesset, *Phys. Rev.*, vol. 46, p. 618, 1934.
- [10] J. Cizek, *J. Chem. Phys.*, vol. 45, p. 4256, 1966.
- [11] M. C. Payne, M. P. Teter, D. C. Allan, T. A. Arias and J. D. Joannopoulos, *Reviews Of Modern Physics*, vol. 64, p. 1046, 1992.
- [12] P. E. Blochl, *Phys. Rev. B.*, vol. 50, p. 17953, 1994.
- [13] F. Bloch, *Zeitschrift für Physik*, vol. 52, p. 555, 1929.
- [14] G. Kresse, M. Marsman and J. Furthmüller, *VASP The Guide*, Vienna, 2013, p. 155.
- [15] H. J. Monkhorst and J. D. Pack, *Phys. Rev. B.*, vol. 13, p. 5188, 1976.
- [16] F. Jensen, *Introduction To Computational Chemistry (Second Edition)*, John Wiley & Sons Ltd., 2007, p. 211.
- [17] R. F. W. Bader, *Atoms In Molecules: A Quantum Theory*, Oxford University Press, New York, 1990.
- [18] H. Jonsson, G. Mills and K. W. Jacobsen, *Classical And Quantum Dynamics In Condensed Phase Simulations*, B. J. Byrne, G. Ciccotti and D. F. Coker, Eds.,

World Scientific, 1998, p. 385.

- [19] W. L. Jorgensen, J. Chandrasekhar, J. D. Madura, R. W. Impey and M. L. Klein, *The Journal Of Chemical Physics*, vol. 79, p. 926, 1983.
- [20] M. W. Mahoney and W. L. Jorgensen, *Journal Of Chemical Physics*, vol. 112, p. 8910, 2000.
- [21] H. J. C. Berendsen, J. R. Grigera and T. P. Straatsma, *The Journal Of Physical Chemistry*, vol. 91, p. 6269, 1987.
- [22] H. J. C. Berendsen, J. P. M. Postma, W. F. van Gunsteren and J. Hermans, *Intermolecular Forces*, Reidel, 1981.
- [23] W. Jorgensen, *J. Chem. Phys.*, vol. 77, p. 4156, 1982.
- [24] J. L. F. Abascal and C. Vega, *The Journal Of Chemical Physics*, vol. 123, p. 234505, 2005.
- [25] C. Vega, J. L. F. Abascal, M. M. Conde and J. L. Aragones, *Faraday Discussions*, vol. 141, p. 251, 2009.
- [26] C. Vega and E. de Miguel, *J. Chem. Phys.*, vol. 126, p. 154707, 2007.
- [27] F. Jensen, *Introduction To Computational Chemistry (Second Edition)*, John Wiley & Sons Ltd., 2007, p. 446.
- [28] L. Verlet, *Phys. Rev.*, vol. 159, p. 98, 1967.
- [29] S. Nosé, *J. Chem. Phys.*, vol. 81, p. 511, 1984.
- [30] W. G. Hoover, *Phys. Rev. A.*, vol. 31, p. 1695, 1985.

## Chapter 4 – Density Functional Theory Calculations

In this chapter the computer simulation of the oxidation of ethylene glycol to hydroxyethanal over various magnesium oxide, aluminium oxide and palladium oxide surfaces, as well as gold nanoparticles will be studied. Hydroxyethanal was chosen as the target product as aldehydes are first oxidation products of primary alcohols. To perform these simulations the periodic DFT code VASP [1] will be used. VASP is a very commonly used software code for density functional theory calculations involving bulk materials and surfaces.

The  $pK_a$  of ethylene glycol is 15.1 [2], indicating that it is a very weak acid so it will not easily dissociate protons in water, therefore a catalyst is needed to accelerate the oxidation of ethylene glycol. Catalysts for alcohol oxidation are often transition metal nanoparticles supported on a metal oxide such as MgO [3] or Al<sub>2</sub>O<sub>3</sub> [4]. Typically in these reactions the nanoparticle will be gold [5], platinum or palladium, or an alloy [6] of those metals in varying ratios. Smaller nanoparticles are more catalytically active and can often form a layer of oxide on their surface in the presence of oxygen [7]. The surfaces studied in this chapter are representative of the different parts of the catalyst, with the MgO and Al<sub>2</sub>O<sub>3</sub> surfaces representing the support material, PdO representing an oxidized palladium surface and the Au<sub>38</sub> and Au<sub>38</sub>O<sub>16</sub> clusters representing clean and oxidized gold nanoparticles respectively.

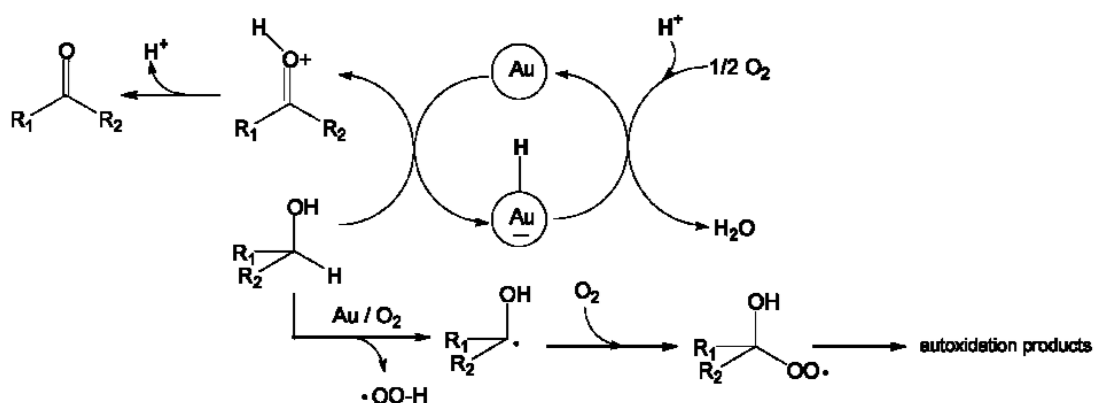


**Figure 1:** A suggested mechanism for the oxidation of an alcohol using a gold catalyst. Image taken from ref. [8].

Two possible reaction mechanisms for the oxidation of an alcohol by a gold catalyst are shown in **Figure 1**. In the first mechanism a C-H bond is broken and the

hydrogen atom leaves as a hydride ion which adsorbs to the catalyst surface. Following this an O-H bond is broken with the hydrogen atom leaving as a proton, which results in the formation of an aldehyde (or ketone). In the second mechanism a hydrogen radical leaves a carbon atom and then molecular oxygen is added to the alcohol molecule which is then oxidised further, but the subsequent oxidation products are not stated (they may be some kind of peroxide species).

In this chapter adsorption of ethylene glycol via its alcohol group oxygen atoms, with both O-H activation followed by C-H activation (**Figure 2a**) and C-H activation followed by O-H activation (**Figure 2b**) to form hydroxyl ethanol are studied. Depending on steric interactions the carbon atom which has dissociated the hydrogen atom in **Figure 2b** may or may not be close enough to interact with the surface that the ethylene glycol has adsorbed to. The adsorption energies and barriers to O-H and C-H activation are recorded and compared to determine the most favourable catalysts for ethylene glycol oxidation.

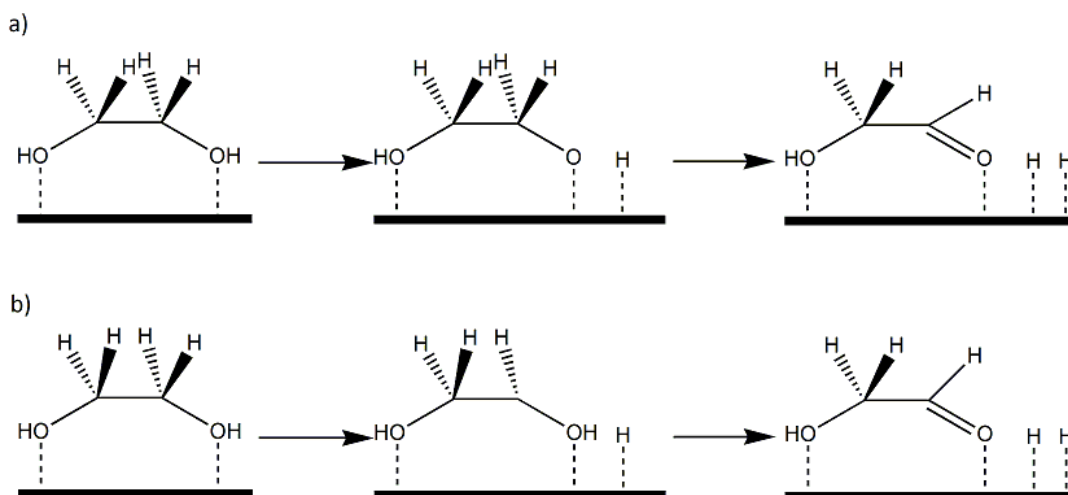


**Figure 2:** Ethylene glycol adsorbed to a surface a) first undergoing O-H activation and then C-H activation and b) first undergoing C-H activation and then O-H activation to form hydroxyethanal.

#### 4.1. Magnesium Oxide

Magnesium oxide is a basic material which is used as a catalyst to replace liquid phase bases such as sodium hydroxide in the oxidation of alcohols. In such reactions the hydroxide ions will accept protons dissociated by alcohol groups, while a transition metal such as gold will catalyse the removal of hydride ions resulting in the formation of an aldehyde. By removing the sodium hydroxide from the reaction

and replacing it with magnesium oxide the reaction has become cleaner as removal and safe disposal of sodium hydroxide from the end products is no longer an issue.

#### 4.1.1. Determining the Appropriate Functional

Three pure DFT functionals (PW91 [9], PBE [10] and RPBE [11]), and two hybrid DFT functionals (PBE0 [12] and HSE06 [13]) were tested for accuracy and performance on a single unit cell of bulk magnesium oxide consisting of four magnesium and four oxygen atoms.

The calculations were performed using VASP with a planewave cut off of 500 eV and  $3 \times 3 \times 3$   $k$ -point sampling. All calculations in this chapter are considered to be converged when the energy difference between electronic iterations is less than  $10^{-4}$  eV and the energy difference between geometric iterations is less than  $10^{-3}$  eV. In order to determine the lattice expansion a series of calculations were performed in which the unit cell was shrunk or expanded by up to 5% from the experimental values of  $a=b=c=4.2112 \text{ \AA}$  [14] and the energy was recorded. A quadratic curve was fitted to compare the energy and expansion of the cell, and from this it is possible to determine the lowest energy expansion of the cell from the minimum of the curve (Figure 3).

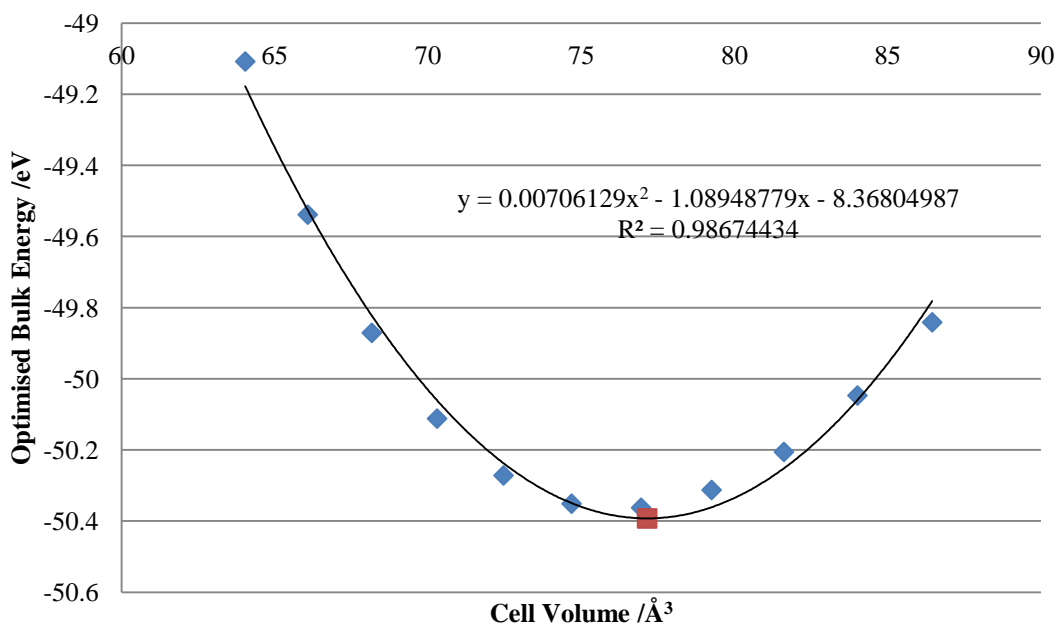


**Figure 3:** Graph showing the cell volume against energy for bulk magnesium oxide calculated using the PW91 functional. The red marker indicates the position of the minimum of the fitted curve.

The percentage expansion of the magnesium oxide bulk unit cell was recorded for each pure and hybrid functional (**Figure 4**).

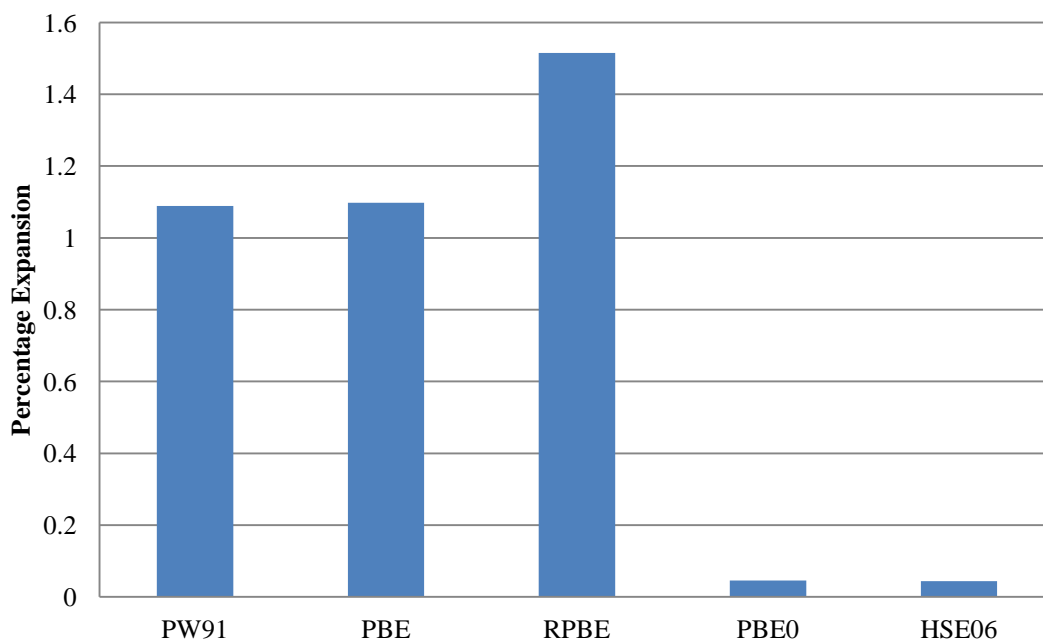


**Figure 4:** Graph showing the percentage expansion of the lattice vectors of bulk magnesium oxide for various pure and hybrid DFT functionals.

Both the PW91 and PBE functionals show an expansion of approximately 1.1% in the lattice vectors. The RPBE functional shows an expansion of approximately 1.5%. The hybrid PBE0 and HSE06 functionals show much smaller expansions at approximately 0.04%.

The time taken complete each calculation was also recorded (**Figure 5**).

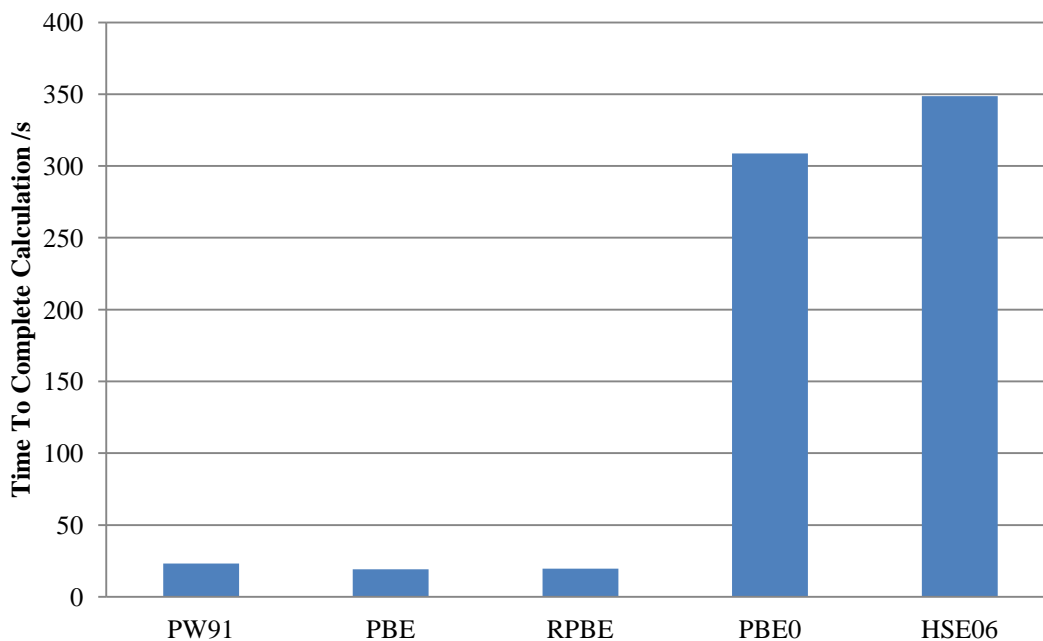


**Figure 5:** Graph showing the CPU time to complete optimisation of bulk magnesium oxide for various pure and hybrid DFT functionals. Eight cores were used for each calculation.

The three pure DFT functionals completed the optimisation of the bulk unit cell quickly (approximately 19 seconds for PBE and RPBE, and 23 seconds for PW91). The hybrid functionals required significantly greater time 308 seconds and 348 seconds for PBE0 and HSE06 respectively.

Planewave basis set convergence was also tested for each functional and it was found that there was little change in bulk energy above a cut off of 500 eV for all of the functionals (**Figure 6**).

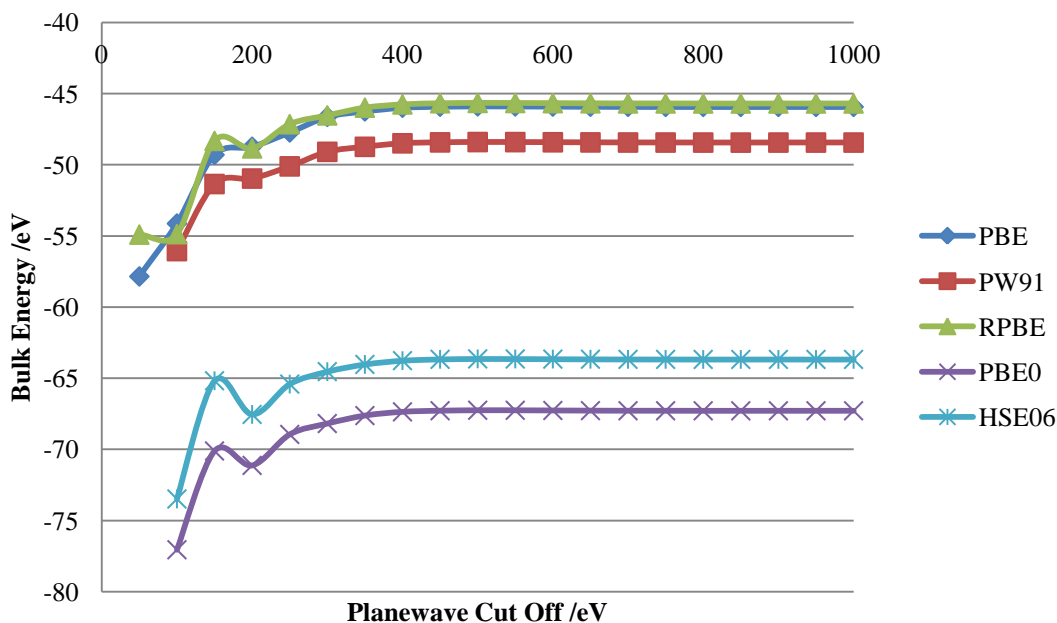


**Figure 6:** Graph showing planewave cut off against bulk energy for magnesium oxide for the different pure and hybrid DFT functionals tested.

While the hybrid functionals show much greater accuracy than the pure DFT functionals the time taken to complete the calculations is significantly greater. The unit cell of bulk magnesium oxide is a relatively small system (only eight atoms and a total of thirty two valence electrons) and since DFT calculations scale as  $N^3$ , calculations using hybrid functionals will quickly become impractical as the size of the system increases. Of the three pure DFT functionals, PBE and PW91 show the smallest expansion in lattice vectors, and PBE shows fastest computation time. Thus the PBE functional appears to be the most appropriate to use for these calculations.

#### 4.1.2. Determining the Lattice Parameters

The bulk unit cell of magnesium oxide has been optimised using the PBE functional at  $3 \times 3 \times 3$   $k$ -points and a planewave cut off of 500 eV. Bulk magnesium oxide has the structure of rock salt. Using the methodology described in **Section 4.1.1.** the optimised lattice parameters were determined to be  $a=b=c=4.2495$  Å, this is an expansion of approximately 1.1% over the experimental values [14]. The lattice parameters are optimised to determine the lowest energy structure of the bulk material and hence any surfaces cleaved from it will have a more favourable arrangement of atoms. This has the effect of reducing the computation time of future calculations.

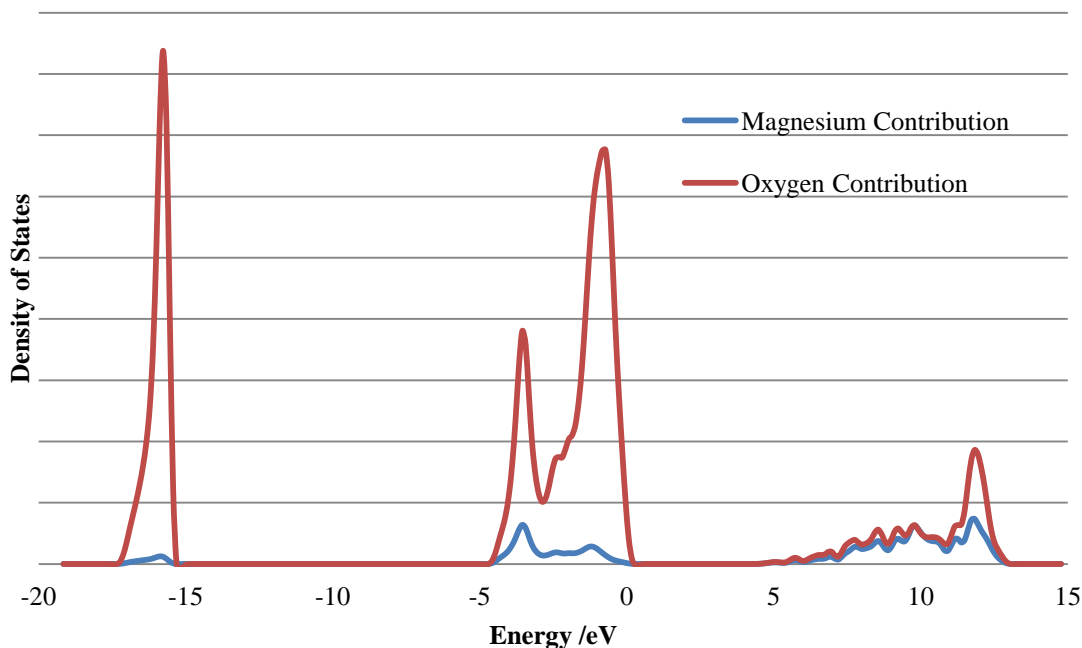


**Figure 7:** Density of states plot for the optimised unit cell of bulk magnesium oxide.

A density of states calculation was performed on the optimised bulk unit cell of magnesium oxide (**Figure 7**). The calculation was performed using the PBE functional with a 500 eV planewave cut off at  $9 \times 9 \times 9$   $k$ -points. The large band gap of approximately 6 eV indicates that it is an insulator. The experimental value for the band gap of MgO as determined by Whited *et al.* is 7.83 eV [15], and the theoretical value calculated using the local density approximation (LDA) is 4.73 eV [16].

#### 4.1.3. The MgO (100) and (130) Surfaces

Magnesium oxide has rock salt structure consisting of alternating magnesium and oxygen atoms. In the bulk structure each atom is coordinated to six other atoms (6c) of the opposite type and all Mg-O distances were calculated to be 2.125 Å. Bader analysis [17] of this structure gives a Bader charge of +1.81 e on the magnesium atoms and a corresponding Bader charge of -1.81 e on the oxygen atoms. The Bader analysis was performed using code from the University of Texas at Austin [18] [19] [20] written by Henkleman *et al.*

To determine the appropriate thickness of each slab of magnesium oxide, surface energy calculations were performed. A 15 Å vacuum gap was applied above each slab and the structures were optimised at  $3 \times 3 \times 1$   $k$ -points. The top three layers of each slab were free to relax, while any layers below those (zero to nine layers

depending on the thickness of the slab) were held fixed to simulate bulk behaviour of those atoms.

The surface energy is defined as the excess energy of an exposed surface compared to that of the bulk material. For all surfaces the surface energy will be positive meaning that it is energetically unfavourable to cleave it from the bulk material. The lower the surface energy is the more stable that surface is. The equation to calculate surface energy is:

$$E_{surface} = \frac{E_{slab} - n \cdot E_{bulk}}{2A} \quad (4.1)$$

Where  $E_{slab}$  is the energy of the slab,  $E_{bulk}$  is the energy of the bulk unit cell per formula unit and  $n$  is the number of formula units present in the slab.  $A$  is the area of the exposed surface defined by:

$$A = |\mathbf{a}| |\mathbf{b}| \sin \theta \quad (4.2)$$

Where  $\mathbf{a}$  and  $\mathbf{b}$  are the surface lattice vectors and  $\theta$  is the angle between them.

From Kiejna *et al.* [21] **Equation 4.1** can be rewritten as:

$$E_{slab} = 2AE_{surface} + nE_{bulk} \quad (4.3)$$

This gives the slab energy as a function of  $n$ . It should be noted that this method is preferred, as the bulk energy is obtained as the gradient of **Equation 4.3** rather than from a series of calculations on differently sized bulk cells scaled to be equivalent to the slab.

The approach used here to calculate the surface energy is to have one face relaxed and the other fixed at the bulk termination of the material. To obtain the surface energy when the lower face of the slab has the bulk termination, the single point energy of the slab ( $E_{surf}^{term}$ ) is also needed. This is obtained by either performing a single point energy calculation on the slab ( $E_{slab}^{SP}$ ), or from the energy of the first complete iteration in a geometry optimisation.

$$E_{surf}^{term} = \frac{E_{slab}^{SP} - nE_{bulk}}{2A} \quad (4.4)$$

From Howard & Willock [22] the energy of the slab becomes:

$$E_{slab} = AE_{surface}^{term} + AE_{surface}^{opt} + nE_{bulk} \quad (4.5)$$

**Equation 4.5** can be rearranged to:

$$E_{surface}^{opt} = \frac{E_{slab} - nE_{bulk}}{A} - E_{surface}^{term} \quad (4.6)$$

A series of geometry optimisations were performed on bulk MgO and slabs of MgO (100) and (130) between three and twelve layers thick. In each slab calculation the atoms in the top three layers of the slab were allowed to relax, while the rest were fixed.

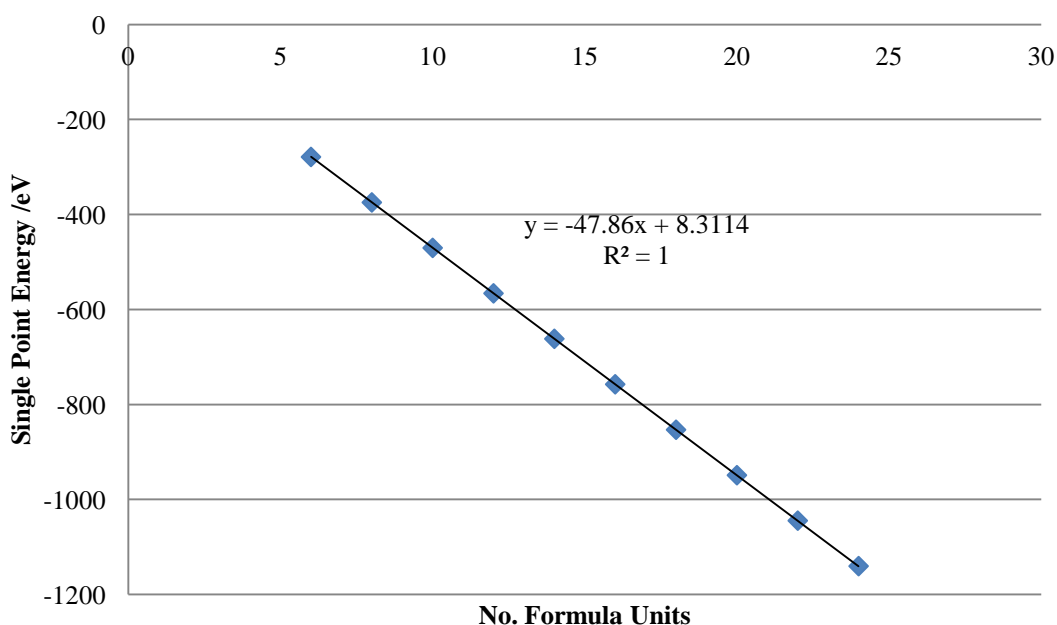


**Figure 8:** Graph showing slab energy against number of formula units for the MgO (100) surface.

By plotting a graph of the number of formula units against the single point slab energy (**Figure 8**) it is possible to determine the bulk energy of a unit cell of the material as it is the slope of the graph (**Equation 4.3**). For magnesium oxide a bulk energy of -47.86 eV is obtained.

Using a similar approach to the MgO (100) surface the bulk energy of MgO obtained by the single point slab calculations for the MgO (130) surface is -47.86 eV. This is consistent with the value obtained from the MgO (100) surface calculations, as well as single point energy calculations on the bulk unit cell.

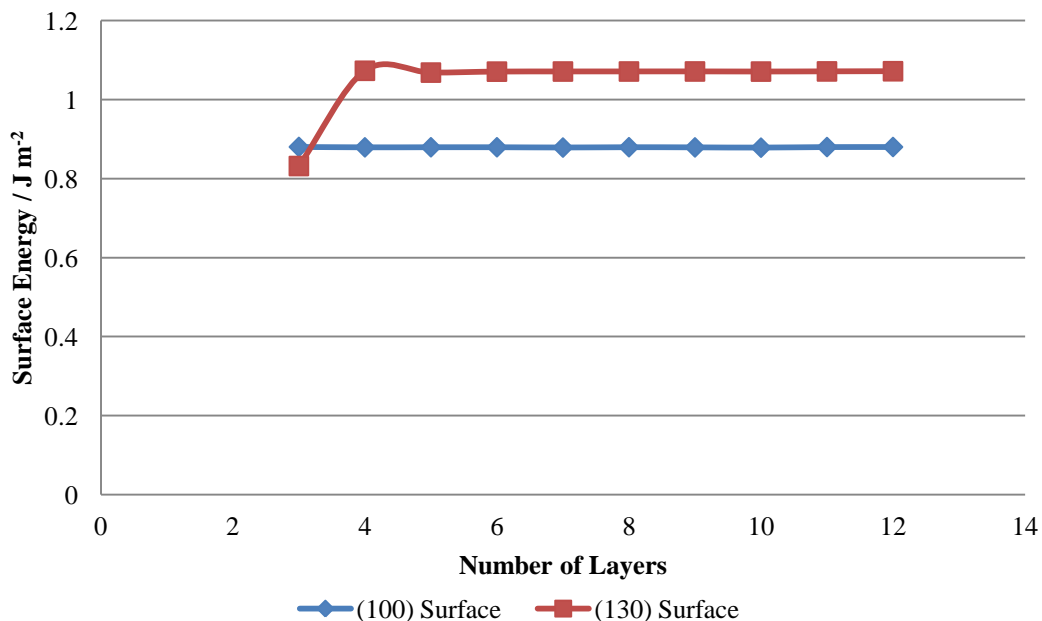


**Figure 9:** Graph showing surface energy against number of layers for the MgO (100) and (130) surfaces.

The surface energy (obtained using **Equation 4.6**) of the MgO (100) surface remains almost constant with respect to the number of layers used in the calculation at approximately  $0.88 \text{ J m}^{-2}$ , and the surface energy for the MgO (130) surface remains almost constant at approximately  $1.07 \text{ J m}^{-2}$  (**Figure 9**) for slab thicknesses of five layers and above. This shows that the stepped surface has a higher surface energy and hence is less stable than the flat surface, which is due to the presence of lower coordinated atoms in the step site of the (130) surface.

The surface energies for both MgO (100) and (130) are positive, meaning that it is energetically unfavourable to cleave these surfaces from bulk magnesium oxide. The surface energy of the (130) surface is higher than that of the (100) surface, which is due to the presence of the four coordinated magnesium and oxygen atoms in the step site. A slab thickness of five layers was determined to be sufficient for both the MgO (100) and (130) surfaces (**Figure 9**), as there is little change in surface energy for this thickness and above. This gives a reasonable thickness of slab while not containing too many atoms as to make the calculations impractical. The lower the surface energy, the more likely that surface is to form when the bulk material is cleaved.

The coordination of atoms in the surface is indicated with the suffix *nc* where *n* is the coordination number of the atom i.e. O5c indicates a five coordinated oxygen atom.

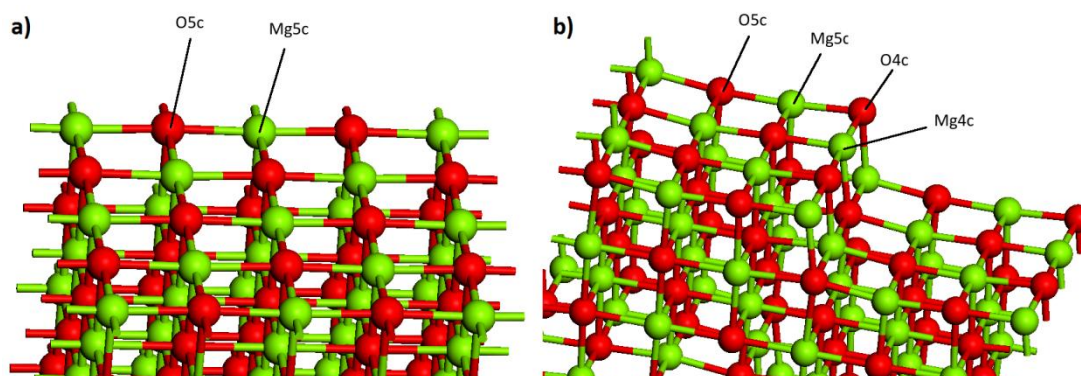


**Figure 10:** The optimised structure of the a) MgO (100) and b) MgO (130) surfaces showing the different types of atom present. Magnesium atoms are in green, oxygen atoms are in red. The 4c and 5c suffixes indicate four and five coordinated atoms respectively.

In the MgO (100) surface (**Figure 10a**) the top layer of atoms are all five coordinated (5c), and those below the surface are six coordinated in the same manner as the bulk structure. In the MgO (130) surface (**Figure 10b**) the top layer of atoms are five coordinated except at the step site where they are four coordinated (4c).

The (100) and (130) surfaces are both cleaved from the optimised bulk unit cell of MgO. In the simulations the (100) surface consists of 40 magnesium atoms and 40 oxygen atoms, and the (130) surface consists of 56 magnesium atoms and 56 oxygen atoms. During optimisation the bottom two layers of each structure were held fixed to simulate bulk behaviour of those atoms, and the top three layers were allowed to relax.

The MgO (100) surface is five layers thick and the  $\text{Mg}_{5c}\text{-O}_{6c}$  distance was measured to be 2.100 Å, the  $\text{Mg}_{6c}\text{-O}_{5c}$  was 2.138 Å and the  $\text{Mg}_{5c}\text{-O}_{5c}$  distance was 2.125 Å. In the bulk structure the  $\text{Mg}_{6c}\text{-O}_{6c}$  distance is 2.125 Å. Bader analysis of the (100) surface gives the  $\text{Mg}_{5c}$  atoms a charge of +1.78 e and the corresponding  $\text{O}_{5c}$  atoms a charge of -1.78 e. The six coordinated magnesium atoms below the surface had charges of +1.78 e (+1.79 e at the centre of the slab), the oxygen atoms charges of -1.77 e (-1.80 e at the centre of the slab).

The MgO (130) surface is five layers thick and the  $\text{Mg}_{4c}\text{-O}_{4c}$  distance was measured to be 2.127 Å, the  $\text{Mg}_{6c}\text{-O}_{4c}$  distance was 2.095 Å, the  $\text{Mg}_{4c}\text{-O}_{6c}$  distance was 2.077

Å, the  $\text{Mg}_{4c}\text{-O}_{5c}$  distance was 1.964 Å, the  $\text{Mg}_{5c}\text{-O}_{4c}$  distance was 2.023 Å and the  $\text{Mg}_{5c}\text{-O}_{5c}$  distances were measured as between 2.003 Å and 2.127 Å depending on their positions in the lattice. For comparison the  $\text{Mg}_{6c}\text{-O}_{6c}$  distance in the bulk structure is 2.125 Å, indicating a contraction at the step site. The four coordinated magnesium atoms had a charge of +1.63 e, and the four coordinated oxygen atoms had Bader charges of -1.62 e and -1.68 e. The five coordinated magnesium atoms had charges between +1.63 e and +1.68 e, and the five coordinated oxygen atoms had charges between -1.63 e and -1.65 e. The magnesium atoms below the exposed surface had a wider range of charges between +1.60 e and +1.74 e, with the higher charges being located on the atoms closer to centre of the slab. The oxygen atoms showed similar behaviour, with the charges ranging from -1.64 e to -1.69 e.

#### 4.1.4. Adsorption of Ethylene Glycol

There are two possible configurations of ethylene glycol in the gas phase, gauche with both alcohol groups on the same side of the molecule and staggered with the alcohol groups on different sides (**Figure 11**). The staggered conformer is the more stable configuration due to the reduction in steric hindrance, with the gauche form being 26 kJ mol<sup>-1</sup> higher in energy calculated using the PBE functional with a 500 eV planewave cut off.

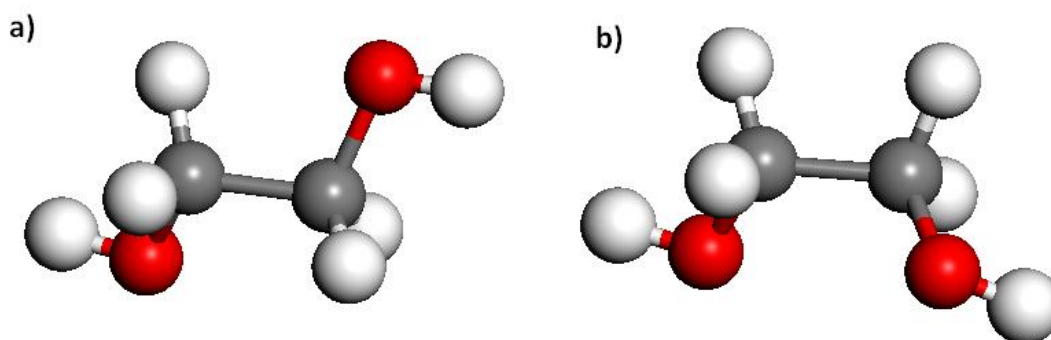


**Figure 11:** The optimise staggered (a) and gauche (b) conformers of ethylene glycol. A single molecule of ethylene glycol was placed in the both configurations over the MgO (100) surface and the system was reoptimised. The staggered conformer was placed such that one of its oxygen atoms was coordinated to a magnesium atom in the surface, and the gauche was places such that both oxygen atoms were coordinated to two separate magnesium atoms. It is not possible to place the

molecule flat on the surface due to steric repulsion between the hydrogen atoms and the surface.

The adsorption energy of a molecule to a surface is calculated using the following formula:

$$E_{adsorption} = E_{system} - (E_{slab} + E_{adsorbate}) \quad (4.7)$$

Where  $E_{system}$ ,  $E_{slab}$  and  $E_{adsorbate}$  are the energies of the complete system, isolated slab and isolated adsorbate respectively. A negative value for the adsorption energy indicates that the adsorption is favourable, and a larger (more negative) value indicates that it is more favourable.

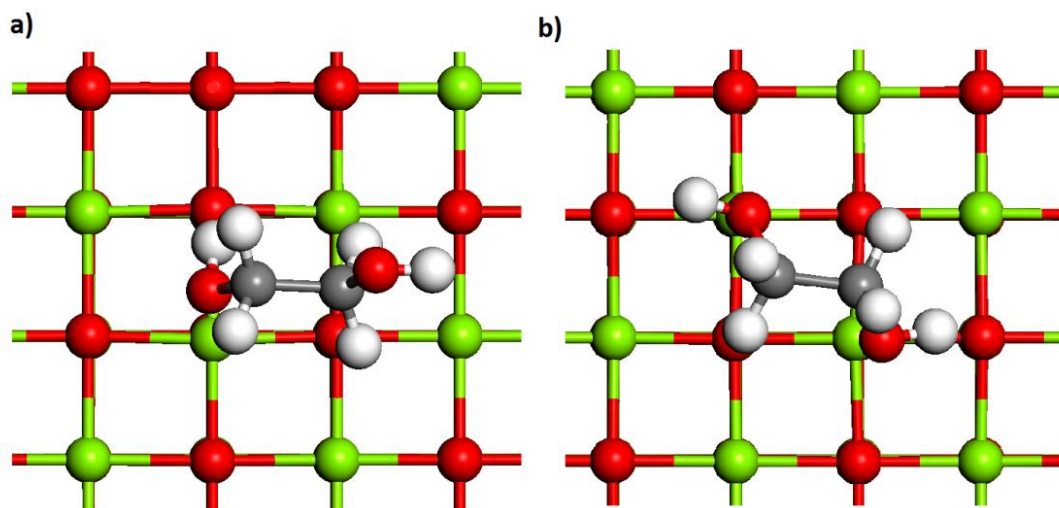


**Figure 12:** Plan view of the optimised structures of the staggered (a) and gauche (b) conformers of ethylene glycol adsorbed to the MgO (100) surface.

The staggered configuration (**Figure 12a**) ethylene glycol adsorbs to the MgO (100) surface with an adsorption energy of  $-46 \text{ kJ mol}^{-1}$ . The (H)O-Mg<sub>5c</sub> distance is  $2.291 \text{ \AA}$ , and the H-O<sub>5c</sub> distance is  $1.677 \text{ \AA}$ .

In the gauche configuration on the MgO (100) surface (**Figure 12b**) the alcohol group oxygen-Mg<sub>5c</sub> distances were measured at  $2.262 \text{ \AA}$  and  $2.167 \text{ \AA}$ , and the alcohol group hydrogen-O<sub>5c</sub> distances were  $2.918 \text{ \AA}$  and  $1.861 \text{ \AA}$ . The adsorption energy was calculated to be  $-92 \text{ kJ mol}^{-1}$ . This configuration allows for O-H bond activation with a hydrogen atom being transferred from an ethylene glycol alcohol group to an O<sub>5c</sub> atom in the surface. Calatayud [23] determined an adsorption energy of  $-0.77 \text{ eV}$  ( $-74 \text{ kJ mol}^{-1}$ ) for the gauche configuration with (H)O-Mg<sub>5c</sub> distances of

2.217 Å and 2.583 Å, and a H-O<sub>5c</sub> distance of 1.723 Å using the PW91 functional and a planewave cut off of 400 eV for this surface. The less favourable adsorption energy determined by Calatayud is due to one of the oxygen atoms being further away from the surface weakening its interaction and hence lowering the adsorption energy.

The staggered conformation is less favourable because only one of the alcohol groups is in close contact with the surface and hence the interaction with the second alcohol group is weaker, thus reducing the adsorption energy. Since the gauche configuration of the ethylene glycol molecule has more favourable adsorption energy to the MgO (100) surface than the staggered configuration all subsequent calculations use the gauche configuration.

Four different configurations for ethylene glycol adsorption on the MgO (130) surface were considered. They are the ethylene glycol molecule adsorbed perpendicular to the step, parallel to the step, on the top terrace site and on the bottom terrace site (**Figure 13**). The adsorption energies and relevant distances are summarised in **Table 1**. Due to periodicity of the system the top and bottom configurations are similar except that the bottom configuration is closer to the step than the top configuration.

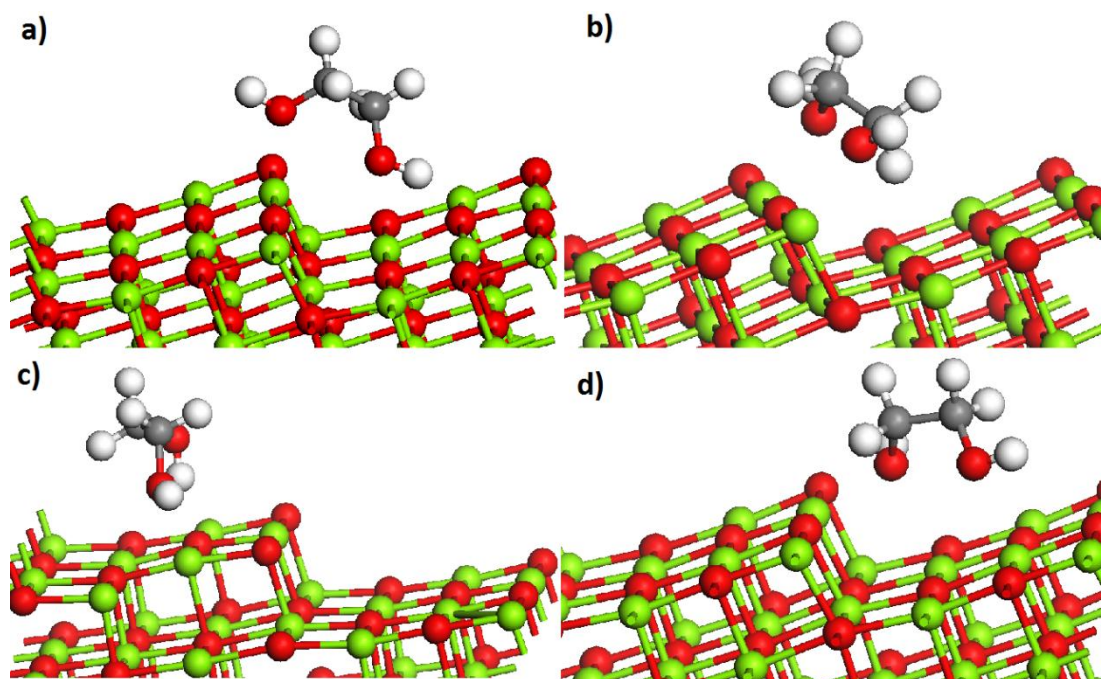


**Figure 13:** The four different adsorption configurations of ethylene glycol on the MgO (130) surface. a) perpendicular, b) parallel, c) top, d) bottom.

**Table 1:** Table showing the electronic adsorption energies and alcohol group oxygen – surface magnesium distances for ethylene glycol over different magnesium oxide surfaces.

System	Adsorption Energy /kJ mol <sup>-1</sup>	(HO) – Mg Distances /Å
MgO (100) gauche	-92	2.262, 2.167
MgO (100) staggered	-46	2.291
MgO (130) perpendicular	-84	2.145, 2.443
MgO (130) parallel	-93	2.122, 2.194
MgO (130) top terrace	-55	2.255
MgO (130) bottom terrace	-99	2.133, 2.454

**Table 1** shows the adsorption energies of ethylene glycol in each configuration. The most favourable configurations found were adsorption to the bottom terrace and parallel to the step on the (130) surface, and on the MgO (100) surface. For the parallel configuration both alcohol group oxygen atoms are coordinated to different Mg<sub>4c</sub> atoms. For the bottom terrace configuration one alcohol group oxygen atom is coordinated to both an Mg<sub>4c</sub> and an Mg<sub>5c</sub> atom, and the other to an Mg<sub>5c</sub> atom. Adsorption of ethylene glycol to the top terrace site is much less favourable than the other configurations tested as only one of the alcohol group oxygen atoms is interacting with a magnesium atom in the surface. The adsorption energy in the top

terrace configuration is comparable to that of ethylene glycol in the staggered conformer adsorbing to the MgO (100) surface as in both systems only one alcohol group oxygen atom is interacting with the surface.

Following adsorption of ethylene glycol to the MgO (100) and (130) surfaces a hydrogen atom was moved from one of the alcohol groups on the ethylene glycol molecule to the nearest oxygen atom on each of the surfaces and the systems were reoptimised (**Figure 14** and **Figure 15** respectively).

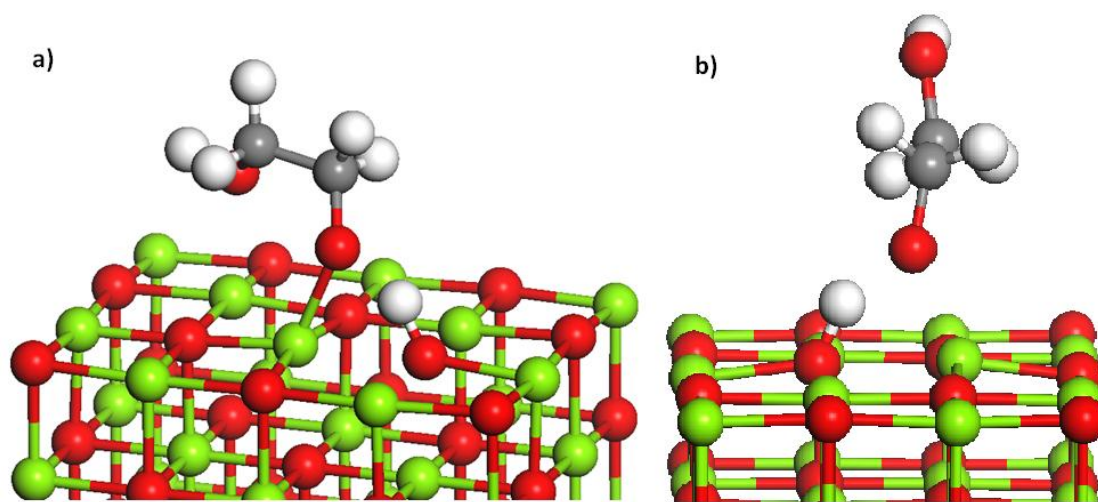


**Figure 14:** The optimised structure of ethylene glycol that has dissociated a hydrogen atom adsorbed on the MgO (100) surface in the gauche (a) and staggered (b) conformations.

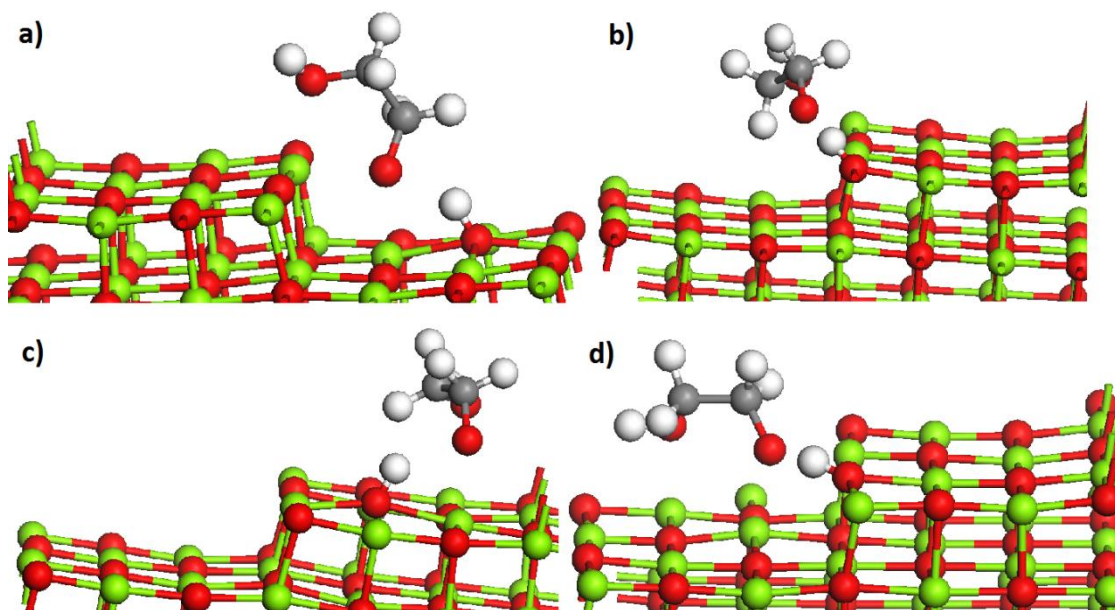


**Figure 15:** The optimised structures of dissociated ethylene glycol in the a) parallel, b) perpendicular, c) top and d) bottom adsorption configurations.

The relative energies of each configuration compared to their respective physisorbed structures and relevant distances are given in **Table 2**.

**Table 2:** Table showing the relative energies of the dissociated structures of ethylene glycol relative to the physisorbed structures.

System	Relative Energy of Dissociated Form /kJ mol <sup>-1</sup>	H-O <sub>5c</sub> Distance /Å	O-Mg <sub>5c</sub> Distance /Å
MgO (100) (O-H) (gauche)	11	1.065	2.022
MgO (100) (O-H) (staggered)	29	1.071	1.992
MgO (130) Perpendicular (O-H)	-7	1.002	2.083, 2.185 (Mg <sub>4c</sub> )
MgO (130) Parallel (O-H)	-67	0.986 (O <sub>4c</sub> )	1.926 (Mg <sub>4c</sub> ), 2.187 (Mg <sub>4c</sub> )
MgO (130) Top (O-H)	-3	0.998	2.143, 2.146 (Mg <sub>4c</sub> )
MgO (130) Bottom (O-H)	-95	0.985	2.142, 1.984 (Mg <sub>4c</sub> )

The removal of a hydrogen atom and placing it onto an oxygen atom is unfavourable on the MgO (100) surface, but it is favourable on the MgO (130) surface particularly for the parallel and bottom configurations (**Table 2**). This occurs because on the MgO (100) surface only the oxygen atom that has dissociated the hydrogen atom is interacting with the surface as the rest of the molecule is too far away from the surface. On the MgO (130) surface in the bottom configuration the oxygen atom that has dissociated the hydrogen atom is coordinated to two different magnesium atoms, one on the bottom terrace site and the other at the step site. In the parallel configuration both ethylene glycol oxygen atoms are coordinated to magnesium atoms in the step site. In the top configuration the oxygen atom that has dissociated the hydrogen atom is coordinated to two different magnesium atoms, one on the top terrace site and the other at the step site. In the perpendicular configuration the oxygen atom that has dissociated the hydrogen atom is coordinated to two different magnesium atoms, one on the bottom terrace site and the other at the step site. This suggests that the more magnesium atoms that the oxygen atom can coordinate to when it dissociates the hydrogen atom the more favourable the dissociation will be. In addition shorter O-Mg distances result in more favourable dissociation as well.

Removal of a hydrogen atom from a carbon atom where the initial removal of a hydrogen atom from the alcohol group was successful was also studied. The second hydrogen atom was placed onto the nearest available oxygen atom.

On the MgO (100) surface the C-H bond reformed and the system returned to an arrangement similar to where only the initial O-H bond breaking has occurred.

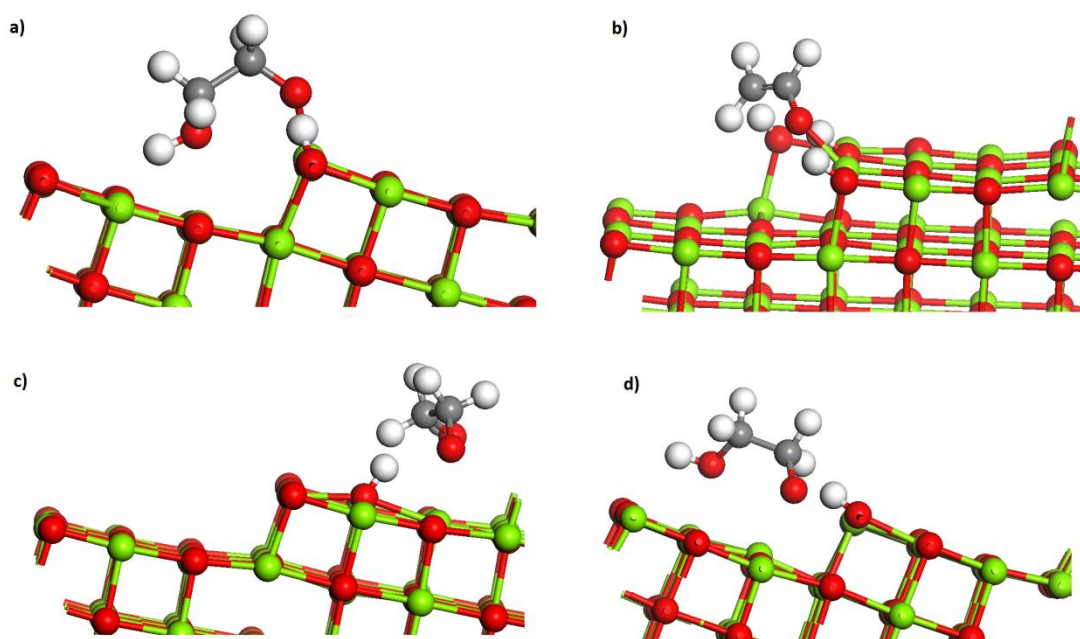


**Figure 16:** The optimised geometries of ethylene glycol adsorbed to the MgO (130) surface in the a) perpendicular, b) parallel, c) top and d) bottom configurations after removal of a second hydrogen atom from the carbon atom.

On the MgO (130) surface in the perpendicular configuration (**Figure 16a**) the ethylene glycol molecule adopted an arrangement where the both hydrogen atoms that had been removed returned to the atoms that they had been removed from, and at the opposite end of the molecule the alcohol group dissociated its hydrogen atom to an  $O_{4c}$  atom in the step site. In the parallel configuration (**Figure 16b**) the ethylene glycol molecule dissociated into chemically unrealistic fragments, suggesting that the end point is not stable. The H- $O_{4c}$  distance is 1.028 Å. In the top terrace configuration (**Figure 16c**) the ethylene glycol molecule returned to an arrangement similar (the molecule moved only very slightly) to the initial state of having the first hydrogen atom removed only. In the bottom terrace configuration (**Figure 16d**) the ethylene glycol molecule returned to an arrangement similar (the molecule moved only very slightly) to the initial state of having the first hydrogen

atom removed only. This data suggests that C-H activation following O-H activation of ethylene glycol is not possible on the MgO (100) or (130) surfaces.

Removal of a hydrogen atom from a carbon atom as the first step and adsorbing it to an oxygen atom on the surface in each configuration was also studied. The two stable configurations (those that generated reasonable energies and geometries compared to physisorbed ethylene glycol) found are shown in **Figure 17**. Relative energies of each configuration compared to the physisorbed structures and relevant distances are given in **Table 3**.

On the MgO (100) surface the ethylene glycol molecule fragmented into various functional groups.

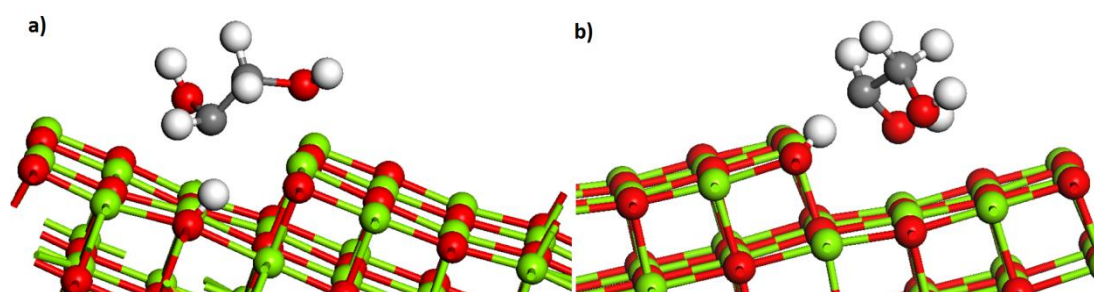


**Figure 17:** The optimised structure of dissociated ethylene glycol adsorbed to a) the step site in the perpendicular configuration on the MgO (130) surface and b) the top terrace site on the MgO (130) surface.

**Table 3:** Table showing the relative energies of the dissociated structures of ethylene glycol relative to the physisorbed structures.

System	Relative Energy of Dissociated Form /kJ mol <sup>-1</sup>	H-O <sub>5c</sub> Distance /Å	C-Mg <sub>5c</sub> Distance /Å
Perpendicular	157	0.996	2.436
Top	50	1.012	2.333

For the unstable configurations, the parallel configuration of the system returned to physisorbed ethylene glycol with the molecule being adsorbed slightly closer to the surface than it was originally. In the bottom configuration the hydrogen atom returned to the carbon atom that it was originally bonded to, however the alcohol group dissociated its hydrogen atom to the surface in a similar fashion to the earlier calculation.

Removal of a hydrogen atom from the alcohol group where the initial removal of a hydrogen atom from the carbon atom was successful was also studied. In the perpendicular configuration the ethylene glycol molecule fragmented into different functional groups which adsorbed to the surface. In the top terrace configuration the geometry of ethylene glycol molecule returned to that of physisorbed ethylene glycol. This data suggests that O-H activation following C-H activation of ethylene glycol is not possible on the MgO (130) surface.

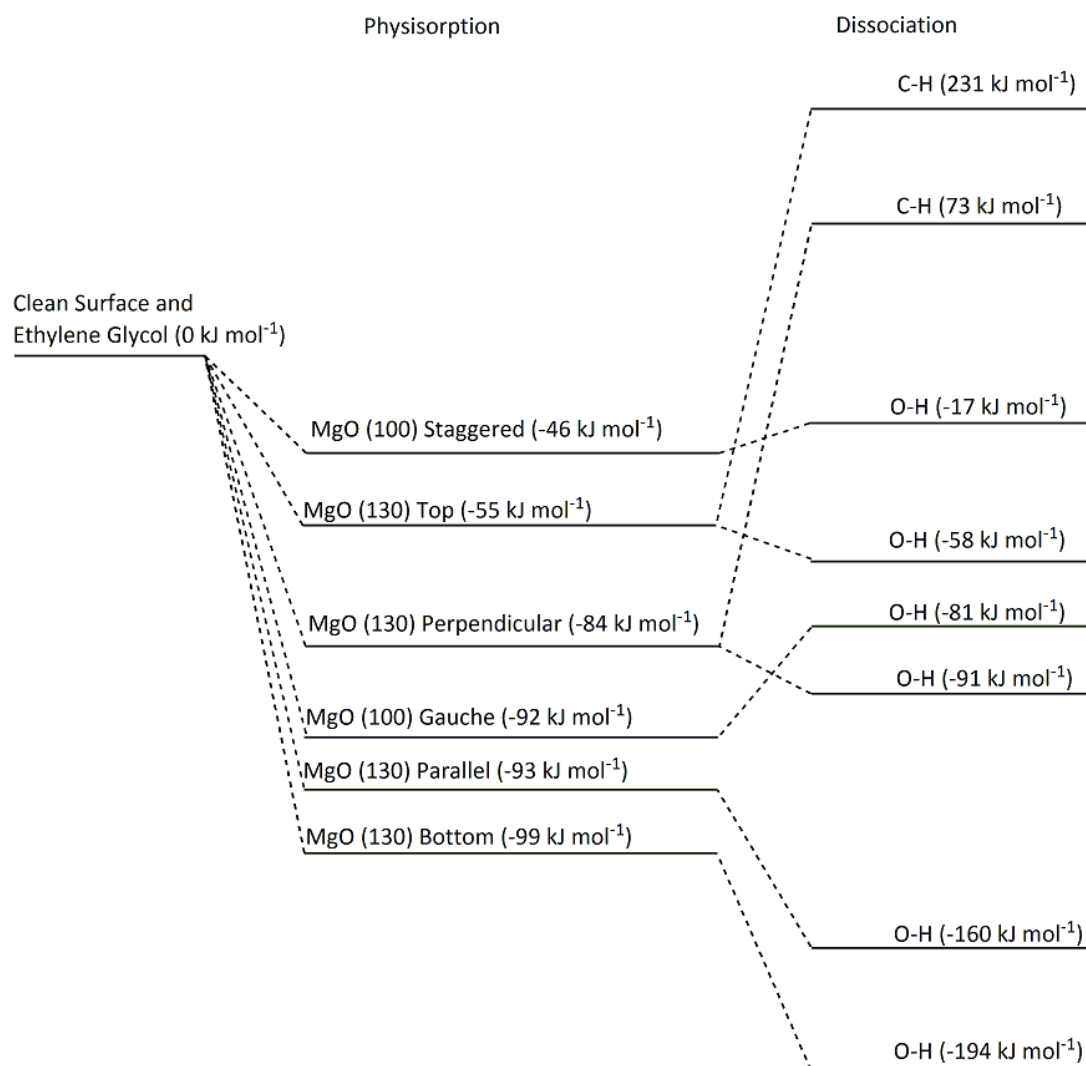


**Figure 18:** Diagram showing the relative energies of the different adsorption and dissociation configurations of ethylene glycol.

From a thermodynamic perspective it is energetically favourable for ethylene glycol to physisorb to both the MgO (100) and (130) surfaces. It is also more energetically favourable for ethylene glycol to dissociate a hydrogen atom from one of its alcohol

groups to an oxygen atom on the MgO (130) surface than to remain as physisorbed ethylene glycol (**Figure 18**). On the MgO (100) surface it is slightly energetically unfavourable for both the gauche and staggered conformers to dissociate a hydrogen atom. The dissociation of a hydrogen atom from a carbon atom is very energetically unfavourable for both systems where the end point was stable.

#### 4.1.5. O-H and C-H Activation Energy Barriers over Magnesium Oxide

Nudged Elastic Band (NEB) [24] calculations were performed to determine the activation energy barrier to the removal of a hydrogen atom from an alcohol group to an oxygen atom on the magnesium oxide surface. This is done by taking the optimised structures of ethylene glycol adsorbed to the surface and dissociated molecule and hydrogen atom adsorbed to the surface (from **Section 4.1.4.**). Once these structures are found the in-house code `inter_vasp` is used to interpolate a series of images between the starting and ending structures. Pictures of the various starting and ending structures for each adsorption configuration are shown in **Section 4.1.4., Figure 12 - Figure 15**. VASP can then be used to optimise each image and calculate their energies. `Inter_vasp` determines the distance that each image has moved away from the starting point and the reaction coordinate of each image is calculated by dividing the distance that the image has moved by the distance of the final image. Vibrational frequency calculations were performed on the starting, ending and transition state geometries of each barrier. Due to the uncertainty principle a quantum mechanical system will have a ground state that is higher in energy than the bottom of the potential well. Geometry optimisations will give the energy of the bottom of the potential well but not the zero point energy and therefore in order to determine the energy of the ground state vibrational frequency calculations will have to be performed to calculate the zero point energy and hence the true ground state of the system, which can then be used to determine the true activation energy barrier. In the vibrational frequency calculations the positions of the atoms comprising the surfaces are fixed and only the adsorbate is free to move. The energies quoted are relative to that of the starting geometry of each calculation.

Once a possible transition state has been located a second NEB calculation consisting of five images is performed using the two points either side as the starting and ending structures. This allows for more accurate description of the transition state.

The transition state energies and relevant distances for O-H activation over the MgO (100) and (130) surfaces are summarised in **Table 4**.

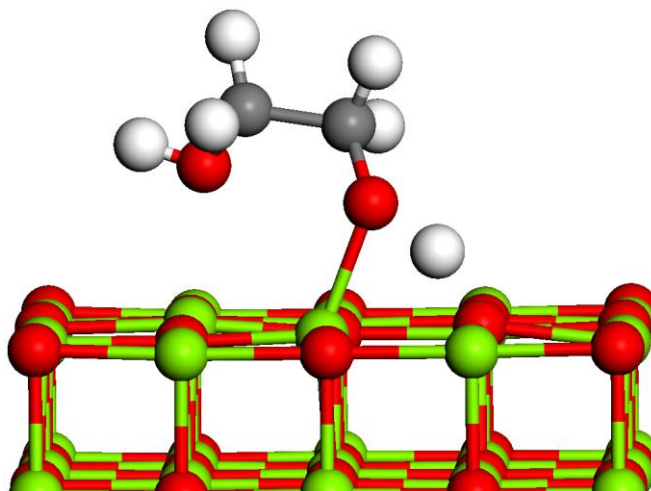


**Figure 19:** The transition state geometry of the O-H activation pathway of ethylene glycol adsorbed on the MgO (100) surface.

A vibrational frequency calculation on the transition state structure (**Figure 19**) gives a single imaginary mode. Visualisation of this mode shows it to be of hydrogen transfer between the alcohol group oxygen atom and a surface oxygen atom.

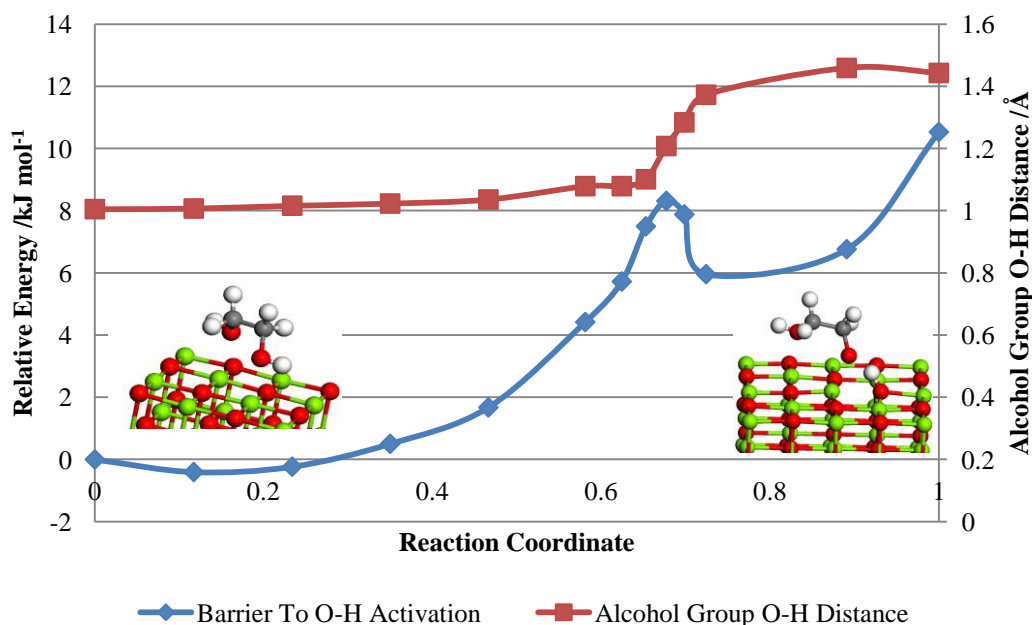


**Figure 20:** Graph showing the barrier to O-H activation of ethylene glycol over the MgO (100) surface.

The energy of the transition state of O-H activation over the MgO (100) surface (**Figure 20**) is  $8.3 \text{ kJ mol}^{-1}$  higher than the starting point. The energy of the ending

point is  $10.5 \text{ kJ mol}^{-1}$  higher than the starting point. With the zero point correction these values become  $-4.7 \text{ kJ mol}^{-1}$  and  $3.9 \text{ kJ mol}^{-1}$  respectively. The zero point corrected transition state energy is lower than that of the starting geometry. The initial lowering of the barrier is caused by the oxygen atom that is dissociating the hydrogen atom moving closer to the surface. The lowering of the barrier after the transition state is caused by reorientation of the ethylene glycol molecule.

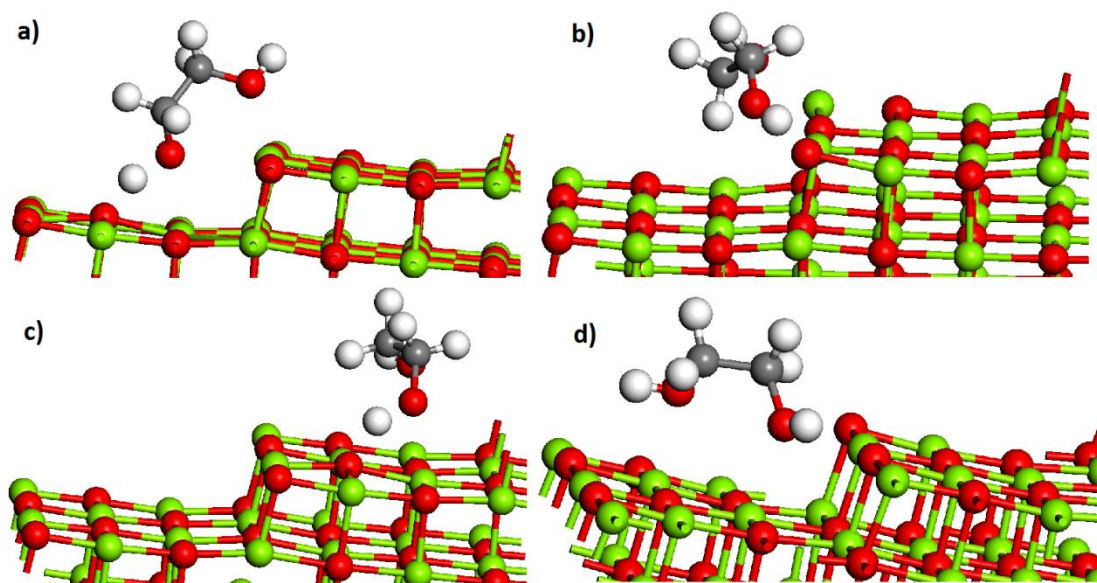


**Figure 21:** The transition state geometries of O-H activation of ethylene glycol in the a) perpendicular, b) parallel, c) top and d) bottom configurations.

Vibrational frequency calculations are performed on the geometries at the peak of each barrier. The presence of imaginary modes indicates that the geometry is a transition state (**Figure 21**). Visualisation of the imaginary modes of each transition state structure showed them to be of hydrogen transfer between the alcohol group and an oxygen atom in the surface.

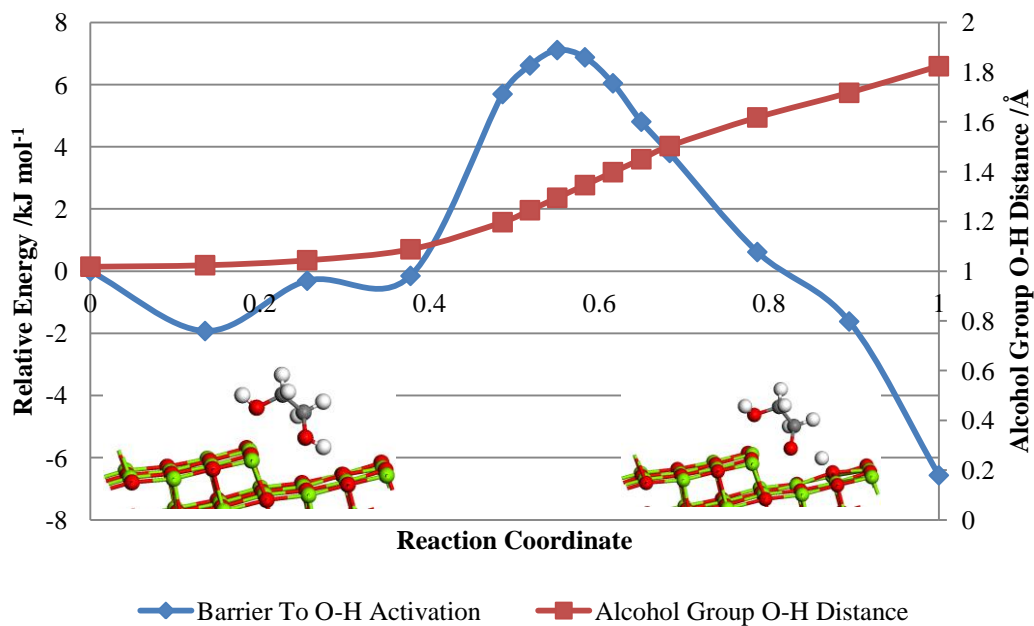


**Figure 22:** Graph showing the barrier to O-H activation of ethylene glycol in the perpendicular configuration over the MgO (130) surface.

The initial lowering of the barrier to O-H activation of ethylene glycol in the perpendicular configuration (**Figure 22**) is caused by the oxygen atom that is dissociating the hydrogen atom moving closer to the surface before dissociating the hydrogen atom.

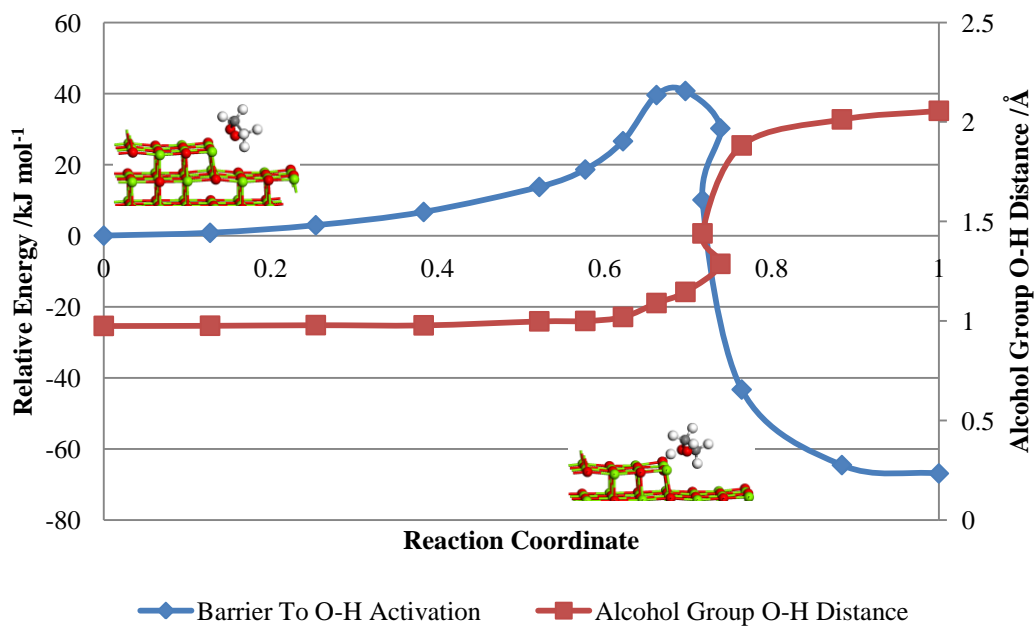


**Figure 23:** Graph showing the barrier to O-H activation of ethylene glycol in the parallel configuration over the MgO (130) surface.

The unusual shape of the barrier in **Figure 23** is caused by a reorientation of the ethylene glycol molecule as it dissociates the hydrogen atom.

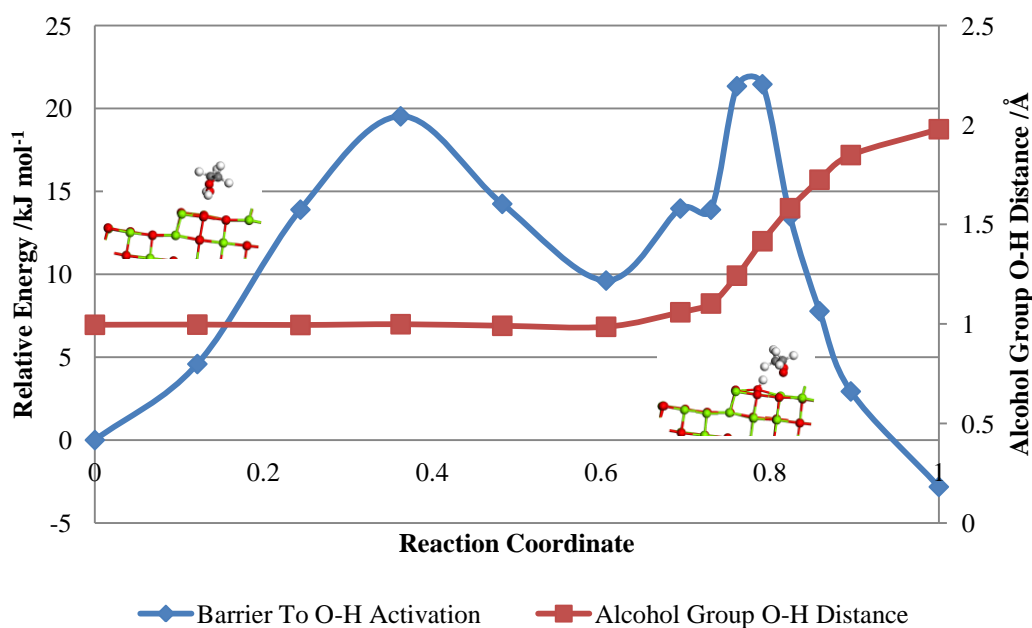


**Figure 24:** Graph showing the barrier to O-H activation of ethylene glycol in the top configuration over the MgO (130) surface.

The initial barrier in **Figure 24** is caused by a reorientation of the ethylene glycol molecule prior to the dissociation of the hydrogen atom.

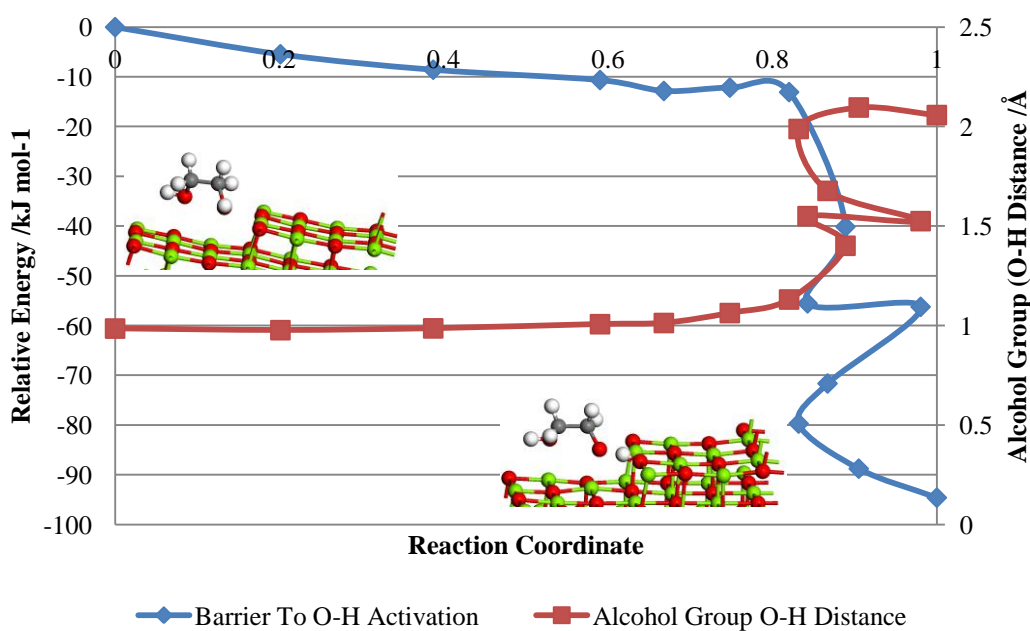


**Figure 25:** Graph showing the barrier to O-H activation of ethylene glycol in the bottom configuration over the MgO (130) surface.

The unusual shape of the barrier in **Figure 25** is caused by reorientation and motion of the ethylene glycol molecule over the surface as it dissociates the hydrogen atom.

**Table 4:** Table showing the transition state energies, geometries and difference in energy between the starting and ending states. Bracketed values indicate zero point energy corrected value. Barriers are shown in **Figure 20** and **Figure 22 - Figure 25**.

System	Transition state energy /kJ mol <sup>-1</sup>	Energy Difference between start and end structures /kJ mol <sup>-1</sup>	Distances /Å		
			(H)O-Mg <sub>5c</sub>	H-O (alcohol group)	H-O <sub>5c</sub>
MgO (100)					
Gauche	8.3 (-4.7)	10.5 (3.9)	2.058	1.208	1.252
MgO (130)					
Perpendicular	7.1 (-2.2)	-6.6 (-5.5)	2.198	1.295	1.211
Parallel	40.7 (28.3)	-66.9 (-69.4)	2.025	1.146	1.511
			(O <sub>4c</sub> )		(O <sub>4c</sub> )
Top	21.5 (7.7)	4.7 (-5.3)	2.180	1.416	1.142
			(O <sub>4c</sub> )		(O <sub>4c</sub> )
Bottom	-13.1 (-23.4)	-94.6 (-94.6)	2.076	1.131	1.489
			(O <sub>4c</sub> )		(O <sub>4c</sub> )

**Table 4** shows the zero point corrected transition state energy for each O-H activation pathway as well as O-H and O-Mg distances. For each barrier the transition state occurs when the two O-H distances are approximately the same, and between 1.1 Å and 1.4 Å. The (H)O-Mg distances of the transition states are comparable to the O-Mg distances found in the surfaces.

C-H activation was studied for ethylene glycol adsorbed to the MgO (130) surface in the perpendicular and top terrace site configurations.

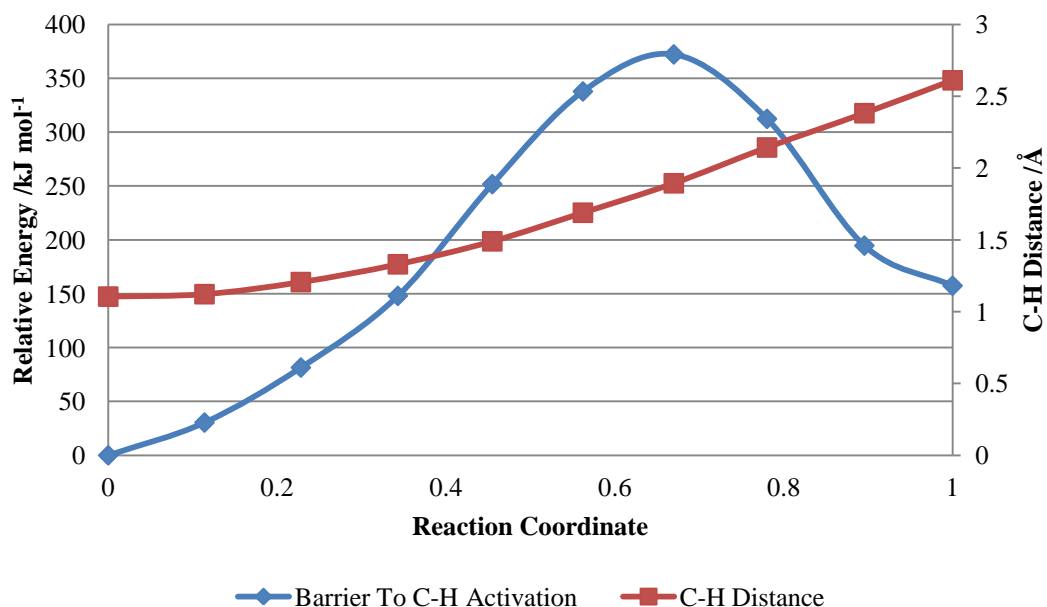


**Figure 26:** Graph showing the barrier to C-H activation of ethylene glycol over the MgO (130) surface with the molecule adsorbed in the perpendicular configuration.

The barrier to C-H activation with ethylene glycol adsorbed in the perpendicular configuration (**Figure 26**) is very large at approximately  $372 \text{ kJ mol}^{-1}$ , the end state is also significantly higher in energy ( $157 \text{ kJ mol}^{-1}$ ) than the initial state. Between images 4 and 8 the hydrogen atom is far enough away from the ethylene glycol molecule and the surface that it is not bonded to anything which is a very energetically unfavourable state.

In the top site configuration the ethylene glycol molecule dissociated into different fragments which resulted in an unphysically large barrier of  $515 \text{ kJ mol}^{-1}$ , suggesting that the pathway found is not realistic.

The very large barriers to C-H activation suggest that it is not possible over the magnesium oxide (100) and (130) surfaces, and thus unlikely to occur in reality. Therefore magnesium oxide alone is not suitable as a catalyst for ethylene glycol oxidation.

## 4.2. Aluminium Oxide

A bulk unit cell (consisting of thirty atoms) of  $\alpha$ -aluminium oxide ( $\text{Al}_2\text{O}_3$ ) was taken from work by Newnham *et al.*, [25] and imported into VASP.  $\alpha$ - $\text{Al}_2\text{O}_3$  is also known as corundum [26] which has a hexagonal structure. The lattice parameters were expanded or shrunk by up to 5% and the resulting electronic energies were

calculated as described in **Section 4.1.1**. These values were then plotted against the volume of the unit cell and a quadratic curve was fitted to the data (**Figure 27**). This allows for the determination of the lattice parameters of the lowest energy structure, which was approximately 1.4% larger than the experimental values of  $a=4.759 \text{ \AA}$ ,  $b=4.759 \text{ \AA}$  and  $c=12.991 \text{ \AA}$  when using the PBE functional at a planewave cut off of 500 eV and  $3 \times 3 \times 3$   $k$ -points.

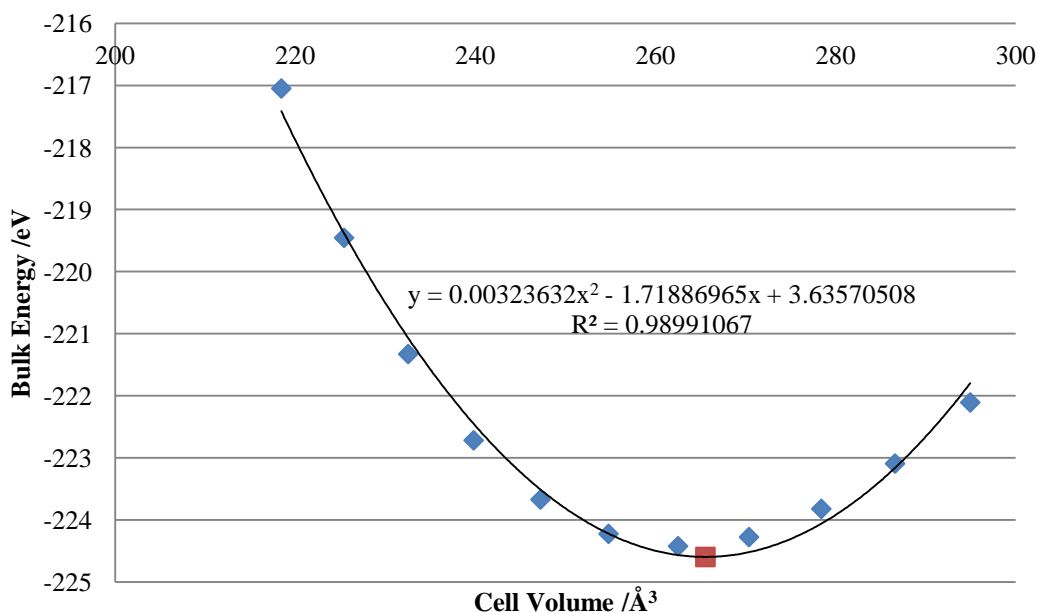


**Figure 27:** Graph showing the cell volume against energy for bulk  $\alpha$ -aluminium oxide calculated using the PBE functional. The red marker indicates the position of the minimum of the fitted curve.

In the optimised bulk structure each aluminium atom is coordinated to six oxygen atoms in an approximately octahedral arrangement with three inter-atomic distances of  $1.881 \text{ \AA}$  and the remaining three of  $1.998 \text{ \AA}$ . Each oxygen atom is approximately tetrahedrally coordinated to four aluminium atoms with two inter-atomic distances of  $1.881 \text{ \AA}$ , and two of  $1.998 \text{ \AA}$ . Bader analysis of the bulk structure gives the oxygen atoms a charge of  $-1.526 e$ , and the aluminium atoms a charge of  $+2.290 e$ . These values are further away from the formal  $-2 e$  and  $+3 e$  for oxygen and aluminium ions respectively than has been found for magnesium oxide at  $+1.81 e$  and  $-1.81 e$  for magnesium and oxygen respectively. This indicates that aluminium oxide is less ionic than magnesium oxide.

A density of states calculation (**Figure 28**) was performed on the optimised bulk structure of aluminium oxide using the PBE functional at  $9 \times 9 \times 9$   $k$ -points with a 500 eV planewave cut off. The cell was hexagonal in shape with the **a** and **b** vectors of length 4.8251 Å, the **c** vector of length 13.1713 Å and the angle  $\gamma$  was  $120^\circ$ . The large band gap of approximately 6 eV shows that aluminium oxide is an insulator. For comparison the optical band gap measured by Aguilar-Frutis *et al.* is 5.63 eV [27], indicating good agreement between theory and experiment. The plot also shows that aluminium is involved in the valence band states, which is consistent with the covalency of  $\text{Al}_2\text{O}_3$ .

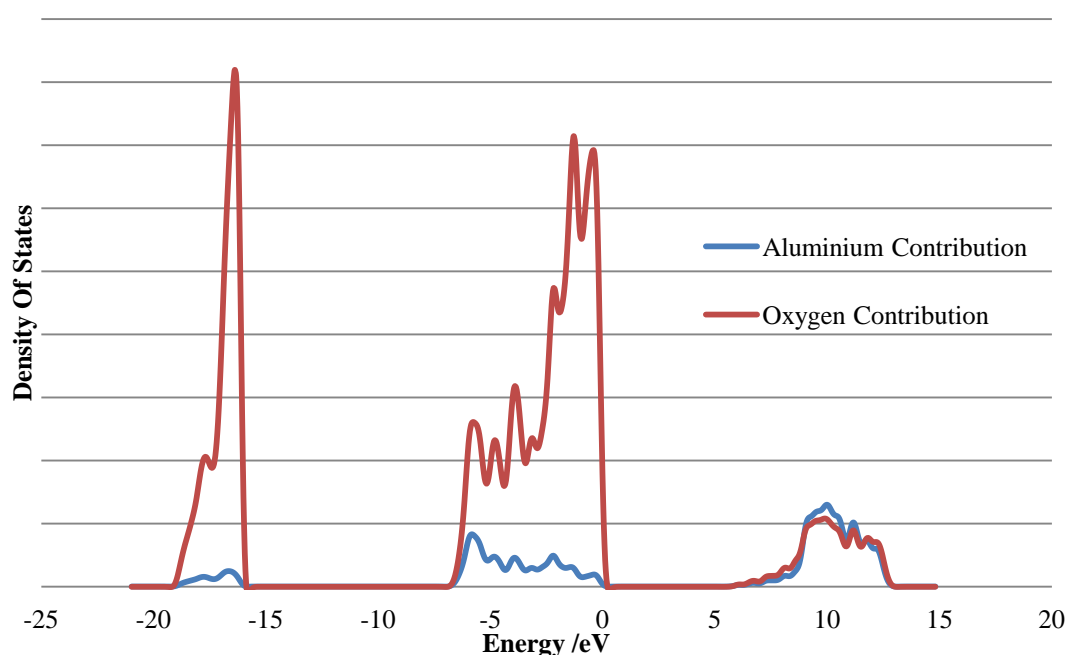


**Figure 28:** Density of states plot for bulk alpha aluminium oxide showing the separate contributions from the aluminium and oxygen atoms.

#### 4.2.1. The $\text{Al}_2\text{O}_3$ (0001) Surface

The (0001) surface of aluminium oxide (**Figure 29**) was cleaved from the optimised bulk material.

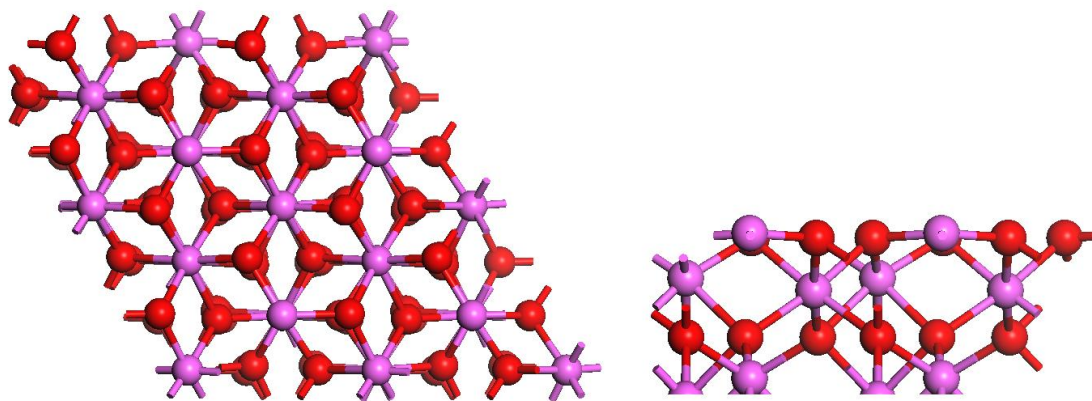


**Figure 29:** The plan (left) and side (right) views of the optimised  $\text{Al}_2\text{O}_3$  (0001) surface. Aluminium in pink, oxygen in red.

The surface energy of the  $\text{Al}_2\text{O}_3$  (0001) surface was determined in the same manner as for magnesium oxide as described in **Section 4.1.3**. The top three oxygen layers (and associated aluminium atoms) of each slab were relaxed, while the remaining atoms were fixed to simulate bulk behaviour of the material. The surface area of the slab is  $80.65 \text{ \AA}^2$ .

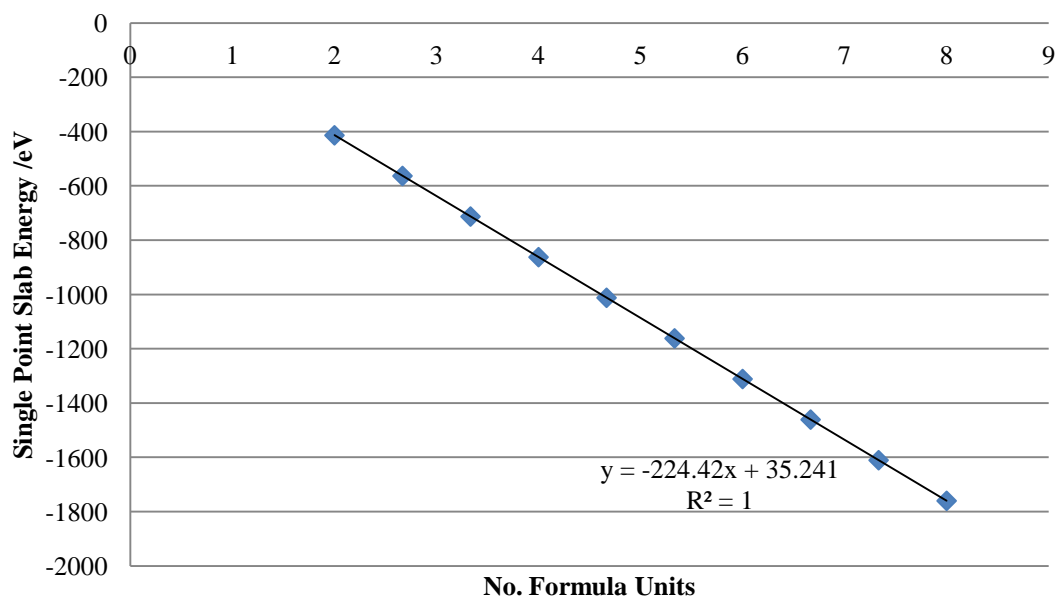


**Figure 30:** Graph showing slab energy against number of formula units for the  $\text{Al}_2\text{O}_3$  (0001) surface.

The energy of the bulk unit cell of  $\alpha\text{-Al}_2\text{O}_3$  obtained from the slab calculations is  $-224.4 \text{ eV}$  (**Figure 30**), which is very similar to the energy from single point energy calculations on the optimised bulk unit cell.

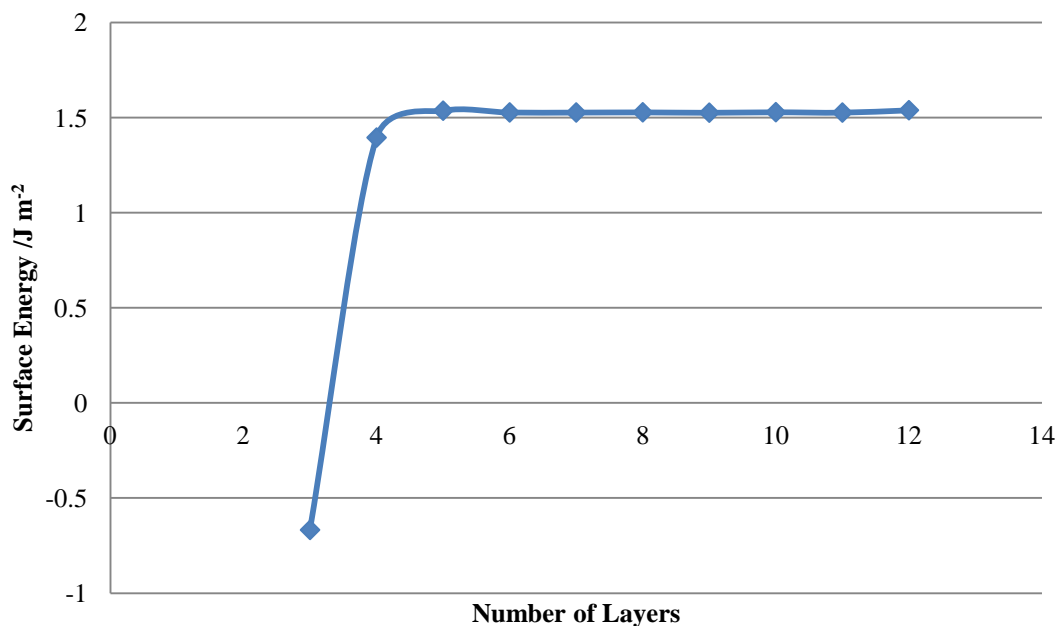


**Figure 31:** Graph showing surface energy against number of layers for the  $\alpha$ -Al<sub>2</sub>O<sub>3</sub> (0001) surface.

The surface energy of the (0001) surface was calculated to be 1.53 J m<sup>-2</sup> (**Figure 31**), using the same methodology as described in **Section 4.1.3**. This value is similar to values of approximately 1.4 J m<sup>-2</sup> obtained by Li and Choi for fully relaxed Al<sub>2</sub>O<sub>3</sub> (0001) surfaces [28]. There is very little change in surface energy for six layers and above and therefore six layers was chosen as the thickness for all Al<sub>2</sub>O<sub>3</sub> (0001) surfaces, while not containing too many atoms as to make calculations impractical.

When relaxed the aluminium atoms in the top layer of the surface sank into the surface by 0.81 Å when compared to the unrelaxed surface, this is comparable to the literature value of 0.7 Å [29]. At the exposed surface the aluminium atoms are coordinated to three oxygen atoms in a triangular arrangement at a distance of 1.707 Å. The oxygen atoms are coordinated to three aluminium atoms in a trigonal pyramidal arrangement, one aluminium atom is in the same plane as the oxygen atom and the two others are slightly below it. The oxygen-aluminium distances are 1.707 Å, 1.822 Å and 1.906 Å. Bader analysis of the slab shows that the oxygen atoms had Bader charges of between -1.41 e and -1.63 e. The oxygen atoms at the upper exposed (relaxed) surface had Bader charges between -1.55 e and -1.59 e. The oxygen atoms located towards the centre of the slab had higher Bader charges and the oxygen atoms at the lower exposed (bulk like) surface had lower Bader charges

at between -1.41 e and -1.47 e. The aluminium atoms had Bader charges between +2.06 e and +2.55 e. The aluminium atoms at the lower exposed surface had the lowest Bader charge of +2.05 e, and those at the upper exposed surface had the highest charge of +2.55 e. The aluminium atoms in the centre of the slab had Bader charges between +2.13 e and +2.48 e, with those further away from the surfaces having the lower charges.

#### 4.2.2. Adsorption of Ethylene Glycol

A single molecule of ethylene glycol was placed close to the surface and the system was reoptimised (**Figure 32**). It was positioned in such a way that both alcohol group oxygen atoms were coordinated to exposed aluminium atoms on the surface.

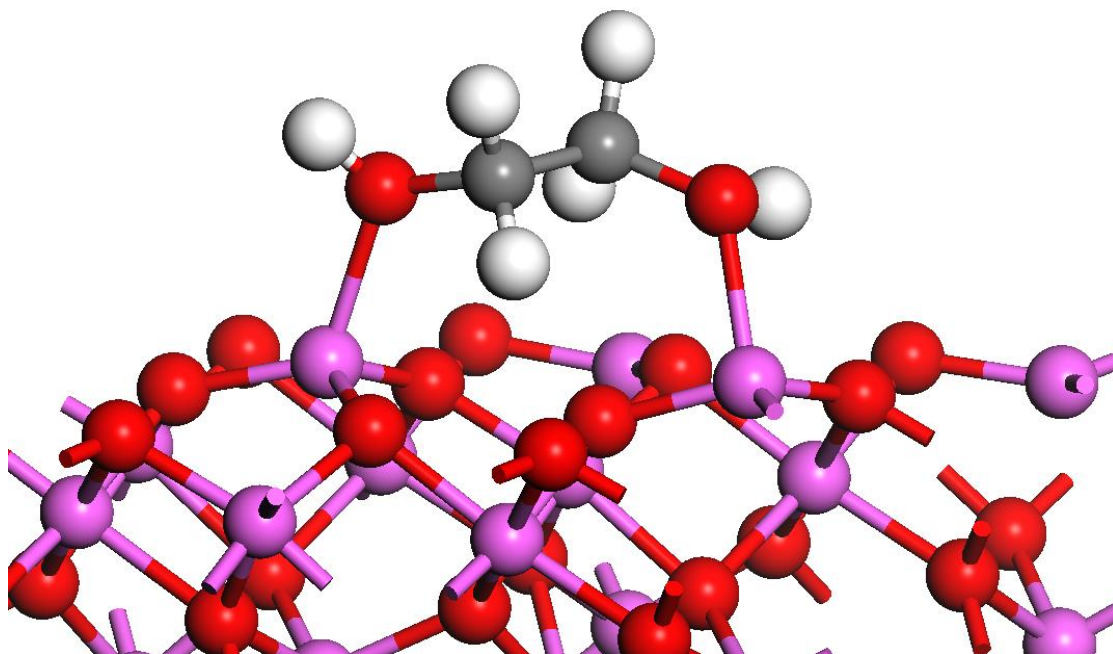


**Figure 32:** The optimised structure of ethylene glycol adsorbed to the Al<sub>2</sub>O<sub>3</sub> (0001) surface.

In the relaxed clean surface the aluminium atoms sink into the surface, however when ethylene glycol is adsorbed to the surface via the oxygen atoms in the alcohol groups the aluminium atoms are raised out of the surface by 0.36 Å and 0.33 Å compared to their positions in the relaxed surface. The alcohol group oxygen-aluminium distances were measured to be 2.036 Å and 2.021 Å. The adsorption energy was calculated to be -168 kJ mol<sup>-1</sup>. This is significantly more favourable than any of the adsorption configurations on magnesium oxide (**Section 4.1.4.**). Bader analysis gives charges of +2.44 e for both of the aluminium atoms that ethylene

glycol adsorbs to, compared with +2.41 e for the same atoms in the clean surface. For an isolated ethylene glycol molecule in the same simulation cell the Bader charge on both oxygen atoms is -1.09 e, this compares with -1.18 e for the adsorbed molecule.

A hydrogen atom was removed from one of the alcohol groups and placed onto the nearest oxygen atom on the surface and the system was reoptimised (**Figure 33**). The alcohol group oxygen-aluminium distances decreased to 1.966 Å and 1.763 Å. The hydrogen-oxygen distance was 0.981 Å. The energy of the dissociated system is -63 kJ mol<sup>-1</sup> lower than that of physisorbed ethylene glycol which is comparable to that of dissociated ethylene glycol in the parallel configuration on the MgO (130) surface at -67 kJ mol<sup>-1</sup>. Bader analysis gives a charge of +2.45 e on the aluminium atom that ethylene glycol chemisorbs to compared to +2.43 e when ethylene glycol is physisorbed. The Bader charge on the oxygen atom increases from -1.19 e to -1.30 e. The Bader charge on the removed hydrogen atom remains at +0.64 e, and the Bader charge on the oxygen atom on which the hydrogen is placed decreases from -1.61 e to -1.49 e.

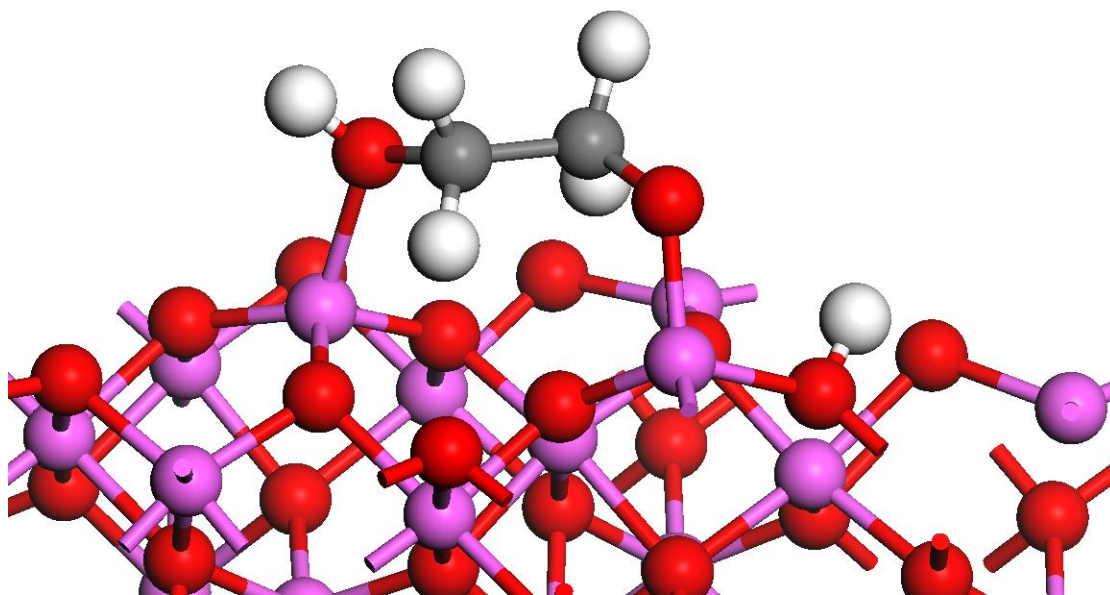


**Figure 33:** Ethylene glycol adsorbed to the Al<sub>2</sub>O<sub>3</sub> (0001) surface with a hydrogen atom removed and chemisorbed to an oxygen atom on the surface.

Following the removal of the hydrogen atom from the alcohol group a second hydrogen atom was removed from the associated carbon atom and placed onto

another oxygen atom on the surface. The end point is not stable and the ethylene glycol molecule dissociated into chemically unreasonable fragments.

A hydrogen atom was removed from one of the carbon atoms and placed onto an oxygen atom on the surface and the system was reoptimised. The end point is not stable either and the ethylene glycol molecule dissociated into chemically unreasonable fragments.

This data suggests that C-H activation is not possible over the  $\text{Al}_2\text{O}_3$  (0001) surface, and therefore aluminium oxide alone is not suitable for ethylene glycol oxidation.

#### 4.2.3. Adsorption of Water

It is known experimentally [30] and in simulation [31] [32] that water will dissociate into hydroxyl groups in the presence of an aluminium oxide surface. In this section calculations are performed to determine the adsorption energy of water molecules and the energy difference between the physisorbed molecules and the molecules dissociated into hydroxyl groups. The geometry of the hydroxylated surface provides a basis for classical molecular dynamics calculations performed in **Chapter 5**.

Initially a single water molecule was adsorbed to an exposed aluminium atom on the  $\text{Al}_2\text{O}_3$  (0001) surface. Two different configurations were tested, one with the plane of the molecule perpendicular to the exposed face (**Figure 34a**) and the other with the plane of the molecule parallel to the exposed surface (**Figure 34b**). The water oxygen-aluminium distances were 1.962 Å and 1.949 Å respectively.

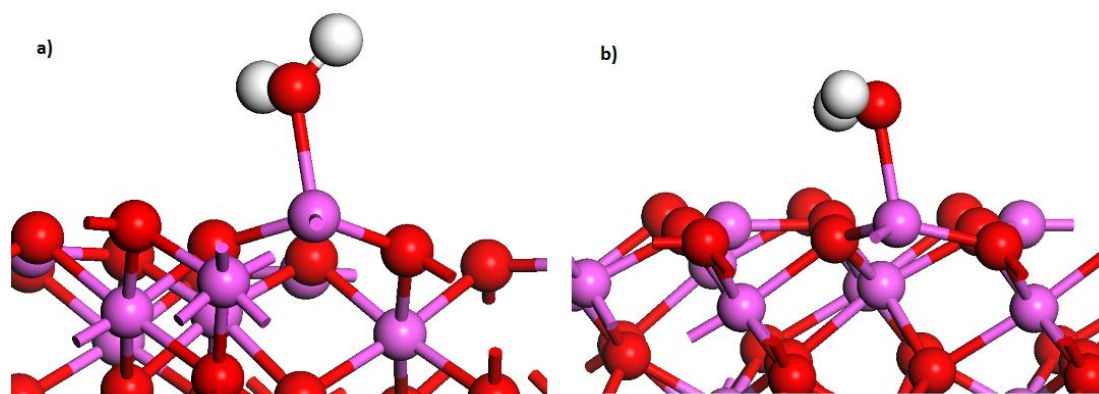


**Figure 34:** The optimised structures of a single water molecule adsorbed approximately perpendicular (a) and parallel (b) to the  $\text{Al}_2\text{O}_3$  (0001) surface.

In the perpendicular configuration the water rotated such that the plane of the molecule is not quite perpendicular to the aluminium oxide surface, this is due to one of the oxygen atom's lone pairs binding to the aluminium atom. In the parallel configuration the hydrogen-surface oxygen distances are 2.240 Å and 2.659 Å. Adsorption of the water molecule caused the aluminium atom to be raised out of the surface by 0.296 Å for the perpendicular configuration and 0.266 Å for the parallel configuration compared to the relaxed surface. The adsorption energies are -109 kJ mol<sup>-1</sup> and -115 kJ mol<sup>-1</sup> respectively. These values compare well with -1.5 eV (-145 kJ mol<sup>-1</sup>) calculated by Thissen *et al.* [33] using the PW91 functional and a planewave cut off of 360 eV. The parallel configuration is more energetically favourable for adsorption due to greater interactions between the hydrogen atoms and oxygen atoms in the surface.

Bader analysis of the perpendicular configuration gives a charge of +2.08 e on the aluminium atom that the water oxygen adsorbs to (compared to +2.55 e for the same atom on the clean surface). This indicates that the water oxygen atom is donating electron density to the surface. The oxygen atom has a Bader charge of -0.77 e and the hydrogen atoms have a Bader charges of +0.56 e and +0.29 e. For an isolated water molecule in the same periodic cell the oxygen atom has a charge of -1.05 e, and the hydrogen atoms have charges of +0.51 e and +0.54 e. The net positive charge of +0.08 e on the adsorbed water molecule and the increase in negative charge on the oxygen atom in the isolated molecule suggest that the aluminium atom is acting as a Lewis acid centre by accepting electron density from the water molecule.

Bader analysis of the of the parallel configuration gives a charge of +2.48 e on the aluminium atom that the water molecule is adsorbed to, the water oxygen has a Bader charge of -1.05 e, and the hydrogen atoms have Bader charges of +0.45 e and +0.57 e. The charges on the hydrogen atoms are similar as in the parallel configuration both atoms are interacting with the surface and hence electron density drawn off them. This also results in electron density remaining on the water oxygen atom rather than being donated to the aluminium atom.

From the parallel configuration a hydrogen atom was removed from the water molecule and placed onto a nearby oxygen atom in the surface, forming two

hydroxyl groups. This configuration was chosen to study dissociation into hydroxyl groups as the adsorption energy is more favourable and the hydrogen atoms are closer to the surface than in the parallel configuration. The system was then reoptimised (**Figure 35**). The oxygen-aluminium distance is 1.736 Å and the surface oxygen-hydrogen distance is 0.969 Å and the hydroxyl group oxygen-hydrogen distance is 0.984 Å. Bader analysis of the system gives a charge of -1.28 e on the surface oxygen forming the hydroxyl group, the associated hydrogen atom has a Bader charge of +0.37 e. The aluminium atom bound to the hydroxyl group has a Bader charge of +2.37 e, the associated oxygen atom has a Bader charge of -1.27 e and the hydrogen atom has a Bader charge of +0.48 e. Compared to physisorbed water in the parallel configuration the oxygen atom has a higher negative charge and the aluminium atom has a lower positive charge indicating that electron density is drawn from the surface by the hydroxyl group.

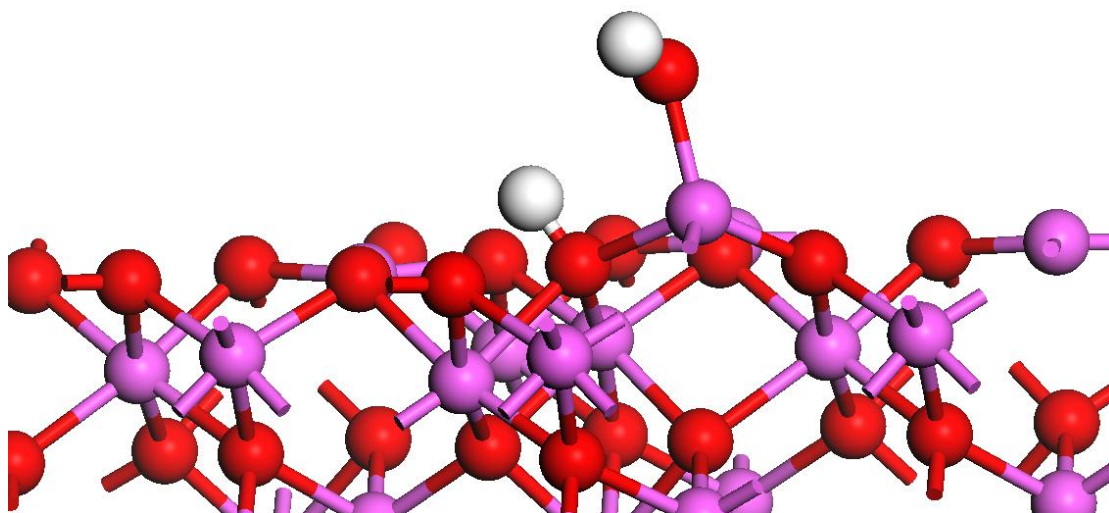


**Figure 35:** A water molecule dissociated into two hydroxyl groups over the  $\text{Al}_2\text{O}_3$  (0001) surface.

In the supercell of the  $\text{Al}_2\text{O}_3$  (0001) surface used there are four exposed aluminium Lewis acid sites. Four water molecules forming a monolayer were adsorbed to the four exposed aluminium atoms in the simulation cell (**Figure 36**). Dissociating all four water molecules will allow for complete coverage of the surface in hydroxyl groups. The barriers to hydroxylation and the relative energies of the surface at different levels of hydroxylation will allow for determination of how hydroxylated the surface will be in the presence of water.

The water oxygen-aluminium distances were 2.022 Å, 2.026 Å, 2.027 Å and 2.046 Å. The total adsorption energy is  $-374 \text{ kJ mol}^{-1}$  ( $-93.5 \text{ kJ mol}^{-1}$  per molecule). Bader analysis of this system gives charges on the water oxygen atoms of between  $-0.95 \text{ e}$  and  $-1.09 \text{ e}$ . The associated aluminium atoms have Bader charges of  $+2.30 \text{ e}$  and  $+2.59 \text{ e}$ . The hydrogen atoms have Bader charges between  $+0.40 \text{ e}$  and  $+0.59 \text{ e}$ , with the hydrogen atoms having the lower charges being associated with the oxygen atoms also having a lower charge.

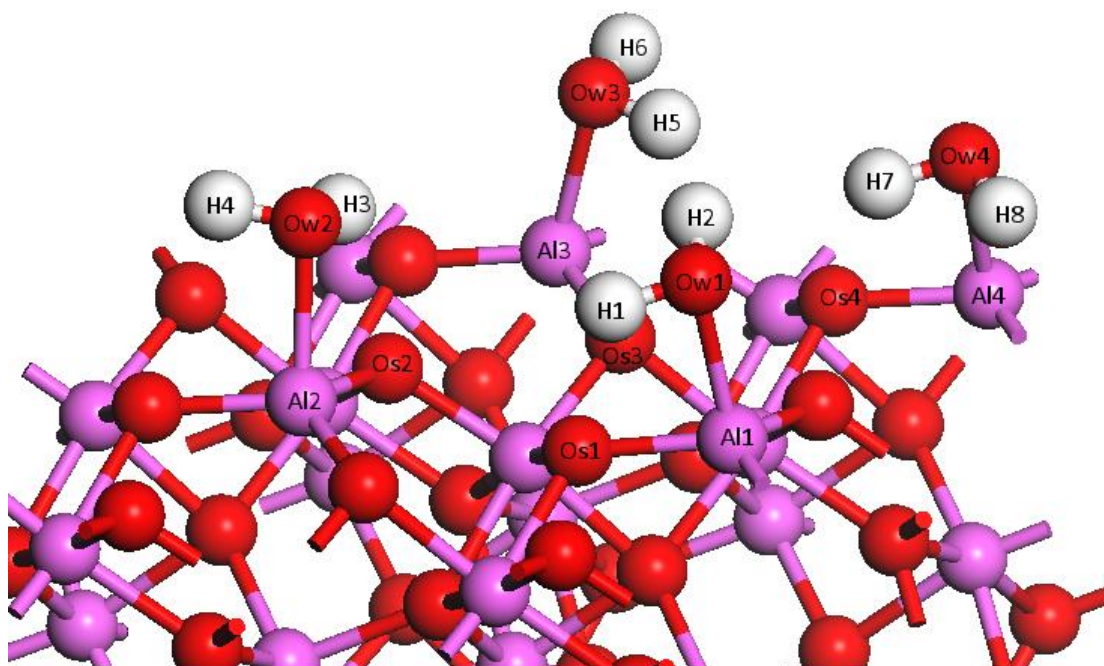


**Figure 36:** Four water molecules adsorbed to the Al<sub>2</sub>O<sub>3</sub> (0001) surface.

These four water molecules were dissociated into hydroxyl groups in four successive calculations. There are many different possible pathways by which successive hydroxylation could be modelled, however only one has been chosen (due to time constraints) to be studied here. Bader charges for the labelled atoms and bond lengths after each dissociation are given in **Table 5** and **Table 6** respectively.

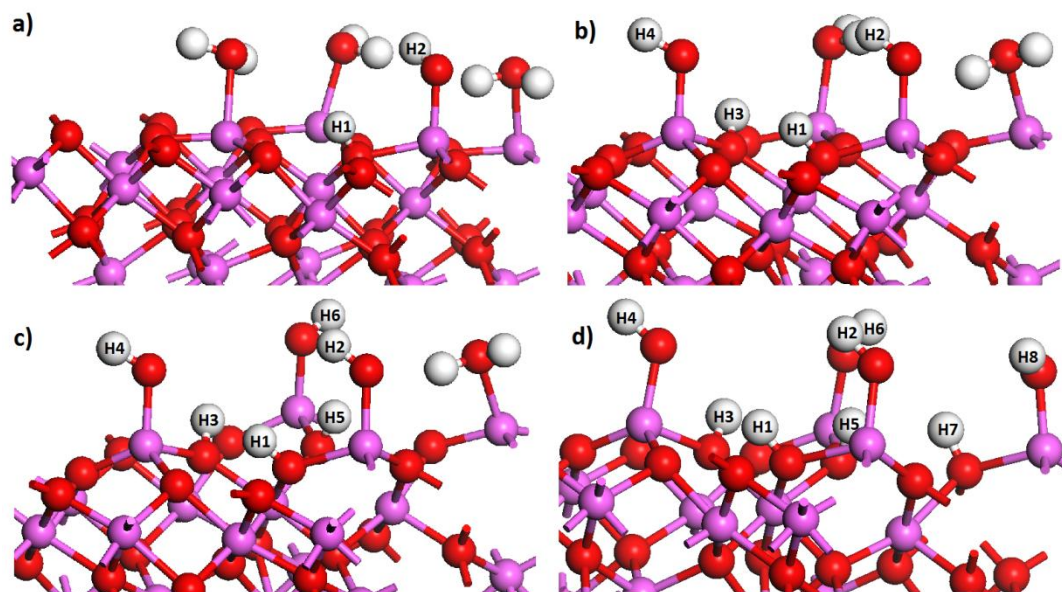


**Figure 37:** Four water molecules successively dissociating into hydroxyl groups over the  $\text{Al}_2\text{O}_3$  (0001) surface. a) First dissociation, b) second dissociation, c) third dissociation, d) fourth dissociation.

In the first dissociation (**Figure 37a**) the bond between H1 and Ow1 is broken and H1 forms a hydroxyl group with Os1. In the second dissociation (**Figure 37b**) the bond between H3 and Ow2 is broken and H3 forms a hydroxyl group with Os2. In the third dissociation (**Figure 37c**) the bond between H5 and Ow3 is broken and H5 forms a hydroxyl group with Os3. In the fourth dissociation (**Figure 37d**) the bond between H7 and Ow4 is broken and H7 forms a hydroxyl group with Os4.

**Table 5:** Table showing Bader charges (in units of e) for selected atoms after each successive dissociation. The hydrogen atoms are labelled in **Figure 37**.

Atom	Dissociation				
	0	1	2	3	4
H1	0.45	0.32	0.15	0.26	0.14
H2	0.53	0.50	0.48	0.49	0.50
H3	0.48	0.51	0.40	0.16	0.20
H4	0.40	0.47	0.42	0.49	0.50
H5	0.56	0.54	0.59	0.44	0.48
H6	0.52	0.57	0.50	0.48	0.47
H7	0.42	0.43	0.42	0.49	0.24
H8	0.59	0.59	0.57	0.59	0.55
Ow1	-0.99	-1.40	-1.24	-1.26	-1.28
Ow2	-0.95	-0.95	-1.31	-1.37	-1.34
Ow3	-1.09	-1.09	-1.05	-1.31	-1.27
Ow4	-1.09	-1.05	-0.99	-1.01	-1.40
Os1	-1.50	-1.22	-0.94	-1.05	-0.94
Os2	-1.55	-1.45	-1.30	-1.03	-1.06
Os3	-1.49	-1.56	-1.48	-1.26	-1.31
Os4	-1.52	-1.44	-1.49	-1.39	-1.13
Al1	2.30	2.46	2.02	2.18	2.21
Al2	2.59	2.16	2.55	2.49	2.40
Al3	2.32	2.39	2.17	2.23	2.27
Al4	2.47	2.37	2.24	2.01	2.52

Bader analysis of the successive dissociations shows that each dissociated hydrogen atom gains some electron density (0.11 e to 0.25 e) from the oxygen atom (0.05 e to 0.28 e) that it chemisorbs to. The hydroxyl group oxygen also gains electron density (0.25 e to 0.41 e) from the aluminium atom it adsorbs to (0.06 e to 0.50 e). The hydroxyl group hydrogen atoms also gain a small amount of electron density after the dissociation (approximately 0.03 e). The amount of charge transfer varies for each atom and each dissociation, this is likely due to changes in the locations of the minima in the Bader surfaces as the geometry of the system changes.

**Table 6:** Table showing bond lengths (in angstroms) after each successive dissociation.

Bond	Dissociation			
	1	2	3	4
H1-Os1	0.978	0.980	0.980	0.980
H2-Ow1	0.968	0.966	0.966	0.964
Ow1-Al1	1.760	1.753	1.741	1.722
H3-Os2		0.978	0.979	0.980
H4-Ow2		0.968	0.968	0.966
Ow2-Al2		1.753	1.743	1.727
H5-Os3			0.978	0.981
H6-Ow3			0.969	0.966
Ow3-Al3			1.741	1.730
H7-Os4				0.980
H8-Ow4				0.969
Ow4-Al4				1.728

The hydroxyl groups formed by the dissociated hydrogen atoms and oxygen atoms in the surface all have bond lengths of around 0.98 Å, and these lengths vary only very slightly between dissociations. The hydroxyl groups formed by the remaining hydrogen and oxygen atoms have slightly shorter bond lengths around 0.966 Å, and these bond lengths again only slightly vary between dissociations. The oxygen-aluminium bond lengths vary more significantly between 1.722 Å and 1.760 Å, and are slightly shorter than the oxygen-aluminium bond lengths formed between the oxygen atom in dissociated ethylene glycol and a three coordinated aluminium atom in the surface. The hydroxyl group oxygen – aluminium distances decrease after each dissociation indicating that the hydroxyl group – hydroxyl group interactions are weaker than the hydroxyl group – water interactions.

#### 4.2.4. Adsorption of Ethylene Glycol and Water

Four water molecules were added to the optimised simulation cell of ethylene glycol adsorbed to the Al<sub>2</sub>O<sub>3</sub> (0001) surface that is described in **Section 4.2.2.** and the system was reoptimised (**Figure 38**). Ethylene glycol is already physisorbed to two aluminium Lewis acid sites and therefore two water molecules were adsorbed to the two remaining Lewis acid sites, while the other two are displaced from the surface.

This allows for determination of the energy required for ethylene glycol to displace two water molecules.

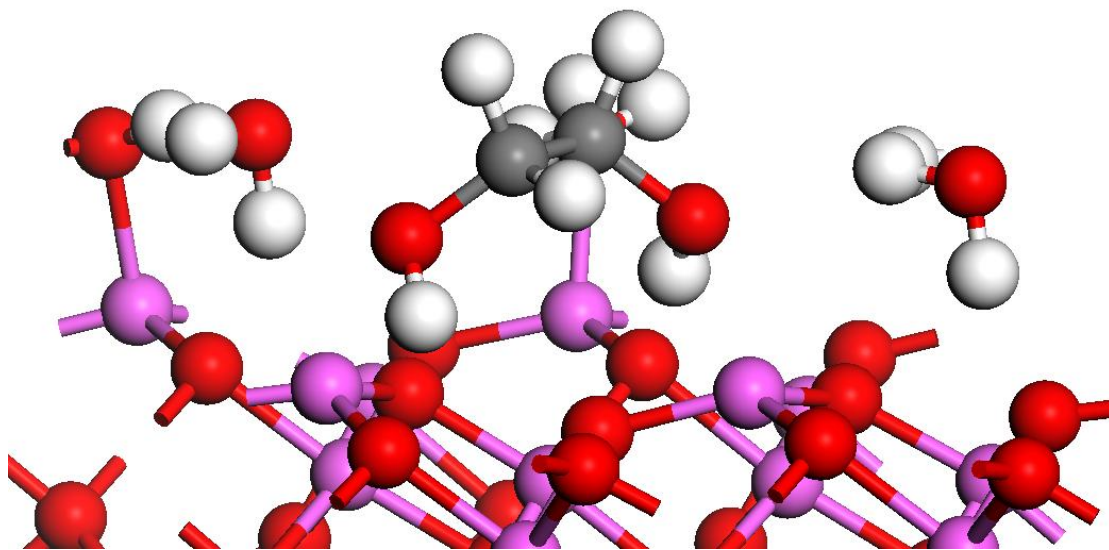


**Figure 38:** The optimised geometry of ethylene glycol and four water molecules adsorbed to the  $\text{Al}_2\text{O}_3$  (0001) surface. It should be noted that a hydrogen atom from one water molecule has crossed the periodic boundary of the cell and reappeared on the other side of the cell.

The alcohol group oxygen-aluminium distances are 2.146 Å and 2.145 Å which are slightly longer than was found when water molecules were not present. For the two water molecules that are adsorbed to aluminium atoms the oxygen-aluminium distances are 1.930 Å and 1.968 Å. The two remaining water molecules are not interacting with any aluminium atoms, however they do form hydrogen bonds with each other and one of the water molecules adsorbed to the surface, as well as with oxygen atoms in the surface. The second adsorbed water molecule is not interacting with anything apart from the surface. The ethylene glycol molecule is not hydrogen bonded to any water molecules. The total adsorption energy for a cluster of ethylene glycol and four water molecules to the surface is  $-377 \text{ kJ mol}^{-1}$ , and the total adsorption energy for the cluster of only four water molecules described in **Section 4.2.3.** to the surface is  $-374 \text{ kJ mol}^{-1}$ . This suggests this it is favourable for ethylene glycol to displace two water molecules from the  $\text{Al}_2\text{O}_3$  (0001) surface, but not significantly and in a real system water and ethylene glycol molecules will be exchanging places continually.

A hydrogen atom was removed from one of the alcohol groups on ethylene glycol and placed onto an oxygen atom on the surface and the system was reoptimised (**Figure 39**).

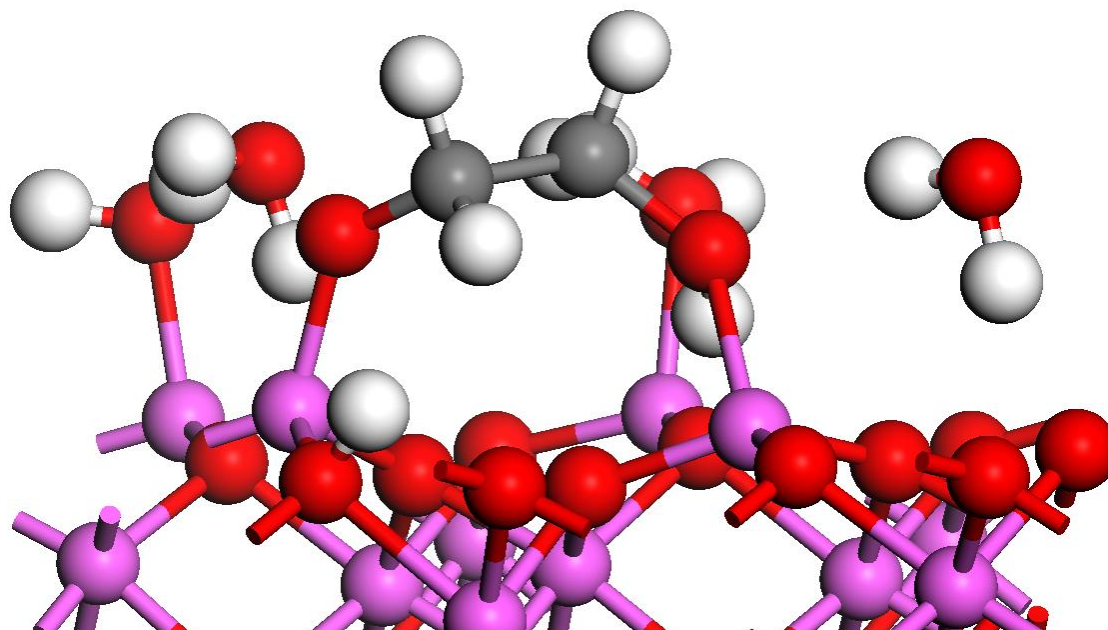


**Figure 39:** The optimised geometry of dissociated ethylene glycol and four water molecules adsorbed to the Al<sub>2</sub>O<sub>3</sub> (0001) surface.

The ethylene glycol oxygen-aluminium distances are 1.767 Å and 2.060 Å, the shorter distance being that of the oxygen atom that dissociated the hydrogen atom. These distances are slightly longer than the distances found in the absence of water molecules. The hydrogen-surface oxygen distance is 0.982 Å. Two water molecules remained adsorbed to aluminium atoms on the surface with the oxygen aluminium distances being 1.912 Å and 1.988 Å. The water oxygen – aluminium distances are shorter than was found for four water molecules adsorbed to the surface and comparable to that of a single adsorbed water molecule.

As in the system without water present a hydrogen atom was then removed from the carbon atom on ethylene glycol and placed onto a second oxygen atom on the surface to form hydroxyethanal, however this state is not stable and the ethylene glycol molecule dissociated into chemically unreasonable fragments.

A hydrogen atom was also removed from a carbon atom as the first step and placed onto the nearest oxygen atom on the surface, however this state is not stable either

and the ethylene glycol molecule dissociated into chemically unreasonable fragments.

#### 4.2.5. O-H Activation Barriers Over Aluminium Oxide

Nudged elastic band calculations were performed to determine the activation energy barrier to O-H activation over the  $\text{Al}_2\text{O}_3$  (0001) surface using the methodology described in **Section 4.1.5**.

O-H activation barriers of water were studied. For the single water molecule adsorbed in the parallel configuration described in **Section 4.2.3**, a total of eight images were interpolated between the physisorbed structure and the dissociated structure. A further five images around the transition state were interpolated using the images either side of the peak of the barrier as starting and ending structures to refine the barrier. Data gathered from NEB calculations is recorded in **Table 7**. The transition state geometries were confirmed by vibrational frequency calculations on the transition state geometry which showed the presence of imaginary modes. Visualisation of the imaginary modes showed them to be of hydrogen transfer between the water molecule and an oxygen atom in the surface.

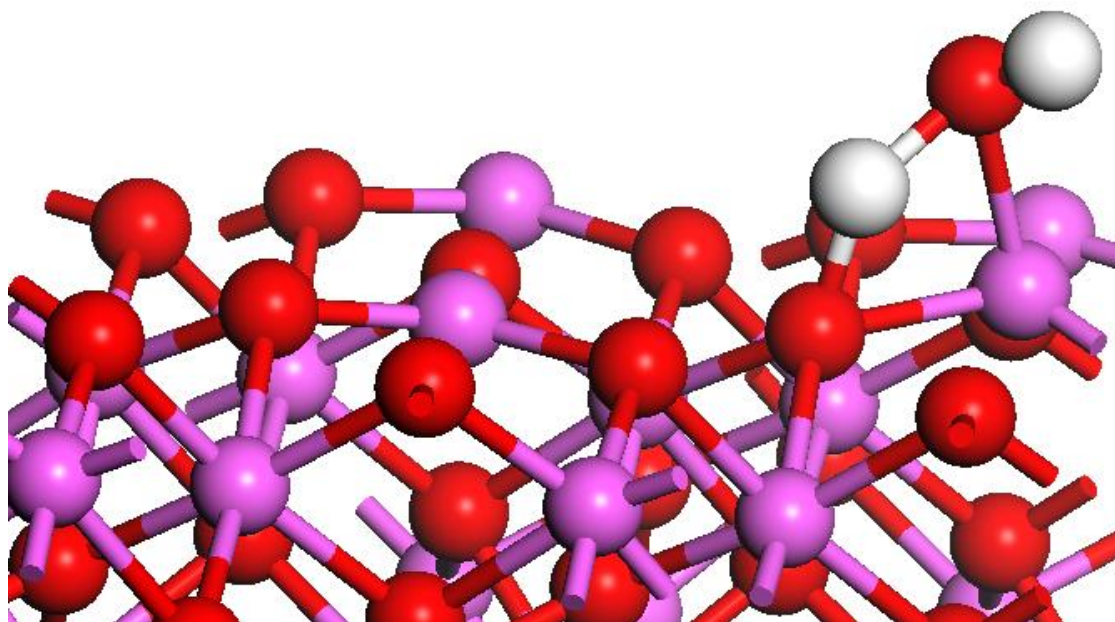


**Figure 40:** The transition state geometry of O-H activation of water on the  $\text{Al}_2\text{O}_3$  (0001) surface.

At the transition state geometry (**Figure 40**) of the O-H activation pathway of the hydrogen-surface oxygen distance is 1.244 Å, the water oxygen-hydrogen distance is 1.270 Å, and the oxygen-aluminium distances is 1.855 Å.

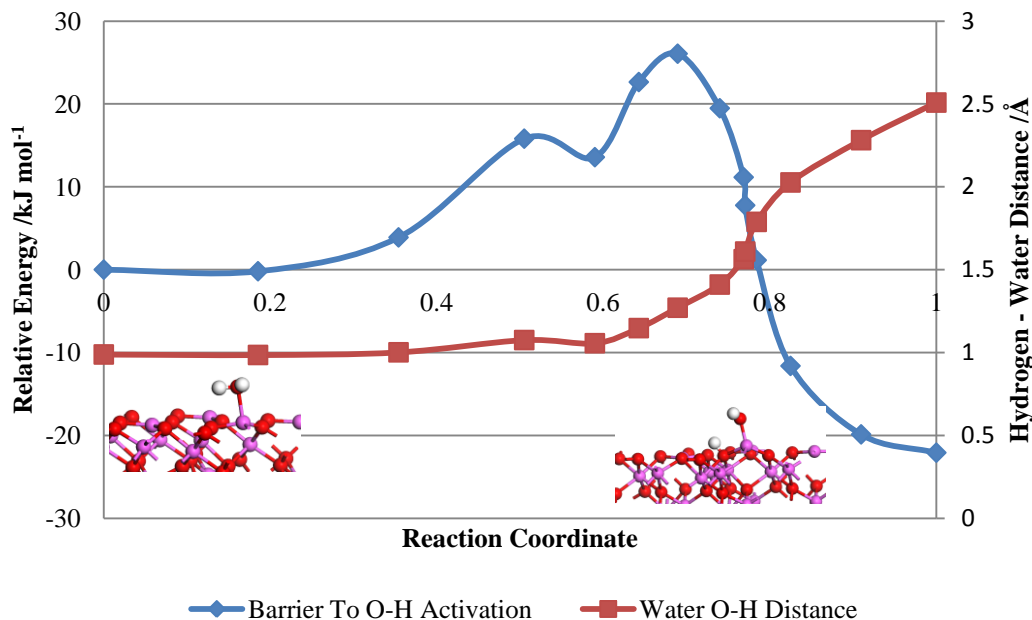


**Figure 41:** Graph showing the barrier to O-H activation of a single water molecule over the Al<sub>2</sub>O<sub>3</sub> (0001) surface.

The energy of the refined transition state of water O-H activation over the Al<sub>2</sub>O<sub>3</sub> (0001) surface (**Figure 41**) is 26.1 kJ mol<sup>-1</sup> higher than the starting point. The energy of the ending point is -22.1 kJ mol<sup>-1</sup> lower than the starting point. With the zero point correction these values become 15.3 kJ mol<sup>-1</sup> and -22.6 kJ mol<sup>-1</sup> respectively. The minimum in the barrier is caused by the water molecule tilting as it begins to dissociate the hydrogen atom.

Successive dissociations of four water molecules into hydroxyl groups over the Al<sub>2</sub>O<sub>3</sub> (0001) were also studied.

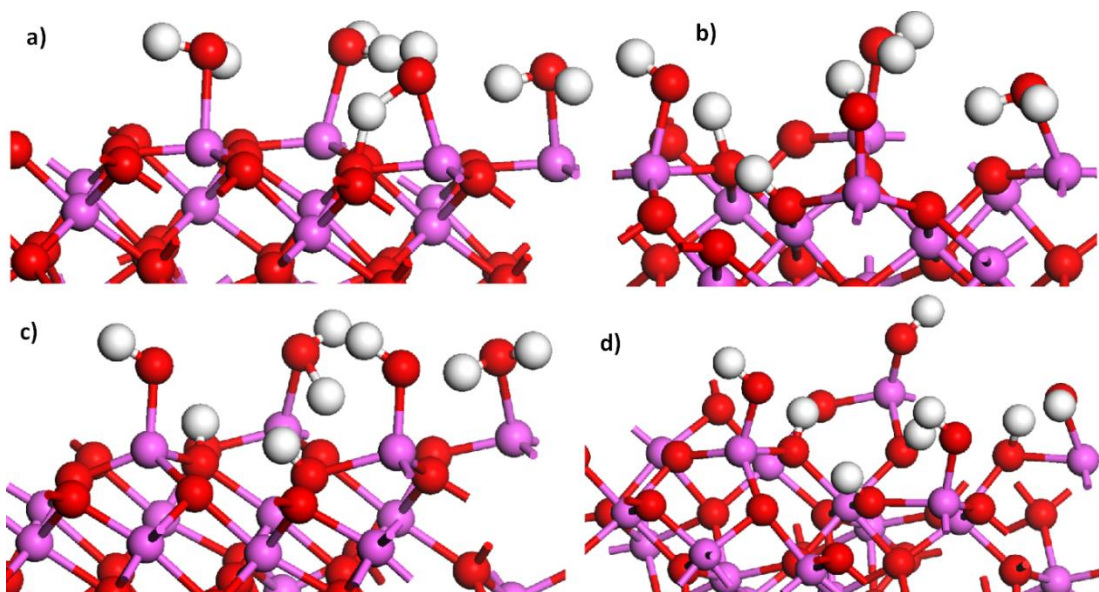


**Figure 42:** The transition state geometries of the successive dissociations of four water molecules over the  $\text{Al}_2\text{O}_3$  (0001) surface. a) First dissociation, b) second dissociation, c) third dissociation, d) fourth dissociation.

**Figure 42** shows the transition state geometries of each of the successive dissociations of four water molecules over the  $\text{Al}_2\text{O}_3$  (0001) surface. The transition state energy, relative energies of the ending state compared to the starting state and relevant bond lengths are given in **Table 7**.

**Table 7:** Table showing the transition state energies and hydrogen-oxygen distances for successive dissociations of four water molecules on the  $\text{Al}_2\text{O}_3$  (0001) surface. Bracketed values show the zero point corrected energies.

Dissociation	Transition State Energy / $\text{kJ mol}^{-1}$	Relative Energy of Ending Configuration / $\text{kJ mol}^{-1}$	Hydrogen-Surface Oxygen Distance / $\text{\AA}$	Hydrogen-Water Oxygen Distance / $\text{\AA}$
Single Molecule	26.1 (15.3)	-22.1 (-22.6)	1.244	1.270
1	6.0 (-2.4)	-74.7 (-72.7)	1.258	1.268
2	14.7 (5.1)	-76.8 (-75.7)	1.373	1.165
3	31.8 (24.9)	-26.6 (-25.2)	1.292	1.251
4	38.9 (27.3)	4.0 (3.1)	1.210	1.298

Data gathered from the NEB calculations (**Table 7**) shows that the O-H activation energy barriers for water over the  $\text{Al}_2\text{O}_3$  (0001) surface are small, particularly for the first two dissociations. Except for the last dissociation then energy of the dissociated state is lower in energy than the previous state. This indicates that the  $\text{Al}_2\text{O}_3$  (0001)

surface will be significantly hydroxylated in the presence of water. The relative energy of the ending configurations for the last two dissociations is significantly less than that of the first two as there are fewer intact water molecules present to stabilise the system. The transition state for all five systems occurs when the dissociating hydrogen atom is between 1.2 Å and 1.3 Å away from both the water oxygen atom that it is leaving and the surface oxygen it is adsorbing to.

O-H activation of ethylene glycol was also studied. A total of eight images were interpolated between the structures of adsorbed ethylene glycol and its dissociated form described in **Section 4.2.2**. A further five images around the transition state were interpolated using the images either side of the peak of the barrier as starting and ending structures to refine the barrier.

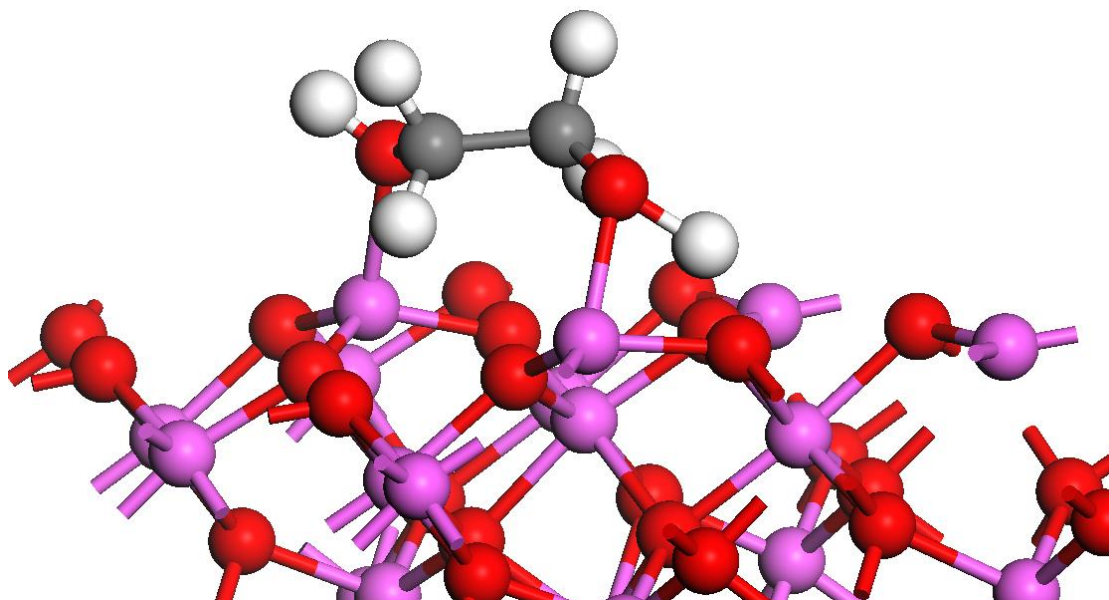


**Figure 43:** The transition state geometry of the O-H activation pathway of ethylene glycol adsorbed on the  $\text{Al}_2\text{O}_3$  (0001) surface.

At the transition state geometry (**Figure 43**) of the O-H activation pathway of the hydrogen-surface oxygen distance is 1.312 Å, the alcohol group oxygen-hydrogen distance is 1.266 Å, and the alcohol group oxygen-aluminium distances are 2.036 Å and 1.874 Å, with the shorter distance being that of oxygen dissociating the hydrogen atom. A vibrational frequency calculation on this structure gives a single imaginary mode. Visualisation of this imaginary mode showed it to be of hydrogen transfer between the alcohol group oxygen atom and an oxygen atom in the surface.

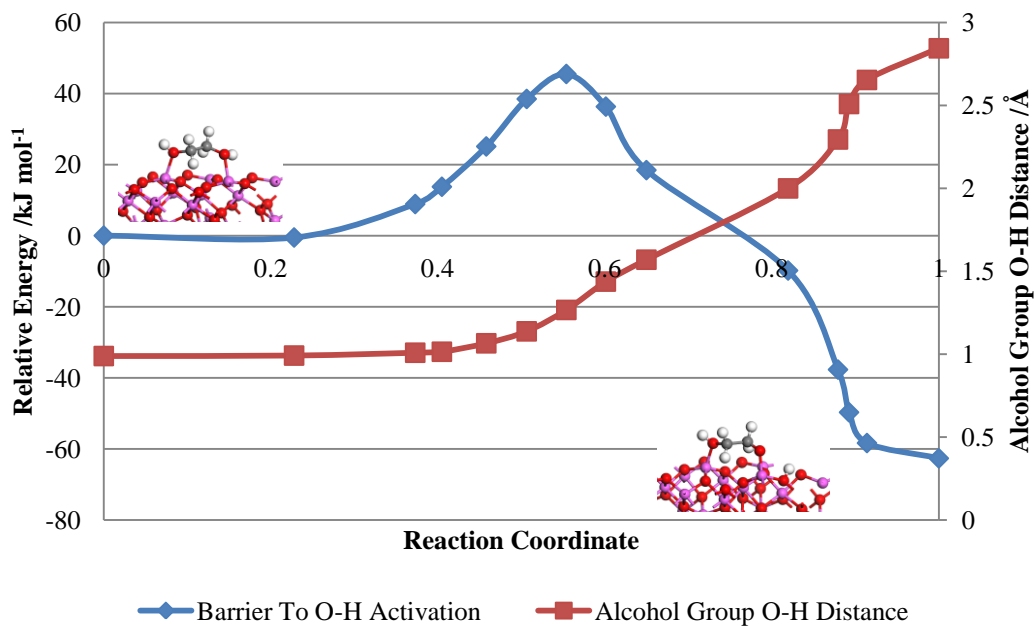


**Figure 44:** Barrier to O-H activation of ethylene glycol over the  $\text{Al}_2\text{O}_3$  (0001) surface.

The energy of the refined transition state of O-H activation over the  $\text{Al}_2\text{O}_3$  (0001) surface (**Figure 44**) is  $45.5 \text{ kJ mol}^{-1}$  higher than the starting point. The energy of the ending point is  $-62.7 \text{ kJ mol}^{-1}$  lower than the starting point. With the zero point correction these values become  $44.4 \text{ kJ mol}^{-1}$  and  $-51.7 \text{ kJ mol}^{-1}$  respectively.

O-H activation of ethylene glycol surrounded by four water molecules as described in **Section 4.2.4**. was also studied.

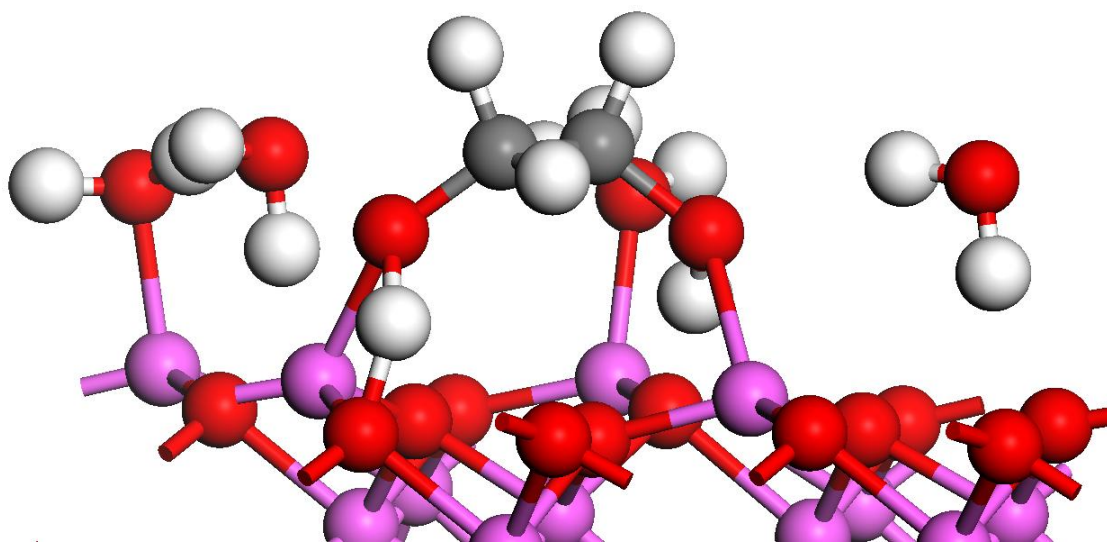


**Figure 45:** The transition state geometry of O-H activation of ethylene glycol surrounded by four water molecules on the  $\text{Al}_2\text{O}_3$  (0001) surface.

At the transition state geometry (**Figure 45**) of O-H activation the hydrogen-surface oxygen distance is 1.219 Å, the alcohol group oxygen-hydrogen distance is 1.217 Å, and the oxygen-aluminium distance is 1.951 Å. A vibrational frequency calculation on this structure gives a single imaginary mode. Visualisation of this imaginary mode showed it to be of hydrogen transfer between the alcohol group oxygen atom and an oxygen atom in the surface.

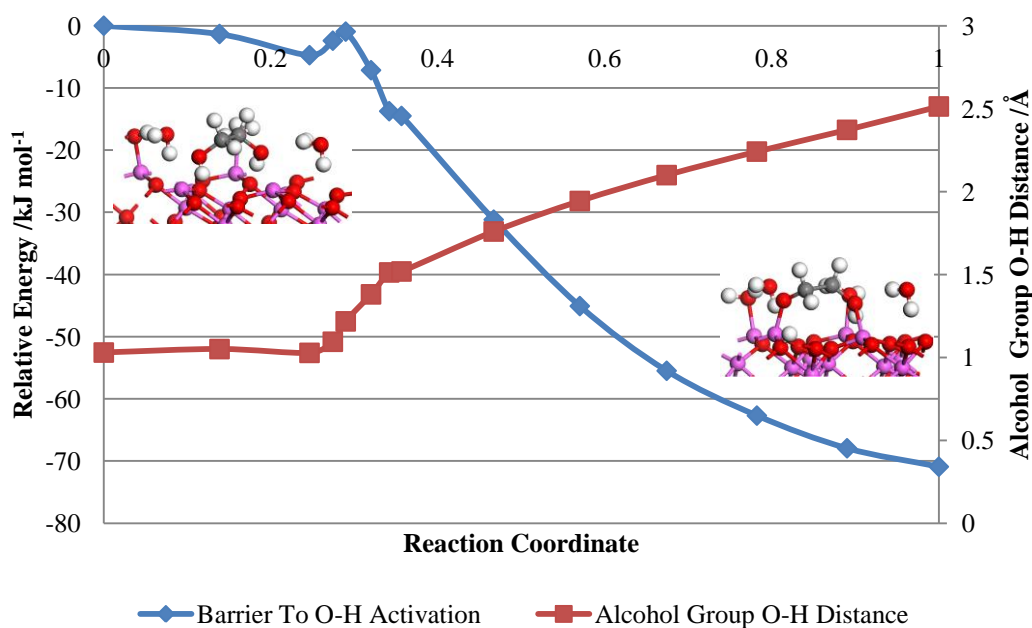


**Figure 46:** Graph showing the barrier to O-H activation of ethylene glycol surrounded by four water molecules over the Al<sub>2</sub>O<sub>3</sub> (0001) surface.

The energy of the refined transition state of O-H activation of ethylene glycol surrounded by four water molecules over the Al<sub>2</sub>O<sub>3</sub> (0001) surface (**Figure 46**) is -0.9 kJ mol<sup>-1</sup> lower than the starting point. The energy of the ending point is -70.9 kJ mol<sup>-1</sup> lower than the starting point. With the zero point correction these values become -10.5 kJ mol<sup>-1</sup> and -68.5 kJ mol<sup>-1</sup> respectively. There is a slight increase in energy of approximately 3.8 kJ mol<sup>-1</sup> before the transition state (where the dissociating hydrogen atom is approximately equidistant between the alcohol group oxygen and the surface oxygen), so this could be considered to be the barrier to O-H activation. However given that each image is lower in energy than the starting configuration the dissociation is effectively barrierless and thermodynamically very favourable.

The transition state energy of O-H activation of ethylene glycol over the Al<sub>2</sub>O<sub>3</sub> (0001) surface is lower by approximately 3.8 kJ mol<sup>-1</sup> with the presence of four

water molecules suggesting that the water molecules stabilise intermediate and ending states of the barrier. This is similar to what has been found with the successive dissociations of the four water molecules on their own on the aluminium oxide surface.

**Table 8:** Table showing the transition state energies, geometries, and differences in energies between the starting and ending states of ethylene glycol dissociation. Bracketed values indicate zero point energy corrected values.

System	Transition State Energy /kJ mol <sup>-1</sup>	Relative Energy of End Structure /kJ mol <sup>-1</sup>	Distances /Å		
			(H)O-Al	H-O (Alcohol Group)	H-O (Surface)
Al <sub>2</sub> O <sub>3</sub> (0001)	45.5 (44.3)	-62.7 (-51.7)	1.874	1.266	1.312
Al <sub>2</sub> O <sub>3</sub> (0001) & 4H <sub>2</sub> O	-0.9 (-10.5)	-70.9 (-68.5)	1.951	1.217	1.219

O-H activation of water requires less energy than O-H activation of ethylene glycol, however compared to the single water molecule the dissociated state of ethylene glycol is more energetically favourable than that of the dissociated state of water. The O-H activation barrier of a single water molecule is greater than that of the first two barriers of the four molecule system. This indicates that the presence of nearby intact water molecules stabilises the system and hence reduces the height of the barrier. The barriers to the third and fourth dissociations are larger than that of the single molecule suggesting that the stabilising effect is limited to water molecules and hydroxyl groups do not have the same effect. The ending state for the first three dissociations is more energetically favourable than the starting state. This coupled with the low O-H activation barriers suggests that in a real system the Al<sub>2</sub>O<sub>3</sub> (0001) surface will be at least partially hydroxylated in the presence of water.

The stabilising effect of nearby water molecules is also shown in the barrier to O-H activation of ethylene glycol surrounded by four water molecules which is downhill all the way, compared to O-H activation without the presence of water molecules which shows a barrier of 46 kJ mol<sup>-1</sup>.

The stabilising effect itself is caused by hydrogen bonding between intact water molecules and the dissociating molecules, hence the reduction in favourability of the end points and increase in barrier height for the successive dissociations of the four water molecule system.

### 4.3. Palladium Oxide

The bulk unit cell of PdO has been optimised using the PBE functional at  $3\times 3\times 3$   $k$ -points with a planewave cut off of 500 eV. A U correction of 6 eV was added to the Pd atoms. This gives the bulk structure a band gap of approximately 1 eV which is similar to the experimental values of 0.8 eV using optical transmittance [34] and 1.5 eV obtained using X-ray photoelectron spectroscopy (XPS) [35]. The U value was determined by performing a series of density of states calculations at  $9\times 9\times 9$   $k$ -points on the bulk structure where the U value was varied between 0 eV and 9 eV and then looking for the band gap on the resulting plots. The Fermi level is at an energy level of zero on each plot.

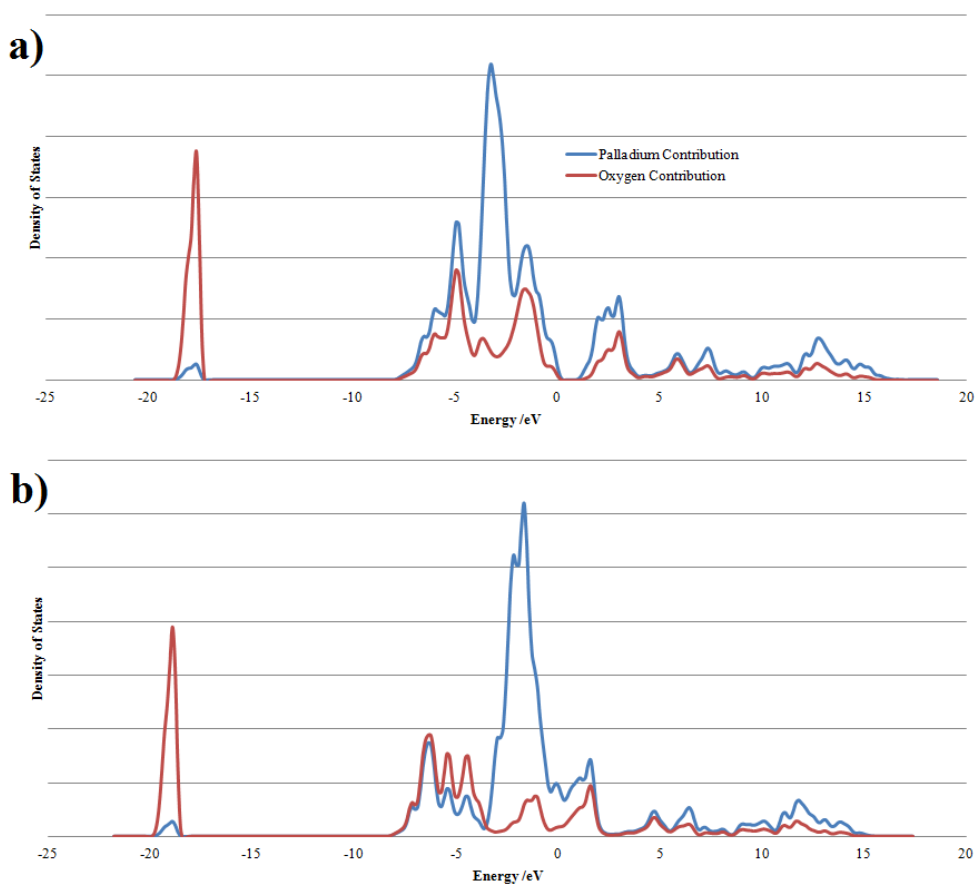


**Figure 47:** Density of states plots for bulk palladium oxide with a) a U correction of 6 eV and b) no U correction.

With a U correction of 6 eV (**Figure 47a**) a band gap of approximately 1 eV is predicted immediately above the Fermi level, but when no U correction applied (**Figure 47b**) no band gap is predicted. There are also available states immediately above the Fermi level.

The optimised lattice parameters calculated with the PBE functional and a U correction of 6 eV using the methodology described for magnesium oxide in **Section 4.1.1**. were  $a=3.0774 \text{ \AA}$ ,  $b=3.0774 \text{ \AA}$  and  $c=5.5462 \text{ \AA}$ . This is an expansion of 1.5% over the experimental values [36].

The PdO (101) surface was chosen as it is a stoichiometric surface that has been experimentally observed to form (using low energy electron diffraction) by oxidising a Pd (111) surface using an oxygen beam under ultra high vacuum [37]. No other terminations were observed to form in this experiment.

There are two different types of palladium atom and two different types of oxygen atom present in the PdO (101) surface: square planar four coordinated palladium ( $\text{Pd}_{4c}$ ), three coordinated palladium ( $\text{Pd}_{3c}$ ), four coordinated tetrahedral oxygen ( $\text{O}_{4c}$ ) and three coordinated oxygen ( $\text{O}_{3c}$ ). In the bulk structure only  $\text{Pd}_{4c}$  and  $\text{O}_{4c}$  are found, but all four types are found in the (101) surface.

In the optimised PdO bulk structure the  $\text{Pd}_{4c}\text{-O}_{4c}$  bonds lengths are all  $2.071 \text{ \AA}$ , and the  $\text{Pd}_{4c}\text{-O}_{4c}\text{-Pd}_{4c}$  bond angles are all  $95.99^\circ$ . Bader analysis of the bulk structure gives a charge of  $+0.97 e$  on the palladium atoms and a corresponding charge of  $-0.97 e$  on the oxygen atoms.

The surface energy of the PdO (101) surface was determined in the same manner as for magnesium oxide and aluminium oxide as described in **Section 4.1.3**. The top three of each slab were relaxed, while the remaining atoms were fixed to simulate bulk behaviour of the material. The surface area of the slab is  $78.04 \text{ \AA}^2$ .

The bulk energy of palladium oxide predicted by the slab method is  $-14.8 \text{ eV}$ , this compares well with the value from single point energy calculations on the palladium oxide bulk unit cell.

Using the same methodology for magnesium oxide described in **Section 4.1.3**. the surface energy of the PdO (101) surface was calculated to be  $0.97 \pm 0.01 \text{ J m}^{-2}$  for

four or more layers (**Figure 48**). The deviation for the eight and nine layer slabs comes from difficulties in converging the energy of the slab with a dipole correction applied perpendicular to the surface and a U correction simultaneously.

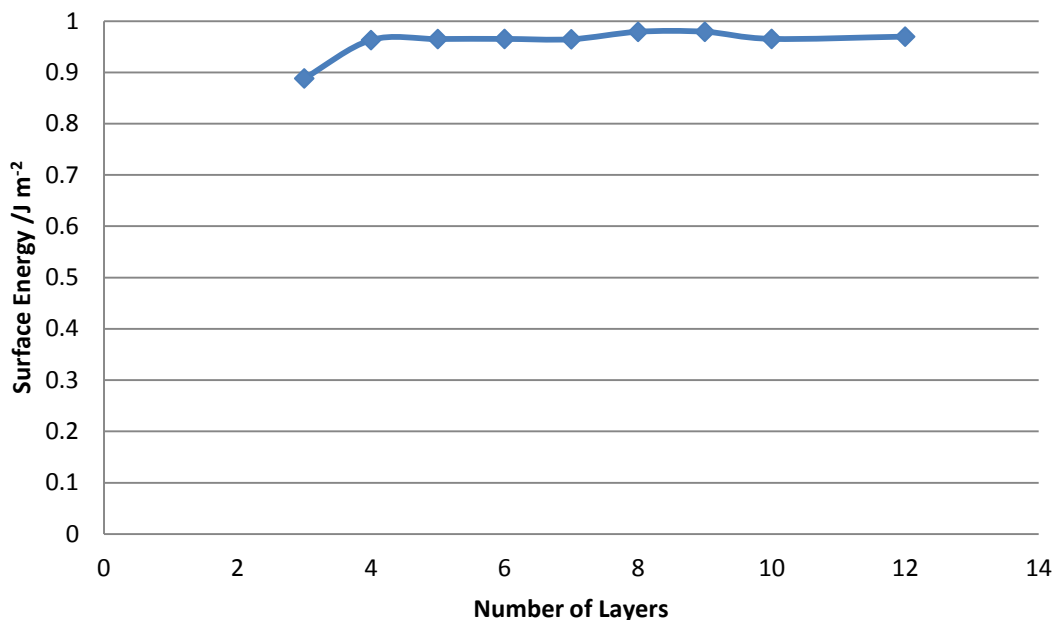


**Figure 48:** Graph showing surface energy against number of layers for the PdO (101) surface.

In the optimised PdO (101) surface the Pd<sup>2+</sup> centres are four coordinate centres in a square planar arrangement and the oxygen atoms are in a near tetrahedral environment with Pd<sub>4c</sub>-O<sub>4c</sub> bond lengths of 2.054-2.066 Å. The Pd<sub>4c</sub>-O<sub>3c</sub> bond length is 2.049 Å and the Pd<sub>3c</sub>-O<sub>3c</sub> bond length is 1.960 Å. The Pd<sub>3c</sub>-O<sub>3c</sub>-Pd<sub>3c</sub> bond angle is 97.37°, the Pd<sub>4c</sub>-O<sub>4c</sub>-Pd<sub>4c</sub> bond angles vary between 97.97° and 116.71°.



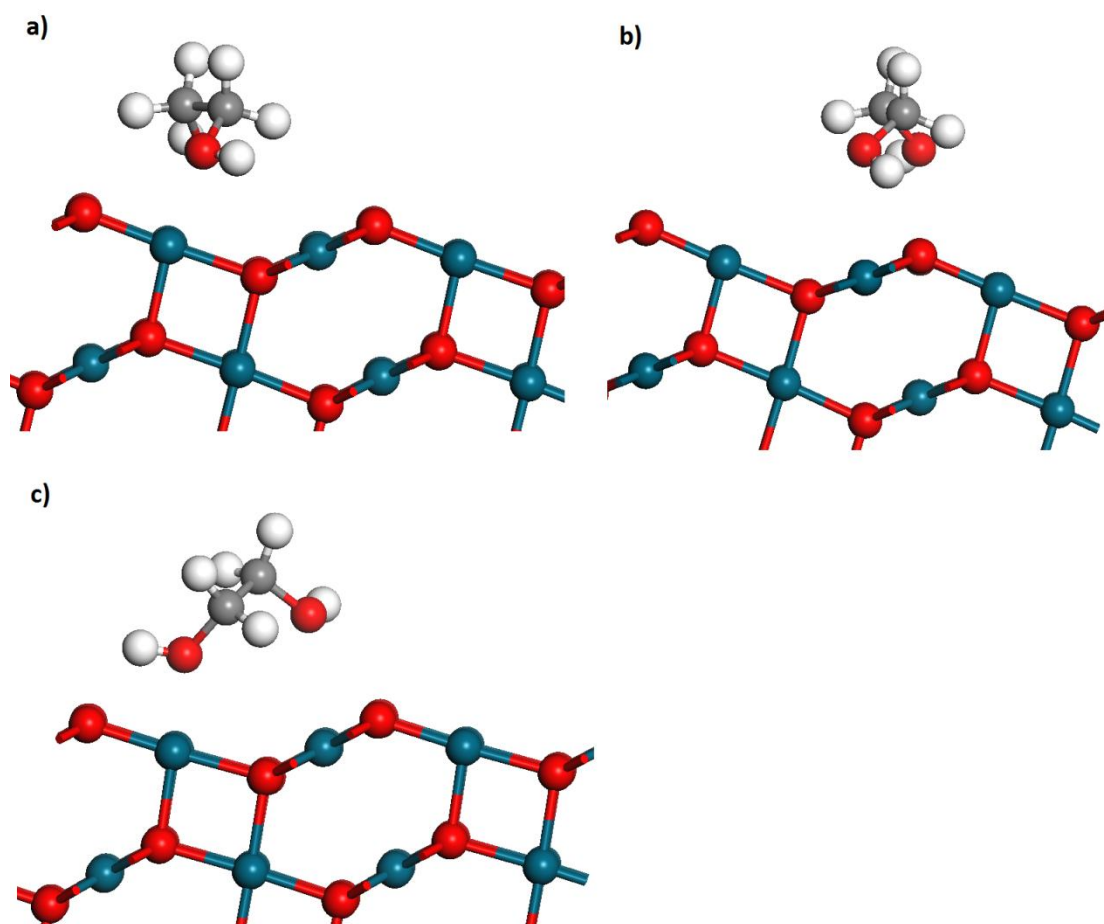


**Figure 50:** The PBE+U optimised geometries of ethylene glycol adsorbed to the PdO (101) surface in the a) 3c3c configuration, b) 4c4c configuration and c) 3c4c configuration.

**Table 9:** Table showing the adsorption energies of ethylene glycol in various configurations over the PdO (101) surface. Bracketed values indicate the PBE adsorption energies without U correction.

Configuration	Adsorption Energy /kJ mol <sup>-1</sup>	O-Pd Distances /Å
3c3c	-135 (-105)	2.191, 2.171
4c4c	-6 (9)	2.961, 3.179
3c4c	-91 (-45)	2.110 (3c), 2.919 (4c)

The O-Pd<sub>4c</sub> distances are much larger than the O-Pd<sub>3c</sub> distances (**Table 9**). Adsorption to Pd<sub>3c</sub> atoms is also much more favourable as they can accept a lone pair of electrons from ethylene glycol's alcohol groups.

Bader analysis of the 3c4c structure gives a net positive charge of +0.1326 e on the ethylene glycol molecule. This indicates a transfer of electron density to the surface suggesting that palladium oxide is acting as a Lewis acid.

Following adsorption of ethylene glycol, a hydrogen atom (H1) from an alcohol group on each structure was removed and placed close to the nearest oxygen atom (OS1) on the PdO (101) surface and the systems were reoptimised. To improve performance the optimisation was first performed using the PBE functional with the U correction turned off, and then this optimised structure was reoptimised with PBE+U.

For the 3c3c structure the nearest surface oxygen was four-coordinated and during the optimisation the structure returned to a 3c3c configuration with one of the hydroxyl groups pointing towards a three-coordinated oxygen in the surface. This alternative 3c3c configuration was shown to be slightly more favourable for adsorption than the first 3c3c configuration found, with an adsorption energy of -111 kJ mol<sup>-1</sup> compared to -105 kJ mol<sup>-1</sup> without U correction, and -135 kJ mol<sup>-1</sup> compared to -144 kJ mol<sup>-1</sup> with U correction. The oxygen-Pd<sub>3c</sub> distances increased slightly to 2.212 Å and 2.180 Å.

For the 4c4c structure the system optimised back to an intact ethylene glycol molecule. The molecule has also twisted such that one of the alcohol group oxygen atoms is pointing away from the surface (the associated hydrogen atom is pointing towards the surface but is 2.509 Å away from the nearest three coordinated oxygen atom). The other alcohol group oxygen atom is 3.200 Å away from the nearest four coordinated palladium atom.

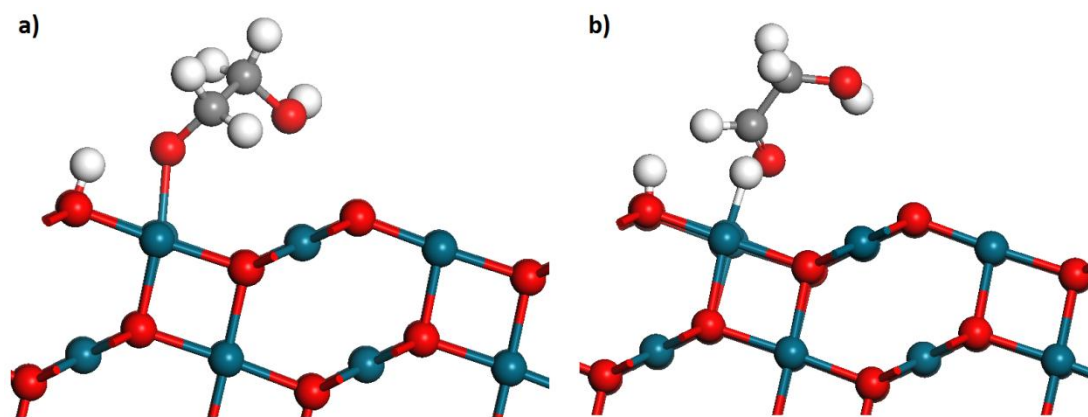


**Figure 51:** a) Ethylene glycol adsorbed over the PdO (101) surface in the 3c4c configuration, with a hydrogen atom chemisorbed to a three coordinated oxygen atom in the surface calculated with PBE+U. b) Hydroxyethanal and two hydrogen atoms adsorbed to the PdO (101) surface.

For the dissociated 3c4c structure (**Figure 51a**) the hydrogen- $O_{3c}$  distance is 0.995 Å, the hydrogen-alcohol group oxygen distance is 1.853 Å and the alcohol group oxygen- $Pd_{3c}$  ( $PdS1$ ) distance is 2.008 Å. This state is  $-14 \text{ kJ mol}^{-1}$  lower in energy than physisorbed ethylene glycol.

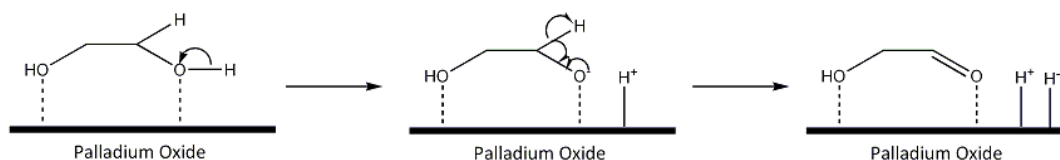
A second hydrogen atom ( $H2$ ) was then removed from the carbon atom and placed onto a three coordinated palladium atom ( $PdS2$ ) in the surface (**Figure 51b**) to form hydroxyethanal. The aldehyde oxygen- $Pd_{3c}$  distance is 2.134 Å, the  $H-O_{3c}$  distance is 0.974 Å and the  $H-Pd_{3c}$  distance is 1.575 Å. This state is  $44 \text{ kJ mol}^{-1}$  higher in energy than the previous state.

Bader analysis was performed on the structures of physisorbed ethylene glycol in the 3c4c configuration (**Figure 50c**), and on the two dissociated states (**Figure 51a** & **Figure 51b**) with the results for selected atoms shown in **Table 10**.

**Table 10:** Table showing the Bader charges (in units of  $e$ ) of selected atoms.

Atom	Ethylene Glycol	PdO (101)	PdO (101) & 3c4c Ethylene Glycol	First Dissociation	Second Dissociation
PdS1		0.77	0.81	0.82	0.83
Alcohol Group Oxygen	-1.12		-1.09	-1.00	-1.06
OS1		-0.79	-0.85	-1.01	-0.99
PdS2		0.77	0.76	0.79	0.54
H1	0.59		0.64	0.64	0.58
H2	0.05		0.09	0.06	-0.12

The Bader charges in **Table 10** show that the first hydrogen atom dissociates with a positive charge, and the second dissociates with a negative charge which suggests the mechanism for ethylene glycol oxidation proposed in **Figure 52**, which is similar to the mechanism suggested by Conte *et al.* [8] in **Figure 1**, except that the hydrogen dissociations happen in the opposite order as the barrier to O-H activation is smaller than the barrier to C-H activation (**Section 4.3.2**).

**Figure 52:** The proposed mechanism for the oxidation of ethylene glycol to hydroxyethanal over a palladium oxide catalyst.

The first step of mechanism for aluminium oxide is likely to be similar as dissociating hydrogen atom also leaves with significant positive charge, however the second step will be different (or require the present of additional catalytic materials) as it was determined that C-H activation is not possible using on aluminium oxide (**Section 4.2.2**).

#### 4.3.2. O-H and C-H Activation Energy Barriers over Palladium Oxide

Nudged elastic band calculations were performed to determine the activation energy barrier to O-H activation over the PdO (101) surface using the methodology described in **Section 4.1.5**. A total of eight images were interpolated between the structures of adsorbed ethylene glycol and its dissociated form described in **Section**

**4.3.1.** Once a possible transition state has been located a second NEB calculation consisting of five images is performed using the two points either side as the starting and ending structures. Vibrational frequency calculations are then performed on the starting, ending and new transition state structures.

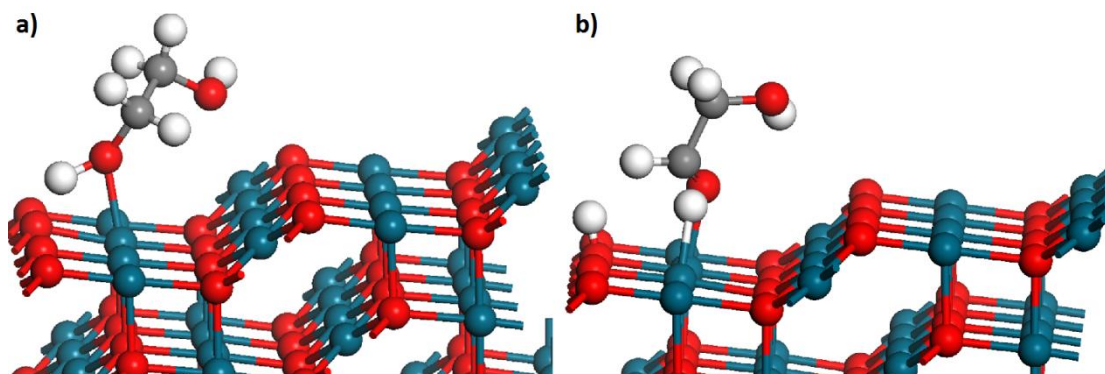


**Figure 53:** The transition state geometries for a) O-H activation and b) C-H activation of ethylene glycol over the PdO (101) surface.

Visualisation of the imaginary modes of the transition state geometries (**Figure 53**) showed them to be of hydrogen transfer between the ethylene glycol molecule and the surface.

At the transition state geometry of O-H activation of the 3c4c configuration (**Figure 53a**) the H-O<sub>3c</sub> distance is 1.309 Å, the alcohol group oxygen-hydrogen distance is 1.192 Å and the alcohol group oxygen-palladium distance is 2.060 Å.

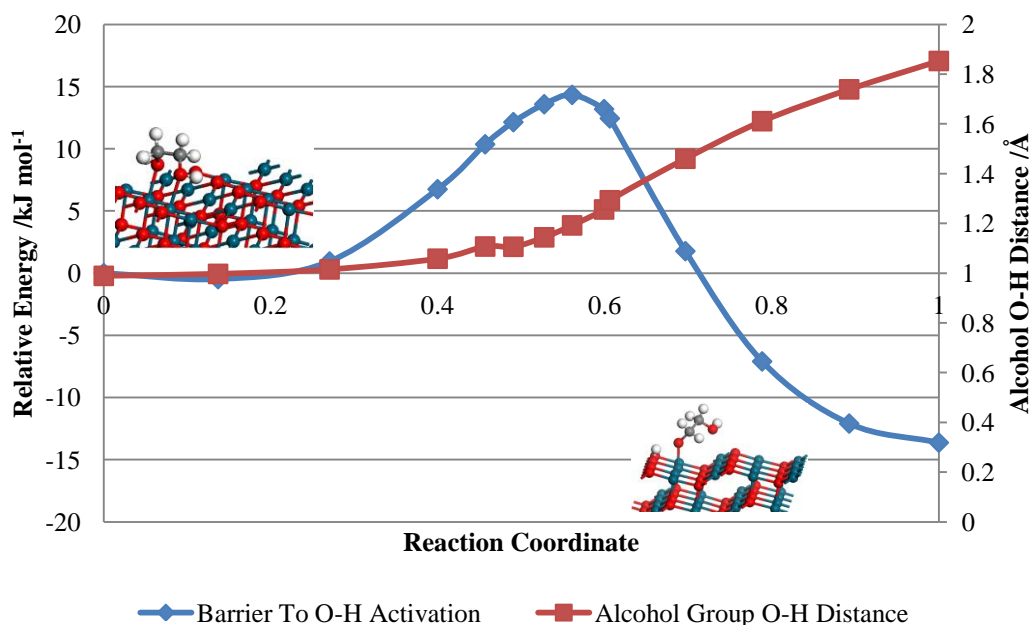


**Figure 54:** Graph showing the barrier to O-H activation of ethylene glycol over the PdO (101) surface.

The energy of the transition state for O-H activation is  $14.3 \text{ kJ mol}^{-1}$  higher than the starting point. The energy of the ending point is  $-13.6 \text{ kJ mol}^{-1}$  lower than the starting point (**Figure 54**). With the zero point correction these values become  $-0.3 \text{ kJ mol}^{-1}$  and  $-16.7 \text{ kJ mol}^{-1}$  respectively.

Following O-H activation of ethylene glycol, C-H activation to form hydroxyethanal was attempted with the second hydrogen atom being placed onto a three coordinated palladium atom. When using PBE+U the middle frames of the barrier are unstable and generate extremely high energies, however when no U correction is used the energies are more reasonable. Therefore the geometry optimisation was performed with no U correction and once this was complete single point energy calculations were performed on each image with the U correction applied.

At the transition state geometry of C-H activation for the 3c4c configuration (**Figure 53b**) the H-Pd<sub>3c</sub> distance is  $1.772 \text{ \AA}$ , the carbon-hydrogen distance is  $1.574 \text{ \AA}$  and the aldehyde group oxygen-palladium distance is  $2.028 \text{ \AA}$ .

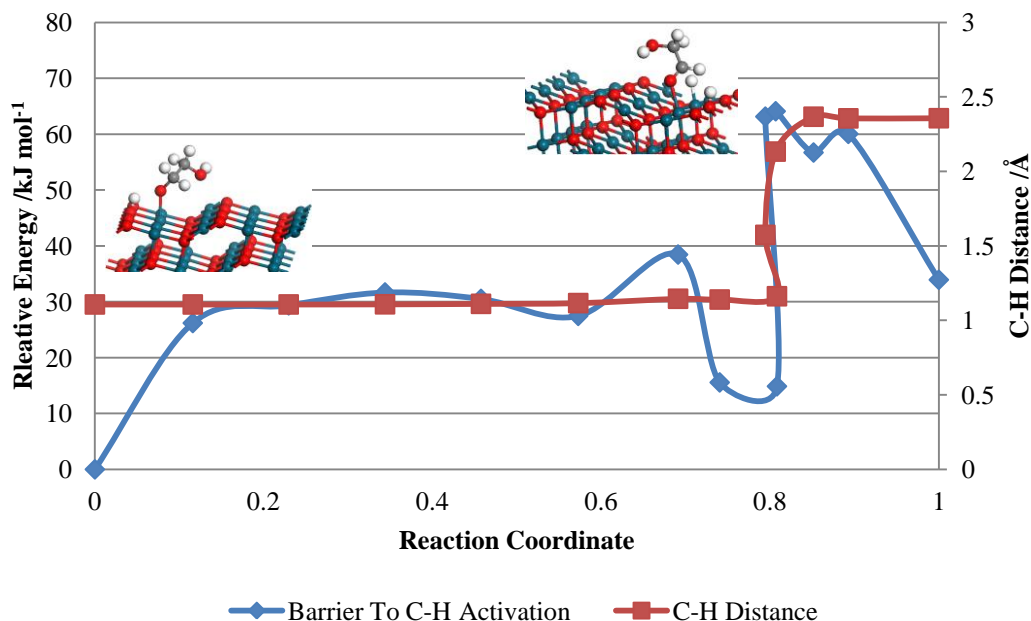


**Figure 55:** Graph showing the barrier to C-H activation following O-H activation of ethylene glycol over the PdO (101) surface.

The energy of the transition state is  $63.1 \text{ kJ mol}^{-1}$  higher than the starting point. The energy of the ending point is  $33.9 \text{ kJ mol}^{-1}$  higher than the starting point (**Figure 55**). With the zero point correction these values become  $49.3 \text{ kJ mol}^{-1}$  and  $23.0 \text{ kJ mol}^{-1}$  respectively. It should be noted that the energies with the U correction applied are approximately  $40 \text{ kJ mol}^{-1}$  higher for each image than without the U correction. The lowering of the barrier prior to the transition state is caused by the molecule reorienting over the surface prior to the dissociation of the second hydrogen atom.

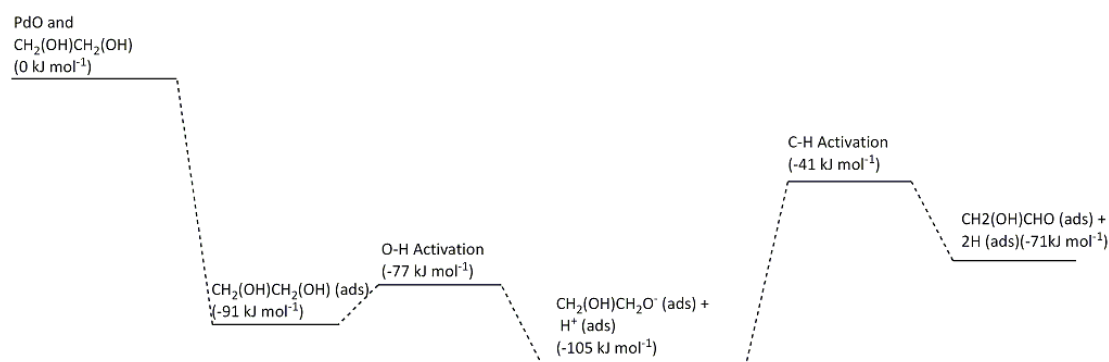


**Figure 56:** Diagram showing the relative PBE+U energies of each step in the oxidation of ethylene glycol in the 3c4c configuration to hydroxyethanal on the PdO (101) surface.

**Figure 56** summarises the energy changes at each step of the reaction relative to the isolated PdO (101) surface and ethylene glycol. It shows that each step of the

reaction is lower in energy than the initial state of the PdO (101) surface and isolated ethylene glycol, and thus is thermodynamically favourable.

#### 4.4. Gold-38 Clusters

##### 4.4.1. Au<sub>38</sub> Cluster

A gold cluster in a periodic box of 25×25×25 Å consisting of thirty eight atoms was optimised in VASP using the PBE functional with a planewave cut off of 500 eV and a single *k*-point (**Figure 57**). The diameter of the cluster is 8.008 Å, and the cluster is 16.9 Å away from its periodic images.

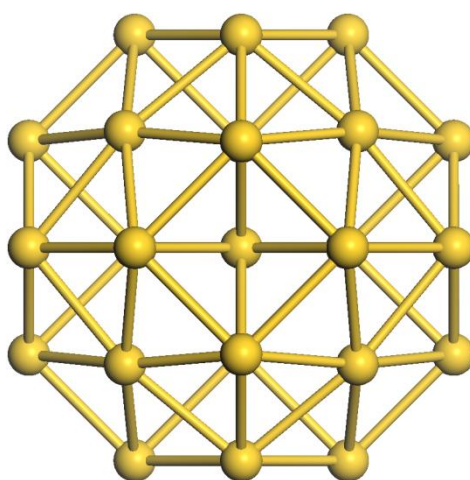


**Figure 57:** The optimised Au<sub>38</sub> cluster.

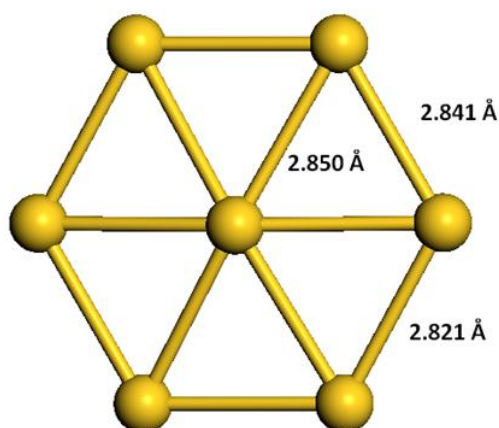


**Figure 58:** A slice of the Au<sub>38</sub> cluster showing a typical (111) face with optimised bond lengths.

On the (100) faces of the structure shown in **Figure 57** the Au-Au bond lengths are all 2.841 Å.

On the perimeter of the (111) face the Au-Au bond lengths alternated between 2.821 Å and 2.841 Å, with longer bonds being between atoms that are also part of an adjacent (100) face. The Au-Au bonds involving the central gold atom are all 2.850 Å long. For comparison the Au-Au bond length in a bulk gold unit cell optimised at the same level of theory (using  $3\times 3\times 3$   $k$ -points) is 2.975 Å.

A single ethylene glycol molecule was placed close to a corner site between the (100) and (111) faces and the system was then reoptimised (**Figure 59**).

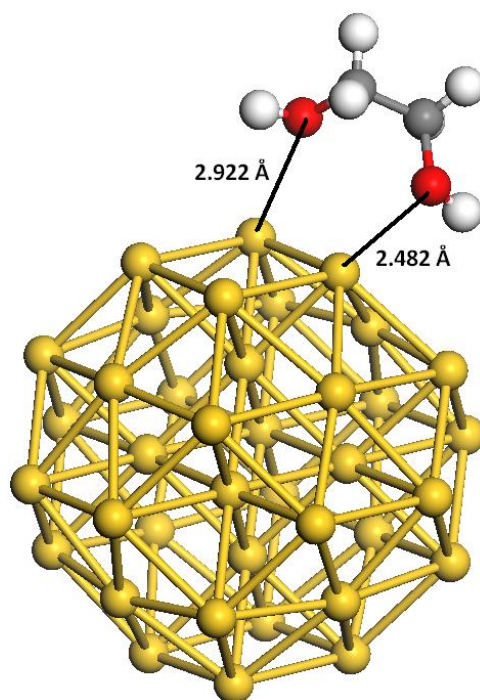


**Figure 59:** Ethylene glycol adsorbed on the corner of an Au<sub>38</sub> cluster.

The adsorption energy is favourable at  $-34\text{ kJ mol}^{-1}$ , with the gold-oxygen distances being measured at 2.482 Å and 2.922 Å. The adsorption also caused slight rearrangement of the gold atoms near the adsorbate with the Au-Au bonds in the (100) face which are closest to the nearest oxygen atom increasing in length to 2.845 Å and 2.878 Å, and in the (111) face the bond between the perimeter gold atom closest to the oxygen and the central gold atom shrank to 2.809 Å, while the perimeter atom to perimeter atom distance increased to 2.894 Å.

A hydrogen atom was then removed from one of the alcohol groups and placed onto the closest accessible gold atom on the surface of the cluster (a perimeter atom on a (111) face), and the system was reoptimised (**Figure 60**). This adsorption configuration is  $53\text{ kJ mol}^{-1}$  higher than the initial adsorbed state.

Other adsorption sites for the hydrogen atom were also studied: a bridging site where the hydrogen atom bridges a perimeter gold atom and the atom in the centre of a (111) face, and directly above the gold atom in the centre of the (111) face.

Adsorption to the bridging site is very unfavourable at  $204 \text{ kJ mol}^{-1}$  above the initial adsorbed state, and adsorption to the central gold atom on a (111) face is also very unfavourable at  $267 \text{ kJ mol}^{-1}$  above the initial adsorbed state. Therefore these adsorption configurations are unlikely to occur in reality.

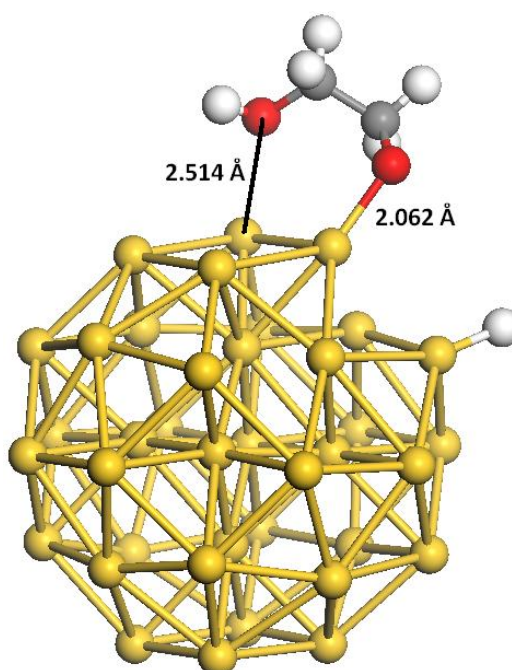


**Figure 60:** The optimised structure of ethylene glycol adsorbed to an  $\text{Au}_{38}$  cluster with a hydrogen atom dissociated to the cluster.

The gold-oxygen distances were reduced to  $2.062 \text{ \AA}$  and  $2.514 \text{ \AA}$ , and the gold-hydrogen distance was measured to be  $1.616 \text{ \AA}$ . The Au-Au bonds in the (100) face bonded to the oxygen atom increased to  $2.895 \text{ \AA}$  and  $2.924 \text{ \AA}$ , and in the (111) face the bond between the perimeter gold atom closest to the oxygen and the central gold atom increased to  $2.838 \text{ \AA}$ , while the perimeter atom to perimeter atom distance increased to  $3.052 \text{ \AA}$ . Bader analysis of this system gives a Bader charge of  $-0.27 e$  on the gold atom that is coordinated to the anionic oxygen atom, compared with  $-0.05 e$  when the hydrogen atom is not dissociated. The anionic oxygen atom has a Bader charge of  $-0.50 e$  compared to  $-0.81 e$  prior to the dissociation of hydrogen.

This indicates a transfer of electron density from the oxygen atom to the gold atom. The gold atom that the hydrogen atom adsorbs to has a charge of 0.02 e compared to +0.25 e prior to the adsorption of the hydrogen atom, indicating a transfer of electron density to the gold atom.

A second hydrogen atom was removed from a carbon atom on the adsorbate to form hydroxyethanal and placed onto another gold atom on the surface of the cluster. This system was again reoptimised (**Figure 61**).

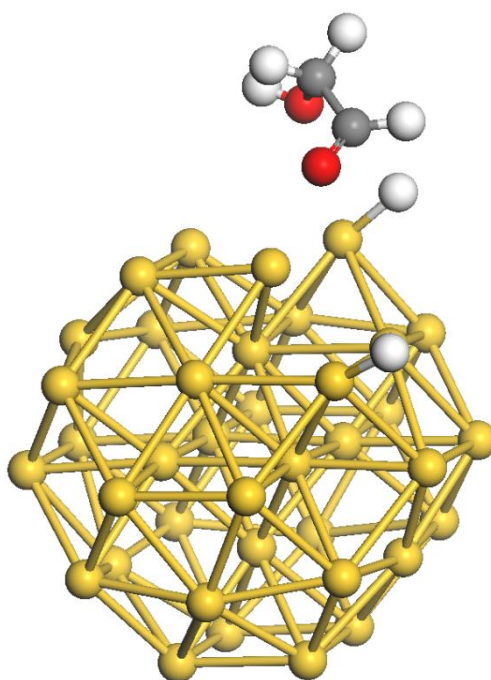


**Figure 61:** Hydroxyethanal and two hydrogen atoms adsorbed on an Au<sub>38</sub> cluster.

The aldehyde group oxygen-gold distance is 2.331 Å and the alcohol group oxygen-gold distance is 2.840 Å. The gold-hydrogen distances are 1.614 Å and 1.635 Å. This state was 76 kJ mol<sup>-1</sup> higher in energy than the previous state, or a total of 129 kJ mol<sup>-1</sup> above the initial adsorbed state of ethylene glycol on the Au<sub>38</sub> cluster. Bader analysis of this system gives a Bader charge of -0.85 e on the aldehyde group oxygen compared to -0.50 e prior to the removal of the second hydrogen atom from ethylene glycol. The gold atom which the second hydrogen atom adsorbs to has a Bader charge of 0.31 e compared to -1.37 e before the adsorption of hydrogen. The second hydrogen atom has a Bader charge of -0.36 e compared to -0.44 e prior to adsorption.

#### 4.4.2. O-H and C-H Activation Energy Barriers with the Au<sub>38</sub> Cluster

For the first activation energy barrier calculation, that of O-H activation, a series of eight frames is linearly interpolated between a starting point of physisorbed ethylene glycol over the Au<sub>38</sub> cluster and an ending point of chemisorbed ethylene glycol and a hydrogen atom on the surface of the cluster.

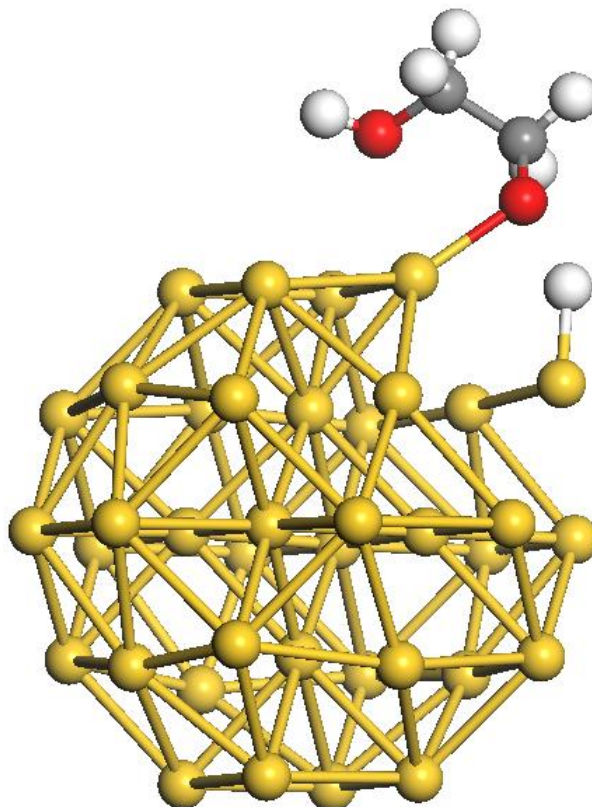


**Figure 62:** The transition state geometry of O-H activation of ethylene glycol over the Au<sub>38</sub> cluster.

At the transition state geometry (**Figure 62**) the O-Au distance is 2.183 Å, the H-Au distance is 1.650 Å and the alcohol group O-H distance is 1.577 Å. A vibrational frequency calculation on this structure gives three imaginary modes. Visualisation of these imaginary modes showed one to be of hydrogen transfer between the alcohol group oxygen and a gold atom on the surface of the cluster.

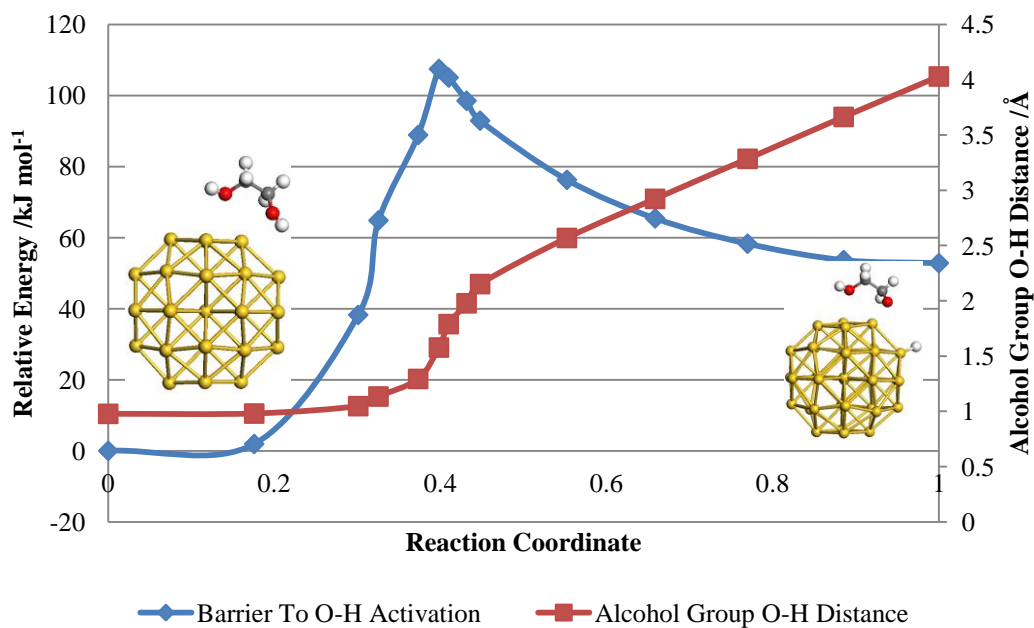


**Figure 63:** Graph showing the barrier to O-H activation of ethylene glycol over an Au<sub>38</sub> cluster.

The energy of the refined transition state of O-H activation over the Au<sub>38</sub> cluster (**Figure 63**) is 107.5 kJ mol<sup>-1</sup> higher than the starting point. The energy of the ending point is 52.8 kJ mol<sup>-1</sup> higher than the starting point. With the zero point correction these values become 89.2 kJ mol<sup>-1</sup> and 35.9 kJ mol<sup>-1</sup> respectively.

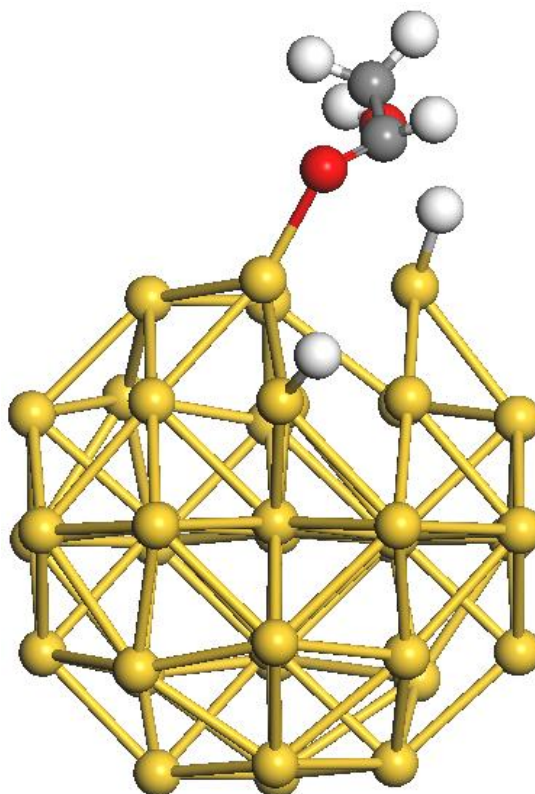


**Figure 64:** The transition state geometry of C-H activation of ethylene glycol following O-H activation over the Au<sub>38</sub> cluster.

At the transition state geometry (**Figure 64**) the O-Au distance is 2.195 Å, the H-Au distance is 1.746 Å and the C-H distance is 1.679 Å. This point is chosen as the transition state as it is where the C-H and H-Au distances are similar, because the barrier is entirely uphill. A vibrational frequency calculation on this structure gives four imaginary modes. Visualisation of these imaginary modes showed one to be of hydrogen transfer between the oxygen atom and the gold atom on the surface of the cluster.

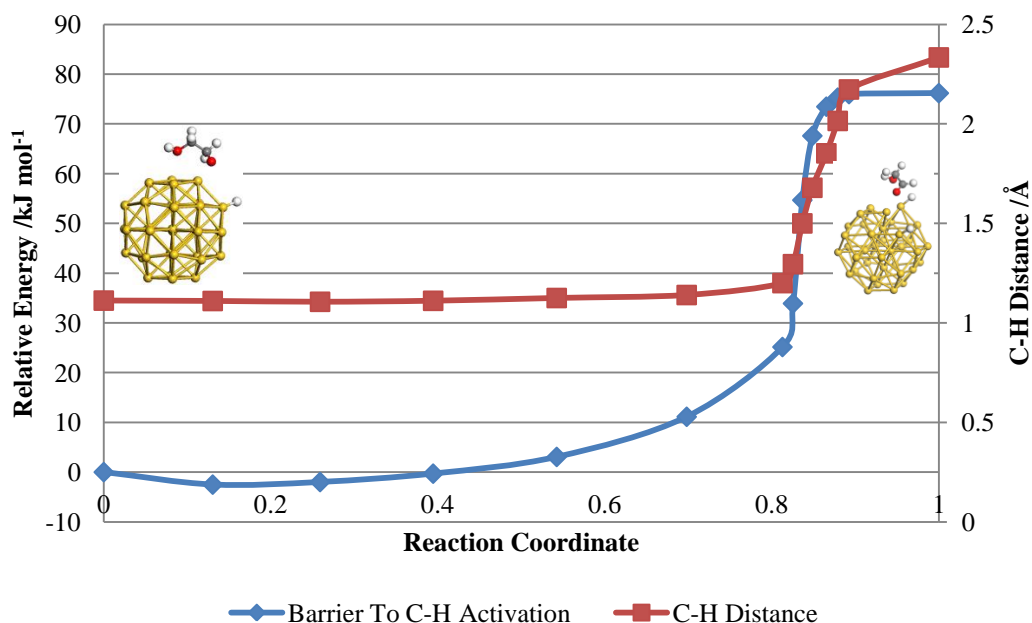


**Figure 65:** Graph showing the barrier to C-H activation following O-H activation of ethylene glycol over an Au<sub>38</sub> cluster.

The energy of the refined transition state of C-H activation over the Au<sub>38</sub> cluster (**Figure 65**) is 67.6 kJ mol<sup>-1</sup> higher than the starting point. The energy of the ending point is 76.2 kJ mol<sup>-1</sup> higher than the starting point. With the zero point correction these values become 49.8 kJ mol<sup>-1</sup> and 58.5 kJ mol<sup>-1</sup> respectively. For the initial part of the barrier there is little change in the C-H distance as the ethylene glycol molecule rearranges itself with respect to the gold cluster. In the C-H activation portion of the barrier the energy increases at each point.

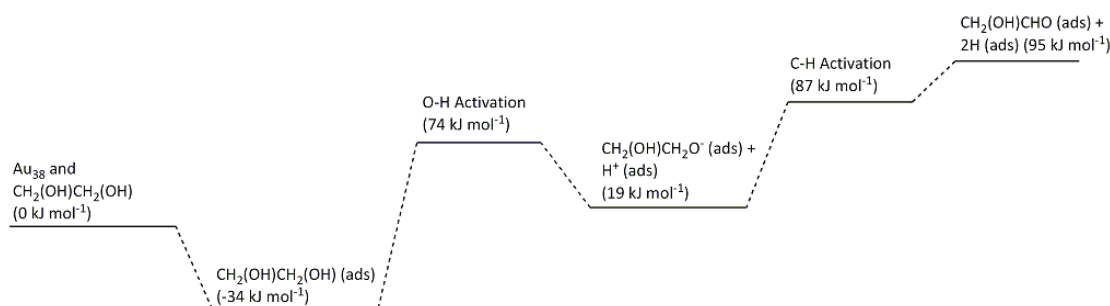


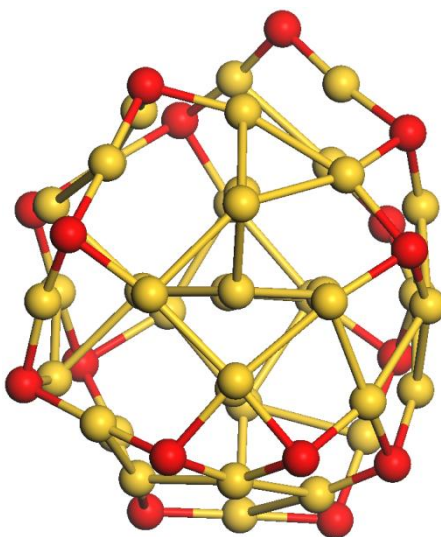
**Figure 66:** Diagram showing the relative energies of each step in the oxidation of ethylene glycol to hydroxyethanal on an Au<sub>38</sub> cluster.

**Figure 66** summarises the energy changes at each step of the reaction relative to the separate Au<sub>38</sub> cluster surface and ethylene glycol. It shows that apart from the first step, each step of the reaction is higher in energy than the initial state of the separate

Au<sub>38</sub> surface and isolated ethylene glycol, and thus is thermodynamically unfavourable. Compared to work by Boronat *et al.* [5] studying ethanol oxidation with an Au<sub>38</sub> cluster using the PW91 functional, it was found that ethanol adsorbs more favourably at -50 kJ mol<sup>-1</sup> and the barriers to O-H and C-H activation are slightly lower at 80 kJ mol<sup>-1</sup> and 41 kJ mol<sup>-1</sup> respectively. These differences are likely due to differences between the PW91 and PBE functionals, and differences in the adsorption geometries. The PBE values are likely to be more accurate as the PW91 functional is known to overestimate adsorption energies [38] [39].

#### 4.4.3. Au<sub>38</sub>O<sub>16</sub> Cluster

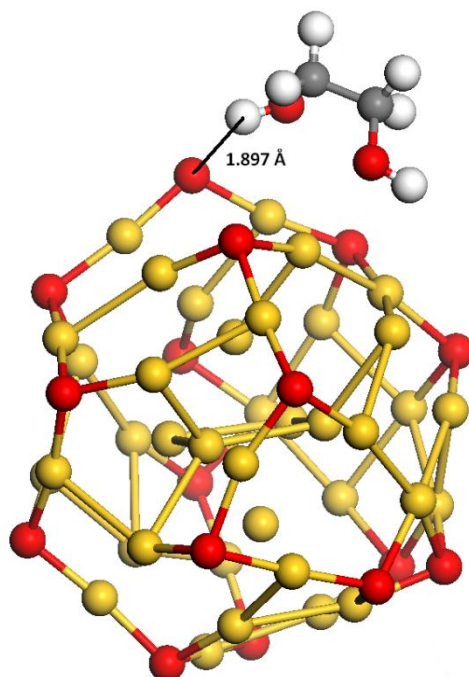
The Au<sub>38</sub>O<sub>16</sub> cluster was chosen because at this level of oxygen coverage the oxygen atoms have formed a monolayer [7], and thus this structure provides a basis for comparison with the other metal oxide surfaces. All calculations performed on the Au<sub>38</sub>O<sub>16</sub> cluster used the same settings as were used with the Au<sub>38</sub> cluster.



**Figure 67:** The optimised structure of an Au<sub>38</sub>O<sub>16</sub> cluster.

In the optimised structure (**Figure 67**) the oxygen atoms formed one corner of a tetrahedron with three gold atoms. The length of the Au-O bonds varied between 1.969 Å and 2.254 Å, with the more linear O-Au-O bonds being shorter than those involving the three-coordinated oxygen atoms. The Au-Au bonds varied between 2.611 Å and 2.780 Å. These values are consistent with work by Corma *et al* [7]. The presence of the chemisorbed oxygen distorts the structure of the Au<sub>38</sub> cluster. Bader analysis of the Au<sub>38</sub>O<sub>16</sub> cluster shows that the gold atoms in the centre of O-Au-O

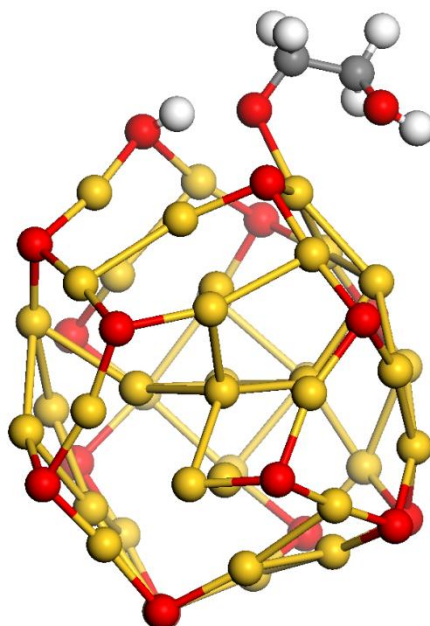
structures have significant partial positive charge (between 0.50 e and 0.71 e) and the bond angles centred on the gold atoms vary between 168° and 176°.



**Figure 68:** Ethylene glycol adsorbed on the  $\text{Au}_{38}\text{O}_{16}$  cluster.

A single configuration of ethylene glycol adsorption to the  $\text{Au}_{38}\text{O}_{16}$  cluster was considered. The ethylene glycol molecule was placed close to the  $\text{Au}_{38}\text{O}_{16}$  cluster in such a way that both of the alcohol group oxygen atoms were interacting with an exposed gold atom and the system was reoptimised. The adsorption energy of ethylene glycol on the  $\text{Au}_{38}\text{O}_{16}$  cluster (**Figure 68**) was favourable at  $-36 \text{ kJ mol}^{-1}$ , which is  $2 \text{ kJ mol}^{-1}$  more energetically favourable than adsorption over the  $\text{Au}_{38}$  cluster. The alcohol group oxygen to gold distances are measured at  $2.541 \text{ \AA}$  and  $2.871 \text{ \AA}$ . A hydrogen bond of length  $1.897 \text{ \AA}$  is also formed between one of the alcohol groups and linearly coordinated oxygen atom on the surface of the cluster. The presence of oxygen on the surface of the cluster inhibits the physisorption of ethylene glycol. Compared to the  $\text{Au}_{38}$  cluster where the ethylene glycol alcohol group oxygen atoms are interacting with the cluster directly, the interaction of ethylene glycol with the  $\text{Au}_{38}\text{O}_{16}$  cluster is via hydrogen bonds to the oxygen atoms of the cluster.

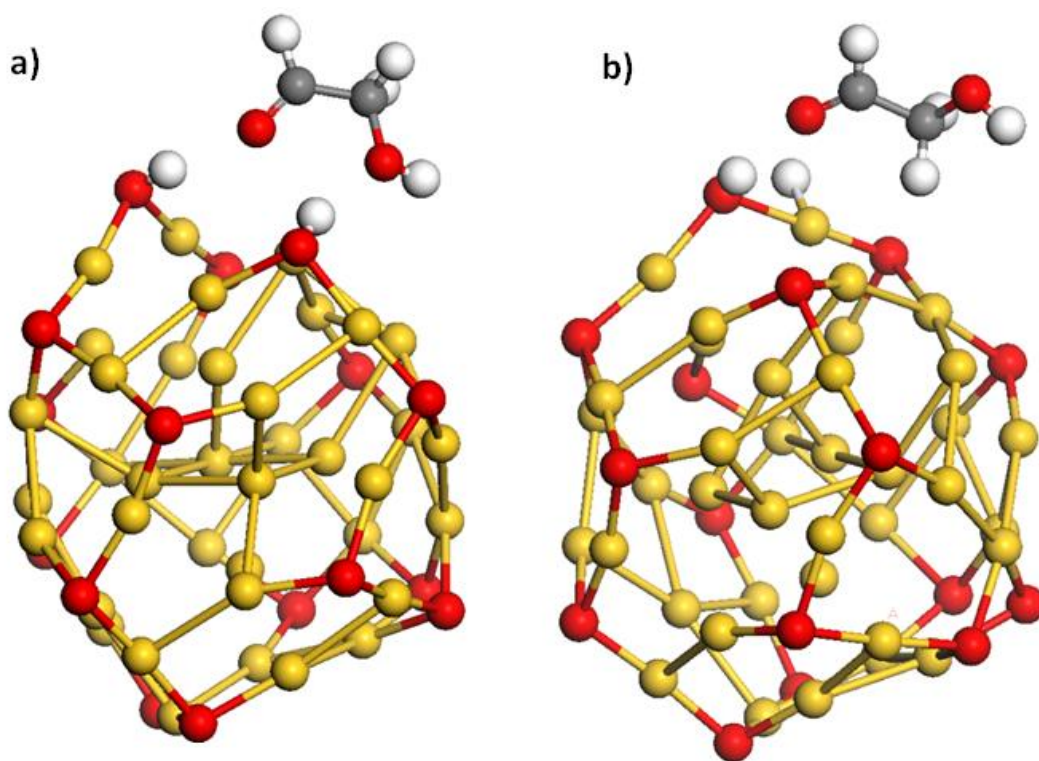
The hydrogen atom forming the hydrogen bond was removed and placed on the nearest oxygen atom on the cluster, and the system was reoptimised (**Figure 69**).



**Figure 69:** The optimised structure of ethylene glycol with a hydrogen atom dissociated to the Au<sub>38</sub>O<sub>16</sub> cluster.

The alcohol group oxygen to gold distances changed to 2.693 Å and 2.187 Å. This state was approximately 8 kJ mol<sup>-1</sup> lower in energy than the initial adsorbed state, indicating that the deprotonated ethylene glycol has chemisorbed to the cluster.

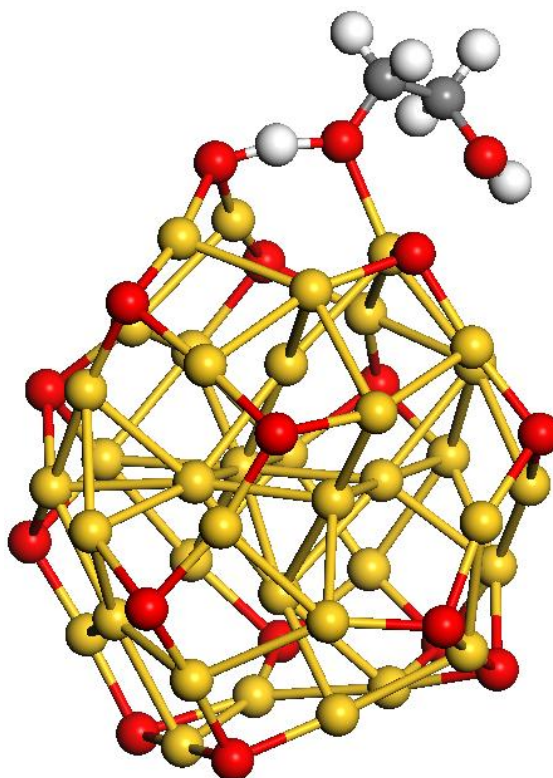
A second hydrogen atom was then removed from a carbon atom on the adsorbate to form hydroxyethanal. This hydrogen atom was placed onto another oxygen atom (**Figure 70a**) or a gold atom (**Figure 70b**) in separate calculations.



**Figure 70:** Hydroxyethanal adsorbed on the Au<sub>38</sub>O<sub>16</sub> cluster a) with both removed hydrogen atoms forming hydroxyl groups on the cluster, b) with one removed hydrogen atom forming a hydroxyl group on the cluster and the other forming a gold-hydrogen bond.

With both removed hydrogen atoms forming hydroxyl groups (**Figure 70a**), the aldehyde group oxygen-gold distance is 2.948 Å and the alcohol group oxygen-gold is 2.914 Å. This system was 120 kJ mol<sup>-1</sup> lower in energy than the previous state, or a total of 128 kJ mol<sup>-1</sup> lower than the initial adsorbed state of ethylene glycol over the Au<sub>38</sub>O<sub>16</sub> cluster.

With one hydroxyl group and one gold-hydrogen group (**Figure 70b**), the aldehyde group oxygen-gold distance was is 3.480 Å, and the aldehyde group oxygen-hydrogen distance is 1.999 Å. This system was 5 kJ mol<sup>-1</sup> higher in energy than chemisorbed state of ethylene glycol for a total of 3 kJ mol<sup>-1</sup> lower in energy than the initial adsorbed state of ethylene glycol over the Au<sub>38</sub>O<sub>16</sub> cluster.

4.4.4. O-H and C-H Activation Energy Barriers with the Au<sub>38</sub>O<sub>16</sub> Cluster

**Figure 71:** The transition state geometry of O-H activation of ethylene glycol over the Au<sub>38</sub>O<sub>16</sub> cluster.

At the transition state geometry (**Figure 71**) the O-Au distance is 2.251 Å, the H-O distance is 1.279 Å and the alcohol group O-H distance is 1.160 Å. A vibrational frequency calculation on this structure gives a single imaginary mode. Visualisation of this imaginary mode shows it to be of hydrogen transfer between the alcohol group oxygen atom and an oxygen atom on the surface of the cluster.

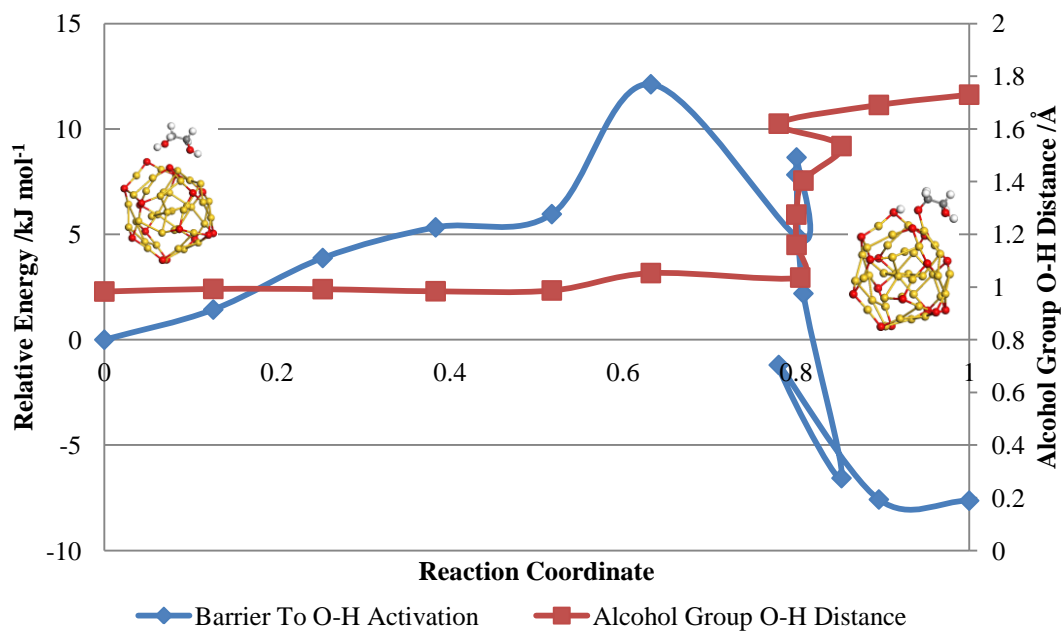


**Figure 72:** Graph showing the barrier to O-H activation of ethylene glycol over an  $\text{Au}_{38}\text{O}_{16}$  cluster.

The energy of the refined transition state of O-H activation over the  $\text{Au}_{38}\text{O}_{16}$  cluster (**Figure 72**) is  $8.6 \text{ kJ mol}^{-1}$  higher than the starting point. The energy of the ending point is  $-7.6 \text{ kJ mol}^{-1}$  lower than the starting point. With the zero point correction these values become  $-3.5 \text{ kJ mol}^{-1}$  and  $-9.5 \text{ kJ mol}^{-1}$  respectively. For the initial part of the barrier there is little change in the O-H distance as the ethylene glycol molecule rearranges itself with respect to the gold cluster, however during dissociation of the hydrogen atom there is significant rearrangement of nearby gold atoms and reorientation of the ethylene glycol molecule resulting in the unusual shape of the barrier.

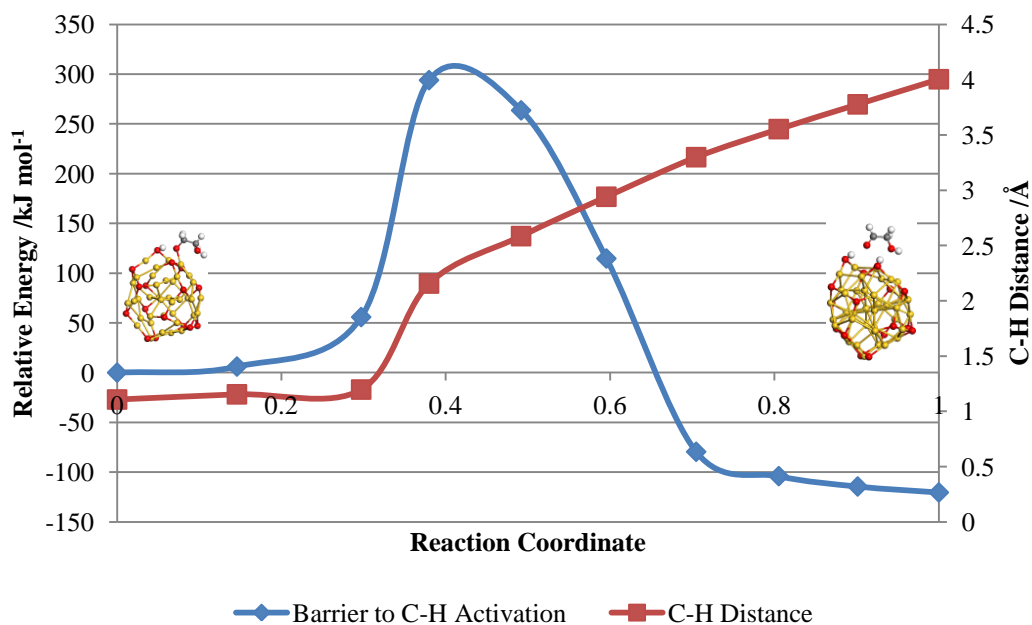


**Figure 73:** Graph showing the barrier to C-H activation following O-H activation of ethylene glycol over the  $\text{Au}_{38}\text{O}_{16}$  cluster. The hydrogen atom is adsorbed to an oxygen atom.

The barrier to C-H activation following O-H activation of ethylene glycol over the  $\text{Au}_{38}\text{O}_{16}$  cluster with the second hydrogen also adsorbing to an oxygen atom (**Figure 73**) is very large at  $294 \text{ kJ mol}^{-1}$ . For the first three images of the barrier the ethylene glycol molecule rotates to bring the dissociating hydrogen atom closer the oxygen atom it will adsorb to before it begins to dissociate the hydrogen atom. This however does not bring the hydrogen atom close enough to the oxygen atom and consequently this results in the hydrogen atom being in free space for the next three images which is a very energetically unfavourable state. In the last four frames the hydrogen atom is close enough to bond to the oxygen atom which is much more favourable and results in a significantly lower energy ending state of  $-120 \text{ kJ mol}^{-1}$ .

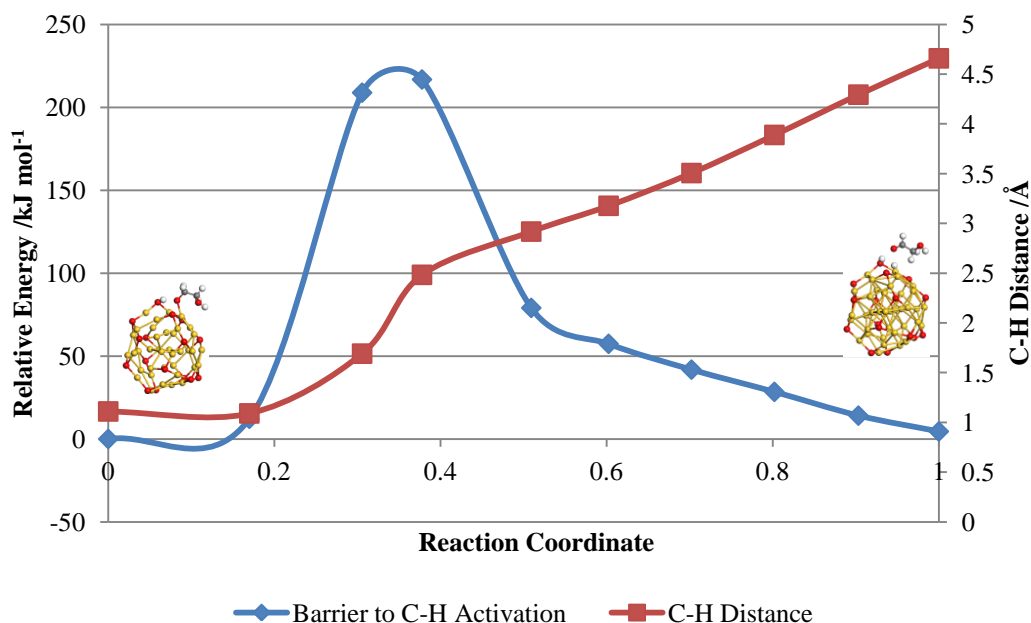


**Figure 74:** Graph showing the barrier to C-H activation following O-H activation of ethylene glycol over the  $\text{Au}_{38}\text{O}_{16}$  cluster. The hydrogen atom is adsorbed to a gold atom.

The barrier to C-H activation following O-H activation of ethylene glycol over the  $\text{Au}_{38}\text{O}_{16}$  cluster with the second hydrogen adsorbing to a gold atom (**Figure 74**) is very large at  $217 \text{ kJ mol}^{-1}$ . For the first two images of the barrier the ethylene glycol molecule rotates to bring the dissociating hydrogen atom closer the gold atom it will adsorb to before it begins to dissociate the hydrogen atom. As with adsorption to the oxygen atom, this rotation does not bring the hydrogen atom close enough to the oxygen atom and consequently this results in the hydrogen atom being in free space for the next two images which is a very energetically unfavourable state. In the remaining images the hydrogen atom is now close enough to be bonded to the gold atom which results in a lowering of energy and the ending state is only  $3 \text{ kJ mol}^{-1}$  higher than the starting state.

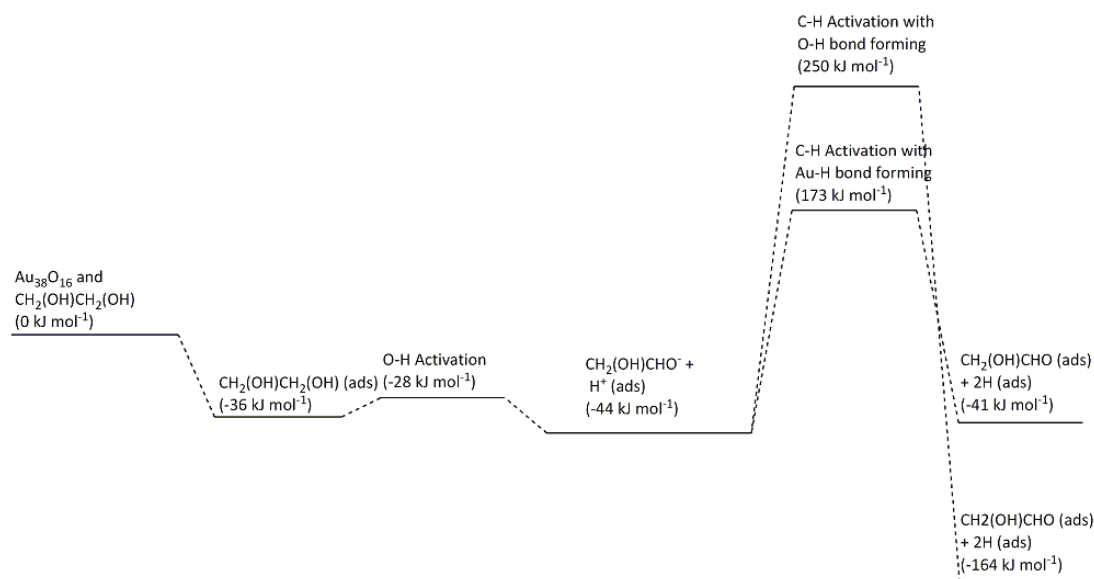


**Figure 75:** Diagram showing the relative energies of each step in the oxidation of ethylene glycol to hydroxyethanal on an  $\text{Au}_{38}\text{O}_{16}$  cluster.

This data suggests (**Figure 75**) that while the ending states for C-H activation following O-H activation of ethylene glycol are very favourable compared to the starting state, the barriers to C-H activation are very high in energy. This is due to the hydrogen atom moving through free space and consequently these are unlikely to occur in reality. The presence of a solvent (such as water) may stabilise the system and reduce the barriers to C-H activation.

#### 4.5. Conclusions

The surface energy of  $\text{Al}_2\text{O}_3$  (0001) is higher than that of the other oxide surfaces studied (**Table 11**). This is due to presence of three coordinated aluminium atoms at the exposed face, while in the bulk structure the aluminium atoms are six coordinated. Compared to the MgO (100) and (130) surfaces the atoms at the exposed face are four or five coordinated and six coordinated in the bulk structure. In the PdO (101) surface the atoms at the exposed face are three or four coordinated, while in the bulk structure they are all four coordinated.

**Table 11:** The surface energies of the different surfaces studied.

Surface	Surface Energy / $\text{J m}^{-2}$
MgO (100)	0.88
MgO (130)	1.07
$\text{Al}_2\text{O}_3$ (0001)	1.53
PdO (101)	0.97

Adsorption of ethylene glycol is most favourable on the Al<sub>2</sub>O<sub>3</sub> (0001) surface, followed by the 3c3c configuration on the PdO (101) surface (**Table 12**). This is due to both alcohol groups adsorbing to two under-coordinated metal atoms which are acting as Lewis acid sites by accepting electron density from the ethylene glycol molecule. In addition, when the alcohol groups adsorb to the undercoordinated metal atoms, the metal atoms attain a configuration closer to what is found in the bulk material (i.e. the three coordinated Al and Pd atoms become four coordinated).

**Table 12:** Table listing the adsorption energy of ethylene glycol on the different surfaces studied. Values in brackets indicate the adsorption energy without a U correction.

System	Adsorption Energy /kJ mol <sup>-1</sup>
MgO (100) gauche	-92
MgO (100) staggered	-46
MgO (130) parallel to the step	-93
MgO (130) perpendicular to the step	-84
MgO (130) bottom terrace site	-99
MgO (130) top terrace	-51
Al <sub>2</sub> O <sub>3</sub> (0001)	-168
PdO (101) 3c3c	-135 (-105)
PdO (101) 3c4c	-91 (-45)
PdO (101) 4c4c	-6 (9)
Au <sub>38</sub>	-34
Au <sub>38</sub> O <sub>16</sub>	-36

The transition state for O-H activation typically occurs when the O-H distance involving both the surface oxygen and the alcohol group (or water) oxygen atom is typically between 1.1 Å and 1.4 Å (**Table 13**). The Au<sub>38</sub> cluster shows the highest barrier to O-H activation, but this is due to the hydrogen atom being located further away from both the surface of the cluster and the ethylene glycol molecule than for the other systems studied, and the initial adsorption geometry not being ideal for O-H activation. For the other surfaces studied the barriers to O-H activation are lower or even negative.

**Table 13:** Table listing the transition state energy of ethylene glycol O-H activation and the hydrogen distances at the transition state on the different surfaces studied. Bracketed values indicate the zero point corrected energy.

System	Transition State Energy /kJ mol <sup>-1</sup>	Alcohol Group O-H Distance At Transition State /Å	Hydrogen – Surface Distance /Å
MgO (100) (gauche)	8.3 (-4.7)	1.208	1.252
MgO (130) parallel to the step	40.7 (28.3)	1.146	1.511
MgO (130) perpendicular to the step	7.1 (-2.2)	1.295	1.211
MgO (130) bottom terrace site	-13.1 (-23.4)	1.131	1.489
MgO (130) top terrace	21.5 (7.7)	1.416	1.142
Al <sub>2</sub> O <sub>3</sub> (0001)	45.5 (44.3)	1.266	1.312
Al <sub>2</sub> O <sub>3</sub> and 4 H <sub>2</sub> O	-0.9 (-10.5)	1.217	1.219
PdO (101) 3c4c	14.3 (-0.3)	1.192	1.309
Au <sub>38</sub>	107.5 (89.2)	1.577	1.650
Au <sub>38</sub> O <sub>16</sub>	8.6 (-3.5)	1.160	1.279

C-H activation is significantly more difficult or not possible over many of the metal oxide surfaces studied, whether attempted as a first or second step in the oxidation of ethylene glycol. This is due to the C-H bond being stronger than the O-H bond. In addition when the hydrogen atom is removed from the alcohol group the oxygen atom will coordinate to a metal atom in the surface. This has the effect of bringing the coordination of the metal atom closer to that which it would have in the bulk material which is a more stable and energetically favourable arrangement. Due to steric hindrance from the alcohol group, the carbon atom has difficulty coordinating to atoms in the surface when a hydrogen atom has been removed. In many of the C-H activation calculations the hydrogen atom has to move a greater distance to the surface than it does in the O-H activation calculations. As a result the hydrogen atom will be in a location where it is not bonded to any other atoms which is a very energetically unfavourable arrangement. When C-H activation is attempted as a second step the hydrogen atom will be carrying some negative charge as it leaves the carbon atom. Placing this hydrogen atom onto a negatively charged oxygen atom on a surface is an energetically unfavourable arrangement. However it is possible to place the hydrogen atom onto a metal atom on one of the reducible surfaces (PdO, Au<sub>38</sub> or Au<sub>38</sub>O<sub>16</sub>) as they are capable of accepting additional electron density,

although the energy of the ending state is higher than that of the starting state. The barriers to C-H activation over palladium oxide and the Au<sub>38</sub> cluster (**Table 14**) are larger than for O-H activation, but not so large that they are unlikely to occur in reality. The barriers to C-H activation on the Au<sub>38</sub>O<sub>16</sub> cluster are extremely large (200-300 kJ mol<sup>-1</sup>), but this is due to the hydrogen atom moving through free space and consequently these are unlikely to occur in reality.

**Table 14:** Table listing the transition state energy of ethylene glycol C-H activation and the hydrogen distances at the transition state on the different surfaces studied. Bracketed values indicate the zero point corrected energy.

System	Transition State Energy /kJ mol <sup>-1</sup>	C-H distance /Å	Hydrogen – Surface Distance /Å
PdO (101) 3c4c	63 (49)	1.574	1.772
Au <sub>38</sub>	68 (50)	1.679	1.746

It should also be noted that in many of the barriers there is a lowering or raising of energy prior to bond breaking occurring. This is due to reorientation of the ethylene glycol molecule over the surface as the minimum energy arrangement for adsorption is often not the same as the ideal arrangement for O-H or C-H activation, and hence the ethylene glycol molecule has to move to find this arrangement.

Given that some of the transition states for O-H activation are lower in energy than the starting geometries it suggests that while a local minimum has been found there are other local minima nearby on the potential energy surface which are found by other images in the barrier calculations, and some of these may be more suitable as starting points for barrier calculations. It is not practical (particularly for systems involving many atoms) to manually explore the potential energy surface to find the most appropriate local minimum, and therefore other methods such as molecular dynamics should be used. *Ab initio* molecular dynamics is still computationally very expensive, but classical molecular dynamics is much faster even for large numbers of atoms. The challenge therefore comes in developing suitable potentials for all possible interactions between atoms. Once the classical molecular dynamics simulation has been performed the data can then be analysed to determine where and in what configuration the adsorbate molecule spends most of its time, and this should provide a starting point for higher accuracy calculations. It is also possible to perform a series of single point energy calculations on different adsorption

configurations to determine which ones might be more favourable and hence more suitable to perform more computationally expensive calculations on, although there is no guarantee of finding all possible adsorption configurations this way.

**Table 15:** Table showing which steps are possible (✓) and which are not (✗) for the different materials studied in the oxidation of ethylene glycol to hydroxyethanal.

Surface	Adsorption	O-H Activation	C-H Activation	Oxidation to Hydroxyethanal
MgO (100)	✓	✓	✗	✗
MgO (130)	✓	✓	✗	✗
Al <sub>2</sub> O <sub>3</sub> (0001)	✓	✓	✗	✗
PdO (101)	✓	✓	✓	✓
Au <sub>38</sub>	✓	✗	✓	✗
Au <sub>38</sub> O <sub>16</sub>	✓	✓	✗	✗

**Table 15** summarises which steps are possible and which are not for the oxidation of ethylene glycol to hydroxyethanal. It shows that adsorption is favourable for all materials studied, O-H activation is possible for every material except the Au<sub>38</sub> cluster, C-H activation is only possible for the PdO (101) surface and the Au<sub>38</sub> cluster. Therefore the only material that can catalyse the oxidation of ethylene glycol to hydroxyethanal is palladium oxide.

The data collected in this chapter suggests that O-H activation of ethylene glycol is thermodynamically favourable and has a low barrier on the magnesium oxide and aluminium oxide surfaces, however C-H activation is either not possible or thermodynamically unfavourable on these surfaces. This indicates that in isolation neither surface is capable of catalysing the oxidation of ethylene glycol to hydroxyethanal. The Au<sub>38</sub> cluster shows a large barrier for O-H activation but a more reasonable barrier for C-H activation, as well as ending states for both dissociations being thermodynamically unfavourable. At the transition states the dissociating hydrogen atom is a long way from both the ethylene glycol molecule and the gold cluster which is a very energetically unfavourable state, and it is possible that more favourable transition state geometries exist based on different initial adsorption geometries, but these have yet to be found. The Au<sub>38</sub>O<sub>16</sub> cluster shows a small barrier

to O-H activation and the end point is thermodynamically favourable, however the C-H activation energy barriers are very high. This is again due to the dissociating hydrogen atom being far away from both ethylene glycol and the  $\text{Au}_{38}\text{O}_{16}$  cluster. The end points are however thermodynamically favourable. The palladium oxide (101) surface appears to be the most suitable as a catalyst for the oxidation of ethylene glycol to hydroxyethanal as both the O-H and C-H activation energy barriers are reasonable and the ending state of physisorbed hydroxyethanal and two chemisorbed hydrogen atoms is thermodynamically favourable compared to the starting state of physisorbed ethylene glycol. This data is consistent with experimental work where the oxidation of an alcohol is possible using a supported transition metal catalyst (like Au/MgO or Pd/Al<sub>2</sub>O<sub>3</sub>), but the reaction is very slow or not possible when only the support material is used [40] [41] [42].

## Bibliography

- [1] G. Kresse and J. Hafner, *Phys. Rev. B.*, vol. 47, p. 558, 1993.
- [2] D. R. Lide, Ed., CRC Handbook of Chemistry and Physics, 86 ed., Boca Raton: Taylor & Francis, 2005, pp. 8-42.
- [3] G. L. Brett, Q. He, C. Hammond, P. J. Miedziak, N. Dimitratos, M. Sankar, A. A. Herzing, M. Conte, J. A. Lopez-Sanchez, C. J. Kiely, D. W. Knight, S. H. Taylor and G. J. Hutchings, *Angew. Chem. Int. Ed.*, vol. 50, p. 10136, 2011.
- [4] S. F. J. Hackett, R. M. Brydson, M. H. Gass, I. Harvey, A. D. Newman, K. Wilson and A. F. Lee, *Angew. Chem.*, vol. 119, p. 8747, 2007.
- [5] M. Boronat, A. Corma, F. Illas, J. Radilla, T. Rodenas and M. J. Sabater, *Journal of Catalysis*, vol. 278, p. 50, 2011.
- [6] T. Kotionova, C. Lee, P. J. Miedziak, N. F. Dummer, D. J. Willock, A. F. Carley, D. J. Morgan, D. W. Knight, S. H. Taylor and G. J. Hutchings, *Catal. Lett.*, vol. 142, p. 1114, 2012.
- [7] M. Bornat and A. Corma, *Journal of Catalysis*, vol. 284, p. 138, 2011.
- [8] M. Conte, H. Miyamura, S. Kobayashi and V. Chechik, *J. Am. Chem. Soc.*, vol. 131, p. 7189, 2009.
- [9] J. P. Perdew and Y. Wang, *Phys. Rev. B.*, vol. 45, p. 13244, 1992.
- [10] J. P. Perdew, K. Burke and M. Ernzerhof, *Phys. Rev. Lett.*, vol. 77, p. 3865, 1996.
- [11] B. Hammer, L. B. Hansen and J. K. Nørskov, *Phys. Rev. B.*, vol. 59, p. 7413, 1999.
- [12] C. Adamo and V. Barone, *J. Chem. Phys.*, vol. 110, p. 6158, 1999.
- [13] A. V. Krukau, O. A. Vydrov, A. F. Izmaylov and G. E. Scuseria, *J. Chem.*

*Phys.*, vol. 125, p. 224106, 2006.

- [14] R. W. G. Wyckoff, *Crystal Structure*, New York: Wiley, 1963.
- [15] R. C. Whited, C. J. Flaten and W. C. Walker, *Solid State Commun.*, vol. 13, p. 1903, 1973.
- [16] D. Waroquiers, A. Lherbier, A. Miglio, M. Stankovski, S. Poncé, M. J. T. Oliveira, M. Giantomassi, G. Rignanese and X. Gonze, *Phys. Rev. B.*, vol. 87, p. 075121, 2013.
- [17] R. F. W. Bader, *Atoms In Molecules: A Quantum Theory*, New York: Oxford University Press, 1990.
- [18] G. Henkelman, A. Arnaldsson and H. Jónsson, *Comput. Mater. Sci.*, vol. 36, p. 254, 2006.
- [19] E. Sanville, S. D. Kenny, R. Smith and G. Henkelman, *J. Comp. Chem.*, vol. 28, p. 899, 2007.
- [20] W. Tang, E. Sanville and G. Henkleman, *J. Phys.: Condens. Matter.*, vol. 21, p. 084204, 2009.
- [21] A. Kiejna, T. Pabisiak and S. W. Gao, *J. Phys: Condens. Matter*, vol. 18, p. 4207, 2006.
- [22] K. L. Howard and D. J. Willock, *Faraday Discuss.*, vol. 152, p. 135, 2011.
- [23] M. Calatayud, *Catalysis Today*, vol. 152, p. 88, 2010.
- [24] H. Jonsson, G. Mills and K. W. Jacobsen, *Classical And Quantum Dynamics In Condensed Phase Simulations*, B. J. Byrne, G. Ciccotti and D. F. Coker, Eds., World Scientific, 1998, p. 385.
- [25] R. E. Newnham and Y. M. de Haan, *Zeitschrift fuer Kristallographie, Kristallgeometrie, Kristallphysik, Kristallchemie*, vol. 117, p. 235, 1962.

- [26] C. E. Housecroft and E. C. Constable, *Chemistry* 2nd Edition, Harlow: Prentice Hall, 2002, p. 618.
- [27] M. Aguilar-Frutis, M. Garcia and C. Falcony, *Applied Physics Letters*, vol. 72, p. 1700, 1998.
- [28] C. Li and P. Choi, *J. Phys. Chem. C*, vol. 111, p. 1747, 2007.
- [29] T. J. Godin and J. P. LaFemina, *Phys. Rev. B.*, vol. 49, p. 7691, 1993.
- [30] J. W. Elam, C. E. Nelson, M. A. Cameron, M. A. Tolbert and S. M. George, *J. Phys. Chem. B*, vol. 102, p. 7008, 1998.
- [31] V. Ranea, I. Carmichael and W. Schneider, *J. Phys. Chem. C*, vol. 113, p. 2149, 2009.
- [32] K. C. Hass, W. F. Schneider, A. Curioni and W. Andreoni, *J. Phys. Chem. B*, vol. 104, p. 5527, 2000.
- [33] P. Thissen, G. Grundmeier, S. Wippermann and W. G. Schmidt, *Phys. Rev. B.*, vol. 80, p. 245403, 2009.
- [34] P. O. Nilsson and M. S. Shivaraman, *J. Phys. C: Solid State Phys.*, vol. 12, p. 1423, 1979.
- [35] T. H. Fleisch and G. J. Mains, *J. Phys. Chem.*, vol. 90, p. 5317, 1986.
- [36] J. Wasser, H. A. Levy and S. W. Peterson, *Acta Crystallographica*, vol. 6, p. 661, 1953.
- [37] H. H. Kan and J. F. Weaver, *Surface Science*, vol. 602, p. L53, 2008.
- [38] C. Chizallet, G. Constantin, M. Che, F. Delbecq and P. Sautet, *J. Am. Chem. Soc.*, vol. 129, p. 6442, 2007.
- [39] X. Ding, Z. Li, J. Yang and Q. Zhu, *J. Chem. Phys.*, vol. 120, p. 9594, 2004.
- [40] G. J. Hutchings, G. L. Brett, Q. He, C. Hammond, P. J. Miedziak, N.

Dimitratos, M. Sankar, A. A. Herzing, M. Conte, J. A. Lopez-Sanchez, C. J. Kiely, D. W. Knight and S. H. Taylor, *Angew. Chem. Int. Ed.*, vol. 50, p. 10136, 2011.

[41] S. F. J. Hackett, R. M. Brydson, M. H. Gass, I. Harvey, A. D. Newman, K. Wilson and A. F. Lee, *Angew. Chem.*, vol. 119, p. 8747, 2007.

[42] B. Jørgensen, S. E. Christiansen, M. L. D. Thomsen and C. H. Christensen, *Journal Of Catalysis*, vol. 251, p. 332, 2007.

## Chapter 5 – Classical Molecular Dynamics Calculations

This chapter will cover the use of DLPOLY 4 [1] to perform classical molecular dynamics simulations on various water and methanol mixtures, as well water and methanol in the presence of a hydroxylated  $\alpha$ -Al<sub>2</sub>O<sub>3</sub> (0001) surface. DLPOLY is a very widely used classical molecular dynamics code that is freely available for academic use.

The efficiency of a catalyst can often depend on the solvents used in the reaction. If a solvent adsorbs more strongly to the catalyst surface than the molecule of interest this can lower the rate of reaction or even prevent the reaction from occurring entirely. Experimentally this can be measured by the ratio of NMR relaxation times  $T_1$  and  $T_2$ , which gives the relative strength of interaction with a surface of the two liquids.  $T_1$  and  $T_2$  are the longitudinal (parallel to the surface) and transverse (perpendicular to the surface) relaxation times respectively. For liquids with stronger surface interactions the  $T_1/T_2$  ratio will be larger. Mitchell *et al.* [2] have used this technique to measure the interaction strengths of water, 2-propanol and butanone with Ru/SiO<sub>2</sub> and Pd/Al<sub>2</sub>O<sub>3</sub> catalysts and it was found that water has the highest  $T_1/T_2$  ratio as it can hydrogen bond with hydroxyl groups present on the catalyst surface. 2-propanol has a weaker interaction than water, and butanone has weaker interaction still. For measurements on mixtures of liquids it was found that 2-propanol cannot completely displace water from the catalyst surface, but water can fully displace 2-propanol over the timescale of the experiment. This indicates that not only does water interact more strongly with the surface, but that it will inhibit the adsorption of alcohol molecules to the surface thus reducing the efficiency of the catalyst.

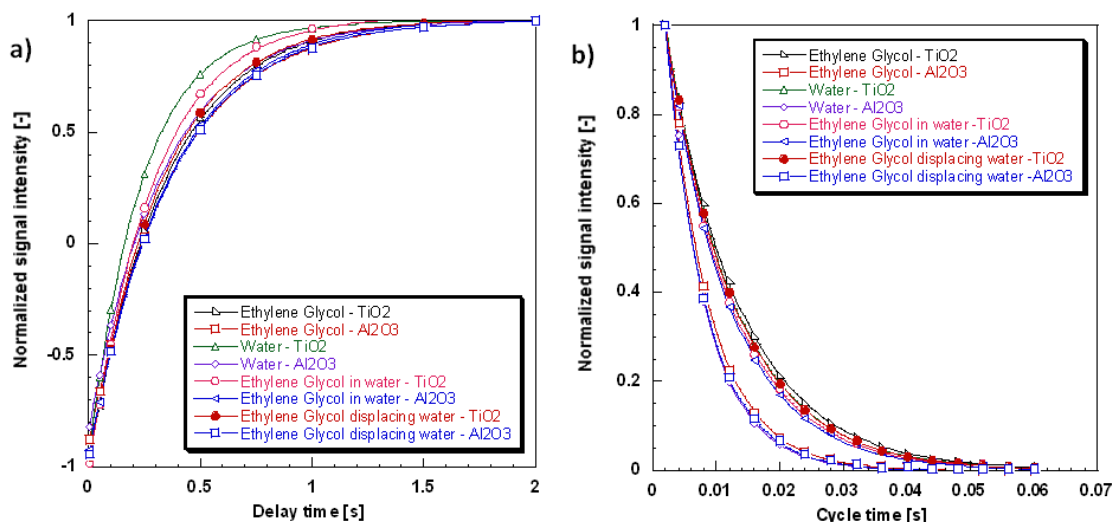


**Figure 1:** Graphs showing NMR relaxation times a)  $T_1$  and b)  $T_2$  for ethylene glycol and water mixtures over  $\text{Al}_2\text{O}_3$  and  $\text{TiO}_2$  surfaces. Data from Carmine D’Agostino, Cambridge.

The graphs shown in **Figure 1** show that ethylene glycol diffuses faster over the  $\text{Al}_2\text{O}_3$  surface than water, and hence water is more strongly bound to the surface. This means that water can displace ethylene glycol from the catalyst surface and inhibit the oxidation of the alcohol.

## 5.1. Water

### 5.1.1. Creating the Systems

C code was written to generate a cubic box of 1,000 TIP4P/2005 water molecules (see **Appendix 2**). This code was then modified to generate SPC/E water molecules and PCFF methanol. Subsequently the code was further modified to generate a randomly ordered cubic arrangement of methanol and water molecules with the concentration of methanol defined by the user, as well as adding water and methanol molecules to a user supplied surface.

### 5.1.2. TIP4P/2005 Water

The TIP4P/2005 [3] model was chosen to model water molecules as it is a commonly used model that gives results consistent with experimental data, such as a maximum density of  $999.972 \text{ kg m}^{-3}$  at 277 K [4]. It is a rigid, four body model. 1,000 water molecules were placed into a cubic box of side length  $31.034 \text{ \AA}$ . The starting volume of the box gives an initial density of  $1000 \text{ kg m}^{-3}$ .

To determine the appropriate barostat and thermostat time constants to use a series of NPT simulations (fixed number of particles, pressure and temperature) at 10 ps, 25 ps, 50 ps, 100 ps, 200 ps and 500 ps time constants were run at 200 K, 300 K and 400 K on a simulation cell of 1,000 TIP4P/2005 water molecules. A Nosé – Hoover barostat and thermostat [5] [6] was used. This barostat and thermostat was chosen because as it is widely used in literature for molecular dynamics simulations involving water, methanol [7] [8] and solid surfaces [9] [10]. The time constant determines how often energy is exchanged with a fictional heat bath to maintain system temperature and pressure. If the time constant is too low, energy will be exchanged more quickly than molecules in the system can move. If the time constant is too large however, energy cannot be exchanged at a sufficient rate to maintain system properties over the length of the simulation.

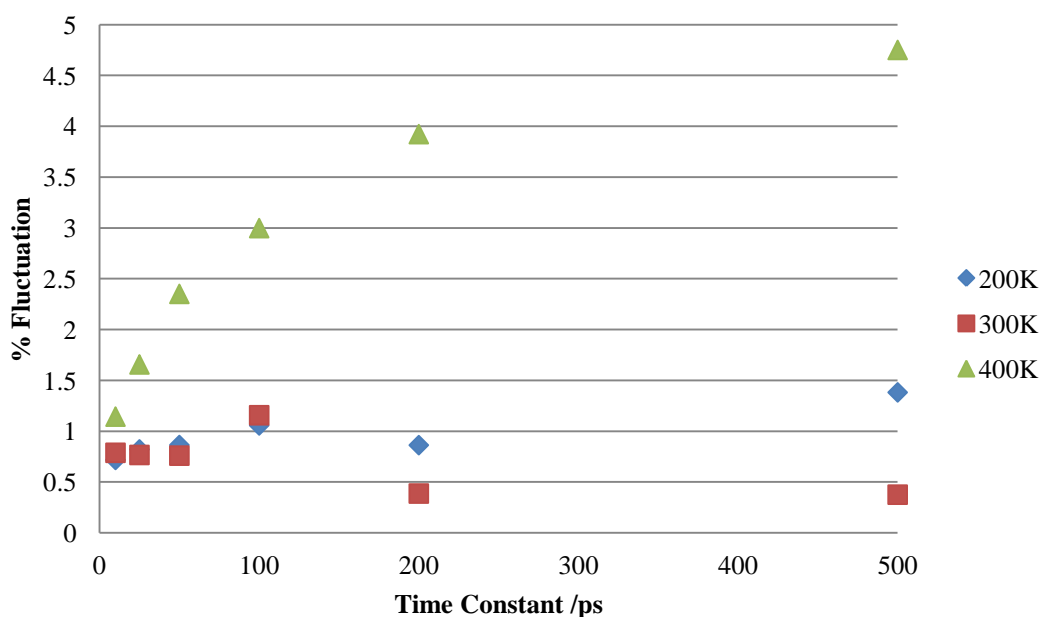


**Figure 2:** Graph showing the percentage fluctuation in system volume for different barostat time constants.

At higher temperatures a larger barostat time constant results in a larger fluctuation in system volume (**Figure 2**). However at lower temperatures there is little difference in fluctuations for smaller time constants. The fluctuations are calculated from the standard deviation in volume and temperature after the system has equilibrated.

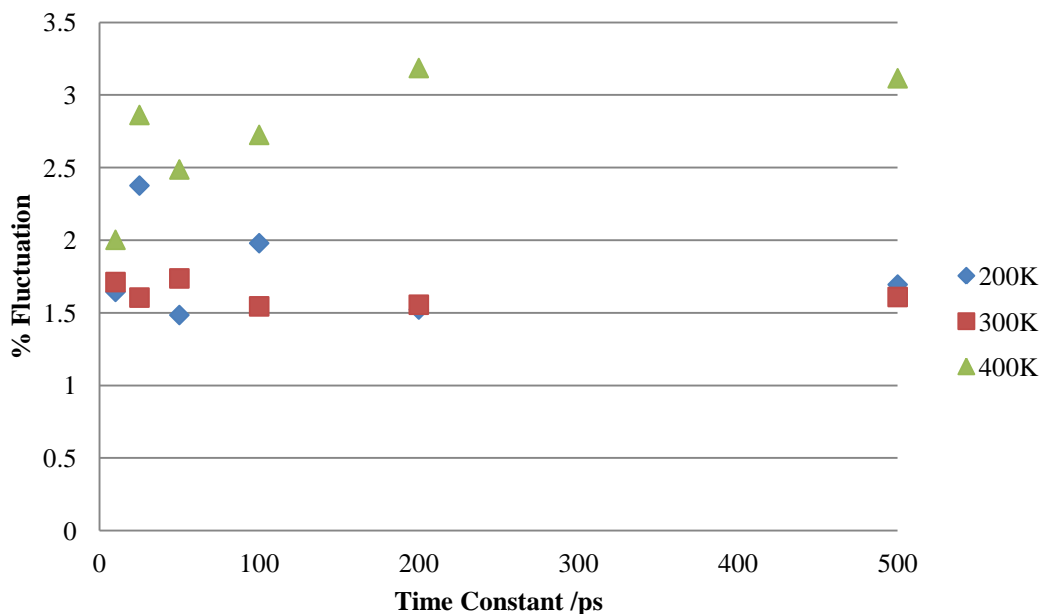


**Figure 3:** Graph showing the percentage fluctuation in system temperature for different thermostat time constants.

At higher temperatures a larger thermostat time constant results in a larger fluctuation in system temperature (**Figure 3**). At 200 K there is a greater fluctuation between different time constants. At 300 K the fluctuation is smallest at the 100 ps time constant.

All of the fluctuations calculated are small relative to the volume and temperature of the system with the smaller time constants showing smaller fluctuations. However the smaller time constants also show more rapid changes in volume and temperature which can lead to larger instantaneous errors. Therefore a barostat and thermostat time constant of 100 ps provides the best balance between accuracy and allowing energy to be exchanged between the system and the fictional heat bath at a reasonable rate.

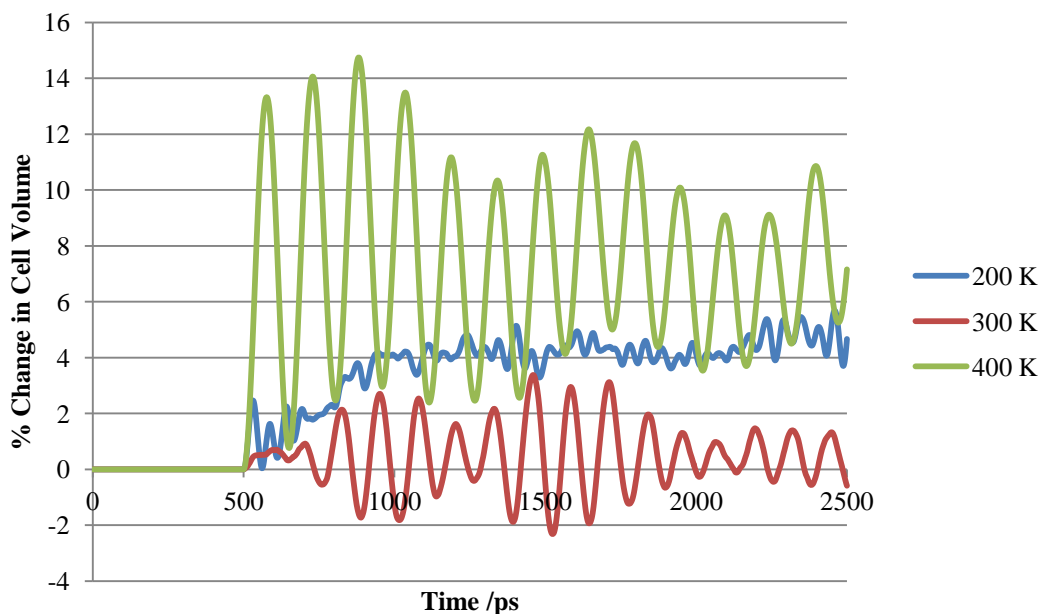


**Figure 4:** Graph showing the percentage change in cell volume as a function of time for 1,000 TIP4P/2005 water molecules at different temperatures with barostat and thermostat time constants of 100 ps. The initial cell volume was  $29890 \text{ \AA}^3$ .

At higher temperatures the cell volume is observed to fluctuate much more than at lower temperatures as more energy is exchanged with the fictional heat bath (**Figure 4**). The period of fluctuation corresponds approximately with the barostat and thermostat time constants of the simulation. The average volume is greatest at 400 K and lowest at 300 K. This is to be expected as water is most dense in its liquid state and less dense as a solid or gas at atmospheric pressure.

A series of NPT simulations were performed for a range of temperatures between 200 K and 400 K. The pressure was fixed at one atmosphere and a van der Waals cut off of  $8.5 \text{ \AA}$  was used for the intermolecular interactions. A Nosé – Hoover barostat and thermostat with time constants of 100 ps was used. A time step of 0.5 femtoseconds was used with total of 1,000,000 equilibration steps and 4,000,000 production steps giving a total simulation time of 2.5 nanoseconds. Data was sampled every 2,000 steps.

The data collected included system volume (allowing calculation of the mean density of the system) and radial distribution functions.

The mean density of the mixture in each simulation is determined by calculating the mass of the molecules in the simulation and time average of the volume of the

system after equilibration. The mass is then divided by the average volume to determine the mean density of the system. The error in density was calculated from the standard deviation in the volume of the system.

Density is given by:

$$\rho = \frac{m}{v} \quad (5.1)$$

And density as a function of time is given by:

$$\rho(t) = \frac{m}{v(t)} \quad (5.2)$$

Assuming that the mass of the system remains constant:

$$\langle \rho(t) \rangle = \left\langle \frac{m}{v(t)} \right\rangle = m \left\langle \frac{1}{v(t)} \right\rangle \quad (5.3)$$

Assuming that the variation in the volume as a function of time is small compared to the absolute value,  $v(t)$  can be written as sum of a constant term and its fluctuation:

$$v(t) = v_0 + \delta v(t) \quad (5.4)$$

If  $\delta v(t) \ll v_0$  then we can use the Taylor expansion:

$$\frac{1}{v(t)} = \frac{1}{v_0 + \delta v(t)} = \frac{1}{v_0 \left(1 + \frac{\delta v(t)}{v_0}\right)} = \frac{1}{v_0} \left(1 - \frac{\delta v(t)}{v_0}\right) \quad (5.5)$$

Therefore:

$$\left\langle \frac{1}{v(t)} \right\rangle = \frac{1}{v_0} \left(1 - \frac{\langle \delta v(t) \rangle}{v_0}\right) \quad (5.6)$$

Also as the volume fluctuations are as likely to be positive as negative:

$$\langle \delta v(t) \rangle = 0 \quad (5.7)$$

And so:

$$\langle \rho(t) \rangle = m \left\langle \frac{1}{v(t)} \right\rangle = \frac{m}{v_0} \quad (5.8)$$

This means that we can use the average volume in the calculation of the average density rather than taking the average of the inverse volume.

**Example for TIP4P/2005 water at 400 K:**

$$m = 3.00684 \times 10^{-23} \text{ kg}$$

$$v_0 = 32094 \text{ \AA}^3$$

$$\left\langle \frac{1}{v(t)} \right\rangle = 0.00003118 \text{ \AA}^{-3}$$

Dividing system mass by average volume:

$$\begin{aligned} \frac{m}{v_0} &= \frac{3.00684 \times 10^{-23}}{32094} = 9.3688 \times 10^{-28} \text{ kg \AA}^{-3} \\ &= 936.88 \text{ kg m}^{-3} \end{aligned}$$

Multiplying system mass by average inverse volume:

$$\begin{aligned} m \left\langle \frac{1}{v(t)} \right\rangle &= 3.00684 \times 10^{-23} \times 0.00003118 = 9.3748 \times 10^{-28} \text{ kg m}^{-3} \\ &= 937.48 \text{ kg m}^{-3} \end{aligned}$$

There is little difference in values between the two methods, and therefore either method is acceptable. We will use the average volume to calculate the average density of the systems being studied. This method also involves less manipulation of the raw data from DLPOLY.

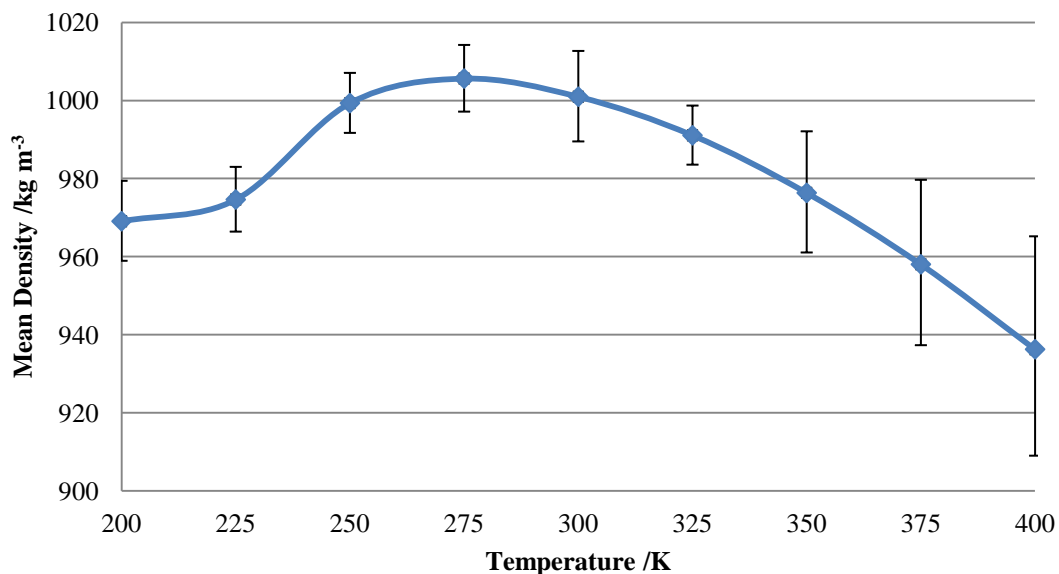


**Figure 5:** Graph showing the mean density of 1,000 TIP4P/2005 water molecules as a function of temperature. Data was sampled every 2,000 timesteps with each timestep being 0.5 fs for 1,000,000 equilibration steps and 4,000,000 production steps giving a total simulation time of 2.5 ns.

The maximum density of TIP4P/2005 water is predicted to be  $1005.615 \text{ kg m}^{-3}$  at approximately 275 K (**Figure 5**), these are very close to the experimental values of  $999.972 \text{ kg m}^{-3}$  and 277 K respectively [4].

At higher temperatures the error in the calculated density of water increases. This is due to the much greater fluctuations in volume at higher temperatures.

The radial distribution function (RDF) describes how the number density of particles varies as a function of distance from a central reference particle. Sharper peaks in the RDF indicate greater ordering in the structure of particles surrounding the central particle.

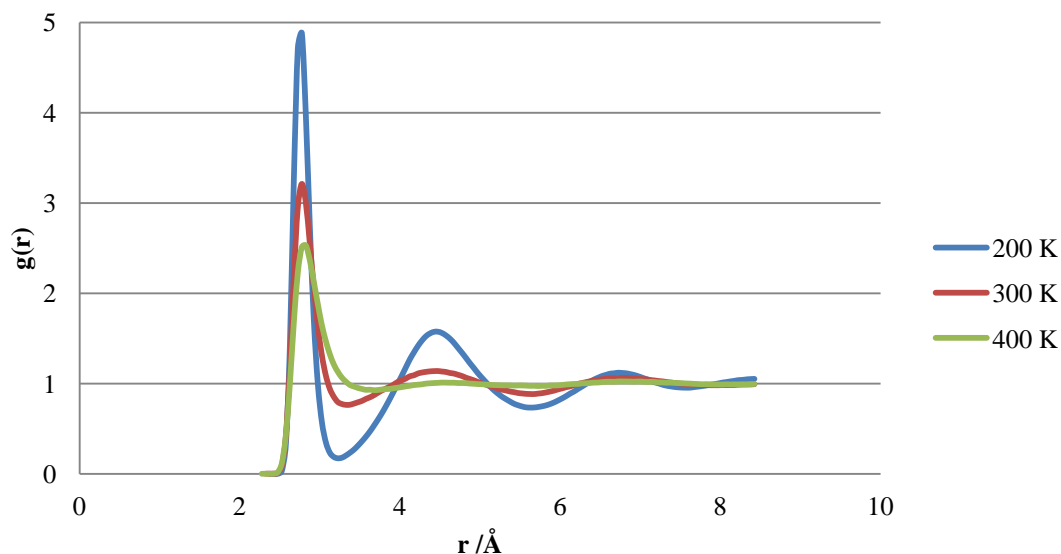


**Figure 6:** The oxygen-oxygen radial distribution function for 1,000 TIP4P/2005 water molecules, with a barostat time constant of 100 ps.

As the temperature increases so does the position of the first minima, indicating that at higher temperatures average oxygen – oxygen distance increases (**Figure 6**). The peaks also become broader as the temperature increases, indicating a less ordered structure as would be expected since solids are typically more ordered than liquids and gasses.

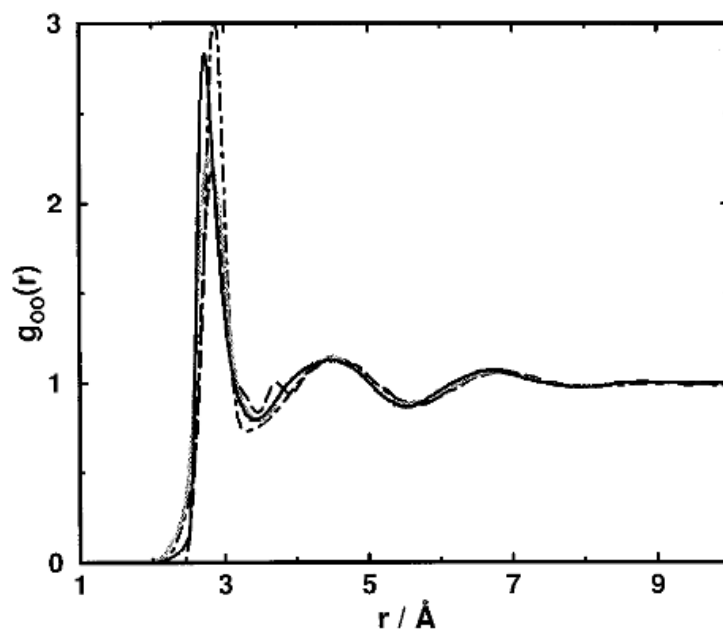


**Figure 7:** Experimental oxygen-oxygen radial distribution function for liquid water at ambient temperature determined by x-ray diffraction (solid line) from ref. [11].

The dashed line and dashed-dotted line indicate data from other x-ray and neutron diffraction experiments respectively.

Comparing simulations with experimental data (**Figure 6** and **Figure 7** respectively) the overall shape of the TIP4P/2005 oxygen – oxygen radial distribution function is consistent with the experimental data although the peak at 300 K is higher for the simulations. The experiments do not specify what temperature they were conducted at (other than ambient) although it is likely to be close to 300 K.

The normalised radial distribution function  $g(r)$  for a three dimensional system is defined by:

$$4\pi r^2 \rho g(r) \delta r = \frac{1}{N_f(N-1)} \sum_{frames} \sum_i \sum_{j \neq i} \delta(r - r_{ij}) \quad (5.9)$$

Where  $4\pi r^2 \rho \delta r$  is the volume of a spherical shell of radius  $r$  and  $\rho$  is the number density of particles in the system.

Provided that  $N$  is large, the right hand side of **Equation 5.9** is the number of particles found at a distance  $r$  averaged over the number of frames in the simulation and all of the atoms sampled.

To integrate the radial distribution function (which is generated as a series of discrete points) trapezoidal integration is needed, whereby the integral is approximated by the sum of a series of trapezia.

**Table 1:** Table showing the average number of oxygen – oxygen contacts in TIP4P/2005 water.

Temperature /K	Average Number Of Oxygen – Oxygen Contacts
200	2.03
300	2.30
400	2.79

**Table 1** shows that as the temperature increases the average number of oxygen – oxygen contacts also increases. This occurs because the water molecules are moving faster and are able to interact with more molecules in the system over the length of the simulation. At higher temperatures some of these interactions are likely to be repulsive collisions rather than attractive hydrogen bonding interactions.

### 5.1.3. SPC/E

The SPC/E [12] model was also chosen to model water molecules, as it is another commonly used model for the study of water systems. Unlike the TIP4P/2005 model the SPC/E model is a flexible three body model. 1,000 water molecules were placed into a cubic box of side length 31.034 Å. The starting volume of the box gives an initial density of approximately 1 g cm<sup>-3</sup>. The simulation parameters were exactly the same as was used with the TIP4P/2005 model. An NPT simulation (fixed number of particles, pressure and temperature) was performed for a series of temperatures between 200 K and 400 K. The pressure was fixed at one atmosphere and a van der Waals cut off of 8.5 Å was used for the intermolecular interactions. A Nosé – Hoover barostat and thermostat with time constants of 100 ps was used. A time step of 0.5 femtoseconds was used with total of 1,000,000 equilibration steps and 4,000,000 production steps giving a total simulation time of 2.5 nanoseconds. Data was sampled every 2,000 steps.

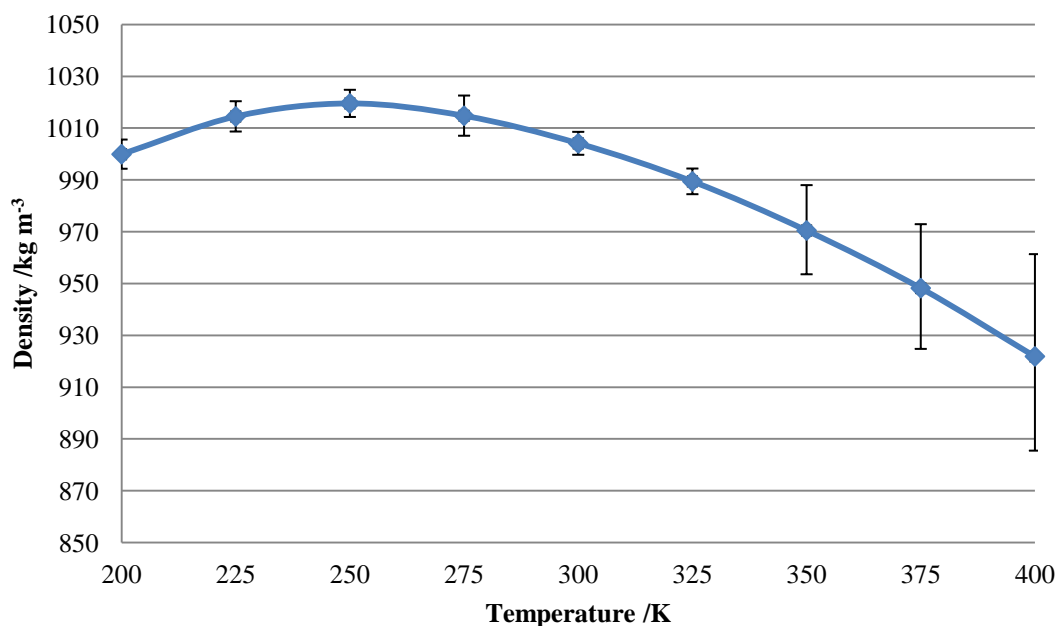


**Figure 8:** Graph showing the mean density of 1,000 SPC/E water molecules as a function of temperature. Data was sampled every 2,000 timesteps with each timestep being 0.5 fs for 1,000,000 equilibration steps and 4,000,000 production steps giving a total simulation time of 2.5 ns.

The maximum density of SPC/E water is 1019.461 kg m<sup>-3</sup> at approximately 250 K (**Figure 8**). The maximum is higher than both the experimental value and that of the

TIP4P/2005 model and the temperature at which it occurs is lower. The density was calculated in the same manner as for the TIP4P/2005 water simulations.

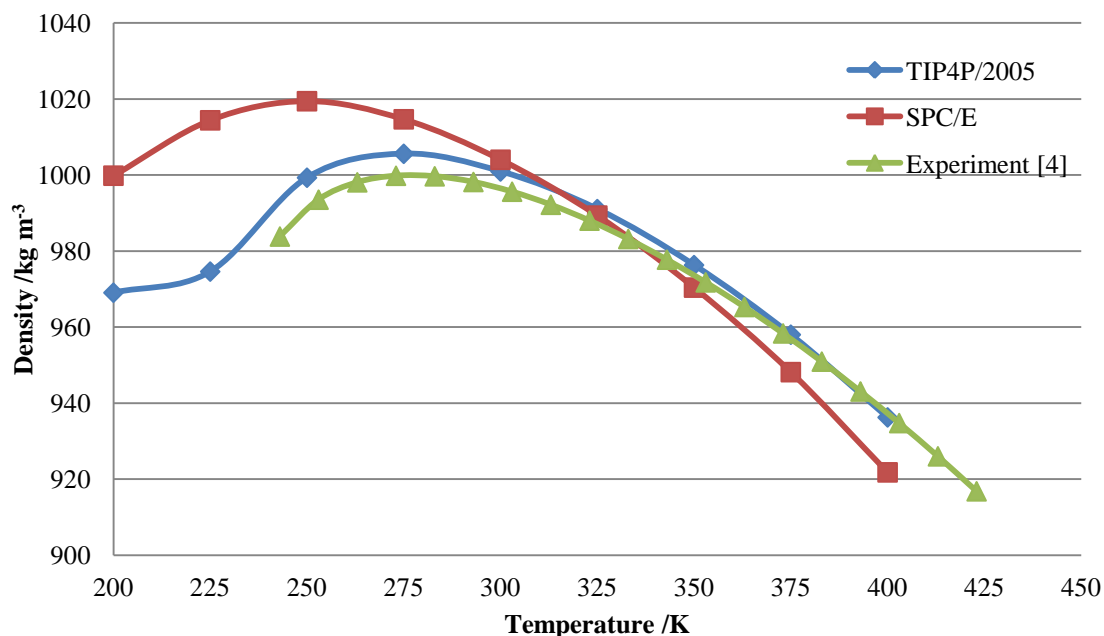


**Figure 9:** Graph comparing simulated TIP4P/2005 and SPC/E water with experimental data from ref. [4].

Comparing experimental data to the two water models (**Figure 9**) it is clear that TIP4P/2005 shows a density profile much closer to experiment than SPC/E over the temperature range studied. TIP4P/2005 is parameterised against a wide range of experimental data and is designed to be a generalised potential applicable to a wide variety of systems allowing it to generate a phase diagram very close to that determined experimentally. The geometry of the molecule is close to that observed experimentally, however it is a rigid model meaning that it cannot change shape during a simulation. In contrast SPC/E is parameterised against a smaller set of experimental data and does not generate a phase diagram that is as accurate. It is however a flexible model, but its equilibrium geometry is further away from the experimental value than TIP4P/2005. All together this results in TIP4P/2005 being a more accurate potential than SPC/E.

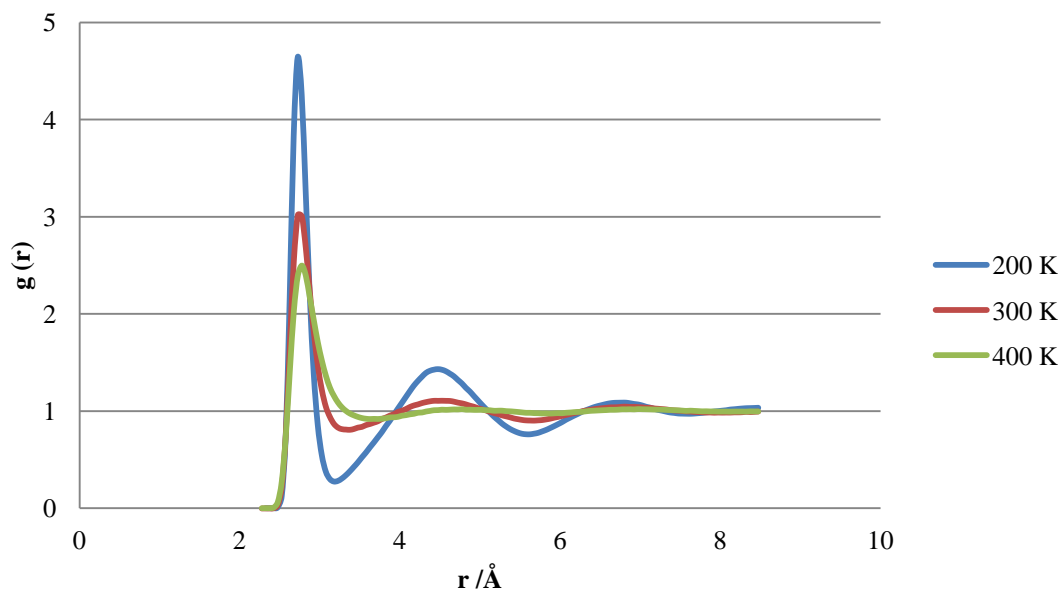


**Figure 10:** The oxygen-oxygen radial distribution function for 1,000 SPC/E water molecules.

As the temperature increases so does the position of the first minima, indicating that at higher temperatures average distance between molecules increases for SPC/E water (**Figure 10**). This is the same as has been observed for TIP4P/2005 water (**Figure 6**).

As described with the TIP4P/2005 model the radial distribution function was integrated to determine the average number of oxygen – oxygen contacts.

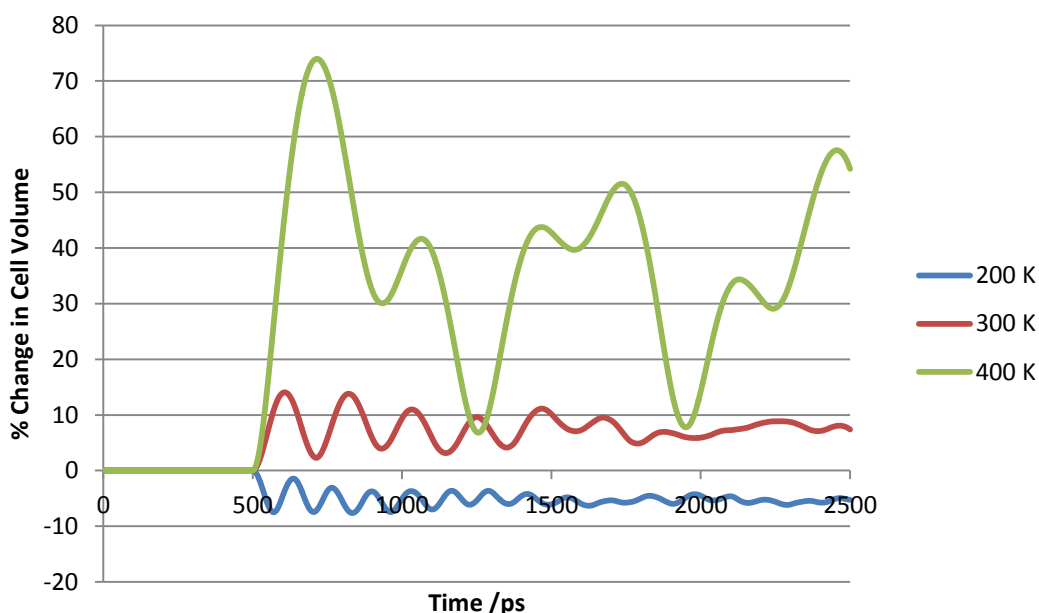
**Table 2:** Table showing the average number of oxygen – oxygen contacts in SPC/E water.

Temperature /K	Average Number Of Oxygen – Oxygen Contacts
200	2.03
300	2.41
400	2.86

**Table 2** shows that as the temperature increases so does the average number of oxygen – oxygen contacts in SPC/E water. At 200 K the average number of oxygen – oxygen contacts in SPC/E water is the same as for TIP4P/2005 water, however at 300 K and 400 K the average number is slightly higher for SPC/E water than TIP4P/2005 water.

## 5.2. Methanol

The PCFF model [13] was chosen to model methanol. 1,000 methanol molecules were placed into a cubic box of side length 40.6 Å. The starting volume of the box gives an initial density of 0.7918 g cm<sup>-3</sup>, the experimental density at 293 K [14]. An NPT simulation (fixed number of particles, pressure and temperature) was performed for a series of temperatures between 200 K and 400 K. The pressure was fixed at one atmosphere and a van der Waals cut off of 8.5 Å was used for the intermolecular interactions. A Nosé – Hoover barostat and thermostat with time constants of 100 ps was used. A time step of 0.5 femtoseconds was used with total of 1,000,000 equilibration steps and 4,000,000 production steps giving a total simulation time of 2.5 nanoseconds. Data was sampled every 2,000 steps.

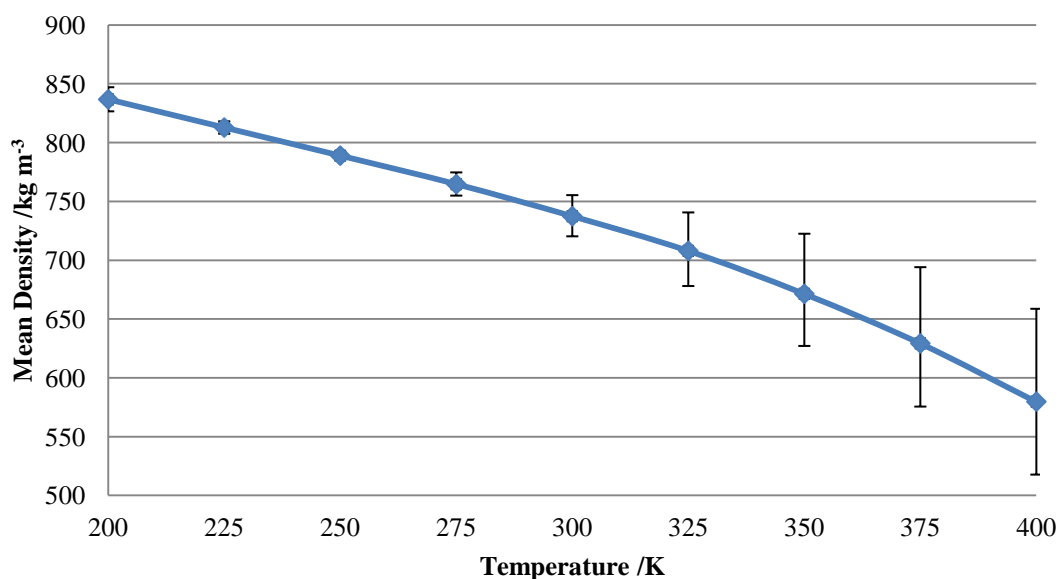


**Figure 11:** Graph showing the percentage change in cell volume as a function of time for 1,000 PCFF methanol molecules at different temperatures with barostat and thermostat time constants of 100 ps. The initial cell volume was 67109 Å<sup>3</sup>.

**Table 3:** Mean volumes of periodic simulation cells of 1,000 methanol molecules at different temperatures.

Temperature /K	Mean System Volume / $\text{\AA}^3$	Standard Deviation / $\text{\AA}^3$
200	63618	780
300	72185	1714
400	91815	11003

At lower temperature the fluctuations in the volume of the periodic cell are much smaller than at higher temperatures as at higher temperatures methanol is above its boiling point. In addition the size of the fluctuations decreases over time (**Figure 11** & **Table 3**). The period of fluctuations in cell volume is approximately the same as the barostat time constant of the simulation at 100 ps. This occurs because the system is responding to energy being exchanged to maintain system properties. For the 200 K and 300 K simulations the size of the fluctuations decreases over time as the system is stabilising and less energy needs to be exchanged.

**Figure 12:** The mean density of 1,000 methanol molecules as a function of temperature. Data was sampled every 2,000 timesteps with each timestep being 0.5 fs for 1,000,000 equilibration steps and 4,000,000 production steps giving a total simulation time of 2.5 ns.

At higher temperatures the error in the calculated density of methanol increases (**Figure 12**). This is due to the much greater fluctuations in volume at higher temperatures.

The density of PCFF methanol was calculated in the same manner as for the TIP4P/2005 and SPC/E simulations. There is no maximum in the density of methanol over the temperature range studied here, and the decrease in density of methanol over the temperature range studied here, and the decrease in density of methanol is linear up to 300 K. Above 300 K the decrease in density is more rapid as the temperature is close to and then exceeds the boiling point of methanol (338 K [14]), this is also the cause of the large fluctuations in volume.

### 5.2.1. Radial Distribution Functions

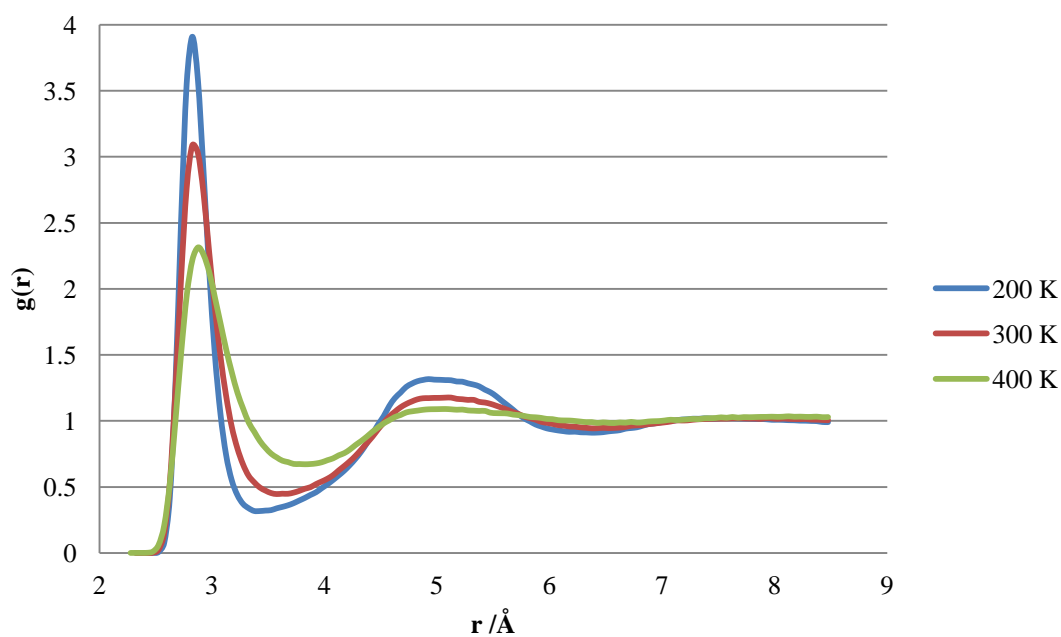


**Figure 13:** The oxygen-oxygen radial distribution function for methanol.

As with the two water models the position of the first minima moves to longer distances as the temperature increases, once again indicating that the hydrogen bond length is also increasing with temperature.

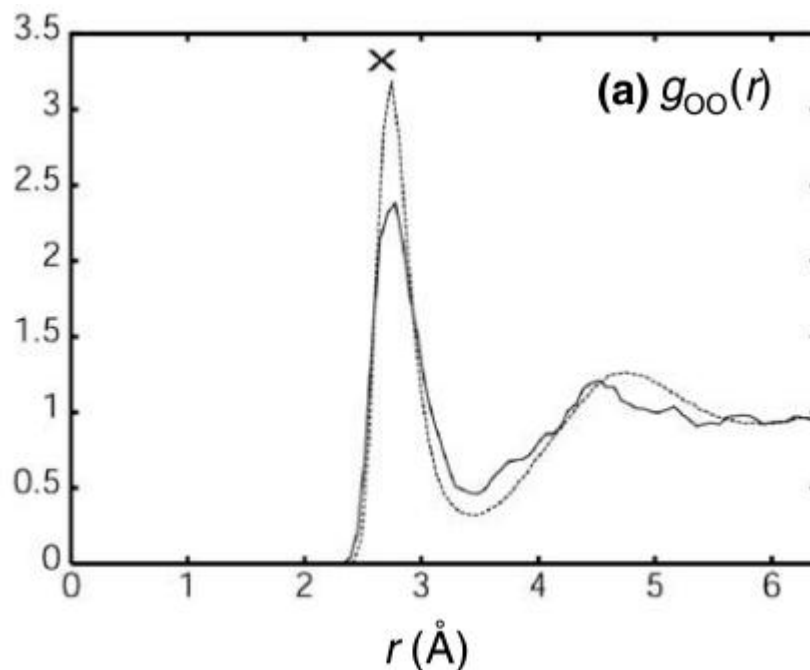


**Figure 14:** The oxygen-oxygen radial distribution function for methanol. The solid line indicates data from Car-Parrinello molecular dynamics [15] and the dotted line indicates data from neutron diffraction experiments [16]. The cross indicates the position of the first peak obtained from other classical molecular dynamics calculations [17].

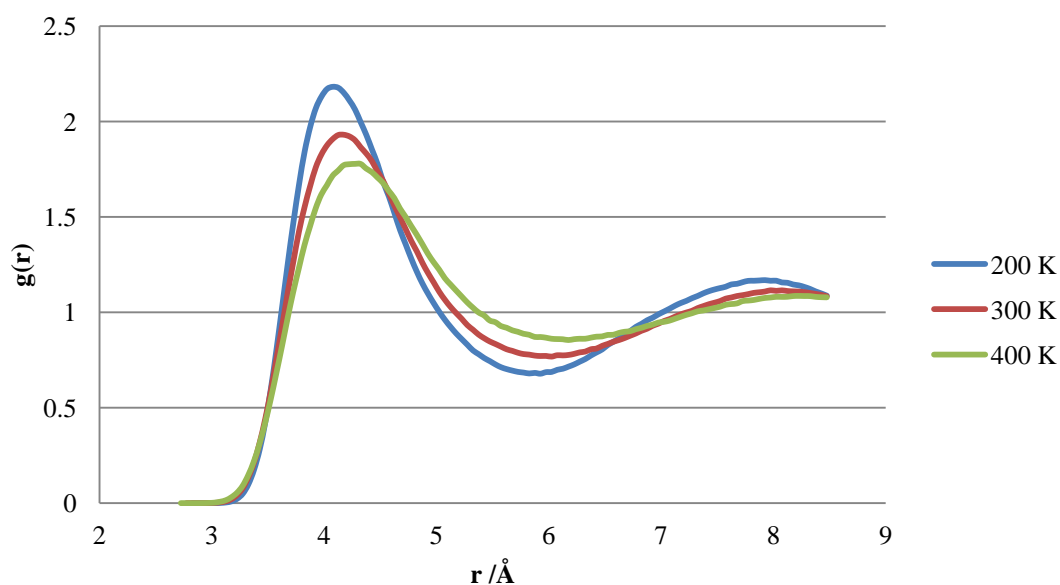
Comparing the radial distribution functions calculated from classical molecular dynamics (**Figure 13**) and those from Car-Parrinello molecular dynamics and experiment (**Figure 14**) the shape of the curve is similar but the peaks are higher in the classical calculations than the DFT calculations. However the classical results are very similar to the experimental results. The DFT calculations only used thirty two methanol molecules and the simulation length was only 6 ps. The authors suggest that the differences between DFT calculations, classical calculations and experiment are due to the small size of the system and larger simulations may produce more accurate results. In addition DFT does not typically model van der Waals interactions well and so the attractive forces between the molecules will be weaker, resulting in less structuring of the molecules.

The radial distribution function of PCFF methanol was integrated to determine the average number of oxygen – oxygen contacts between methanol molecules.

**Table 4:** Table showing the average number of oxygen – oxygen contacts in PCFF methanol.

Temperature /K	Average Number Of Oxygen – Oxygen Contacts
200	1.09
300	1.10
400	1.07

**Table 4** shows that average number of oxygen – oxygen contacts in PCFF methanol remains roughly constant at approximately 1.1.

**Figure 15:** The carbon – carbon radial distribution function for methanol.

The carbon – carbon radial distribution function (**Figure 15**) shows a much broader peak than the oxygen – oxygen radial distribution function. This suggests that the – OH group interaction (hydrogen bonding) in methanol is stronger than the methyl group interaction (van der Waals forces) as expected.

### 5.3. Water – Methanol Mixtures

#### 5.3.1. Combining the Potentials

The water molecules were modelled using the TIP4P/2005 model, the methanol molecules were modelled using the PCFF model and the hydroxylated Al<sub>2</sub>O<sub>3</sub> surface was modelled using the CLAYFF [18] model.

Van der Waals Interactions between these models are described by combining the TIP4P/2005, PCFF and van der Waals interactions according to the CLAYFF combining rules:

$$R_0 = \frac{1}{2}(R_a + R_b) \quad (5.10)$$

$$D_0 = \sqrt{D_a D_b} \quad (5.11)$$

However DLPOLY does not support potentials expressed in the form that the CLAYFF van der Waals interactions are given:

$$E_{VDW} = D_0 \left[ \left( \frac{R_0}{r} \right)^{12} - 2 \left( \frac{R_0}{r} \right)^6 \right] \quad (5.12)$$

Therefore the PCFF and TIP4P/2005 potentials are first converted to CLAYFF form and the combining rules are applied to generate the coefficients for all necessary pairs of atoms. These are then converted to a simple 12-6 potential for use in DLPOLY. Having all of the potentials in the same form makes them simpler to work with and compare values of the coefficients for the van der Waals interactions.

The PCFF van der Waals interactions are a 9-6 potential of the form:

$$E_{VDW} = \frac{E_0}{3} \left[ 6 \left( \frac{r_0}{r} \right)^9 - 9 \left( \frac{r_0}{r} \right)^6 \right] \quad (5.13)$$

In order to obtain compatible PCFF parameters in CLAYFF 12-6 form the van der Waals energy as a function of distance was generated as a series of points between 3 Å and 8 Å for each atom pair. Gnuplot was then used to fit a 12-6 curve to the data, and the new  $D_0$  and  $R_0$  coefficients are then read from the gnuplot output. Example plots for the oxygen – oxygen and carbon – carbon interactions are shown in **Figure 16** and **Figure 17** respectively. The 12-6 conversion does not provide an exact match for the original 9-6 potential as it is not possible to replicate a 9-6 potential with only

a 12-6 function. It does however provide a reasonable approximation, as the sum of the square errors are 0.004889 and 0.009983 for the oxygen – oxygen and carbon – carbon interactions respectively.

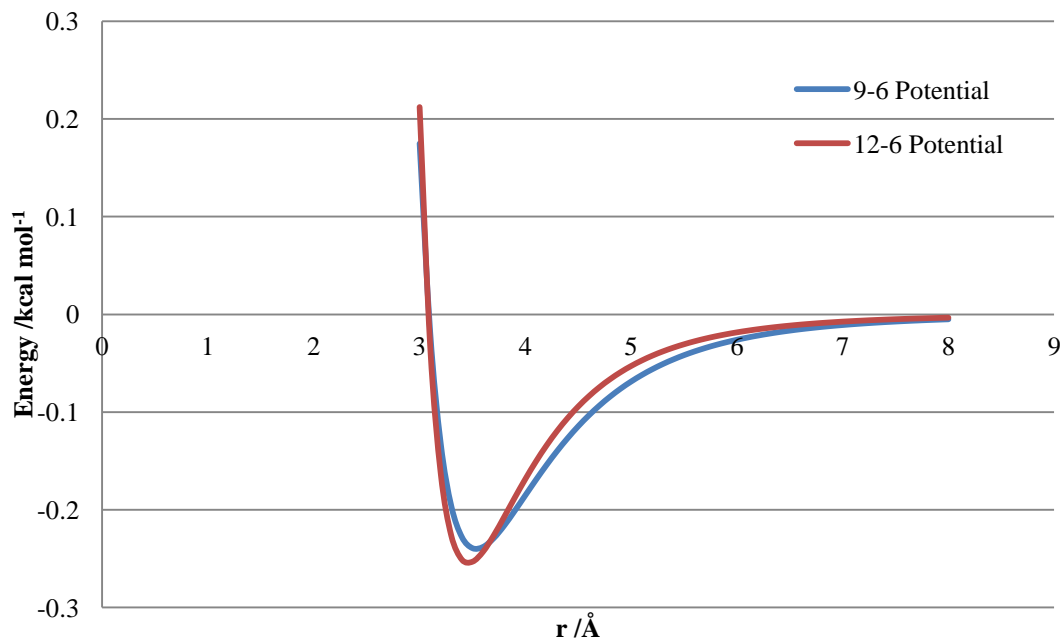


**Figure 16:** Graph showing the oxygen - oxygen van der Waals interaction for PCFF methanol. The original 9-6 potential is in blue and the converted 12-6 potential is in red.

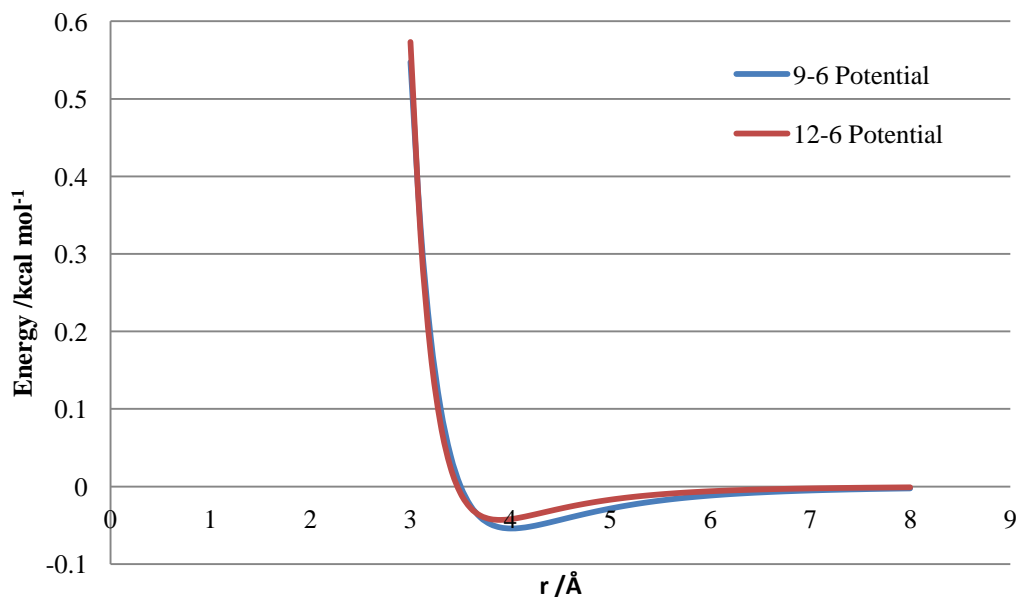


**Figure 17:** Graph showing the carbon - carbon van der Waals interaction for PCFF methanol. The original 9-6 potential is in blue and the converted 12-6 potential is in red.

The TIP4P/2005 van der Waals interactions are a Lennard-Jones potential of the form:

$$E_{VDW} = 4\varepsilon \left[ \left( \frac{\sigma}{r} \right)^{12} - \left( \frac{\sigma}{r} \right)^6 \right] \quad (5.14)$$

By equating coefficients it is found that:

$$\varepsilon = D_0 \quad (5.15)$$

$$\sigma = \left( \frac{1}{\sqrt[6]{2}} \right) R_0 \quad (5.16)$$

$E_0$ ,  $r_0$ ,  $\varepsilon$ ,  $\sigma$ ,  $D_0$  and  $R_0$  are all empirical parameters derived by fitting the models to experimental data.

Since all three potentials are of different forms in order to combine them, they must all be converted to the same form. In this case a simple 12-6 potential of the following form is used:

$$E_{VDW} = \frac{A}{r^{12}} - \frac{B}{r^6} \quad (5.17)$$

CLAYFF and TIP4P/2005 are simple to convert, with CLAYFF giving:

$$A = D_0 R_0^{12} \quad (5.18)$$

$$B = D_0 R_0^6 \quad (5.19)$$

And TIP4P/2005 giving:

$$A = 4\varepsilon\sigma^{12} \quad (5.20)$$

$$B = 4\varepsilon\sigma^6 \quad (5.21)$$

The values for all  $A$  and  $B$  parameters of the needed combinations of atoms are given in the example DLPOLY FIELD file shown in **Appendix 1**.

### 5.3.2. Simulating the Water – Methanol Mixtures

A series of randomly generated mixtures of 1,000 water and methanol molecules were generated with methanol concentrations between 2% and 98%. As with the pure water and pure methanol simulations, an NPT simulation (fixed number of particles, pressure and temperature) was performed for a series of temperatures

between 200 K and 400 K. The pressure was fixed at one atmosphere and a van der Waals cut off of 8.5 Å was used for the intermolecular interactions. A Nosé – Hoover barostat and thermostat with time constants of 100 ps was used. A time step of 0.5 femtoseconds was used with total of 1,000,000 equilibration steps and 4,000,000 production steps giving a total simulation time of 2.5 nanoseconds. Data was sampled every 2,000 steps.

The mean density of the system is calculated in the same manner as for the pure water and pure methanol simulations.

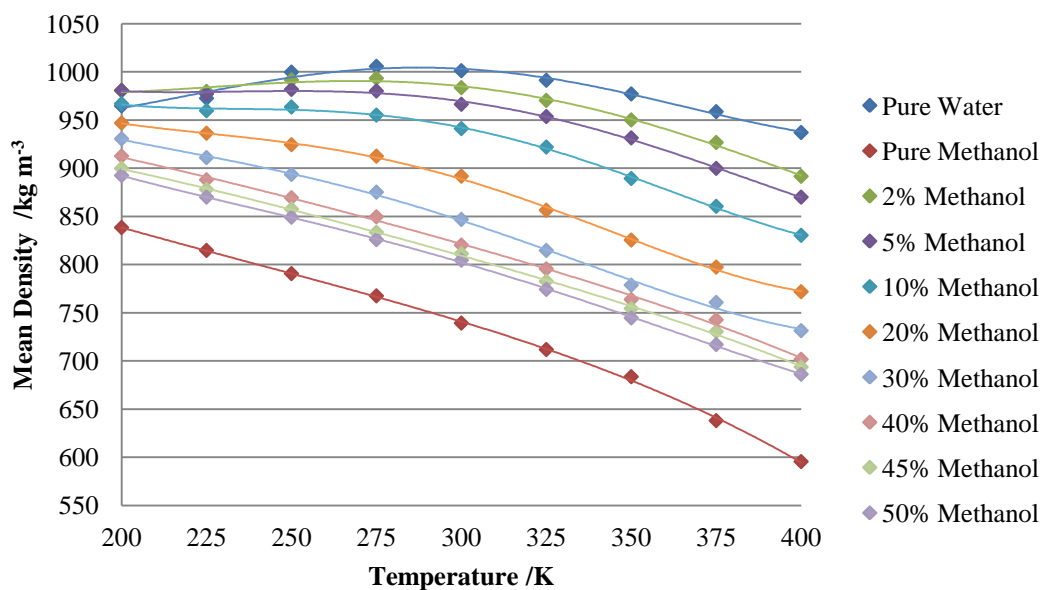


**Figure 18:** Graph showing the density as a function of temperature for a range of different concentrations of methanol between 2% and 50%. The trend lines are all fourth order polynomials fitted to the data. Data was sampled every 2,000 timesteps with each timestep being 0.5 fs for 1,000,000 equilibration steps and 4,000,000 production steps giving a total simulation time of 2.5 ns.

At 2%, 5% and 10% concentration of methanol (**Figure 18**), the density as a function of temperature of each of the mixtures shows a similar trend to that of pure TIP4P/2005 water, with the absolute density being progressively less for each mixture. Above 10% concentration of methanol there is no maximum density of the mixture over the temperature range studied. This is due to their being sufficient numbers of methanol molecules present that the hydrogen bonding network of the water molecules is disrupted and mixture can no longer maintain the long range structural properties of water and instead the structural properties of methanol begin

to dominate the system. At 10% methanol concentration and below there is still enough water present for the mixture to behave in a similar fashion to pure water.

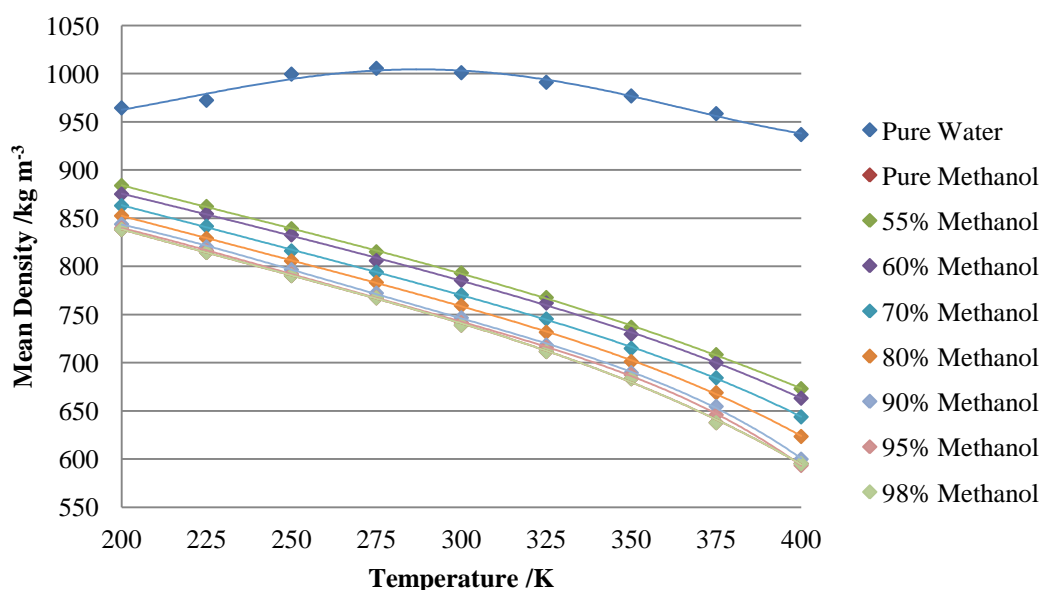


**Figure 19:** Graph showing the density as a function of temperature for a range of different concentrations of methanol between 50% and 98%. The trend lines are all fourth order polynomials fitted to the data. Data was sampled every 2,000 timesteps with each timestep being 0.5 fs for 1,000,000 equilibration steps and 4,000,000 production steps giving a total simulation time of 2.5 ns. The curve for pure methanol is obscured under the curve for 98% methanol.

As the concentration of methanol increases the density as a function of temperature shows the same trend as that of pure methanol and the absolute value of the density also decreases as the methanol concentration increases (**Figure 18** & **Figure 19**).

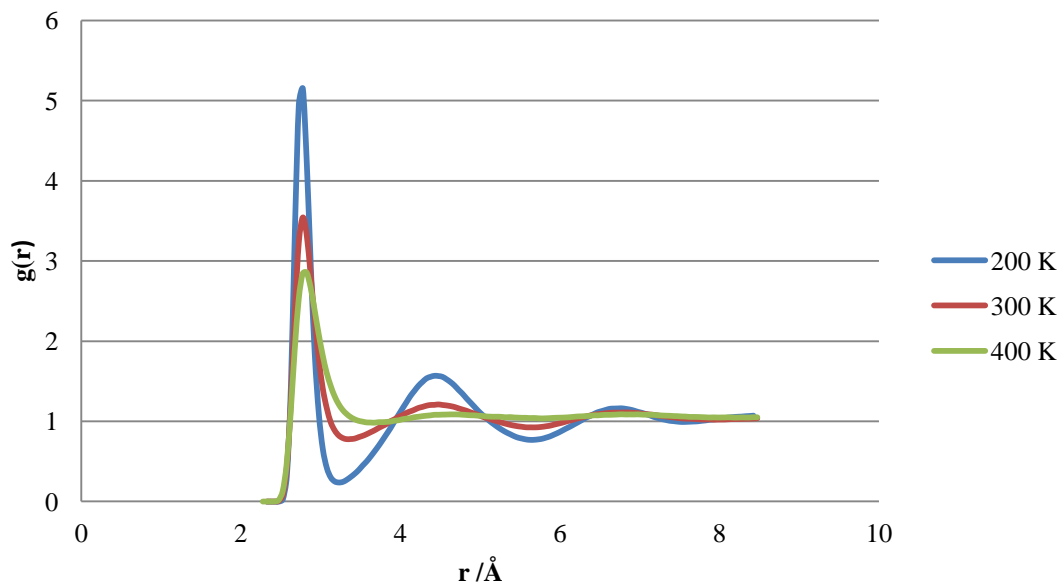


**Figure 20:** The water oxygen - water oxygen radial distribution function for a 2% methanol solution.

The water oxygen – water oxygen radial distribution function for a 2% methanol solution (**Figure 20**) does not look significantly different from that of pure TIP4P/2005 water (**Figure 6**) except that the peak is sharper. As the methanol concentration increases so does the sharpness of the peaks. This indicates that the presence of methanol causes some clustering of the water molecules. Sharper peaks indicate that there is not much variation in the oxygen – oxygen distance, suggesting that there is greater ordering in the structure of the molecules. At higher temperatures the radial distribution functions become broader indicating a more disordered arrangement of molecules. The increase in water oxygen – water oxygen peak sharpness as a function of methanol concentration indicates that repulsive interactions between water and methanol favour increased ordering of water molecules into clusters or cages such as might be found in clathrates.

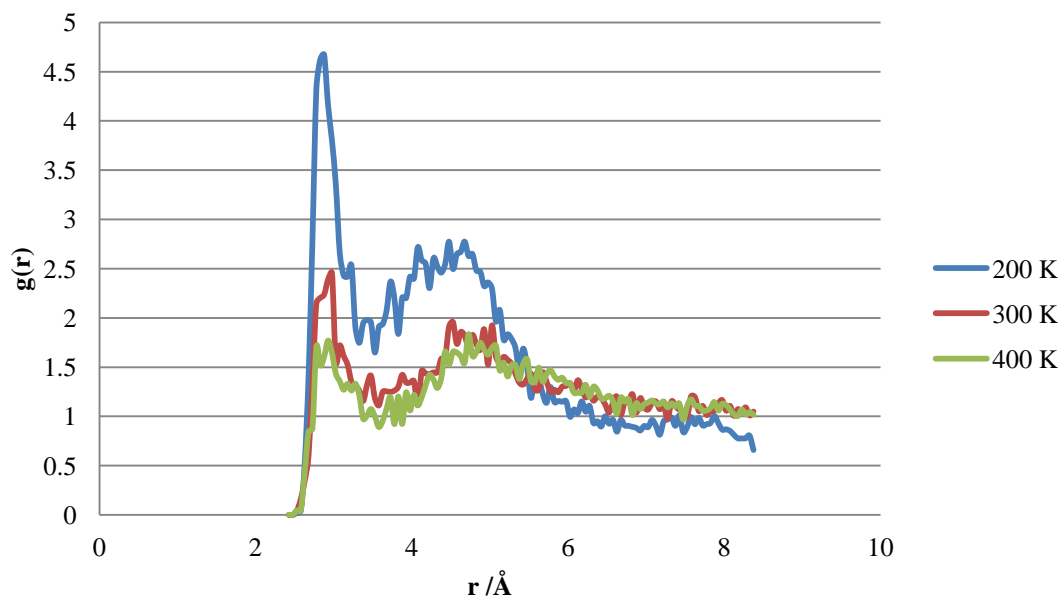


**Figure 21:** The methanol oxygen - methanol oxygen radial distribution function for a 2% methanol solution.

The methanol oxygen – methanol oxygen radial distribution function for a 2% methanol solution (**Figure 21**) is very noisy because there are only twenty methanol molecules present.

Visualisation of the DLPOLY HISTORY file showed that at 200 K most of the methanol molecules were isolated from each other, with the occasional cluster of two or three molecules forming (**Figure 22**). To visualize the molecular dynamics trajectories the program VMD [19] was used.

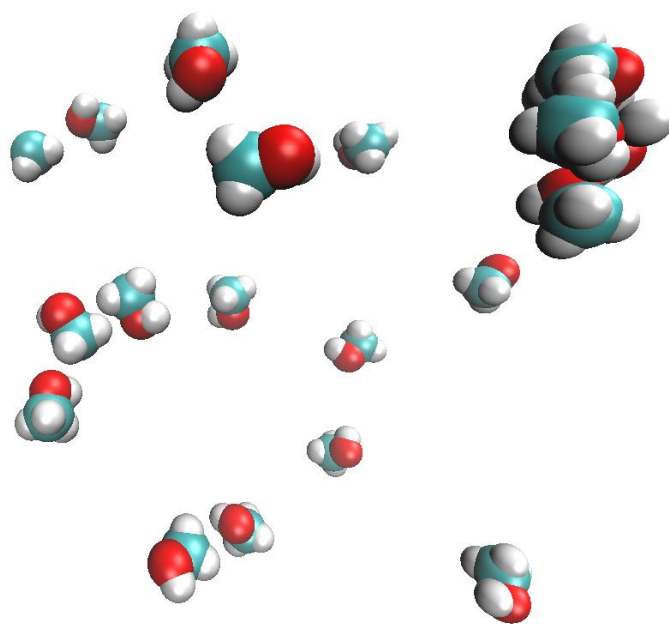


**Figure 22:** The 2% methanol mixture molecules at 200 K showing some clustering of methanol molecules. Water molecules have been omitted for clarity.

At 300 K most of the methanol molecules were isolated, however a large cluster of approximately twelve molecules did form (**Figure 23**) which persisted for approximately 70 ps before breaking into several smaller clusters of two or three molecules. For the remainder of the simulation most of the methanol molecules groups together in clusters of two or three molecules.

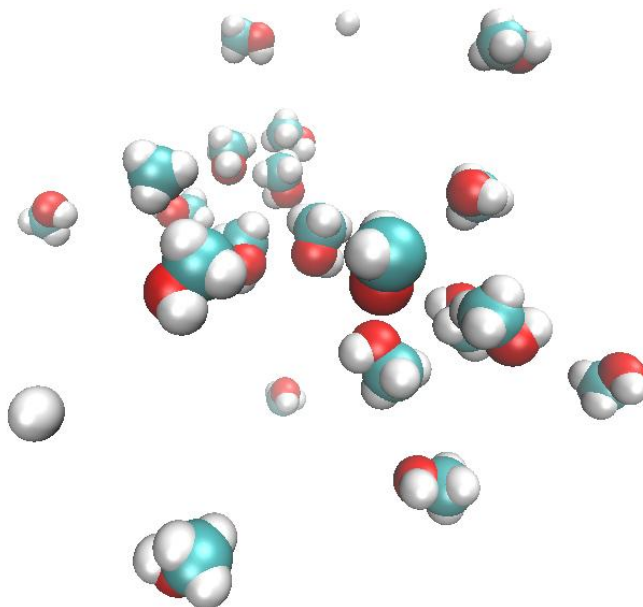


**Figure 23:** The 2% methanol mixture molecules at 300 K showing a large cluster of methanol molecules. Water molecules have been omitted for clarity.

At 400 K the occasional pair of methanol molecules was observed to briefly form before separating due to their kinetic energy (**Figure 24**).

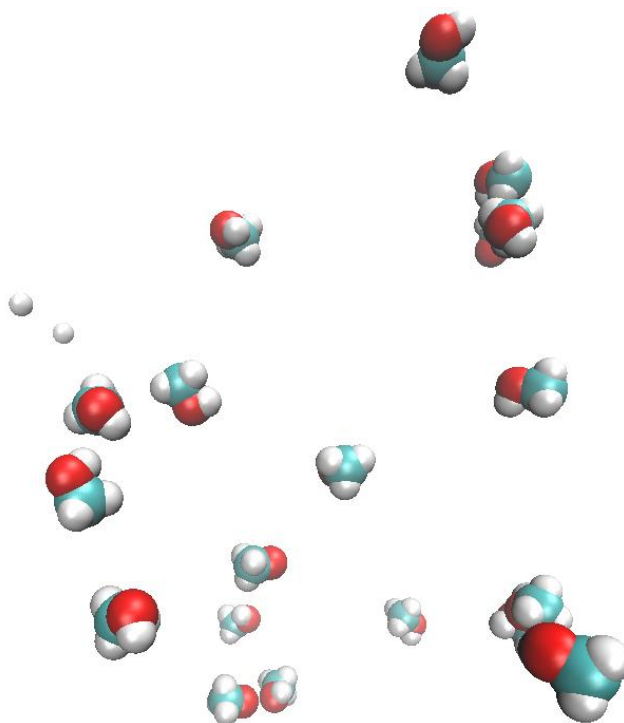


**Figure 24:** The 2% methanol mixture molecules at 400 K showing a several pairs of methanol molecules. Water molecules have been omitted for clarity.

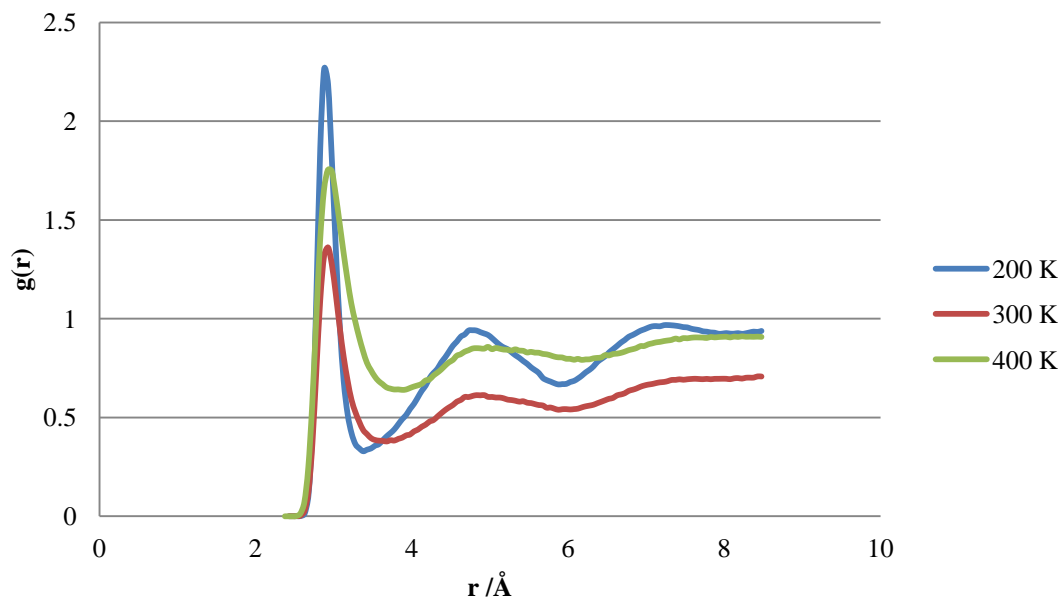


**Figure 25:** The water oxygen - methanol oxygen radial distribution function for a 50% methanol solution.

The water oxygen – methanol oxygen radial distribution at 400 K is above that at 300 K for the simulations of methanol concentration between 10% and 80%, an example for 50% methanol concentration is shown in **Figure 25** and the radial distribution functions for the other concentrations looked similar. This occurs because at higher temperatures there is less clustering of water and methanol with other molecules of the same type and hence a greater likelihood of interactions with molecules of the other type (**Figure 26**).

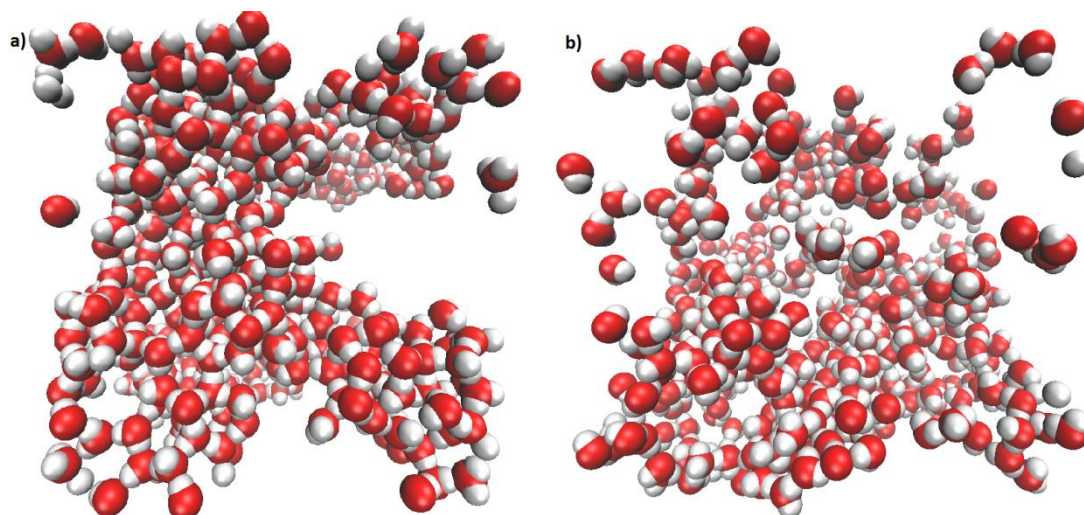


**Figure 26:** Water molecules in the 50% methanol mixture at a) 200 K, and b) 400K. Large voids in the 200 K simulation show that there is more clustering of molecules of the same type together. Methanol molecules have been omitted for clarity.

For the more extreme concentrations of water or methanol the trend in the radial distribution functions is what would be expected with the peaks becoming broader at higher temperatures (**Figure 20** & **Figure 27** for example) indicating less ordering in the system.

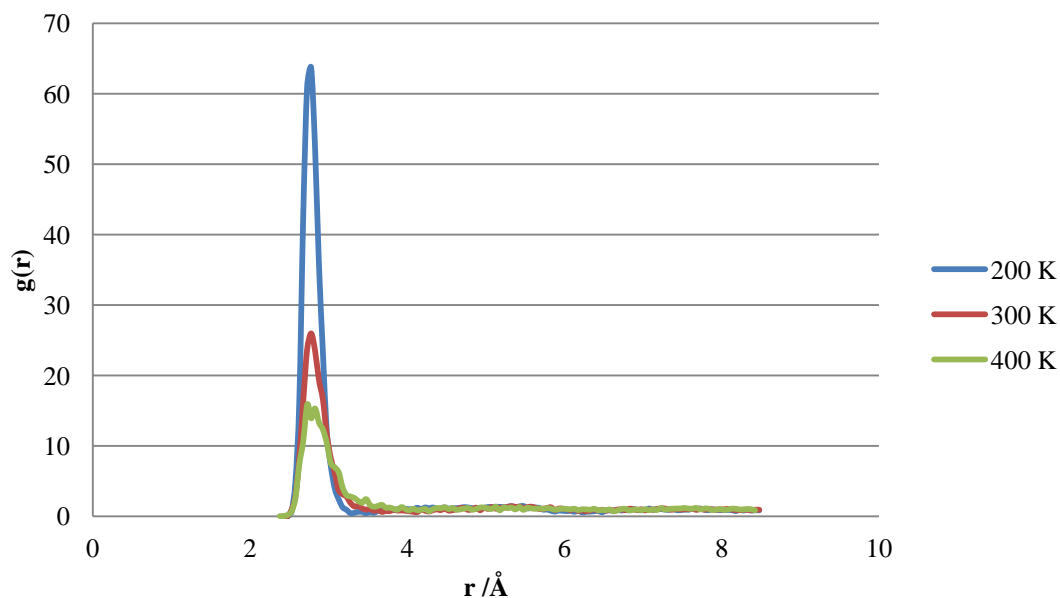


**Figure 27:** The water oxygen - water oxygen radial distribution function for a 98% methanol solution.

The water molecules in the 98% methanol solution are initially isolated from each other (**Figure 27**). Visualisation of the DLPOLY HISTORY file showed that at 200

Some of the water molecules quickly form into clusters of two or three molecules, with others remaining isolated. Over the course of the simulation the isolated molecules also begin to form into clusters (**Figure 28**).

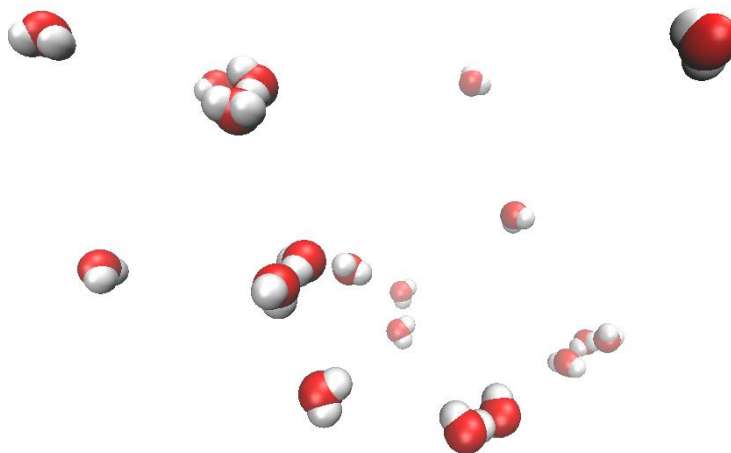


**Figure 28:** The 98% methanol mixture molecules at 200 K showing some clustering of water molecules. Methanol molecules have been omitted for clarity.

At 300 K there was less clustering of the water molecules, with only the occasional pair or trio being observed to form for short durations. The clusters break apart and the molecules form new clusters with other isolated molecules (**Figure 29**).

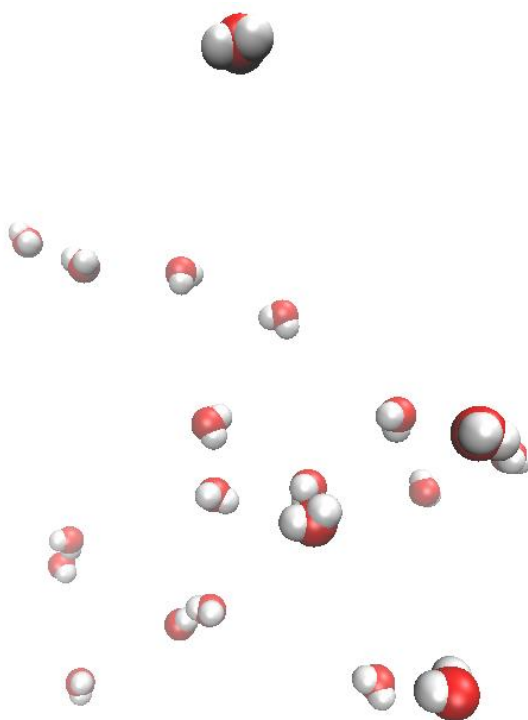


**Figure 29:** The 98% methanol mixture molecules at 300 K showing less clustering of water molecules than at 200 K. Methanol molecules have been omitted for clarity.

At 400 K most of the water molecules remain isolated from each other with the occasional pair forming before breaking apart due to their kinetic energy (**Figure 30**).

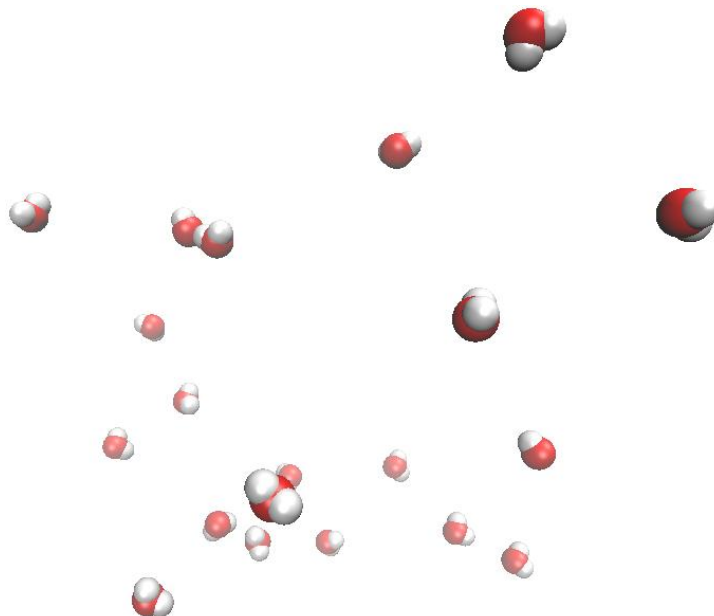


**Figure 30:** The 98% methanol mixture molecules at 400 K showing mostly isolated water molecules than at 200 K. Methanol molecules have been omitted for clarity.

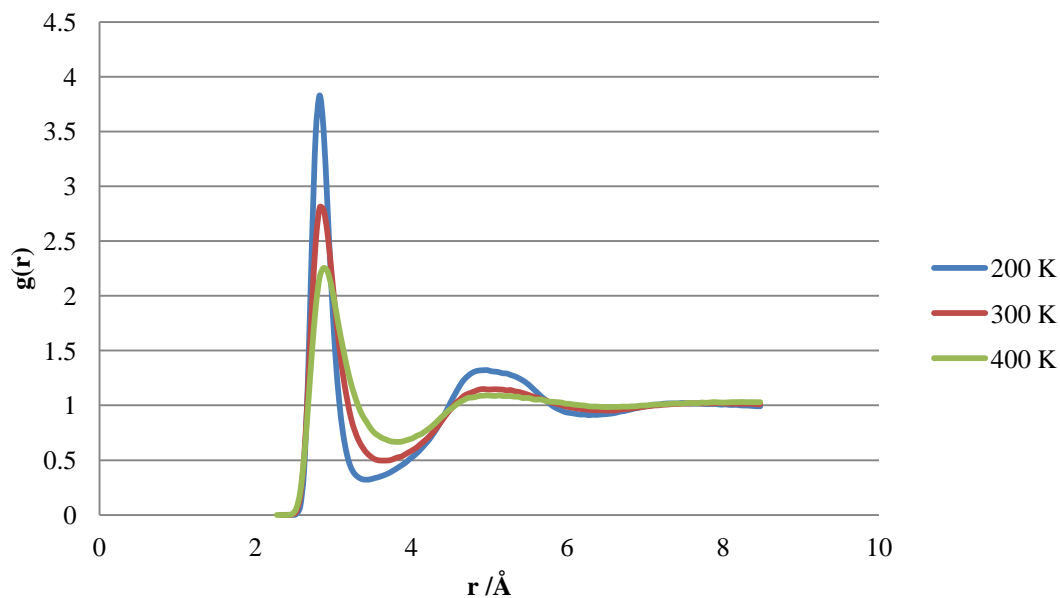


**Figure 31:** The methanol oxygen - methanol oxygen radial distribution function for a 98% methanol solution.

As the concentration of a molecule decreases the peaks in the radial distribution function of that molecule interacting with the same species become sharper

indicating that the molecules form clusters, typically of 2-3 molecules at 2% concentration. At higher temperatures the position of the first minimum in the radial distribution functions shifts to the right indicating that on average the molecules are further away from each other (**Figure 31**), and the second peak in the radial distribution function is lower indicating less ordering of the molecules at greater distances. There are an increased number of oxygen – oxygen contacts at higher temperatures as the increased kinetic energy of the molecules allows for a greater likelihood of interaction between molecules.

Once all of the radial distribution functions for the different concentrations of water/methanol solutions were collected they were integrated using trapezoidal integration to calculate the average number of oxygen – oxygen contacts between the molecules as described in **Section 5.1.2**. The average number of contacts are plotted in **Figure 32 - Figure 34**.

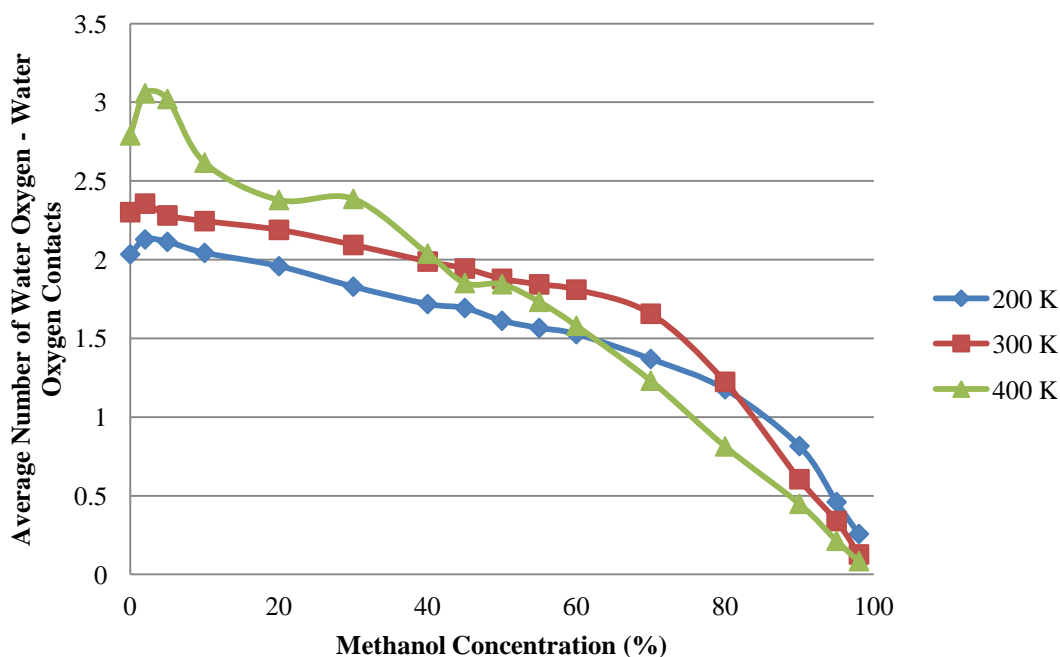


**Figure 32:** Graph showing the average number of water oxygen – water oxygen contacts.

As the methanol concentration increases the average number of water oxygen – water oxygen contacts decreases (**Figure 32**). At higher temperatures the average number of water oxygen – water oxygen contacts increases for higher concentrations of water. This occurs because the molecules have a higher energy and hence are

moving faster and therefore can interact with a greater number of other water molecules over the course of the simulation. This also means that as the concentration of methanol increases there is less opportunity for water molecules to interact with each other and form clusters, and any clusters that do form are more easily broken up. The increase in water oxygen – water oxygen contacts at 2% and 5% concentration is caused by repulsive interactions with methyl groups favouring additional ordering of the water molecules as is found in clathrates.

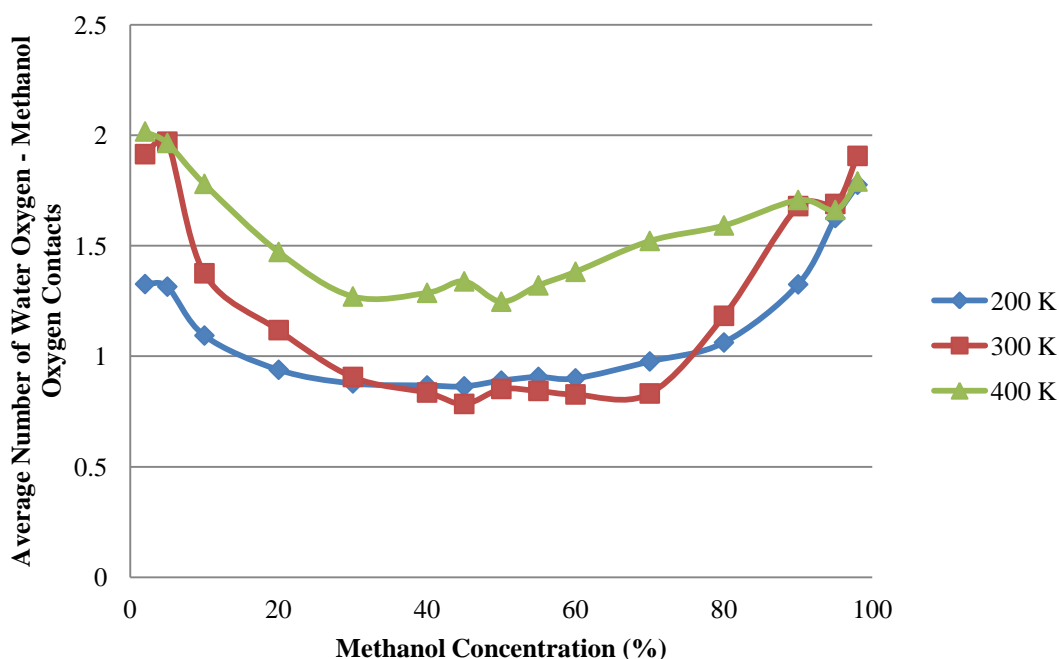


**Figure 33:** Graph showing the average number of water oxygen – methanol oxygen contacts.

The average number of water oxygen – methanol oxygen contacts is greatest at the highest concentrations of either methanol or water (**Figure 33**). Except at very low and very high concentrations of methanol there are more water – methanol contacts at 400 K than at lower temperatures. This occurs because there is less clustering of water and methanol molecules at higher temperatures, and therefore more likelihood of water and methanol molecules interacting with each other instead. At the extremes of concentration there are the greatest number of water – methanol contacts as the molecule in excess completely saturates the other type of molecule.

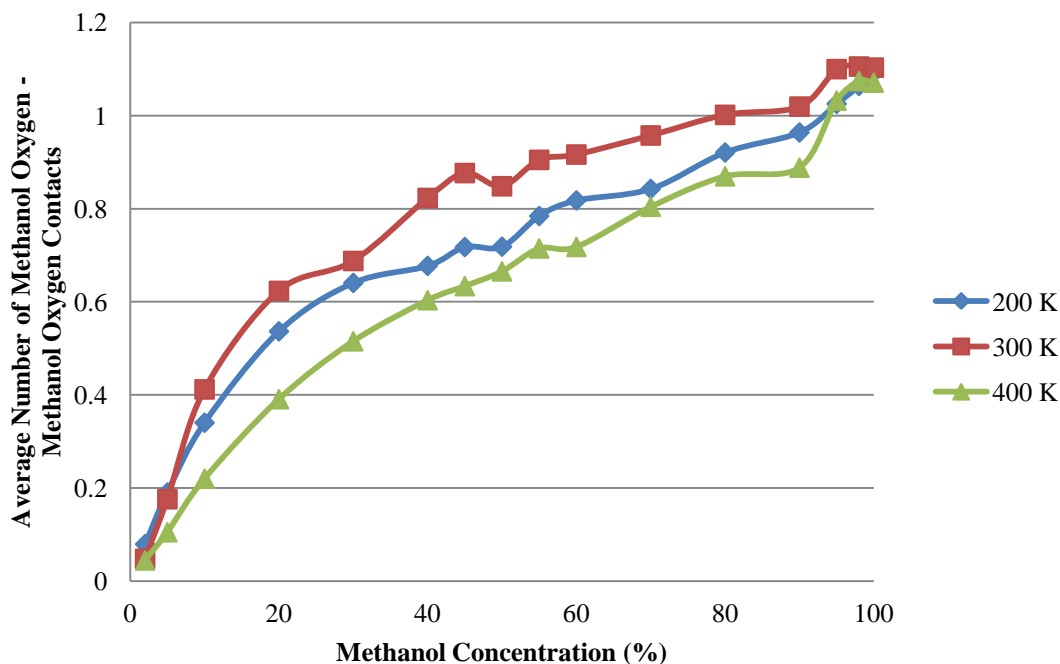


**Figure 34:** Graph showing the average number of methanol oxygen – methanol oxygen contacts.

As the methanol concentration increases the average number of methanol – methanol contacts increases (**Figure 34**). The average number of methanol – methanol contacts is greatest at 300 K and lowest at 400 K. This occurs because at higher temperatures the methanol molecules have higher kinetic energy and hence are moving faster, and therefore aggregates of methanol molecules are more easily disrupted and broken up. At 200 K there is more clustering of the methanol molecules as evidenced by the sharper peaks in the radial distribution functions, however due to the lower kinetic energy of the molecules it is difficult for the clusters to aggregate into larger structures by incorporating isolated methanol molecules and increase their oxygen – oxygen contacts or hydrogen bonding as they may never get close enough to the clusters to interact. At 300 K the methanol molecules are able to cluster together and incorporate additional isolated molecules because their kinetic energy is not so high that it breaks clusters apart, but high enough that the molecules are capable of interacting and incorporating isolated molecules.

#### 5.4. The $\text{Al}_2\text{O}_3$ (0001) Surface

In the presence of water DFT studies have shown that aluminium oxide is easy to hydroxylate (**Chapter 4, Section 4.2.3**). A fully hydroxylated aluminium oxide

surface (consisting of 270 atoms) was built and Materials Studio and imported into VASP [20], where it was optimised using the PBE functional [21]. A 35 Å vacuum gap was applied above the surface.

Water and methanol molecules were then inserted into the vacuum gap and the resulting structure was imported to DLPOLY where the *ifold* command was used to create a 2×2×1 supercell.

The fully hydroxylated supercell of the Al<sub>2</sub>O<sub>3</sub> (0001) surface (**Figure 35**) consists of 648 oxygen atoms (of which 72 atoms formed hydroxyl groups) and 432 aluminium atoms (of which 72 were tetrahedrally coordinated and the remaining 360 were octahedrally coordinated within the bulk of the slab). There were also 72 hydroxyl groups bonded to the tetrahedrally coordinated aluminium atoms.

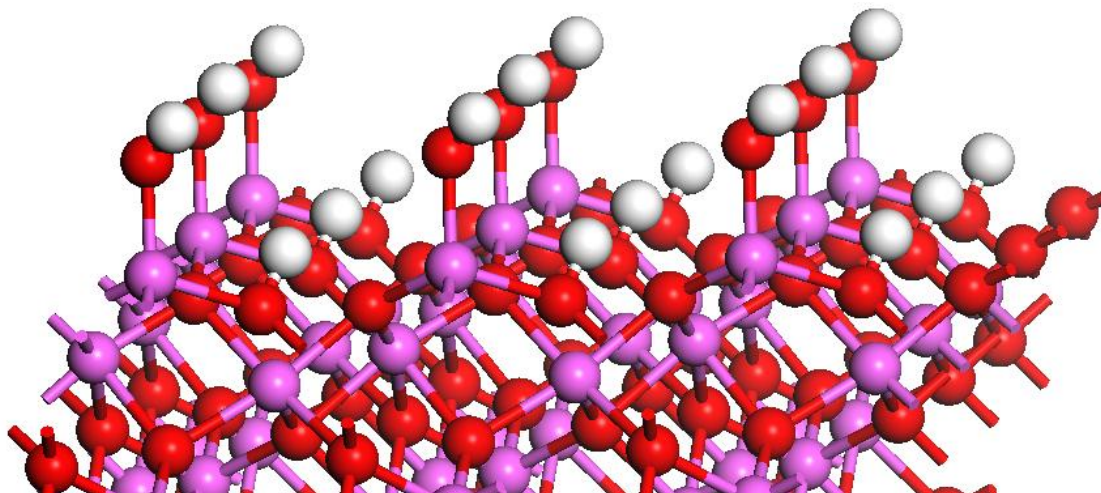


**Figure 35:** The fully hydroxylated Al<sub>2</sub>O<sub>3</sub> (0001) surface.

The aluminium oxide surface was modelled using the CLAYFF potential, the water molecules were modelled using the TIP4P/2005 potential and the methanol molecules were modelled using the PCFF potential. How these potentials are combined is described in **Section 5.3.1**. As with the earlier water and methanol simulations a van der Waals cut off of 8.5 Å was used.

#### 5.4.1. TIP4P/2005 Water

628 TIP4P/2005 water molecules forming ten layers were then inserted into the vacuum gap and an NPT calculation was then performed at 300 K on the system.

The two different hydroxyl groups present in the simulations are shown in **Figure 36**. They are where a hydrogen atom is bonded to an oxygen atom that is part of the surface (**Figure 36a**), and where an –OH group is bonded to an aluminium atom that is part of the surface (**Figure 36b**).

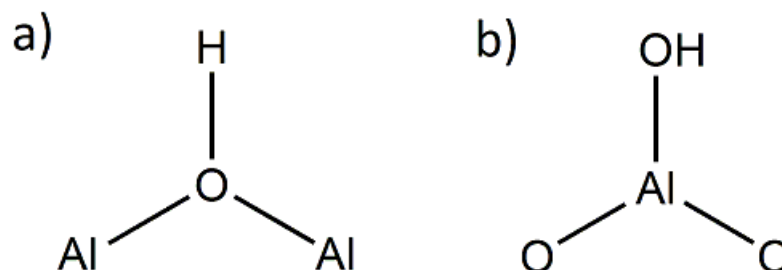


**Figure 36:** a) the surface oxygen bound hydroxyl group and b) the aluminium bound hydroxyl group.

**Table 5:** Table showing the average number of oxygen – oxygen contacts at 300 K.

Oxygen Contact Type	Average Number of Oxygen – Oxygen Contacts
Water – Water (Pure)	2.30
Water – Water (Surface)	1.99
Water – Hydroxyl Group	0.25
Water – Hydroxyl Group (Al)	1.56

Compared to pure TIP4P/2005 water which has on average 2.30 oxygen – oxygen contacts with other water molecules, TIP4P/2005 water in the presence of a hydroxylated  $\text{Al}_2\text{O}_3$  surface has 1.99 oxygen – oxygen contacts (**Table 5**). This is due to water forming hydrogen bonds with the hydroxyl groups instead of other water molecules hence reducing the number of hydrogen bonds that can be formed with other water molecules. TIP4P/2005 water has 1.56 oxygen – oxygen contacts with the hydroxyl groups bonded to the aluminium atoms in the surface. There are fewer oxygen – oxygen contacts with the hydroxyl groups formed by the oxygen atoms in the surface due the steric hindrance from the other hydroxyl groups making it difficult for water molecules to approach close enough to form hydrogen bonds. In this potential the water – water interaction is stronger than the water – hydroxyl group interaction both in terms of the electrostatic interactions and the van der Waals interactions (**Appendix 1**), hence water – water interactions are favoured.

Visualisation of the DLPOLY HISTORY file showed that the water molecules closest to the hydroxylated surface remained close to the surface throughout the simulation. The water molecules that were further away from the surface were less constrained by interactions with the hydroxyl groups and were able to move much more freely. Visualisation also showed a void within the vacuum gap which is likely due to there being too few water molecules present to completely fill the gap.

#### 5.4.2. PCFF Methanol

424 PCFF methanol molecules forming eight layers were inserted into the vacuum gap and an NPT simulation was then performed at 300 K on the system.

**Table 6:** Table showing the average number of oxygen – oxygen contacts at 300 K.

Oxygen Contact Type	Average Number of Oxygen – Oxygen Contacts
Methanol – Methanol (Pure)	1.10
Methanol – Methanol (Surface)	1.47
Methanol – Hydroxyl Group	0.21
Methanol – Hydroxyl Group (Al)	1.97

Compared to pure PCFF methanol which has on average 1.10 oxygen – oxygen contacts with other methanol molecules, PCFF methanol in the presence of a hydroxylated  $\text{Al}_2\text{O}_3$  surface has 1.47 oxygen – oxygen contacts (**Table 6**). PCFF methanol also has 1.97 oxygen – oxygen contacts with the hydroxyl groups bonded to the aluminium atoms in the surface. There are fewer oxygen – oxygen contacts between the hydroxyl groups formed by the oxygen atoms in the surface due the steric hindrance from the other hydroxyl groups.

Visualisation of the DLPOLY HISTORY file showed that methanol molecules closest to the hydroxylated surface remained close to the surface throughout the simulation with the alcohol group oriented towards the surface. This accounts for the large number for the hydroxyl group – methanol contacts as well as the increase in methanol – methanol contacts. The methanol molecules that were further away from the surface were less constrained by interactions with the hydroxyl groups and were able to move much more freely.

### 5.4.3. TIP4P/2005 Water and PCFF Methanol

268 TIP4P/2005 water molecules and 272 PCFF methanol molecules (50.4% methanol concentration) forming nine layers were inserted into the vacuum gap and an NPT calculation was then performed at 300 K on the system.

**Table 7:** Table showing the average number of oxygen – oxygen contacts. Bracketed values are those for the 50% methanol – water mixture.

Oxygen Contact Type	Average Number of Oxygen – Oxygen Contacts
Water – Water	1.28 (1.88)
Methanol – Methanol	0.75 (0.85)
Water – Methanol	1.89 (0.85)
Water – Hydroxyl Group	0.39
Water – Hydroxyl Group (Al)	1.66
Methanol – Hydroxyl Group	Unusual RDF (see <b>Figure 37</b> )
Methanol – Hydroxyl Group (Al)	0.38

Water has significantly more oxygen – oxygen contacts with the surface hydroxyl groups than methanol (**Table 7**). Compared to the 50% methanol mixture there are significantly more oxygen – oxygen contacts between water and methanol, but fewer water – water and methanol – methanol contacts. This indicates that the presence of the surface reduces the likelihood of molecules of one type clustering together and excluding the other type of molecule. There is also significant water oxygen – hydroxyl group oxygen contact, although not to the same extent as with the pure water slab simulation, due to some of the water molecules being displaced by methanol molecules. The methanol oxygen – hydroxyl group oxygen contacts are much lower in the mixed slab simulation than in the pure methanol slab simulation as most of the methanol molecules are displaced by water molecules. This also indicates that the water – hydroxyl interactions are stronger than the methanol – hydroxyl interactions.

Visualisation of the DLPOLY HISTORY file showed that as with the pure water and pure methanol simulations the molecules closest to the hydroxylated surface remained close to the surface throughout the simulation, while those further away

from the surface were able to move more freely. It also showed there were more water molecules than methanol molecules closer to the surface during the simulation, which accounts for the larger number of water – hydroxyl contacts than methanol – hydroxyl contacts.

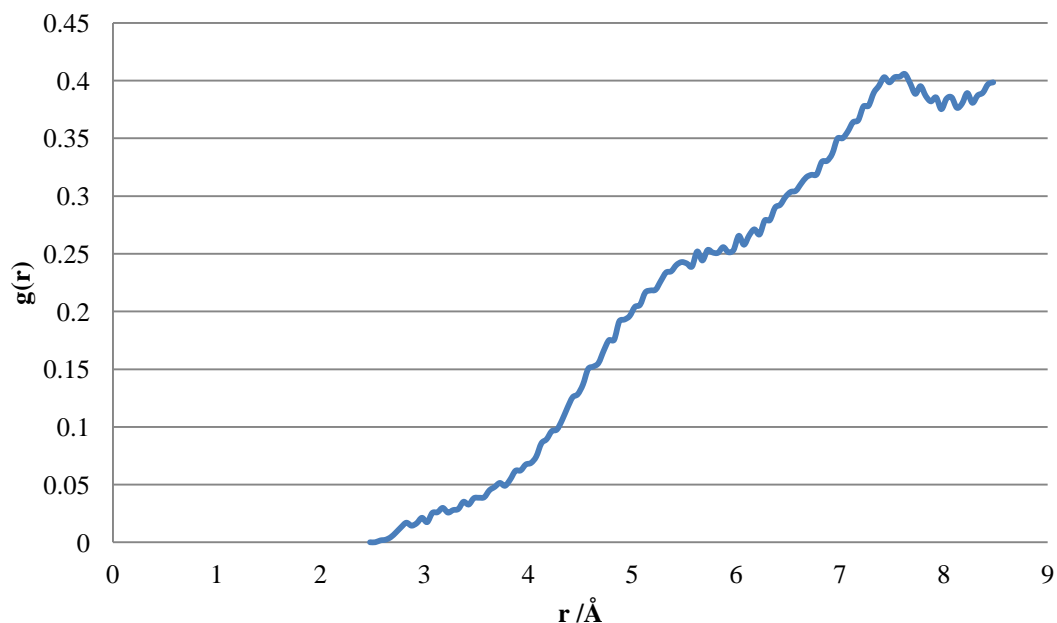


**Figure 37:** The methanol oxygen - hydroxyl group oxygen radial distribution function.

The radial distribution function for methanol – hydroxyl group oxygen (**Figure 37**) is very unusual as it shows the first minimum at a much greater distance (approximately 8 Å) than the other radial distribution functions generated by these simulations. This is due to steric hindrance from water molecules and the other aluminium bound hydroxyl groups preventing the methanol molecules from approaching and interacting with the surface hydroxyl groups

## 5.5. Conclusions

The TIP4P/2005 water model provides a much better description of water over the 200 K to 400 K temperature range than the SPC/E model. As the temperature increases there are more oxygen – oxygen contacts between water molecules, with SPC/E predicting slightly more than TIP4P/2005. SPC/E predicts slightly more oxygen – oxygen contacts than TIP4P/2005 because the oxygen van der Waals interactions are slightly stronger for SPC/E water than for TIP4P/2005 water. The increase in the number of oxygen – oxygen contacts as a function of temperature is

caused by the molecules having greater kinetic energy and thus being able to move faster and have more temporary interactions with other molecules.

The amount of oxygen – oxygen contacts in pure methanol remains almost constant (at approximately 1.1 per molecule) over the 200 K to 400 K temperature range simulated. This occurs because methanol can only donate one hydrogen bond but accept two, and the bulky methyl group causes steric hindrance preventing large numbers of alcohol groups getting close together. On the hydroxylated  $\text{Al}_2\text{O}_3$  surface methanol forms more oxygen – oxygen contacts than in pure methanol because the favourable interaction with the surface hydroxyl groups causes an ordering of the methanol molecules closest to the surface with more alcohol groups in close proximity to each other than is found in pure methanol.

Water interacts more strongly than methanol with the hydroxylated  $\text{Al}_2\text{O}_3$  surface due to the higher partial charge on the water hydrogen atoms in the potential. This data is consistent with experimental data comparing the interactions of water and 2-propanol by Mitchell *et al.* [2]. The stronger interaction with water prevents methanol from forming as many hydrogen bonds to the surface as it is difficult for methanol to displace water from the surface. In addition methanol's bulky methyl group causes steric hindrance with surface hydroxyl groups and other methanol molecules further reducing the interaction with the surface, and the steric effect will be even larger for bigger molecules such as ethylene glycol and glycerol.

Given that once molecules are adsorbed to the surface they do not move significantly over the course of the simulation it is likely that the presence of water will inhibit any reaction occurring on the surface and reduce the efficiency of the catalyst. However since these are classical simulations in which no bond breaking occurs it is possible that in reality an alcohol molecule could dissociate a proton to a hydroxyl group which then desorbs from the surface as a water molecule, then allowing the alcohol to adsorb directly to the surface. A quantum mechanical simulation could be used to study this possibility, but at present these are still very computationally expensive to perform.

## Bibliography

- [1] I. Todorov, W. Smith, K. Trachenko and M. T. Dove, *J. Mater. Chem.*, vol. 16, p. 1911, 2006.
- [2] D. Weber, J. Mitchell, J. McGregor and L. F. Gladden, *J. Phys. Chem. C.*, vol. 113, p. 6610, 2009.
- [3] J. L. F. Abascal and C. Vega, *Journal Of Chemical Physics*, vol. 123, p. 234505, 2005.
- [4] G. S. Kell, *Journal of Chemical Engineering Data*, vol. 20, p. 97, 1975.
- [5] S. Nosé, *J.Chem. Phys.*, vol. 81, p. 511, 1984.
- [6] W. G. Hoover, *Phys. Rev. A.*, vol. 31, p. 1695, 1985.
- [7] T. Kosztolanyi, I. Bako and G. Palinkas, *Journal of Molecular Liquids*, vol. 126, p. 1, 2006.
- [8] T. S. van Erp and E. J. Meijer, *Chem. Phys. Letts*, vol. 333, p. 290, 2001.
- [9] S. Kerisit, S. C. Parker and J. H. Harding, *J. Phys. Chem. B*, vol. 107, p. 7676, 2003.
- [10] N. H. de Leeuw and S. C. Parker, *Phys. Rev. B*, vol. 58, p. 13901, 1998.
- [11] J. M. Sorenson, G. Hura, R. M. Glaeser and T. Head-Gordon, *J. Chem. Phys.*, vol. 113, p. 9149, 2000.
- [12] H. J. C. Berendsen, J. R. Grigera and T. P. Straatsma, *J. Phys. Chem*, vol. 91, p. 6269, 1987.
- [13] H. Sun, *Macromolecules*, vol. 28, p. 701, 1995.

- [14] J. G. Stark and H. G. Wallace, *Chemistry Data Book*, 2nd Edition in SI ed., London: John Murray Ltd, 1982.
- [15] J. Handgraaf, T. S. van Erp and E. J. Meijer, *Chem. Phys. Letts.*, vol. 367, p. 617, 2003.
- [16] T. Yamaguch, K. Hidaka and A. K. Soper, *Mol. Phys.*, vol. 96, p. 1159, 1999.
- [17] M. Haughney, M. Ferrario and I. R. McDonald, *J.Phys. Chem.*, vol. 91, p. 4934, 1987.
- [18] R. T. Cygan, J. Liang and A. G. Kalinichev, *J. Phys. Chem. B*, vol. 108, p. 1255, 2004.
- [19] W. Humphrey, A. Dalke and K. Schulten, *J. Molec. Graphics*, vol. 14, p. 33, 1996.
- [20] G. Kresse and J. Hafner, *Phys. Rev. B.*, vol. 47, p. 558, 1993.
- [21] J. P. Perdew, K. Burke and M. Ernzerhof, *Phys. Rev. Letts.*, vol. 77, p. 3865, 1996.

## Chapter 6 – Conclusions and Future Directions

### 6.1. Conclusions

In this work periodic density functional theory calculations have been performed on the adsorption of ethylene glycol and water to various metal oxide surfaces and nanoparticles. Classical molecular dynamics calculations have also been performed on various water and methanol mixtures, and water and methanol in the presence of a fully hydroxylated aluminium oxide surface.

Hybrid DFT has been shown to produce more accurate lattice parameters for bulk materials than pure DFT, but at an impractically greater computational cost.

Adsorption of ethylene glycol has been shown to be favourable to all of the surfaces and clusters studied, but it is most favourable to the  $\text{Al}_2\text{O}_3$  (0001) and PdO (101) surfaces and least favourable to the  $\text{Au}_{38}$  and  $\text{Au}_{38}\text{O}_{16}$  clusters. Water adsorption has also been shown to be very favourable to the  $\text{Al}_2\text{O}_3$  (0001) surface. Comparing the adsorption energies for water and ethylene glycol on the  $\text{Al}_2\text{O}_3$  (0001) surface suggests that it is favourable for ethylene glycol to displace two water molecules and adsorb to the surface, but not significantly and in a real system water and ethylene glycol molecules are likely to be continually exchanging places.

The magnitude of O-H activation barriers varies depending on the surface and adsorption configuration of ethylene glycol, with the PdO (101) and MgO (130) surfaces and  $\text{Au}_{38}\text{O}_{16}$  giving the smallest barriers. This is due to the lower coordination of the oxygen atom that accepts the dissociating hydrogen atom.

C-H activation is either not possible or has a very large barrier on the  $\text{Al}_2\text{O}_3$  and various MgO surfaces. This is because these surfaces are non-reducible and the hydrogen atom dissociates carrying significant negative charge. To place this hydrogen atom onto an oxygen atom on these surfaces will require a significant amount of energy. On the reducible  $\text{Au}_{38}$  and  $\text{Au}_{38}\text{O}_{16}$  clusters there are large barriers to C-H activation, however this is due to the hydrogen atom moving through free space for part of the barrier and consequently this is unlikely to occur in reality. Different initial adsorption structures for ethylene glycol to these clusters and the presence of explicitly modelled solvent molecules may result in more realistic (and

favourable) barriers. The PdO (101) surface is also reducible and it is the only material in this work to show small barriers to both O-H and C-H activation, as well as thermodynamic favourability. This occurs as it is energetically favourable for an  $O_{3c}$  atom to absorb the first dissociating hydrogen atom which dissociates with significant positive charge, and for a  $Pd_{3c}$  atom to adsorb the second dissociating hydrogen atom which dissociates with significant negative charge, which leads to the mechanism proposed in **Section 4.3.1**.

Nudged elastic band calculations have shown that it is energetically favourable to achieve almost complete hydroxyl group coverage of the  $\alpha\text{-Al}_2\text{O}_3$  (0001) surface from dissociating water molecules with small activation energy barriers, however this is for a  $2\times 2$  surface and it is unknown if this remains true for larger surfaces.

The TIP4P/2005 water model provides a much better description of water over the 200 K to 400 K temperature range than the SPC/E model. As the temperature increases there are more oxygen – oxygen contacts between water molecules, with SPC/E predicting slightly more than TIP4P/2005. SPC/E predicts slightly more oxygen – oxygen contacts as the oxygen – oxygen Van der Waals interactions are slightly stronger for SPC/E water than for TIP4P/2005 water. The increase in oxygen – oxygen contacts as a function of temperature is caused by the molecules having greater kinetic energy and thus being able to move faster and have more temporary interactions with other molecules.

The amount of oxygen – oxygen contacts in pure methanol remains almost constant (at approximately 1.1 per molecule) over the 200 K to 400 K temperature range simulated as methanol can only donate one hydrogen bond, but accept two. On the hydroxylated  $\text{Al}_2\text{O}_3$  surface methanol forms more oxygen – oxygen contacts than in pure methanol. This occurs because the favourable interaction with the surface hydroxyl groups causes an ordering of the methanol molecules closest to the surface with more alcohol groups in close proximity to each other than is found in pure methanol.

Water interacts more strongly than methanol with the hydroxylated  $\text{Al}_2\text{O}_3$  surface due to the higher partial charge on the water hydrogen atoms in the potential. This prevents methanol from forming as many hydrogen bonds to the surface hydroxyl groups. In addition the relatively bulky methyl group of the methanol molecule

causes steric hindrance with surface hydroxyl groups and other methanol molecules further reducing the interaction with the surface, and this steric effect will be even greater for larger alcohols such as ethylene glycol and glycerol.

A solvent that interacts more strongly with the surface of a catalyst than the reactant molecule will reduce the efficiency of the catalyst. By comparing the adsorption energies of different solvent molecules it is possible to suggest which solvents would be most efficient to use experimentally.

Of the materials studied in this work, palladium oxide has been shown to be the most efficient material for the oxidation of ethylene glycol to hydroxyethanal as it is a reducible material which can adsorb dissociating H<sup>+</sup> ions from ethylene glycol, unlike the non-reducible materials. In addition the geometry of the PdO (101) surface is more favourable for the adsorption of ethylene glycol than the Au<sub>38</sub> and Au<sub>38</sub>O<sub>16</sub> clusters. The presence of solvent molecules may change this as it has been shown that the presence of water molecules can significantly reduce the size of activation energy barriers. The combination of different catalyst materials may also lead to the development of a new catalyst that is more efficient than any single material in isolation.

This work should hopefully provide some new insight into the interactions of alcohols and water with catalyst surfaces and allow for the development of new catalytic materials.

## **6.2. Future Directions**

While there are many different DFT functionals in existence, the PBE functional was chosen as it offered the best balance between computation speed and accuracy of the functionals available in VASP, however newer versions of VASP have added new functionals and new features such as Grimme's D2 dispersion correction [1] to the calculations it can perform. These new functionals and features should be tested to see if they improve the performance and accuracy of calculations on the systems being studied.

Ethylene glycol and methanol are only two of many commercially and industrially important alcohols, the calculations performed in this work can be easily extended to include other alcohols such as glycerol and propanol.

Further oxidation reactions of ethylene glycol can also be studied, such as the oxidation to hydroxyethanoic acid or glyoxal, as well as the oxidation of other molecules such as glycerol to acrolein.

Since the barriers to O-H and C-H activation are small on some surfaces but not on others it opens up the possibility of combining different materials to improve the catalysis. In this scenario one material would perform the first step of the reaction and the other would perform the second step. For example a gold nanoparticle supported on an aluminium oxide surface where the aluminium oxide support catalyses O-H activation and the gold nanoparticle catalyses C-H activation. The results obtained in this work suggest that the support material does play some role in the activity of the catalyst and this merits further investigation. Different combinations of materials could be tested to determine the most efficient combination to use, as well as the interface and binding between the materials.

Given the very low barriers to hydroxylation of aluminium oxide it is likely that any real aluminium oxide surface will be at least partially hydroxylated in the presence of water. This will likely have significant effects on the adsorption and reactions of ethylene glycol with this surface. Therefore calculations on aluminium oxide surfaces at different levels and arrangements of hydroxylation should be performed. Similar calculations on other easily hydroxylated surfaces should also be performed and compared.

There are many different surface terminations of the metal oxides which have not been studied in this work. The calculations performed here can be easily extended to include additional surface geometries such as corners, kinks and different step sites. The effects of oxygen or metal atom defects can also be studied, as well as doping with different atoms.

There is a vast array of different catalytic metal oxides and only a few have been studied here. Calculations on any of these may lead to greater insight into the behaviour of metal oxide catalysts. Experimentally, nanoparticles consisting of alloys of several different metals such as gold, platinum and palladium are often used for the oxidation of alcohols. Calculations on different sized and shaped nanoparticles of different ratios and arrangements of metal atoms may also be of interest.

Classical molecular dynamics can be used to determine probable adsorption sites by analysing the positions of adsorbate molecules before performing DFT calculations. These probable configurations can then be imported into VASP (or another suitable program) for higher accuracy calculations. If suitable classical potentials for the metals and metal oxides being studied do not exist they will be developed as necessary using experimental data if it is available or high level *ab initio* data if it is not available.

Hybrid quantum mechanics/molecular mechanics codes (QM/MM) such as NWChem [2] could also be used to model a surface and adsorbate at high accuracy (QM), and a large number of solvent molecules at lower accuracy (MM). Molecular modelling on GPU (graphics processing unit) is an emerging field where calculations are performed using specialised graphics cards rather than general purpose CPUs. Typically this requires the use of more specialised hardware and specifically modified software but it does show promise for significantly speeding up calculations.

## **Bibliography**

- [1] S. Grimme, *J. Comp. Chem.*, vol. 27, p. 1787, 2006.
- [2] M. Valiev, E. J. Bylaska, N. Govind, K. Kowalski, T. P. Straatsma, H. J. J. van Dam, D. Wang, J. Nieplocha, E. Apra, T. L. Windus and W. A. de Jong, *Computer Physics Communications*, vol. 181, p. 1477, 2010.

## Appendices

### Appendix 1 – DLPOLY FIELD Files

#### DLPOLY FIELD File for TIP4P/2005 Water

```
Water TIP4P/2005
UNITS kcal
MOLECULES 1
TIP4P/2005 water
NUMMOLS 1000
ATOMS 4
  ow    15.9996   0.0000   1
  hw    1.00080  0.5564   1
  hw    1.00080  0.5564   1
  M     0.10000  -1.1128   1
rigid 1
4 1 2 3 4
FINISH
VDW 1
  ow    ow lj 0.18519  3.1589
close
```

#### DLPOLY FIELD File for SPC/E Water

```
Water SPC/E
UNITS kcal
MOLECULES 1
SPC/E water
NUMMOLS 1000
ATOMS 3
  O     15.9996  -0.8476   1
  H1    1.00080  0.4238   1
  H2    1.00080  0.4238   1
CONSTRAINTS 3
1 2 1.0000
1 3 1.0000
2 3 1.63299
FINISH
VDW 1
  O     O lj 0.15539  3.16555
close
```

#### DLPOLY FIELD File for PCFF Methanol

```
Methanol - PCFF
UNITS kcal
MOLECULES 1
Methanol
NUMMOLS 1000
ATOMS 6
```

```

c3_1  12.011000 -0.026000  1
oh_1  15.999000 -0.557000  1
ho_1  1.008000  0.424000  1
hc_1  1.008000  0.053000  3
BONDS 5
quar  2  1  800.79080  1.42000 -2505.58530  5252.05680
quar  2  3  1065.01240  0.96500 -3848.71500  8019.06320
quar  1  4  690.00000  1.10100 -2075.67000  3378.40000
quar  1  5  690.00000  1.10100 -2075.67000  3378.40000
quar  1  6  690.00000  1.10100 -2075.67000  3378.40000
ANGLES 7
quar  1  2  3  105.41220  105.80000  -36.32700  -39.47240
quar  2  1  4  117.08920  108.72800  -32.42640  -49.60240
quar  2  1  5  117.08920  108.72800  -32.42640  -49.60240
quar  2  1  6  117.08920  108.72800  -32.42640  -49.60240
quar  4  1  5  79.28200  107.66000  -38.76300  -9.72720
quar  4  1  6  79.28200  107.66000  -38.76300  -9.72720
quar  5  1  6  79.28200  107.66000  -38.76300  -9.72720
DIHEDRALS 3
cos3  4  1  2  3  0.18630 -0.43380 -0.21210
cos3  5  1  2  3  0.18630 -0.43380 -0.21210
cos3  6  1  2  3  0.18630 -0.43380 -0.21210
FINISH
VDW 10
oh_1  oh_1  nm  0.2400  9  6  3.5350
oh_1  c3_1  nm  0.1062  9  6  3.8091
oh_1  ho_1  nm  0.0033  9  6  3.1498
oh_1  hc_1  nm  0.0615  9  6  3.3189
c3_1  c3_1  nm  0.0540  9  6  4.0100
c3_1  ho_1  nm  0.0011  9  6  3.5728
c3_1  hc_1  nm  0.0233  9  6  3.6691
ho_1  ho_1  nm  0.0130  9  6  1.0980
ho_1  hc_1  nm  0.0016  9  6  2.6693
hc_1  hc_1  nm  0.0200  9  6  2.9950
CLOSE

```

### DLPOLY FIELD File for CLAYFF Al<sub>2</sub>O<sub>3</sub>, TIP4P/2005 Water and PCFF

#### Methanol

Title FIELD file generated by DLPOLY\_prep

UNITS kcal

MOLECULES 7

Molecule1

NUMMOLS 144

ATOMS 1

o 15.999000 -1.050000 1

FINISH

Molecule2

NUMMOLS 18

ATOMS 2

oh 15.999000 -0.950000 1

```
ho 1.008000 0.425000 1
BONDS 1
harm 1 2 1108.2698 1.0000
FINISH
Molecule3
NUMMOLS 18
ATOMS 2
oah 15.999000 -0.950000 1
hoa 1.008000 0.425000 1
BONDS 1
harm 1 2 1108.2698 1.0000
FINISH
Molecule4
NUMMOLS 18
ATOMS 1
az_2 26.982000 1.575000 1
FINISH
Molecule5
NUMMOLS 90
ATOMS 1
az_1 26.982000 1.575000 1
FINISH
Molecule6
NUMMOLS 39
ATOMS 4
ow 15.9996 0.0000 1
hw 1.00080 0.5564 1
hw 1.00080 0.5564 1
M 0.10000 -1.1128 1
rigid 1
4 1 2 3 4
FINISH
Molecule7
NUMMOLS 36
ATOMS 6
c3_1 12.011000 -0.026000 1
oh_1 15.999000 -0.557000 1
ho_1 1.008000 0.424000 1
hc_1 1.008000 0.053000 3
BONDS 5
quar 2 1 800.79080 1.42000 -2505.58530 5252.05680
quar 2 3 1065.01240 0.96500 -3848.71500 8019.06320
quar 1 4 690.00000 1.10100 -2075.67000 3378.40000
quar 1 5 690.00000 1.10100 -2075.67000 3378.40000
quar 1 6 690.00000 1.10100 -2075.67000 3378.40000
ANGLES 7
quar 1 2 3 105.41220 105.80000 -36.32700 -39.47240
quar 2 1 4 117.08920 108.72800 -32.42640 -49.60240
quar 2 1 5 117.08920 108.72800 -32.42640 -49.60240
quar 2 1 6 117.08920 108.72800 -32.42640 -49.60240
```

```

quar 4 1 5 79.28200 107.66000 -38.76300 -9.72720
quar 4 1 6 79.28200 107.66000 -38.76300 -9.72720
quar 5 1 6 79.28200 107.66000 -38.76300 -9.72720
DIHEDRALS 3
cos3 4 1 2 3 0.18630 -0.43380 -0.21210
cos3 5 1 2 3 0.18630 -0.43380 -0.21210
cos3 6 1 2 3 0.18630 -0.43380 -0.21210
FINISH
VDW 55
o o 12-6 629342.2025 625.459
o oh 12-6 629342.2025 625.459
o oah 12-6 629342.2025 625.459
o ow 12-6 678422.6357 678.496
oh oh 12-6 629342.2025 625.459
oh oah 12-6 629342.2025 625.459
oh ow 12-6 678422.6357 678.496
oah oah 12-6 629342.2025 625.459
oah ow 12-6 678422.6357 678.496
ow ow 12-6 731321.0213 736.025
az_1 az_1 12-6 196.1051 0.0323
az_1 az_2 12-6 196.1051 0.0323
az_2 az_2 12-6 196.1051 0.0323
o az_1 12-6 12703.8646 4.80626
o az_2 12-6 12703.8646 4.80626
oh az_1 12-6 12703.8646 4.80626
oh az_2 12-6 12703.8646 4.80626
oah az_1 12-6 12703.8646 4.80626
oah az_2 12-6 12703.8646 4.80626
ow az_1 12-6 13720.2788 5.21870
ow az_2 12-6 3016.57923 2.65415
oh_1 oh_1 12-6 748553 872.194
c3_1 c3_1 12-6 523841 300.724
ho_1 ho_1 12-6 1.09113 0.067564
hc_1 hc_1 12-6 14031.6 33.3174
oh_1 c3_1 12-6 648683 511.451
oh_1 ho_1 12-6 3643.91 7.07437
oh_1 hc_1 12-6 108725 169.197
c3_1 ho_1 12-6 3775.53 4.1766
c3_1 hc_1 12-6 101601 98.2287
ho_1 hc_1 12-6 398.293 1.45282
o oh_1 12-6 687088.226531306 738.9837923989
oh oh_1 12-6 687088.226531306 738.9837923989
oah oh_1 12-6 687088.226531306 738.9837923989
ow oh_1 12-6 740548.395112913 801.5802568598
az_1 oh_1 12-6 14201.0786981151 5.7460996803
az_2 oh_1 12-6 3064.565477092 2.8952382935
o c3_1 12-6 581421.99099512 436.4230211926
oh c3_1 12-6 581421.99099512 436.4230211926
oah c3_1 12-6 581421.99099512 436.4230211926
ow c3_1 12-6 627126.327479055 473.5666063451

```

```

az_1 c3_1 12-6      10814.527604142   3.2192116428
az_2 c3_1 12-6      2554.8279957159   1.6971255022
o  ho_1 12-6        1665.0374266839   9.2146385397
oh ho_1 12-6        1665.0374266839   9.2146385397
oah ho_1 12-6       1665.0374266839   9.2146385397
ow ho_1 12-6        1787.4085270577   9.9751594378
az_1 ho_1 12-6       59.8536095855     0.0944920575
az_2 ho_1 12-6       8.0470587327      0.0375799408
o  hc_1 12-6        96986.5929332917  146.6534741073
oh hc_1 12-6        96986.5929332917  146.6534741073
oah hc_1 12-6       96986.5929332917  146.6534741073
ow hc_1 12-6        104454.860689569  159.016598891
az_1 hc_1 12-6       2226.3843362928   1.2017673518
az_2 hc_1 12-6       439.1094986709    0.578887433
CLOSE

```

## Appendix 2 – Source Codes

### Source Code To Generate A Cubic Box Of TIP4P/2005 Water

```

/*****
/***** Routine to generate a box of TIP-4P/2005 water *****/
/***** started Dave Willock & Chris Lee Feb 2012 *****/
/*****/

#include <stdio.h>
#include <string.h>
#include <limits.h>
#include <math.h>
#include "maxima.h"
#include "constants.h"
#include "structures.h"

void write_car( FILE *p_file, int *p_header_line, int *p_title_line,
               int *p_date_line, atom *p_molecule, int pbc,
               double *p_abc, int num_atoms, int do_header);

int write_config(atom *p_molecule, int num_atoms, double *p_latt_vec);

int main()
{
  /*** parameters from J Chem Phys, 120, 9665, (2004) ***/
  double roh=0.9572, theta=104.52, dm=0.1546; /** Angstrom and degrees **/

  double qM= -1.1128, qH; /*** electron charge ****/
  double epsilon = 0.18519; /*** kcal mol-1 ****/
  double sigma = 3.1589; /*** Angstrom ****/

  /*** array to hold atoms ****/
  atom molecule[MAX_ATOMS];

  int want_mols=1000; /*** Number of molecules required, should be nice cube ****/
  int naside;

  /*** lattice vector information ****/

```

```

double abc[6], latt_vec[9];

int ia,ib,ic,abc=TRUE;

/** density setting ***/
double density=1.0;      /** g cm-3 ***/
double mol_mass=18.0;    /** molecular mass of water g mol-1 ***/
double gcm3_to_molsA3 = 0.602214;/** conversion factor for density and mol_mass ***/
                        /** to molecules per cubic Angstrom ***/
double volpmol, gap;

/** Additional variables ***/

int i, iatom, num_atoms, natomspmol;

/**Start of code ***/

/** Work out required gap between molecules for the density set on a simple cubic lattice
***/
volpmol= mol_mass / (gcm3_to_molsA3 * density);
gap = pow(volpmol, 1.0/3.0);

printf("Density implies volume per molecule = %10.6f, gap= %10.6f\n", volpmol, gap);

naside= pow(want_mols, 1.0/3.0)+1;
printf("Want %d molecules so %d on a side\n", want_mols, naside);

abc[0]= gap * naside; abc[1]= gap * naside; abc[2]= gap * naside;
abc[3]= 90.0; abc[4]= 90.0; abc[5]= 90.0;
latt_vec[0]=abc[0]; latt_vec[1]=0.0; latt_vec[2]=0.0;
latt_vec[3]=0.0; latt_vec[4]=abc[1]; latt_vec[5]=0.0;
latt_vec[6]=0.0; latt_vec[7]=0.0; latt_vec[8]=abc[2];
printf("So periodic boundaries will be %10.6f %10.6f %10.6f %10.6f %10.6f %10.6f\n",
      abc[0], abc[1], abc[2],
      abc[3], abc[4], abc[5]);

qH = -qM/2.0;

/** Change theta to radians ***/
theta = theta/RAD_TO_DEG;

/** Oxygen atom at origin ***/

strcpy(molecule[0].label,"O");
strcpy(molecule[0].elem,"O");

molecule[0].x = 0.0;
molecule[0].y = 0.0;
molecule[0].z = 0.0;

molecule[0].part_chge = 0.0;

/** H atoms in xz plane ***/

strcpy(molecule[1].label,"H1");

```

```

strcpy(molecule[1].elem,"H");

molecule[1].x = roh * sin(theta /2.0);
molecule[1].y = 0.0;
molecule[1].z = roh * cos(theta /2.0);

molecule[1].part_chge = qH;

strcpy(molecule[2].label,"H2");
strcpy(molecule[2].elem,"H");

molecule[2].x = -roh * sin(theta /2.0);
molecule[2].y = 0.0;
molecule[2].z = roh * cos(theta /2.0);

molecule[2].part_chge = qH;

/**** M charge holder along z ****/

strcpy(molecule[3].label,"M");
strcpy(molecule[3].elem,"D");

molecule[3].x = 0.0;
molecule[3].y = 0.0;
molecule[3].z = dm;

molecule[3].part_chge = qM;

printf("First molecule: \n");

for (i=0; i<4; i++)
    printf("%s %10.6f %10.6f %10.6f %s %10.6f\n", molecule[i].label,
        molecule[i].x,
        molecule[i].y,
        molecule[i].z,
        molecule[i].elem,
        molecule[i].part_chge);

/**** Create simple cubic lattice ****/

num_atoms=4;
natomspmol=4;

for (ia=0; ia < naside; ia++)
{
    for (ib=0; ib < naside; ib++)
    {
        for (ic=0; ic < naside; ic++)
        {
            if (ia != 0 || ib != 0 || ic != 0 )
            {
                for ( iatom=0; iatom < natomspmol; iatom++)
                {
                    molecule[num_atoms]= molecule[iatom];
                    molecule[num_atoms].x += ia * gap;
                }
            }
        }
    }
}

```

```
        molecule[num_atoms].y += ib * gap;
        molecule[num_atoms].z += ic * gap;
        num_atoms++;
    }
}
}
}

printf("%d\n\n", num_atoms);
for (i=0; i<num_atoms; i++)
    printf("%s %10.6f %10.6f %10.6f\n", molecule[i].elem,
          molecule[i].x,
          molecule[i].y,
          molecule[i].z);

i= write_config(&molecule[0], num_atoms, &latt_vec[0]);

return 0;
```